Author:
Johnson, Mack H

Title:
Low Q-factor Silicon Photonic Cavities for Optical Filtering and Single-Photon Detection

Low Q-factor Silicon Photonic Cavities for Optical Filtering and Single-Photon Detection

By

MACK HENRY JOHNSON

Quantum Engineering Centre for Doctoral Training
UNIVERSITY OF BRISTOL

A dissertation submitted to the University of Bristol in accordance with the requirements of the degree of DOCTOR OF PHILOSOPHY in the Faculty of Science.

SEPTEMBER 2019

Word count: 52,078

Abstract

Integrated silicon photonics offers great promise for both classical and quantum photonic applications. The high index-contrast of the silicon-on-insulator material system enables compact sub-micron size waveguides to be realised. Furthermore, the technology is compatible with on-chip single-photon detectors. This thesis targets the design and fabrication of components relevant for a dedicated detector chip that can be used in chip-to-chip quantum photonic experiments where high performance single-photon detectors and on-chip optical filters are required.

A design for optical filtering on-chip is presented based on ring resonators that is fully compatible with single-photon detector design and fabrication. An absorptive nanowire can be fabricated onto the ring resonator and the device can be operated in the critical coupling regime. Design considerations for the nanowire are given and up to 33 dB extinction is shown in a single ring, whilst up to 52 dB extinction is shown in a linear cascade of three rings. This low Q-factor filtering approach promises to suppress the build up of electric field intensity inside the critically coupled resonators, preventing spurious non-linear effects such as single-photon generation within the cavity. The advantages and disadvantages of this technology are discussed and contrasted with existing approaches.

A waveguide crossing for SOI strip waveguides based on multi-mode interference is designed and experimentally measured with 0.043 dB device loss and -50.2 dB crosstalk with a footprint of 14.3 x 14.3 μm^2. Furthermore, the backscatter of the waveguide crossing was also evaluated to be between -35 and -55 dB by optical time-domain reflectometry. This technology can find applications in dense on-chip integration, where many low loss interconnect components are required such as large port optical switching networks and larger scale quantum photonic experiments.

Finally, considerations for experimental realisation of a previous on-chip detector proposal based on a racetrack resonator operating in the critical coupling regime is considered. The cavity design is modified by implementing the designed waveguide crossing, allowing the nanowire to be routed to electrical contacts without inducing significant losses. The structure is further modified according to practical considerations for the detector, which improves the loss of the crossing structure to 0.0125 dB. Studies of the absorption of the nanowire in the waveguide crossing region are performed. The detection efficiency and timing jitter are explored for the modified design, showing that detection efficiencies on-chip above 95% can be reached under certain conditions. Racetrack resonators with the waveguide crossing region are experimentally tested, showing similar performances to standard racetrack resonators. Furthermore, 24 dB of critical coupling is observed in these structures, which is necessary for a high performance detector.

Dedications and acknowledgements

Although the research here has been carried out by me, I would like to start by immediately thanking the Quantum Engineering Centre for Doctoral training for providing the opportunity to branch out from my undergraduate degree which was half-chemistry and half-physics. This past has led to me personally being the butt of many jokes. However, the cross-disciplined nature of the programme and its intake across cohorts has many great aspects and the opportunities we have had has been incredible. I have met some great theoretical and experimental talent and I hope for the first cohort that we continue to brag about being the first cohort (and necessarily the best). Unfortunately, I wish they got to see me in a better condition (see below). I would like to thank QETLabs for the wide range of research and general expertise in photonics from silicon multi-project wafer runs to NV centres in diamond and quantum dots.

In the detector group of QETLabs I would like to thank Dondu Sahin, Jorge Barreto, Ben Slater, Antonio Gentile, Gerardo Villarreal, Nicola Tyler and Rob Heath. You guys are great and I strongly believe you will reap the rewards of your hard work. I've enjoyed the many laughs and socials we have had as a group.

I would like to give a special shout out to my undergraduate friends who studied Chemical Physics with me. We started our degrees from day 1 as a minority (there were 15 of us amidst the mass 100+ strong hordes of Chemistry and Physics students). Because we were not many, we took the opportunity to become close over the course of our undergraduate studies. They are all wonderful people and I have loved the times I have had with them. I am sure we will continue to conquer more mountains and drink incommensurate quantities of alcohol to boot.

I would like to thank my family for the support during my PhD. My mum, my brother (and his wife as of February 2018) have all been very understanding about what it takes and have had to bare me at the worst of times, whilst also having to go through a terrible time themselves. Unfortunately it is with great regret to mention at this point that my dad cannot be here to see this document in its final form. Up until his death due to cancer in August 2015, he supported me in many aspects of my life, including the decision to study a PhD, which was eventually made from many discussions in the final year of my undergraduate degree. Two weeks after his death, I started the research element of my PhD and I have suffered ever since. This has been coupled with other deaths that have occurred during the course of my studies, including grandparents (it deeply saddens me to say none of my grandparents are alive to see this document) and an ex-girlfriend of mine who died in a car crash in Malaysia in 2018. These tragedies have been no easy task to endure, but I am thankful to have found the strength to get through it. It is sad to look back on this period of my life and to think that the people I met during this PhD saw a very low self-esteem, depressed and fairly anti-social version of me. The issue of mental health is a

very serious one and unfortunately this could not be any more pertinent for the University of Bristol given events in the last few years. We cannot see into the minds of those suffering - we cannot fathom what they are experiencing on a daily basis. The thought that someone might appear well on the outside, but in their mind they are contemplating suicide or suffering from depression really frightens me, given I can relate to the latter from my own experiences. As a special mention, I would like to thank the heavyweight boxer Tyson Fury for spreading awareness on the seriousness of mental health issues during his comeback to boxing in 2018. One quote Tyson said stays with me - "If mental health can bring somebody as big and as strong as me to my knees, then it can bring anybody to their knees." To see you overcome your problems and come back with the mindset you have today is unbelievable. You are an inspiration champ, thank you for what you have done. If I hadn't of watched your appearance on the Joe Rogan podcast I may not have reached a better mental state like I am in now.

Finally, my last acknowledgement goes to Guthrie Govan. Although you are not a scientist, you are a real example of what it means to be the epitome - the best - at what you do. Since I discovered you playing guitar on YouTube in around 2005 or 2006, I was awestruck and as a result I started to search for new videos of you playing virtually every day. I remember seeing you play twice with The Aristocrats in 2014 and 2015. Your ability is unbounded. Your ability to improvise flawlessly and create incredible solos (for example, the solos on Steve Wilson's song 'Ancestral', or Jason Becker's song 'River of Longing') continues to amaze me. You show finesse, skill, and an uncanny ability to play every genre of music in a way that is rivaled by no one. In my opinion you are above the greats in all their respective genres and are the most talented guitar player to ever live. I am amazed at how you can be so humble with your ability. I also love the way that fellow musicians react to you, often laughing but in a 'Oh my god, he's so good!' kind of way. It's also great to see you gaining attention from the likes of Hans Zimmer and Dizzee Rascal and touring with them. I will never forget the moment your string broke during Thelma and Louise in 2016 and you were able to utilise slide guitar to remain in tune until you were handed a replacement guitar. That was a display of virtuosity. If Hans Zimmer tells you that you are truly remarkable, you better believe it. His description of your talent really resonates with how you inspire me. You have set the bar for virtuosity and diversity so unbelievably high that there won't be another person like you. You are my greatest inspiration in life. Thank you.

AUTHOR'S DECLARATION

I declare that the work in this dissertation was carried out in accordance with the requirements of the University's Regulations and Code of Practice for Research Degree Programmes and that it has not been submitted for any other academic award. Except where indicated by specific reference in the text, the work is the candidate's own work. Work done in collaboration with, or with the assistance of, others, is indicated as such. Any views expressed in the dissertation are those of the author.

SIGNED: ..... DATE: .....

List of Publications and Conferences

Publications

[1] J.Adcock, E. Allen, M. Day, S. Frick, J. Hinchliff, **M. Johnson**, S. Morley-Short, S. Pallister, A. Price, S. Stanisic, *"Advances in Quantum Machine Learning"*, arXiv:1512.02900, 2015.

[2] B. Truscott, M. Kelly, K. Potter, **M. Johnson**, M. Ashfold, Y. Mankelevich *"Microwave Plasma-Activated Chemical Vapor Deposition of Nitrogen-Doped Diamond. I. N_2/H_2 and NH_3/H_2 Plasmas"*, J. Phys. Chem. A., **119**, 12962-12976, 2015.

[3] F. Ortiz-Huerta, L. Chen, M. Taverne, J. Hadden, **M. Johnson**, D. Ho, J. Rarity, *"Fabrication of hybrid Fabry-Pérot microcavity using two-photon lithography for single-photon sources"*, Optics Express, **26**, 33245, 2018.

[4] **M. Johnson**, M. Thompson, D. Sahin, *"Low-loss, low-crosstalk silicon-on-insulator waveguide crossing for scalable integrated photonics applications"*, Submitted, 2019.

Conference Contributions

[1] 683rd WE-Heraeus-Seminar: Physics and Applications of Superconducting Nanowire Single Photon Detectors, Bad Honnef, Germany (2018). Presented a talk titled "Practical considerations of superconducting nanowire single-photon detectors in a racetrack cavity".

[2] Bristol Quantum Information Technologies workshop, Bristol, UK (2018). Presented a poster titled "Racetrack Superconducting Nanowire Single-Photon Detector".

[3] Nanoscale Quantum Optics MP 1403 - Early stage researcher workshop, Budapest, Hungary (2017). Presented a talk titled "Cavity enhanced-SNSPD – mode crossing design".

[4] GW4 Nanofabrication Workshop, Bath, UK (2017). Presented a talk titled "Dump the pump : On-chip optical filtering in integrated photonics".

Table of Contents

List of Tables

List of Figures

Figure **Page**

List of Abbreviations

BOX Buried Oxide

CMOS Complementary Metal-Oxide-Semiconductor

CNOT Controlled-NOT

DDE Device Detection Efficiency

EBL Electron Beam Lithography

FDTD Finite-Difference Time Domain

FSR Free Spectral Range

FWHM Full Width Half-Maximum

HF Hydrofluoric Acid

HSQ Hydrogen Silsesquioxane

LIDAR Light Detection and Ranging

MEMs Micro-Electro-Mechanical Systems

MMI Multi-Mode Interference

MZI Mach-Zehnder Interferometer

Nb Niobium

NbN Niobium Nitride

NbTiN Niobium Titanium Nitride

PMMA Poly-Methyl Methacrylate

PMT Photomultiplier Tube

QETLabs Quantum Engineering Technology Labs, University of Bristol

QKD Quantum Key Distribution

RIE Reactive Ion Etching

SDE System Detection Efficiency

SEM Scanning Electron Microscopy

SFWM Spontaneous Four-Wave Mixing

Si Silicon

Si_3N_4 Silicon Nitride

SiO_2 Silicon Dioxide

SNSPD Superconducting Nanowire Single-Photon Detector

SOI Silicon-on-Insulator

SPAD Single-Photon Avalanche Photodiode

TES Transition Edge Sensor

TMAH Tetra-Methyl Ammonium Hydroxide

TPA Two-Photon Absorption

VBSMZI Variable Beam Splitter Mach-Zehnder Interferometer

VLPC Visible-Light Photon Counters

WSi Tungsten Silicide

CHAPTER 1

INTRODUCTION

The concept of a single photon dates back to the early 20th century, when Einstein used quantisation of the electromagnetic field to successfully explain phenomena such as the photoelectric effect in 1905 [1]. Einstein described the electromagnetic waves as carrying discrete packets of energy. This was a resurgence of the concept of particle-like behaviour, which had previously been rejected for hundreds of years since the works of Fresnel and Huygens whose works (among others) amounted significant evidence to the wave theory of light, which were formulated beautifully in Maxwell's equations in 1865 [2]. Maxwell's equations were based on prior research with visible light over hundreds of years. However, these equations predicted a whole spectrum of electromagnetic waves, whose frequencies and wavelengths were linked to a fundamental constant c, called the speed of light. Succeeding works such as that of Hertz in 1886 confirmed the existence of radio waves experimentally, giving credence to Maxwell's work. Figure 1.1 shows an example of a electromagnetic wave.

Today, the electromagnetic spectrum is well understood and electromagnetic waves are ubiquitous in our everyday lives. One significant point of interest, which involves single photons is quantum computing applications. One of the photons degrees of freedom (such as the polarisation, or time of flight) can be exploited to make a two-level system known as a qubit [3]. The qubit is easily contrasted with the bit in a classical computer; the bit takes a binary value of 0 or 1, whereas in a qubit all values in between can be possible. This is known as superposition. This property as well as quantum entanglement, where certain two and higher dimensional qubits form a state where each qubit cannot be described independently, can be utilised in a quantum computer to gain a speed up advantage over classical computational methods [4–6].

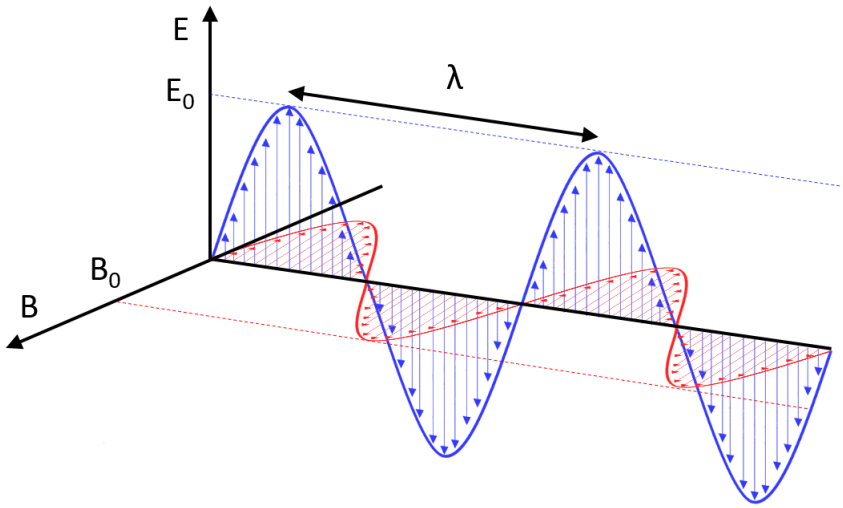

Figure 1.1: Electromagnetic wave. B and E denote the magnetic and electric field components of the wave respectively, whilst B_0 and E_0 describe their amplitudes. The fields are orthogonal, but their amplitudes are related by $E_0 = cB_0$. λ describes the wavelength, which is related to the speed of light c by $c = \nu\lambda$, where ν is the frequency.

A seminal work was produced by Hong, Ou and Mandel, which demonstrated that two single-photons incident on a balanced beamsplitter can undergo quantum interference [7]. This is shown in Figure 1.2. The quantum interference effect between these two photons is such that if a detector is placed in each rail after the beamsplitter (as in Figure 1.2(a)), and both of these photons arrive at the beamsplitter at the same time with the same properties, they will tend to bunch (register a click in the same detector) according to the permutations of each photons transmission and reflection probabilities at the beam splitter (Figure 1.2(i)-(iv)). The result is a drop in coincidence counts (registering a click at the same time) as shown through the characteristic dip in Figure 1.2(b). This result is contrary to the classical result, where an incident coherent source such as a laser will result in a balanced amplitude splitting at the beamsplitter [8]. The quantum interference is a method of inducing interactions between photons, which are very important for the realisation of gates used in linear optical quantum computing architectures [9]. Developments followed such as the work by Reck [10], which enable any NxM unitary to be implemented as a series of 2 x 2 beam splitters. These findings enabled the demonstrations of two-qubit logic gates in the early 21st century with bulk optics, which are crucial for quantum computing schemes [9, 11, 12].

The photon is a great candidate for a quantum computing architecture for a number of reasons, including its multiple degrees of freedom that can be used to produce a qubit. Another very good reason for choosing to use photons is their inherent immunity to decoherence [13]. That is to say, it does not interact with its environment, which is typically demonstrated by crossing

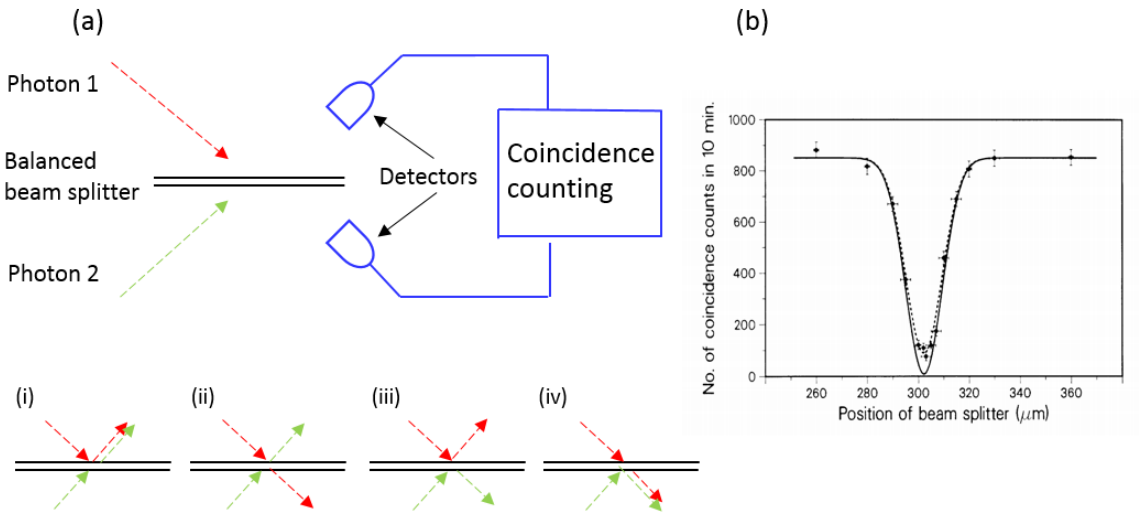

Figure 1.2: Schematic illustrating quantum interference. (a) Two single photons are incident on a balanced beam splitter. There are two detectors, with counting logic for coincidences. (i) through (iv) shows the possible combinations of reflection and transmission for photons 1 and 2 at the beamsplitter. (ii) and (iii) cancel out due to the phase considerations at the beamsplitter, leaving the bunched permutation of (i) and (iv). (b) is the signature dip (known as the HOM dip) from [7]. The dip indicates that the photons have bunched at one of the detectors.

two laser beams with each other, observing that they pass through each other unperturbed. This has an inherent advantage over matter-based systems which suffer from their specific issues, such as vibrational motion of ions in an ion trap [14, 15]. However, this is a double-edged sword; the quantum interference is required for realisation of two-qubit gates, whose desired output is non-deterministic (they occur with some success probability not equal to 1). One typical example is a controlled-NOT (CNOT) gate with success probability $\frac{1}{16}$ as described in [16]. The CNOT gate is a two-qubit gate, which operates on a control and target qubit. This gate will perform an operation on the target qubit depending on the state of the control qubit. If the control qubit is $|0\rangle$, then the target qubit remains unchanged. Conversely, if the control qubit is $|1\rangle$, then the target qubit is flipped from $|0\rangle$ to $|1\rangle$ and vice versa. The CNOT gate, coupled with one-qubit gates can enable any operation to be performed on the qubits, which is known as universal quantum computation [3, 17]. The non-deterministic operation in these gates are intrinsic to the gates itself (for example, the overall gate will produce a large quantum state, and part of the state pertaining to the desired operation is post-selected) and do not consider other effects such as non-ideal detection efficiencies. These begin to highlight some of the challenges for quantum computing with photons. However, before the challenges can be addressed, integrated silicon photonics will now be discussed to motivate our interest in this architecture.

1.1 Integrated Photonics in Silicon

The concept of integrated photonics was first proposed by Miller in 1969 with the motivation of miniaturisation [18]. This formulates the appeal of integrated optics very succinctly : scalability and reliability. Scalability stems from the size - where features are fabricated by lithographic methods (some of which are discussed in Chapter 3 and utilised in this work) onto chips. The reliability of an integrated photonic chip over other photonic architectures such as bulk optics also stems from the size, since bulk optic setups require many mirrors with precise alignment of crucial components such as beamsplitters, whereas in integrated photonics this is already satisfied, as long as the structural features are designed to their specifications. Furthermore, since these features are all on the same chip, there is greater stability since the whole chip can be packaged and operated at a similar temperature. A significant breakthrough for integrated photonics in silicon (Si) came in 1995, when LETI demonstrated their Smart Cut technology, which enabled control of the cladding thickness whilst preserving a high quality crystalline Si layer [19]. This was crucial for realisation of small on-chip features (for example, waveguides of dimensions 220 nm thick x 500 nm wide for silicon-on-insulator (SOI)) and dense integration. Given the waveguide widths are sub-micron, many waveguides can be fabricated onto a chip, highlighting the scalability of integrated photonics. The following sections will now guide through some of the advantages of silicon photonics.

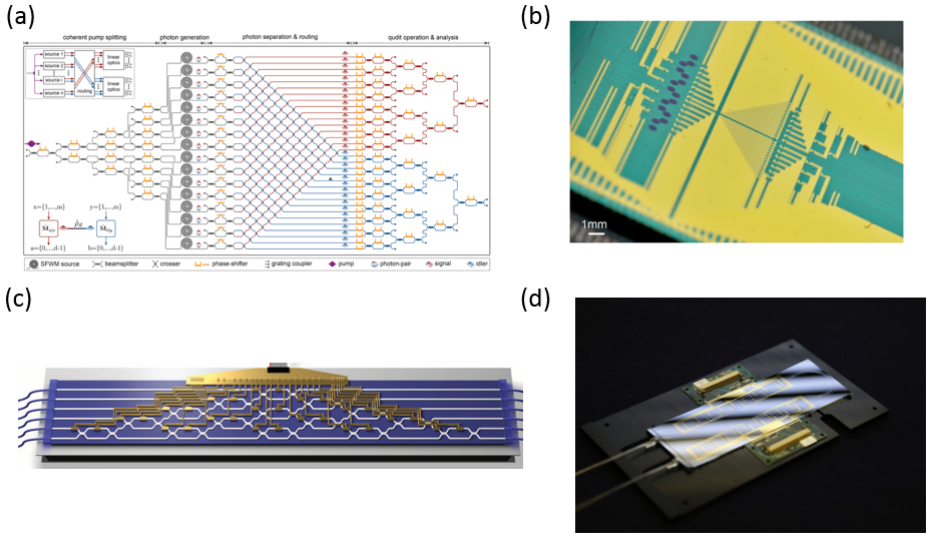

Figure 1.3: Integrated photonic demonstrations. (a) and (b) are from [20] using an SOI chip. (c) and (d) are from [21], using a silica-on-silicon chip.

1.1.1 Desirable Properties

Silicon is an optically transparent material in the infrared, with very low absorption for wavelengths larger than the visible region owing to its band gap of 1.10 eV [22]. Within this band lie important telecommunication bands, typically at 1310 nm and 1550 nm. Particularly, the appeal of the 1550 nm band stems from the established fibre technology designed for operation at this wavelength with minimal dispersion and optical losses, providing an ideal and compatible architecture with existing technologies. This compatibility with standard telecommunication equipment is one of many advantages of the material. To complement this, there are some other advantages which are now going to be discussed. To contrast, one disadvantage will also be given.

1.1.1.1 Compatibility

The transition to integrated photonics is a natural transition much like that of integrated electronics in the 20th century. Silicon-based material systems such as SOI, silica-on-silicon and silicon nitride (Si_3N_4) are all ideal material systems for integrated photonics due to their compatibility with integrated electronics. Complementary metal-oxide-semiconductor (CMOS) foundries can enable fabrication of both electronic and photonic components. This has been utilised in some impressive demonstrations including those performed at QETLabs [20, 21, 23] and elsewhere [24, 25]. Figure 1.3 shows some of the chips and their designs. Figure 1.3(a) demonstrates on-chip single-photon sources and electronics (shown in Figure 1.3(b), where gold wires denote electrical connections) to manipulate light [20]. Figure 1.3(c) and Figure 1.3(d) show a chip with off-chip single-photon sources and detectors [21]. This also uses electronics to implement a reconfigurable Reck scheme for realising any unitary operation on six spatial modes.

1.1.1.2 Non-linearity

The crystalline structure of silicon is centrosymmetric, which means that it does not exhibit a natural second order non-linearity. In recent years, second order nonlinearities have been demonstrated through electrical straining or introduction of an Si_3N_4 layer [26, 27]. However, a third order non-linearity exists naturally. An important third order non-linear process is called spontaneous four-wave mixing (SFWM), where two photons of a given wavelength mix in a non-linear medium to produce two correlated photons of new wavelengths [28]. The new wavelengths are governed by momentum conservation conditions i.e. $2\omega_p = \omega_i + \omega_s$, resulting in a photon with a wavelength above and below the pump wavelength. These are denoted signal and idler respectively. The spacing of these photons relative to the pump depends on phase-matching, which relates to the waveguide geometry. The considerations of source design will not be discussed in this work but the spacing of the signal and idler photons relative to the pump will be important for filtering considerations (See Figure 1.6 later). On the SOI material system, SFWM was first demonstrated with waveguides in 2006 [29] and with ring resonators in 2009

[30]. This makes silicon attractive for integrated photonics, since entangled photon pairs can produced on-chip, mitigating losses that arise from coupling to and from the chip (discussed later).

Although it will not be discussed in detail this thesis, silicon suffers from a non-linear loss mechanism called two-photon absorption (TPA), where the absorption of two photons promotes an electron from the valence band to the conduction band. This occurs when the energy of the two photons exceeds half of the band gap E_g, where E_g is 1.10 eV. This means that for wavelengths shorter than 2 μm, TPA can be significant [31]. This mechanism starts to occur at high pump powers, limiting the maximum power (and therefore the maximum signal and idler count rates) that can be delivered on-chip. High extinction filters are required to remove the intense pump signal from the signal and idler signals before they are detected. For a detailed discussion of two-photon absorption and other non-linear mechanisms such as free carrier absorption, see the following references [31–33].

1.2 Single-Photon Detectors and Integration On-Chip

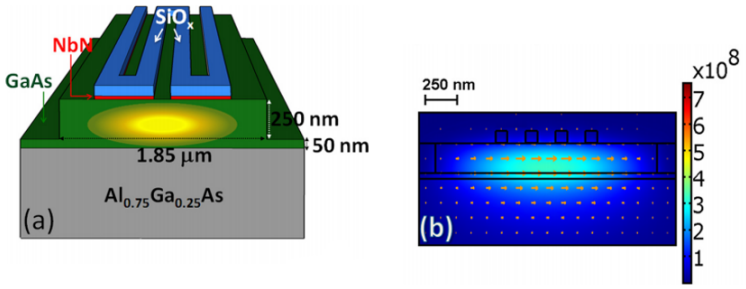

Figure 1.4: The first demonstration of a waveguide-integrated SNSPD from [34]. (a) is the device schematic whilst (b) shows the evanescent coupling mechanism for the nanowire to absorb photons propagating in the waveguide beneath.

Given that SOI is compatible with electronics, an ideal goal to strive for is the integration of high performance on-chip detectors. The superconducting nanowire single-photon detector (SNSPD) was first discovered by Golt'sman in 2001 [35]. The device technology is discussed in detail in Chapter 2. The key motivation for the use of SNSPDs lies in their superior performance over conventional detectors such as single-photon avalanche diodes (SPAD), photomultiplier tubes (PMT) and visible-light photon counters (VLPC) in detection efficiency, timing speed and timing jitter, which are summarised in various reviews [36, 37]. Table 1.1 compares these single-photon detection technologies. SPAD and PMT detectors tend have reasonable detection efficiencies up to 55%, whilst offering room temperature operation (in the case of PMTs). However, they also

Technology	Jitter (FWHM)	Dark count rate	Photon count rate	Optical range	Detection Efficiency	Working temp
GaAsP PMT	80 ps	< 10 kcps	10 Mcps	Visible	40%	300K
InGaAs PMT	400 ps	250 kcps	n/a	Near-infrared	2%	300K
VLPC	2 ns	20 kcps	100 kcps	Visible	88%	6.9K
Si SPAD	20 ps	< 100 cps	1 Mcps	Visible	55%	55K
InGaAs SPAD	140 ps	12 kcps	197 Mcps	Near-infrared	45%	200K
TES	25 ns	neglible	1 Mcps	Visible to mid-infrared	>97%	100mK
SNSPD	5 ps	< 10 cps	25 Mcps	Ultraviolet to mid-infrared	>90%	< 4K

Table 1.1: Comparison of various single-photon detection technologies. This table is reproduced from [36].

have larger jitters and increased dark count rates relative to SNSPDs, meaning their signal to noise ratio and timing resolution are slightly compromised in comparison. In general, the SNSPD offers superior performance in all areas, for wider optical bandwidth. The compromise for facilitating SNSPDs is the requirement of operation temperatures below 4K, which requires more sophisticated cryogenic operation relative to the SPAD, PMT and VLPC technologies.

The early SNSPDs were addressed using optical fibres. These SNSPDs are ideal for free space applications. However, when addressing integrated photonic circuits on-chip, this leads to coupling losses which degrade the overall detection efficiency of the system (which is also true for the PMT, SPAD and VLPC photon detection technologies). For this reason, an approach adopting the use of waveguide-integrated SNSPDs was proposed in 2009 [38], where photons propagating in a waveguide are absorbed by an SNSPD resting above the waveguide, allowing the detector to be located on-chip and circumvent coupling losses, as shown in Figures 1.4(a) and 1.4(b). The first waveguide-integrated SNSPD was demonstrated in 2011 [34]. This was demonstrated on the gallium arsenide platform and demonstrations on silicon-based material systems followed shortly after [24, 39, 40], with detection efficiencies up to 96% [39, 41]. It should be noted that the transition edge sensor (TES) is another single-photon detection technology that has been demonstrated on-chip with up to 88% efficiency [42]. However, the TES requires sophisticated

cryogenic operation (100 mK), whilst its timing jitter and photon count rates are inferior to the SNSPD, which reduces its potential. These advancements with waveguide-integrated SNSPDS have proven the accessibility of high speed, high performance detectors on-chip to make the realisation of an integrated silicon photonic quantum computer possible. The next sections will outline our approach with integrated single-photon detectors that highlight future goals for integrated photonics.

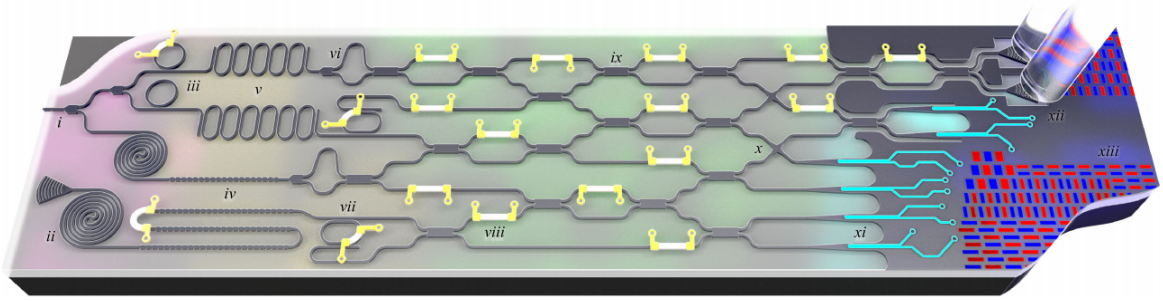

Figure 1.5: Schematic of an integrated photonic chip as conceived in [43]. The relevant areas of the chip for the discussion of a detector chip are labelled (v) on-chip filter, (xi) superconducting nanowire single-photon detector and (xii) fibre-to-chip grating coupler.

1.2.1 Fully Integrated Quantum Photonics Circuit

The ultimate goal is to fully integrate all components (sources, light manipulation and detectors) onto a single chip. One example is shown in Figure 1.5, which highlights a reconfigurable chip, with on-chip single-photon sources based on spirals in this case (ii) and SNSPD's (xi). This represents significant quantum engineering challenges, since all the features will have to be considered, including the spectral response and performance for each component. If such a large set of conditions are satisfied, then a fully integrated chip is appealing because it will not incur losses from coupling on and off of the chip. Furthermore, the system is small and can be packaged easily whilst obtaining greater stability than coupling to off-chip components which will be susceptible to their own fluctuations. So far, a fully integrated chip has not been demonstrated. One of the disadvantages of a fully integrated approach in silicon is the necessitating of all pump light filtering to performed on-chip. Single-chip demonstrations have attained up to 66 dB extinction [44, 45]. However, recently an extinction of 95 dB has been demonstrated [46], which leaves promise in fully integrated on-chip filtering approaches for the future. While this is a significant advancement, the level is still not adequate for full on-chip integration (see Section 1.2.2.1 for a calculation).

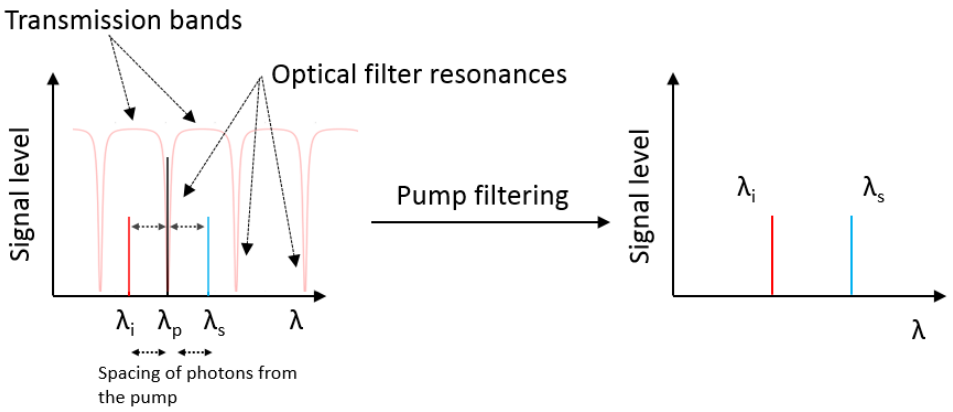

Figure 1.6: Filtering unwanted pump photons from the spectrally correlated signal and idler photons. (Left) Signal level, showing the wavelength spacing of the photons relative to the pump. An optical filter response is shown (transparent and red). The signal and idler are in transmission bands and the pump is in an optical resonance. (Right) after applying the filter, only the signal and idler pass through.

1.2.2 Chip-to-Chip

The second approach is an intermediate goal which separates functionalities onto separate chips. Figure 1.5 shows the grating coupler (xii), a device which couples photons from a waveguide into a fibre and vice versa. This can be used to route photons from one chip (for example a chip with single-photon generation and a linear optical circuit) to another (detector chip). The approach is modular and the detector chip enables characterisation of any other chip through chip-to-chip coupling via optical fibre. The flexibility of this approach makes a detector chip a very appealing utility to have for performing various experiments. This concept is the focus of this thesis and is met with certain challenges that are highlighted below.

1.2.2.1 Challenges

For the realisation of a detector array chip, there are some clear challenges which are now outlined. Firstly, given that chips are optically pumped by a laser to produce photon pairs by processes such as SFWM, the wavelength separation of the produced photon pairs relative to the pump is important. Since resonant cavities are spectrally selective, it is important that these elements are designed to couple certain photon frequencies but reject others. This depends on the method of photon generation. As an example, the separation of signal and idler photons relative to the pump as given in the original works were 5 nm for the waveguide [29] and 10 nm for the ring [30]. Figure 1.6 depicts an approach for filtering the pump, which can be implemented with on-chip elements described in the next chapter. The level to which the pump is filtered is also significant. As calculated by Piekarek et al., 130 dB of pump filtering is required in order to bring

the signal level down to the noise floor of the detector based on 1 mW laser input power and kHz dark count rates, such to attain a good signal to noise ratio for detecting single-photons [47]. A filtering level of 130 dB has been realised with off-chip elements such as wavelength-division multiplexers and fibre-Bragg gratings, but these incurred transmission losses as large as 3.8 dB [48], motivating the desire to use on-chip components. So far, 100 dB of pump filtering has been demonstrated in chip-to-chip experiments involving cascaded Mach-Zehnder interferometer (MZI) lattice filters, fifth order coupled-ring optical waveguide (CROW) filters and ring resonators with a distributed Bragg reflector [47, 49, 50]. For this reason, it is necessary for the detector chip to provide 40-50 dB of extra pump filtering to compliment filtering from the main computational chip(s).

Secondly, high performance detectors are required with a high yield. These performance metrics includes high detection efficiencies and count rates. The concept of an SNSPD in an SOI racetrack cavity was proposed in 2016 [51], which are an ideal element, since the racetrack cavity introduces spectral selectivity whilst enhancing the detection efficiencies to beyond 95 % with short < 5 μm nanowires. This is important, since SNSPD technologies have been shown to be prone to fabrication defects [52, 53], which degrades the detector performance and ultimately the overall yield of working devices on-chip. Finally, although not explored in this thesis, the detector chip should optimise the devices used for coupling into and off of the chip. These devices will be mentioned in the next chapter and are an important consideration for overall system performance.

1.3 Thesis Outline

In this thesis, the crucial elements that form the basis of a detector array chip for chip-to-chip experiments are addressed. Chapter 2 describes the underlying theory for the relevant integrated silicon photonic devices that are used in this work. Furthermore, SNSPDs and aspects of their operation are also discussed. Chapter 3 outlines the fabrication methods used in this thesis and discusses the development of in-house fabrication for the various integrated photonic components shown in Chapter 2 at the University of Bristol. The experimental setup used for characterisation of the fabricated devices is also shown. Chapter 4 discusses a unique approach to realising critical coupling in integrated photonic ring resonator cavities, which has relevance in on-chip optical filtering applications. Chapter 5 shows the development of an SOI photonic interconnect device that will be useful for dense on-chip component integration applications, seeing implementation in optical switches and quantum photonics experiments. This device is a side product of practical considerations for experimental realisation of a cavity-enhanced SNSPD, which is covered in Chapter 6. Together, these cover the important aspects of a detector chip for quantum photonic experiments : pump rejection whilst reducing spurious non-linear effects in the optical filtering stage and cavity-enhanced SNSPDs that are simple to fabricate with high performance.

CHAPTER 2

THEORY

2.1 Integrated Silicon Photonics Toolbox

In this section, various relevant integrated photonic components for the SOI platform will be discussed, highlighting the principles behind their operation and their applications in integrated photonics. Also, each component will be briefly discussed in its relevance to the work presented in this thesis and how they are applied for the work shown in the succeeding chapters.

2.1.1 Waveguides

2.1.1.1 Geometric Picture of the waveguiding mechanism

In the simplest terms, waveguides are means of transporting electromagnetic energy from one destination to another destination. For SOI, dielectric waveguides are relevant and are the building blocks of integrated photonics. Light is confined within a high refractive index medium (called the core) by a lower refractive index medium (called the cladding). A geometric ray-optics picture intuitively describes the principles needed to understand light propagation in a waveguide and is discussed below. A full description requires solving the Maxwell equations in the presence of boundary conditions and can be found in various texts [54]. Figure 2.1 shows light rays (representing plane waves travelling in the direction of the arrow) in the high refractive index medium coloured red. The light rays all travel at the speed $v_1 = \frac{c}{n_1}$, where c is the speed of light in vacuum and n_1 is the refractive index of the relevant medium. However, the rays differ in their angles of incidence θ_i measured normal to the interface. The first two light rays can be observed to bend away from the normal which is explained through part of the wavefront meeting the lower index medium first, causing this part of the wavefront to speed up, travelling at a speed $v_2 = \frac{c}{n_2}$. This introduces a change in speed along the wavefront which manifests as a

bending of the wavefront until the entire wavefront has passed into the lower index material, where it continues to propagate in its new direction characterised by $\theta_{r'}$. This effect is known as refraction, and the angles θ_i and $\theta_{r'}$ are related n_1 and n_2 by Snell's law:

$$n_1 sin(\theta_i) = n_2 sin(\theta_{r'}) \tag{2.1}$$

Snell's law can be used to describe the angle of the refracted light given the relative speeds of light wave in their respective media. For the third ray, there is a unique angle of incidence $\theta_i = \theta_c$ where the light ray appears to not pass into the lower index medium but instead travel parallel to the interface. In this regime, $sin(\theta_{r'}) = 1$, and θ_c denotes the critical angle, which is given by:

$$\theta_c = \arcsin(\frac{n_2}{n_1}) \tag{2.2}$$

The final light ray shows what happens for the case where $\theta_i > \theta_c$. The light ray appears to be completely reflected in the high index medium. This is known as total internal reflection.

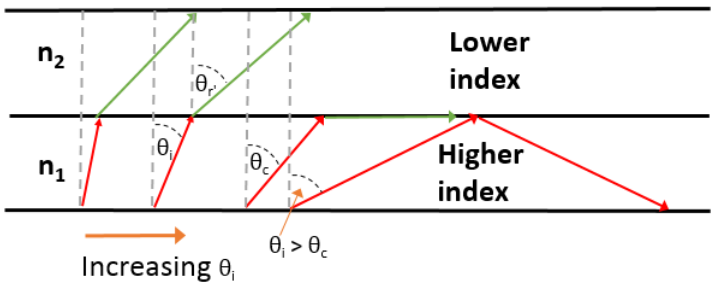

Figure 2.1: Diagram to illustrate the dynamics of a light ray propagating through a high refractive index medium and its interaction at an interface with a medium of lower refractive index.

With the concept of total internal reflection understood, the next step is to understand how this can be used in integrated optics. Consider Figure 2.2. The high index material n_1 lies in between two materials of lower refractive indices of n_2 and n_3 respectively. Total internal reflection occurs, so θ_i is greater than the critical angle given by Equation 2.2. The light then bounces back and hits the lower interface, where n_1 and n_2 now dictate the light propagation. Firstly consider n_2 = n_3, which is commonly used for SOI. The critical angle will be the same for both interfaces and thus rays satisfying $\theta_i > \theta_c$ will also undergo total internal reflection at this interface. The result is the confinement of the light in the layer with n_1, appearing to travel through the high index layer in a zig-zag path through repeated reflections. The light wave travels with an angular frequency ω, a vacuum wavelength of λ and with a wavevector kn_1. The magnitude of k is related to λ and ω by:

$$k = \frac{2\pi}{\lambda} = \frac{\omega}{c} \tag{2.3}$$

For a guided mode, an important term called the propagation constant β describing the component of k that propagating through the waveguide. β is related to k through:

$$\beta = \frac{\omega}{v_p} = kn_1 sin(\theta_{ref'}). \tag{2.4}$$

The analysis so far suggests that an infinite number of waveguide modes can be excited so long as $\theta_i > \theta_c$. However, not all of these modes can propagate due to destructive interference of the wave with itself. To determine the allowed modes, the phase shift during the light propagation has to be considered. If the layer with n_1 has a thickness z, then it will pick up a phase shift of $kn_1 zsin(\theta_i)$ when travelling from the lower film boundary to the upper boundary. At the upper boundary there will be a phase shift ϕ_u. The reflected wave will pass back to the lower boundary, accumulating another $kn_1 zsin(\theta_i)$ phase shift. Finally, at the lower boundary the reflected wave will encounter a phase shift ϕ_l. In order to be a waveguide mode, these phase shifts have to satisfy constructive interference (add up to 2π):

$$2kn_1 zsin(\theta_i) - 2\phi_u - 2\phi_l = 2m\pi. \tag{2.5}$$

where m is an integer representing the mode number. The origin of the phase shifts ϕ_u and ϕ_l can be understood from the Fresnel equations. For $\theta_i < \theta_c$ we expect a partial reflection R and transmission T such that $R + T = 1$. The Fresnel equations are:

$$R_{TE} = \frac{n_1 cos(\theta_i) - n_2 cos(\theta_{r'})}{n_1 cos(\theta_i) + n_2 cos(\theta_{r'})}, \tag{2.6}$$

$$R_{TM} = \frac{n_2 cos(\theta_i) - n_1 cos(\theta_{r'})}{n_2 cos(\theta_i) + n_1 cos(\theta_{r'})}. \tag{2.7}$$

for TE and TM polarised light, which signify no component of the electric and magnetic field in the direction of propagation respectively. When $\theta_i > \theta_c$ and $|R| = 1$ due to total internal reflection, R becomes a complex number with a phase shift given by:

$$tan(\phi_{TE}) = \frac{\sqrt{n_1^2 sin^2(\theta_i) - n_2^2}}{n_1 cos(\theta_i)}, \tag{2.8}$$

$$tan(\phi_{TM}) = \frac{n_1^2}{n_2^2} \frac{\sqrt{n_1^2 sin^2(\theta_i) - n_2^2}}{n_1 cos(\theta_i)}. \tag{2.9}$$

Equation 2.5 can then be thought of as a dispersion relation from which the β can be obtained as a function of λ. However, since allowed modes are related to differing θ_i, it becomes helpful to introduce the effective index n_{eff}:

$$n_{eff} = \eta_1 sin(\theta_i), \tag{2.10}$$

where n_{eff} is bounded by the refractive indices of the core and the cladding layers. In the case of the Maxwell equation analysis, it is equivalent to satisfying the condition that k is a real number. The combination of these indices as well as the height and width of the waveguide affects the number of modes that can propagate in the guided medium. Single-mode and multi-mode operation can be utilised in effective ways. For instance, bigger waveguides may be manipulated as shown with the multi-mode interference devices in Section 2.1.5, but single-mode waveguides may avoid contamination effects that would occur in with multi-mode waveguides (such as coupling to an unwanted polarisation). In general, the different allowed modes in a waveguide will have different n_{eff}, which effects the speed of light in a waveguide, given by:

$$v_p = \frac{c}{n_{eff}}, \tag{2.11}$$

analogously to classical optics, it is also helpful to introduce a quantity called the group index n_g, which describes the velocity at which energy in the pulse travels, given by:

$$n_g = n_{eff} - \lambda \frac{dn_{eff}}{d\lambda}. \tag{2.12}$$

Equation 2.12 is important as it appears in important quantities such as the free spectral range of ring resonators as discussed in Section 2.1.4. Other considerations of n_g include single-photon sources based on SFWM and the wavelength separation of signal and idler photons relative to the pump. However, this will not be discussed here.

Finally, the radiation and substrate modes refer to both unguided modes that are not supported in the waveguide i.e. they do not satisfy Equation 2.5. However, for modes that are supported in the waveguide, the modes can extend out of the high index contrast region (as shown in Section 2.1.1.4. These radiation modes can penetrate into the low-index region. This can be referred to as evanescent coupling and forms the basis for many optical components such as directional couplers in Section 2.1.3 and ring resonators in Section 2.1.4. This mechanism is also used for waveguide-integrated SNSPDs (see Section 2.2) and the concept in Chapter 4. The analysis given in this section is valid for situations where the dimensions of the waveguide are larger than the wavelength of the propagating light. However, when the wavelength of light is comparable or larger than the dimensions of the waveguide, the geometric optics picture fails to accurately describe the full dynamics and an electromagnetic treatment is required [55, 56].

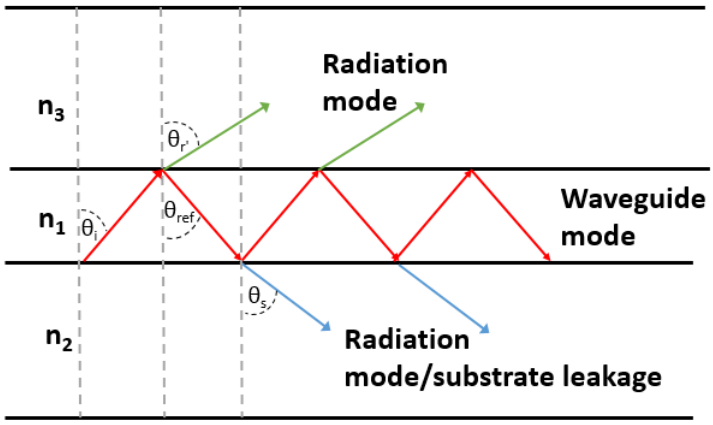

Figure 2.2: Schematic to describe waveguiding and potential loss mechanisms.

2.1.1.2 Maxwell Analysis for waveguides

In this section we will use derivations from various sources [57, 58] to understand the mathematics that describe wave propagation. Firstly, we start with the relevant Maxwell equations in a dielectric and lossless medium. These are:

$$\nabla \times E = -\mu \frac{\partial H}{\partial t}, \tag{2.13}$$

$$\nabla \times H = \epsilon \frac{\partial E}{\partial t}, \tag{2.14}$$

where E represents the electric field, H is the magnetic field, ϵ and μ are the permittivity and permeability of the medium respectively. ϵ and μ are related to their free space counterparts ϵ_0 and μ_0 through:

$$\epsilon = \epsilon_0 n^2, \tag{2.15}$$

$$\mu = \mu_0, \tag{2.16}$$

using a vector identity, one can transform Equations 2.13 and 2.14 into:

$$\nabla^2 E + \nabla(\frac{1}{n^2}\nabla n^2 E) - \epsilon_0 \mu_0 n^2 \frac{\partial^2 E}{\partial t^2} = 0, \tag{2.17}$$

$$\nabla^2 H + \frac{1}{n^2}\nabla n^2 \times (\nabla \times H) - \epsilon_0 \mu_0 n^2 \frac{\partial^2 H}{\partial t^2} = 0. \tag{2.18}$$

These two equations are general and hold for an inhomogenous medium with a variation of refractive index position i.e. $n = n(x, y, z)$. In the case of optical waveguides, the direction of propagation (through the waveguide) can be assumed to have a constant refractive index, leading to $n(x, y)$. In this case the solutions to Equations 2.17 and 2.18 can be described as monochromatic waves:

$$E(r,t) = E(x,y)e^{i(\omega t - \beta z)}, \tag{2.19}$$

$$H(r,t) = H(x,y)e^{i(\omega t - \beta z)}. \tag{2.20}$$

If the refractive index distribution $n(x, y)$ that defines the waveguide are known, then the necessary information for the waveguide modes are captured within the field amplitudes $E(x, y)$ and $H(x, y)$ as well as the propagation constants β. As was depicted in the geometric picture of waveguiding, modes are defined uniquely by their propagation constants β, which geometrically correspond to the reflected ray angles which satisfy constructive interference according to Equation 2.5. Polarisation is determined by the associated components of the electric field. For example, TE modes have only transverse electric field components whilst TM modes have only transverse magnetic field components. By recognising these and substituting the solutions of Equations 2.19 and 2.20 into Equations 2.17 and 2.18 to eventually arrive at the following (example shown for electric field only):

$$\frac{d^2 E_y(x)}{dx^2} + (k_0^2 n^2(x) - \beta^2) E_y(x) = 0. \tag{2.21}$$

Equation 2.21 is a wave equation for TE modes in planar structures. To obtain valid solutions for a given geometry, additional conditions will need to be imposed. These include boundary conditions at interfaces. In terms of E and H, these are [57]:

$$E_t^{(1)} = E_t^{(2)}, \tag{2.22}$$

$$H_t^{(1)} = H_t^{(2)}, \tag{2.23}$$

where the subscript t denotes the tangential component of the electric field and the superscripts (1) and (2) denote the media which lie either side of the interface. These equations describe

the continuity of the electric and magnetic fields. The general solution for planar waveguides - in particular, the slab waveguide is of the form:

$$E_j(x) = A_j e^{i\gamma_j x} + B_j e^{-i\gamma_y x}, \tag{2.24}$$

where the subscript j represents the jth region (meaning core, cladding or substrate), A_j and B_j represent constants to be determined through imposing boundary conditions. Equation 2.24 satisfies Equation 2.21 under the condition:

$$\gamma_j = \sqrt{k_0^2 n_j^2 - \beta^2}. \tag{2.25}$$

The parameters of Equation 2.25 define the behaviour of the mode with propagation constant $\beta = kn_{eff}$ in the jth region of the waveguide. This is the point where the geometric optics picture given in Section 2.1.1.1 meets the present analysis. In the geometric picture of waveguiding, waveguide modes with discrete angles that satisfy total internal reflection and the constructive interference condition given by Equation 2.5 are guided in the core. The angles relate to the effective refractive index experienced by the mode as it propagates through the waveguide. There are two conditions that can be observed when analysing the solution of Equation 2.25:

- $\beta < k_0 n_j$ (or $n_{eff} < n_j$) corresponds to γ_j real. This would mean that Equation 2.24 will correspond to oscillatory functions.
- $\beta > k_0 n_j$ (or $n_{eff} > n_j$) corresponds to γ_j complex. In this case, the solutions to Equation 2.24 correspond to exponential functions.

In general, to calculate the full field profile, Maxwell's equations have to be formulated in every region of space. The analysis above is relevant for a slab waveguide where the refractive index profile in the core can be formulated in 1D. This is not the case for strip and rib waveguides (shown in the next section) that we use in integrated photonics for various applications. We desire these waveguide structures since they operate with lower loss, allow dense integration and have small effective mode area (particularly relevant for the strip waveguide), which is required for non-linear processes used in quantum photonics. In these cases, exact treatment of the modes is not possible. Approximations such as the Marcatilli and effective index method [58] can be used to simplify the analysis, but will not be shown here. Commercial software such as Lumerical and FIMMWAVE have mode solver functionalities built-in, allowing determination of the modes in a waveguide given knowledge of the waveguide dimensions, refractive indices of the layers and the wavelength of interest. The accuracy of the calculation will depend on the resolution of the mesh (number of spatial steps within the simulation window to calculate the electric and magnetic fields). Higher resolution meshes will return more accurate results for the waveguide modes at

the expense of larger computer memory requirements and time. For an example of a waveguide mode calculated using Lumerical, see Section 2.1.1.4. Generally, waveguide modes will have an oscillatory function corresponding to the mode number and polarisation in the core layer, with evanescent fields decaying outside of the core (into the cladding). The shape of the mode profile is important experimentally (for the context of loss, see Section 2.1.1.4), whilst the evanescent field can be exploited to make various integrated photonic components. For examples, see Section 2.1.3 and 2.1.4.

2.1.1.3 Types of waveguide and properties

Electromagnetic waves can be guided using different geometries and materials. For example, optical fibres are waveguides and more sophisticated technologies such as graphene-micofiber and hollow core fibre have been utilised as waveguiding systems [59–61]. In integrated photonics, waveguides are fabricated in a material with a higher index compared to its surroundings. For example, in SOI, the waveguides are fabricated in Si, with a buried oxide (BOX) lower cladding and an upper cladding of SiO_2 or air. Figure 2.3 shows three different types of waveguide on the SOI platform. The first is similar to the film stack and is generally less commonly used called the slab waveguide. Slab waveguides have been implemented with photonic crystals for slow-light applications [62] and used as part of on-chip photodetector designs at λ =1550 nm. [63]. Out of these designs, the ones commonly used for integrated photonics are the rib and strip waveguide. The rib waveguide can be fabricated through electron beam lithography to define a waveguide of a desired width and then this is transferred to the Si layer through partial etching. The strip (sometimes also referred to as a wire) waveguide is formed using the same lithographic process but the film is fully etched. Strip waveguides can be found in many quantum photonic and non linear silicon photonic demonstrations such as four-wave mixing and correlated photon pair generation [64–67]. This is due to their smaller effective mode area, owing to a larger non-linearity with respect to the rib waveguide and can be deduced from having a sub-micron size core (typically 400-600 nm) with high index contrast which yields high confinement.

Finally, other waveguides such as the slot waveguide have been proposed and experimentally demonstrated in 2004 [68, 69]. The slot waveguide in these works was formed by two small Si strip waveguides of width 220 nm and are separated by a gap of 100 nm, where the material in the gap is a low-index material (usually air or SiO_2). The result is that the mode is carried in the gap. This is due to the discontinuity of the displacement field D in the low-index material at a high-index contrast interface. Since there are two high-contrast interfaces at a separation smaller than the evanescent field decay, the light is confined at a high intensity in the gap. Initially, it was postulated to be useful for sensing applications and was confirmed with studies in 2011 where methane at concentration of 100 ppm in nitrogen was measured using a 300 μm photonic crystal slot waveguide [70].

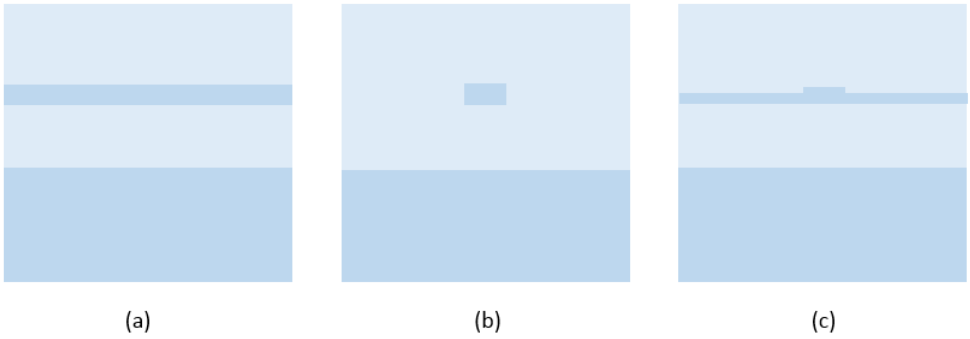

Figure 2.3: (a) Slab, (b) Strip and (c) Rib waveguides. The film stack from the bottom up is : Substrate, BOX, Si, SiO_2.

For a specific material system, the dimensions of the waveguide determines the number of modes they can guide. Generally, integrated quantum photonic experiments go for single-mode operation and components are designed primarily based on that respective mode to avoid contamination or loss of state purity from multi-mode effects. Figures 2.4(a) and (b) show the modes that propagate in a 220 nm thick SOI wire waveguide with widths between 400 and 700 nm, for air and SiO_2 upper claddings. Since BOX forms the lower layer, the effective cut off for the mode can be taken to be $n_{eff} < 1.44$ based on the low-index material considerations to satisfy total internal reflection, which was discussed in Section 2.1.1.1. In both cases, the fundamental TE mode and TM modes are supported throughout all waveguide widths. For TE_{01}, it can be observed for the case of air cladding that it is unable to propagate until a waveguide width of 600 nm or greater is achieved. This is in contrast with the case for SiO_2 cladding, where it is able to propagate from around 450 nm. Other phenomena such as mode mixing occur at a waveguide width of 650 nm due to the phase matching (equal n_{eff} for TM_{00} and TE_{01}). When comparing the effects of the upper cladding, it can be observed that the n_{eff} for all modes in Figure 2.4(b) are larger than their respective counterparts in Figure 2.4(a). One way to understand this is to think of the guided mode n_{eff} to depend on the relative amounts of high index material (the waveguide dimensions) and the refractive index of the cladding. Since SiO_2 has a larger refractive index than air, the guided mode n_{eff} can be expected to be larger for a given waveguide width and wavelength.

Dispersion is the variation of the refractive index with wavelength i.e. $n(\lambda)$. The dispersion is a combination of the natural material dispersion in the high index material and the confinement properties of the waveguide - the waveguide dispersion. Figure 2.5 shows the variation of n_{eff} for various width strip waveguides on SOI with SiO_2 upper cladding. These considerations

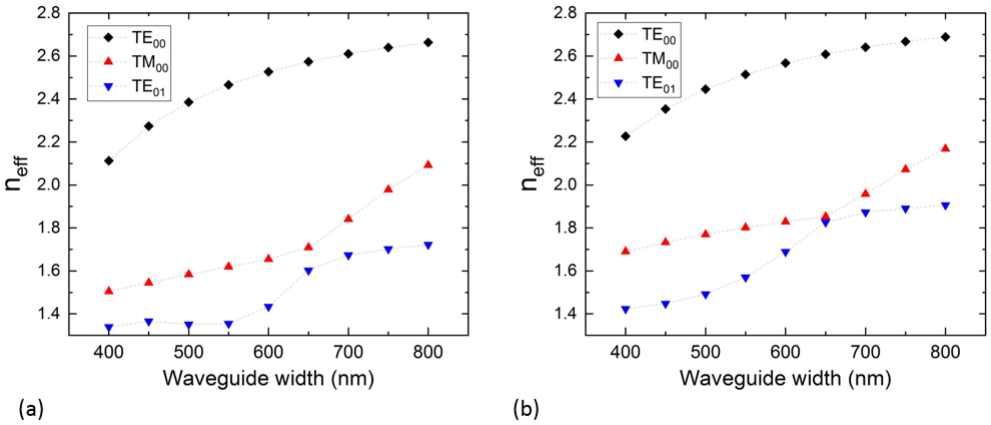

Figure 2.4: Modes supported in a 220 nm SOI wire waveguide with (a) Air and (b) SiO_2 upper cladding. These spectra were simulated in Lumerical MODE solutions for a wavelength of 1550 nm.

are important for various applications such as achieving phase matching for single-photon generation from SFWM (because they are related to n_g and designing various integrated photonic components such as beam splitters and ring resonators for broadband responses.

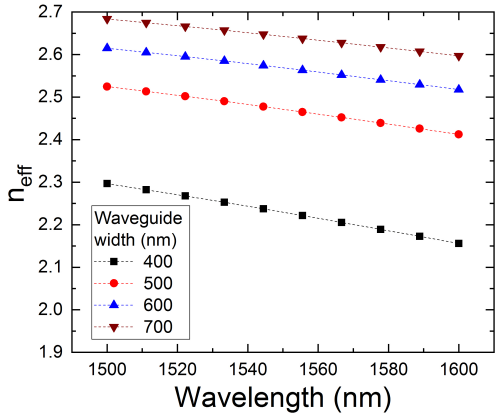

Figure 2.5: SOI strip waveguide dispersion for various widths. These spectra were simulated in Lumerical MODE solutions.

2.1.1.4 Linear and bending losses

Losses are an important aspect for SOI waveguides. The losses for a waveguide are generally quoted in dB/cm and are representative of the standard propagation losses for light as it travels

through an integrated photonic circuit. Other losses can be waveguide-independent, such as coupling losses which will be discussed in Section 2.1.2. Loss mechanisms in integrated photonics can include [71, 72]:

- Losses caused by fabrication processes
- Losses caused by waveguide bends

The fabrication process involves the patterning the waveguides with electron beam lithography followed by etching. Surface roughness is caused by both of these processes since the quality of the resist and the etching process are contributing factors. Generally, this results in a roughness on the vertical side walls of the waveguide, which is coupled with the fact that SOI is a high contrast material and that scattering losses scale with the index contrast as Δn^3 [73]. Figures 2.6(a) and 2.6(b) show TE and TM mode profiles in a 220 nm x 500 nm SOI strip waveguide with SiO_2 upper cladding. It can be observed that the TE mode profile has greater overlap with the sidewalls, whereas the TM mode is concentrated on the top and the bottom of the waveguide. The sidewall overlap can be alleviated by increasing the width of the waveguide, but care must be taken to avoid multi-mode waveguiding if operation in a single-mode regime is desired.

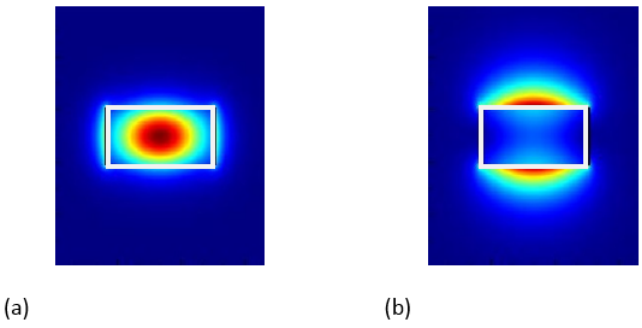

Figure 2.6: Electric field intensity profiles of (a) TE and (b) TM fundamental modes supported in an SOI strip waveguide (shown by the white outline).

Waveguide bends are important on-chip because they allow design flexibility and routing - the ability to use more of a chip efficiently. However, they are also a mechanism for loss. Some investigations in loss due to bends have been performed in the context of optical waveguides and

for fibres [74–78]. The geometrical picture of waveguiding in Section 2.1.1.1 can be considered in a waveguide bend. As the waveguide bends, the critical angle condition changes. For very small bends, this is expected to cause loss due to a series of refractions occurring (i.e. the incident angle is below the critical angle). In terms of larger radius bends, the loss is expected to be smaller and in the limit of an infinite bend radius, the loss will tend to the standard linear losses caused by mechanisms discussed above. In terms of field profiles, the travelling waveguide mode gets pushed to the edges when the bend is encountered. This means that there is more electric field spilling out into the outer cladding as shown in Figure 2.7.

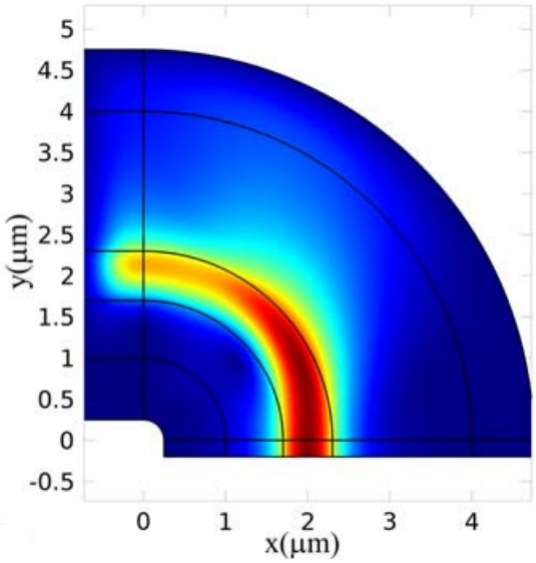

Figure 2.7: 3D Finite element simulation of light propagation around a 90 degree bend. It can be observed that the mode gets pushed to the edge of the waveguide, causing the evanescent field to extend further into the cladding. Figure taken from [75].

Generally to investigate waveguide losses, the cut-back method is commonly used. This method involves fabricating a selection of waveguides with differing lengths which are known. From measurements of all the waveguides, it is possible to extract the waveguide loss through plotting the output power transmission as a function of waveguide length. Other methods of measuring the losses from an integrated photonic circuit can involve using ring resonators, since their Q-factor is a representation of the losses in the cavity. This will be discussed in Section 2.1.4. Typical values for linear losses in SOI wire waveguides are smaller than 1 dB/cm [79]. However, it was investigated that when using TE-mode wire waveguides, the losses were reported to be in this range when considering wires 500 nm wide, but exceeded 1 dB/mm for 400 nm wide [80]. This is explained as a result of lower confinement characteristics with smaller width waveguides, causing a larger amount of sidewall overlap. Other material systems such as Si_3N_4 have also

achieved propagation losses below 1 dB/cm [81, 82].

2.1.1.5 Relevance to this work

The work in Chapters 4, 5 and 6 are designed specifically for the TE mode propagation based on 220 nm thick by 500 nm wide SOI strip waveguides. The strip waveguides are designed for direct compatibility with the quantum photonic experiments being performed by other members of QETLabs.

2.1.2 Grating Couplers

2.1.2.1 General advantages and disadvantages

In integrated optics, light can be coupled in to the circuit by two methods: edge coupling [83] or using grating couplers [84, 85]. Since optical fibres typically have diameters on the order of μm, there is a mismatch between the mode travelling in the optical fibre and the small waveguides with sub-micron dimensions. Therefore, the mode mismatch between the fibre and the chip has to be addressed in order to take advantage of the small waveguides. The grating coupler is an example of an integrated photonic component performing this function. The grating coupler has advantages over edge coupling in integrated photonics. These include the ability to be patterned anywhere on the chip - for this reason grating couplers allow for a higher component density than edge couplers. Furthermore, they are easy to align to and beyond their fabrication they do not require extra considerations, such as polishing the edge of the chip to reduce insertion losses. On the other hand, grating couplers have a limited bandwidth and generally have higher coupling losses relative to edge coupling, which has achieved insertion loses of 0.35 dB [83]. Recent advancements have significantly reduced the coupling losses of grating couplers relative to edge coupling (insertion losses down to 0.5 dB [86]) and some of the methods used to achieve this will be shown.

2.1.2.2 Theory

The theory for the grating coupler in this section uses the reference [87]. Figure 2.8 shows a schematic of a basic grating coupler on the SOI platform. The simplest design for a grating coupler is a series of gratings in a line followed by a taper into a waveguide. Generally, the footprint of the component is on the order of 10-100 μm. The grating coupler uses diffraction to couple light out of plane (from or to optical fibre). From Figure 2.8, various relevant parameters for the grating are shown. The period of the grating is Λ. The width of the grating is W. From W and Λ a useful quantity called the fill factor (often referred to as the duty cycle) can be defined:

$$FF = \frac{W}{\Lambda}. \tag{2.26}$$

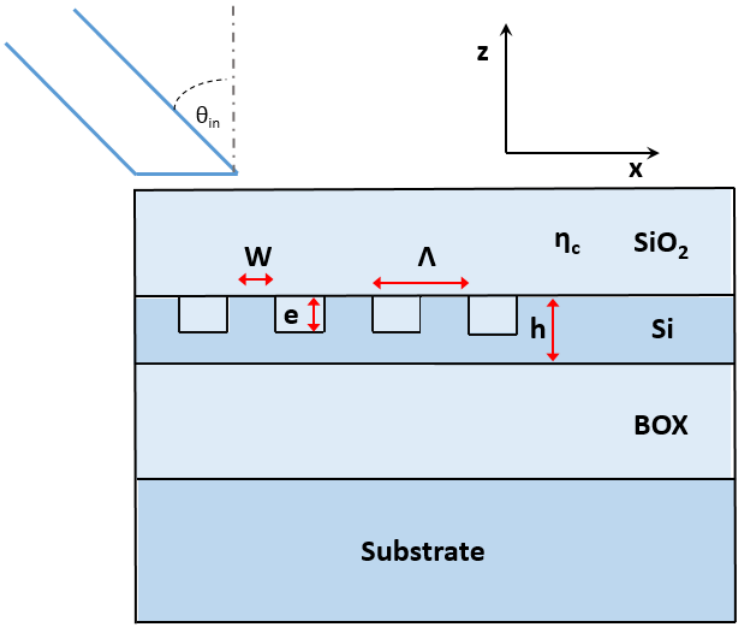

Figure 2.8: Schematic of an SOI grating coupler. Light travelling from the fibre is diffracted by the gratings into the waveguide (+x direction).

The fill factor depends on the effective indices of the grating teeth and the regions between the grating teeth, which depend on cladding index n_c, the thickness of the Si device layer h and the etch depth e. A fully etched grating coupler corresponds to $e = h$ with the effective index between the teeth given by n_c. For an example of a fully etched grating, see the inset of Figure 2.9(a). The angle θ_{in} corresponds to the angle between the surface normal and the propagation direction of the incident light. If the propagation constant of the waveguide is $\beta = kn_{eff}$ and the incident wave is travelling from the fibre into the grating (in the x direction), perpendicular to the grating teeth, the Bragg condition for diffraction is given by:

$$\beta - k_x = mK \tag{2.27}$$

and

$$K = \frac{2\pi}{\Lambda}. \tag{2.28}$$

Where K gives the k-space period for the grating, which depends on the real space period Λ according to Equation 2.28. Equation 2.27 can be thought of as a momentum conservation condition. The quantity m is an integer representing the diffraction order whilst the x component of the diffracted wave is k_x. Through constructive interference, the diffracted wave k is preserved, resulting in a diffracted angle of:

$$sin\theta_d = \frac{k_x}{k} = n_{eff}\frac{\lambda}{\Lambda}. \tag{2.29}$$

Equation 2.29 gives the angle of the diffracted light that travels into the cladding with wavevector k and refractive index n_c. From using Snell's law (Equation 2.1) to convert the diffracted angle in the cladding θ_d to the diffracted angle in air θ_{in} and rearranging Equation 2.27 we arrive at:

$$\Lambda = \frac{\lambda}{n_{eff} - sin(\theta_{in})}. \tag{2.30}$$

It is possible to use Equation 2.30 to calculate what the period Λ of the grating should be for a desired wavelength λ and a desired fibre angle θ_{in}. n_{eff} in this case describes the effective index in the grating region. This can be considered as a weighted average depending on FF:

$$\eta_{eff} = FFn_{eff,t} + (1-FF)n_{eff,g} \tag{2.31}$$

where $n_{eff,t}$ is the effective index in the teeth region and $n_{eff,g}$ is the effective index in the gaps etched with depth e. Since n_{eff} is not the same as the waveguide effective index, these have to be matched through using an adiabatic taper to reduce loss. The considerations in Equation 2.31 are important for distinguishing the differences between shallow and fully etched grating couplers. In a fully etched grating coupler, There are larger index mismatches in the teeth section of the grating, resulting in larger Fresnel reflections than a shallow etched grating. The resulting effect are stronger Fabry-Perot oscillations that occur in the waveguide, causing an oscillation ripple in the grating coupler transmission spectrum (see fabricated devices in Chapter 3). Also, some of the reflected light may be directed towards the substrate, manifesting as a reduction of coupling efficiency for the grating coupler.

2.1.2.3 Figures of merit

A typical transmission spectrum from a grating coupler is shown in Figure 2.9(b). The key figure of merits for a grating coupler are:

- **Footprint**. The size of the component effects how many gratings can be fabricated on a chip. This effects scalability and will be important for high dimensionality quantum photonic experiments, or simply addressing many different structures on a chip for testing purposes.

- **Coupling efficiency**. Also known as the insertion loss. This can be quoted as the loss per coupler, or extracted from a fibre to fibre measurement on a straight waveguide. It is taken from the peak of the grating coupler envelope i.e. $T(\lambda) = T_{max}$. The assumption in this calculation is that both grating couplers are identical in design, therefore their coupling efficiencies will be the same.

- **3 dB bandwidth**. This determines the bandwidth of the grating coupler and is measured by checking where the transmission level drops by 3 dB in either direction from the peak wavelength λ_{max}. Furthermore, a larger bandwidth also generally implies a slower rate of change along the peak of the envelope. This can be important for experiments involving photons of different wavelengths when implemented with off-chip elements or in chip-to-chip schemes.

- **Peak wavelength/fibre array angle**. These two are related by Equation 2.30. If the fibre incident angle can be adjusted, the peak wavelength λ_{max} can be shifted. This can be important incase the fibre array holder is polished at an angle that does not yield optimal transmission at the designed wavelength of grating coupler.

- **Extinction Ratio**. Grating couplers can be designed to accept certain polarisations of light and reject other polarisations [88]. For example, it may be desirable to have a high TE-TM extinction ratio to reduce coupling out erroneous TM light from laser to chip for an experiment designed in TE polarisation. On the other hand, it is also possible to design gratings that allow coupling of both TE and TM polarisation [89].

2.1.2.4 Designs, considerations and seminal work

The first grating couplers were fabricated by Bogaerts et. al over ten years ago on the GaAs-AlOx [91] platform and followed by implementation on SOI soon after [84, 85]. The first gratings showed coupling efficiencies of 7 dB. Furthermore, since they implemented gratings in a line they were relatively large, requiring tapers of over 100 μm to convert the mode efficiently. This encouraged research into reducing the grating coupler footprint. Since then, efforts have been made to reduce the size of the grating coupler as well as increasing the coupling efficiencies. These involve using parabolic gratings in order to focus the light into the waveguide [92, 93]. An example of a focusing grating is shown in Figure 2.9(a). The phase-matching condition for a focusing grating takes a form:

$$n_{eff} r = n_f r sin(\theta) cos(\phi) + N\lambda, \tag{2.32}$$

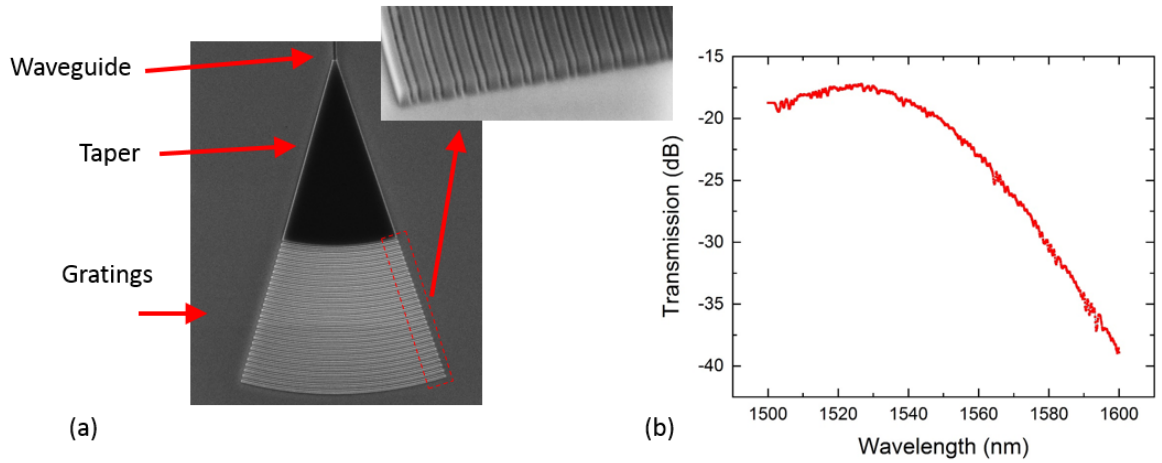

Figure 2.9: (a) SEM image of a focusing grating fabricated in this work. Inset shows a cross section of the grating teeth along the edge marked with a red box. Design based on [90]. (b) Experimental transmission spectrum from a grating coupler fabricated in (a).

implying:

$$r = \frac{N\lambda}{n_{eff} - n_f sin(\theta)cos(\phi)}. \tag{2.33}$$

Equation 2.32 implies the phase matching condition, where r is the radius measured from the start of the waveguide to the end of the grating. If the propagation of the light from the grating into the waveguide travels along the x direction, then the angle ϕ is measured with respect to this axis, n_f is the effective index of the fibre and N is the diffraction order. This can be rearranged into Equation 2.33, which gives the required radius to achieve efficient spot size conversion. The equation describes a family of confocal ellipses with a focusing point on the waveguide.

Apodisation is a method that has been employed to improve the coupling efficiency. The idea is to further improve the mode matching by varying a parameter with the geometric dimension. In terms of the mode matching, the fields power exponentially decays along the direction of propagation in the grating region:

$$P = P_0 e^{-2\alpha x}, \tag{2.34}$$

where P is the power in the waveguide at position x, P_0 indicates the incident power before reaching the gratings and α is known as the leakage factor (sometimes also referred to as the coupling strength) of the grating. The coupling strength is important because it is ncessary to

consider for mode matching the electric field distributions of the light in the fibre and in the grating. This can be formalised as:

$$\alpha = \frac{G^2(x)}{1 - \int_0^x G^2(t)dt}, \tag{2.35}$$

where $G(x)$ is a Gaussian function generally representing the fundamental guided mode of a single-mode fibre. The theoretical coupling efficiency for a uniform grating is 80%, corresponding to a loss of 0.97 dB [94]. Apodisation has been used for various different SOI designs including hexagonal shaped grooves on the <111> crystallographic plane [95]. Tang et. al used the lag-effect of the dry etching process to fabricate a grating with an apodised etching depth, achieving a coupling efficiency of 64% (1.9 dB loss) [96]. In 2015, Bozzola presented a design that achieved a nominally high coupling efficiency 89% (0.5 dB loss) using apodisation on the 340 nm Si platform whilst suggesting that the maximum coupling efficiency on 220 nm SOI is 65% (1.87 dB loss) [86]. However, the authors suggest that the injection on 340 nm thick SOI is multi-moded, requiring an efficient design to couple into a single-mode. In 2017, Marchetti et al. showed an experimental demonstration on 260 nm SOI with a coupling efficiency of 81% (0.9 dB loss). This was achieved through using a linear apodisation on the grating fill factor with a shallow-etched grating. Generally, apodisation results in an increase in the coupling efficiency of the grating at an expense in the bandwidth. The mechanism for this tradeoff can be thought of in terms of the mode matching and Equation 2.30. Since the mode matching to the fibre becomes stronger with apodisation, the coupling efficiency increases due to the better greater overlap - inferred from a spatially varying α in Equation 2.35. However, since Equation 2.30 applies, a change in λ results in a change of fibre array angle, meaning that the more focused light of the apodised grating is more sensitive to angle mismatch. Other apodised designs such as fully etched photonic crystal structures on SOI have been demonstrated with an efficiency of 67% (1.74 dB loss), with a 3 dB bandwidth of 60 nm [97].

Other methods of improving the efficiency involve the use of a reflective material underneath or above the substrate [94, 98–101]. As a notable example, the fully etched photonic crystal grating of [97] was improved to 0.58 dB loss with a 3 dB bandwidth of 71 nm by using a bonded aluminium mirror [102]. The gain in coupling efficiency for this strategy is met at the expense of extra fabrication steps and sometimes with materials that are not CMOS compatible. To contrast this approach, the use of sub-wavelength structures to engineer the effective index region in the grating can also be effective [90, 103, 104]. For example, the sub-wavelength focusing grating coupler by Wang et al. achieved 4.1 dB per coupler and 3.2 dB when apodised for the TE mode, with a 3 dB bandwidth of 52 nm [90] for the 220 nm thick SOI platform. The advantage of the sub-wavelength grating design in this work is that it is fully etched, meaning it can be fabricated in the same step as the waveguides with no additional requirements. This design was then apodised in a later work, achieving 3.2 dB loss per grating with a 1 dB bandwidth of 37 nm [105].

2.1.2.5 Relevance to this work

The grating coupler is a crucial part of addressing the components discussed in Chapters 4 and 5. Certain designs were attempted and are discussed in Chapter 3. For the demonstrations shown in these chapters, the simplicity of fabrication as well as reducing Fabry-Perot reflection effects were desired. For this reason, fully etched gratings were studied to enable a fast solution for optical testing.

2.1.3 Directional Couplers

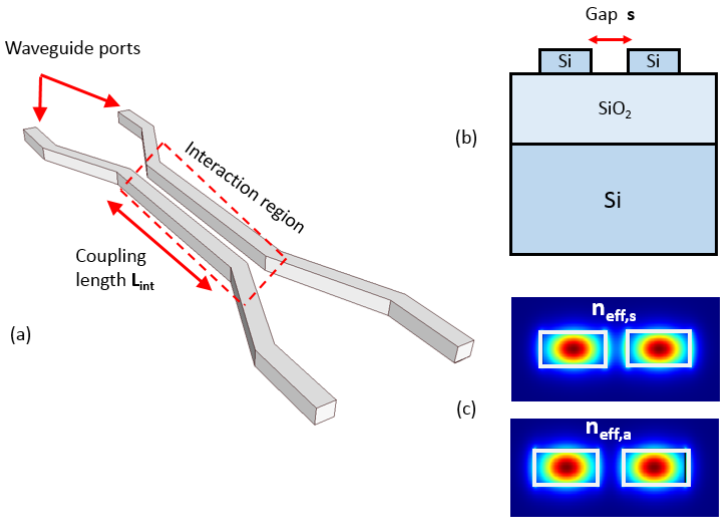

Figure 2.10: (a) Basic schematic of the directional coupler device. (b) Cross-section of the interaction region to show how the gap (or separation) s is defined. (c) Symmetric and asymmetric supermodes in the interaction region.

The directional coupler is an integrated photonic device used for transferring power from one waveguide to an adjacent waveguide. The evanescent field that extends out of the waveguide shown in Figures 2.6(a) and 2.6(b) can be used to couple light into another waveguide. This technique can be used to design 50:50 beam splitters (otherwise known as 3 dB couplers) [106–108]. Whilst the directional coupler can be used to simply redirect light into another waveguide, they are usually implemented as a component to form another structure such as the MZI, which is a crucial component for reconfigurable integrated photonics, enabling realisation of some demonstrations which are discussed in Section 2.1.3.2.

2.1.3.1 Theory

The theory for the directional coupler here is taken from Huang [109]. A basic schematic for the device is given in Figure 2.10(a). Two waveguides are spaced sufficiently far apart that they

behave independently. Assuming that their dimensions are equal, then they will have their waveguide effective indices n_{eff}. To connect the isolated region with the interaction region, they are brought together by waveguide bends (although for simplicity they are shown as sharp kinks in Figure 2.10(a)). In the interaction region, the evanescent fields of the waveguide overlap and the waveguide excites supermodes, which come in a pair - one is asymmetric and the other is symmetric. The mode profiles are shown in Figure 2.10(c). These have effective indices $n_{eff,a}$ and $n_{eff,s}$ which are related to n_{eff} by:

$$n_{eff,s} = n_{eff} + \frac{\Delta n}{2}, \tag{2.36}$$

$$n_{eff,a} = n_{eff} - \frac{\Delta n}{2}, \tag{2.37}$$

where $\Delta n = n_{eff,s} - n_{eff,a}$. The physical meaning is that the directional coupler excites two waveguide modes in the interaction region which travel at different speeds. Δn can be interpreted as a phase difference which allows power to be transferred from one waveguide to the other. The magnitude of Δn is controlled by the gap s between the two waveguides (defined in Figure 2.10(b)):

$$\Delta n \propto exp^{-As}, \tag{2.38}$$

where A is some constant of proportionality. The gap s and the interaction length L_{int} determine the power splitting ratio C:

$$C = sin^2(\frac{\pi \Delta n L_{int}}{\lambda}). \tag{2.39}$$

Equation 2.39 is plotted for various gaps in Figure 2.11. Design of the directional coupler therefore involves choosing a gap where coupled-modes are present and then extending L_{int} until the desired C is obtained. All of the theory above applies to other waveguide modes present. For example, if a waveguide allows a TE and a TM mode to propagate, then there will be supermodes for both in the interaction region. There will then be a unique Δn for each, which result in a unique power splitting C_{TE} and C_{TM}.

In terms of tolerances, the largest cause of performance deviation in a standard directional coupler comes from the gap. From the relation in Equation 2.38, an exponential dependence of Δn on s can be observed. This is shown in Figures 2.12(a) and 2.12(b), where the supermodes and the corresponding Δn are plotted as a function of s for the fundamental TE mode. Power splitting between waveguides can generally be assumed to be negligible for > 1 μm separation. This data

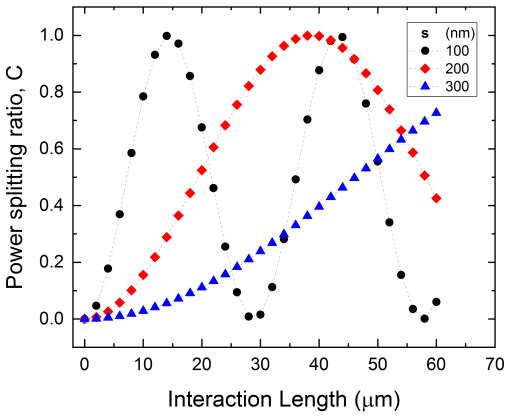

Figure 2.11: Splitting ratio C for the TE mode of a SOI directional coupler with 500 nm waveguides. The data is shown as a function of interaction length L_{int} for various size gaps s. The 300 nm gap shows a large tolerance to L_{int} for designing a 50:50 splitter.

was simulated in Lumerical MODE Solutions for 220 nm x 500 nm SOI strip waveguides in SiO_2 cladding. Generally, it is desirable to fabricate directional couplers with a larger gap to be in a regime with lower gradient around the desired splitting ratio to reduce performance degradation from small deviations from ideal dimensions. However, when considering achieving a desired C with a larger gap, this results in a longer interaction region, which increases the device footprint and also incurs more loss (discussed in Section 2.1.1.4). To alleviate the footprint, strategies such as decreasing the waveguide width at the interaction region have been utilised [106], which can be interpreted as expanding the evanescent field. This allows a larger gap to be fabricated whilst maintaining strong coupling (at negligible expense to the device footprint).

As seen in Equation 2.39, naturally there is a wavelength dependence on the splitting ratio. Furthermore, the waveguide dispersions $n_{eff,a}$ and $n_{eff,s}$ depend on wavelength based on similar principles to those shown for the isolated waveguides in Section 2.1.1. Figure 2.13 shows the variation of C with λ based on an evanescent coupler design for an experiment done by a fellow PhD student Callum Wilkes (see Section 2.1.3.2). This design had L_{int} = 27 μm and s = 300 nm on 220 x 500 nm SOI strip waveguides. It can be observed that the power splitting ratio has a strong dependence on wavelength, varying from 30:70 at 1500 nm to 70:30 at 1600 nm. Similar trends for the wavelength dependence have been observed in [110]. If a flat band-profile is desired, the standard evanescent coupler design may not be appropriate, and should be replaced by either a multi-mode interference device (in Section 2.1.5) or by a more sophisticated design that has a flatter band profile. This is more desirable for applications such as optical switching, where consistent performance over a larger bandwidth enables more channels that can be switched simultaneously, which in turn leads to greater capacity and data rates [111].

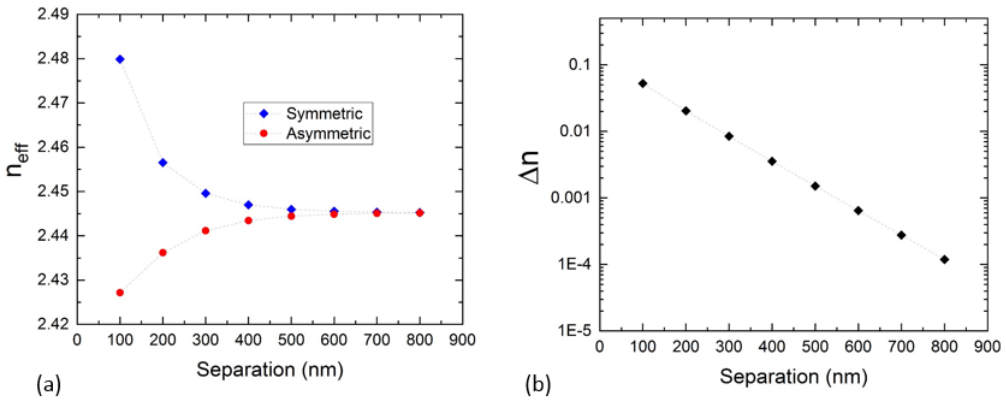

Figure 2.12: (a) Effective indices of the symmetric and asymmetric supermodes $n_{eff,s}$ and $n_{eff,a}$ and their dependence on the waveguide separation in the interaction region. (b) Δn as a function of gap.

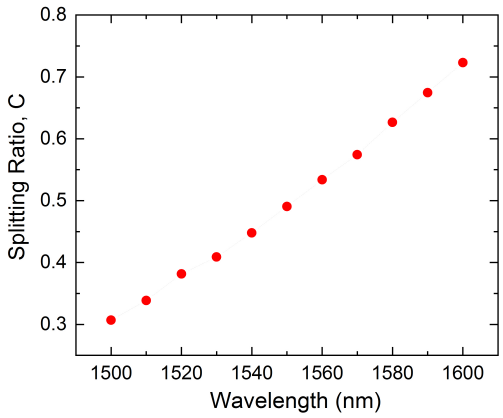

Figure 2.13: Splitting ratio C as a function of wavelength for a directional coupler with L_{int} = 27 μm, s = 300 nm on 220 nm x 500 nm SOI waveguides.

2.1.3.2 Demonstrations

In quantum photonics, the ability to prepare accurate states for quantum process tomography is essential. For this reason, the MZI structure needs to be able to access the full range of states. Generally, 50:50 splitting is achieved, but the degree to which 100:0 is achieved is more difficult. High extinction ratio MZI's have been realised and improved through nested structures as well as self-optimisation algorithms to make variable beamsplitters (VBSMZI), and 60-65 dB extinction ratios have been achieved with VBSMZI structures in recent years [112, 113], improving on earlier designs where up to 50 dB were achieved [114]. Figure 2.14(a) shows a schematic of the

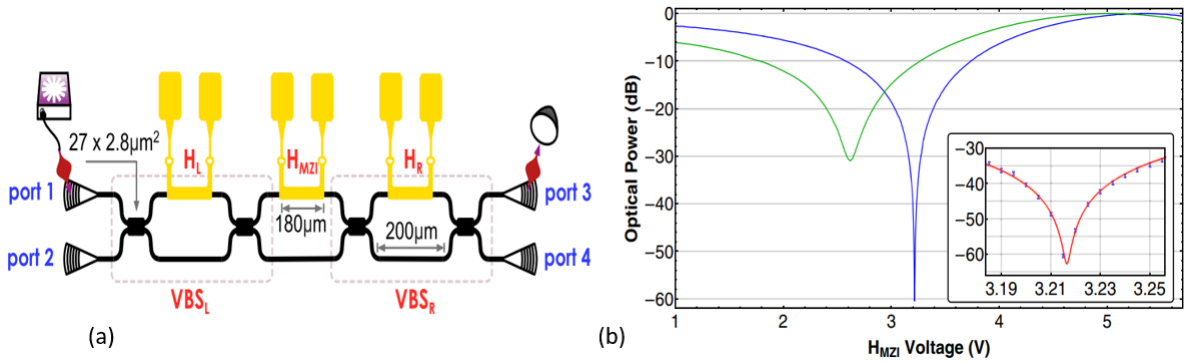

Figure 2.14: (a) Schematic of the VBSMZI. Optical input and output ports as well as heaters are also shown. (b) Measured extinction ratio. Both figures were originally presented in [112].

structure which achieved 60 dB [112]. This VBSMZI can be considered as three concatenated MZI's. The MZI component itself consists of two directional couplers with a thermo-optic phase shifter in between operating on one of the waveguides (denoted H in Figure 2.14(a)). Figure 2.14(b) shows the measured difference in optical power between two ports. The blue curve is from the VBSMZI and for comparison a standard MZI is shown by the green curve. The inset graph is a zoom in on the bottom of the blue curve.

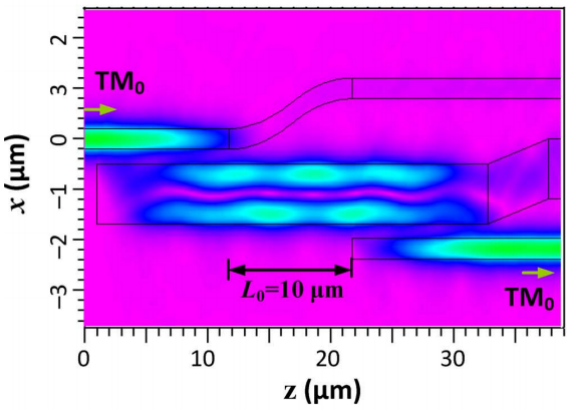

Figure 2.15: FDTD simulation of three waveguides forming an asymmetric directional coupler. Originally presented in [115].

More demonstrations include power splitting between different waveguide modes. In the previous demonstrations, the power splitting has occurred using identical waveguides and involves a transfer of power from one waveguide to another for a single waveguide mode. On the other hand, it is also possible to exchange power from one waveguide mode to another using a directional coupler. This is achieved through satisfying phase matching conditions. The work by Dai et. al shows an excellent example of power splitting using asymmetric directional couplers

[115]. Figure 2.15 shows an electromagnetic simulation of the device. The middle waveguide has a larger width to index match the TM_{00} mode in the upper and lower waveguide with the TM_{01} mode in the middle waveguide. Also (although not shown here), the TE_{00} mode is designed to pass through the top waveguide without interacting with the centre waveguide. This forms a polarising beam splitter with a polarisation extinction ratio of 15 dB over a bandwidth 50 nm. More recently, other designs have achieved extinction ratios better than 20 dB based on bent and symmetric directional coupler devices [116, 117].

2.1.3.3 Relevance to this work

The theory for the directional coupler is important for this thesis since the designs implemented in Chapters 4 and 6 utilise the racetrack resonator geometry. In the racetrack ring resonator, the coupling region can be adequately described by the coupled-mode theory that is relevant to the directional coupler. The well-defined coupling region is desirable for achieving critical coupling, which is described in more detail in the next section. For the detector in Chapter 6, we will ignore the TM mode due to reasons given in the fabrication process (Chapter 3).

2.1.4 Ring Resonators

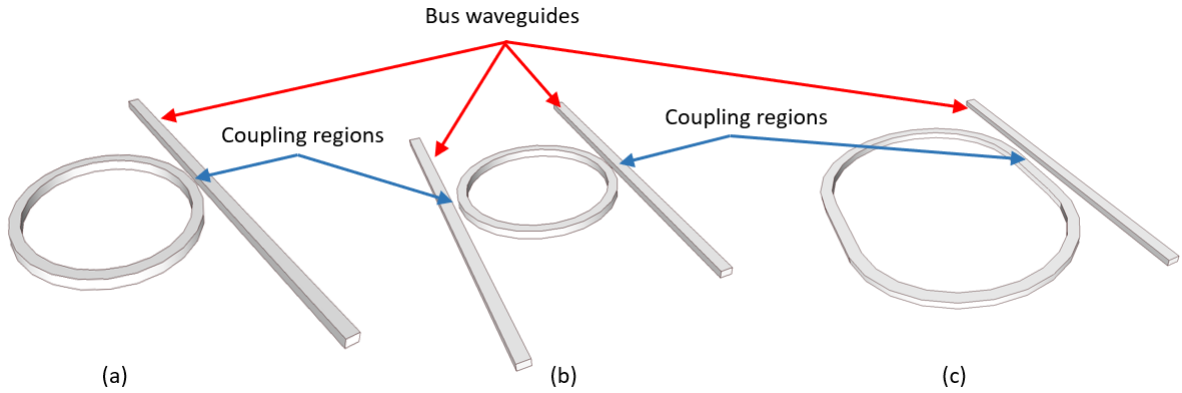

Figure 2.16: Different types of ring resonators. (a) and (b) are circular rings in the all-pass and add-drop configuration respectively, whilst (c) is an all-pass racetrack ring resonator. Coupling regions and bus waveguides are shown by the blue and red arrows respectively.

Ring resonators are a type of integrated photonic cavity. They are the building blocks used for single-photon source generation [118–121], optical filtering [44–46], wavelength division multiplexing [122, 123] and can also find applications in other areas such as sensing [124–130]. The operational principle of the ring resonator starts with a waveguide (typically called the bus waveguide) which approaches the ring. The ring waveguide and the bus waveguide can exchange energy through evanescent fields, as described by the coupled-mode theory discussed in Section 2.1.3. There is an interference effect that occurs between light which does not couple to the ring

(travelling through the bus waveguide) and light that couples back into the bus waveguide from the ring. The interference effect results in different operating conditions which will be discussed in Section 2.1.4.1. Figure 2.16 shows some various configurations for integrated photonic ring resonators. Rings can be in the all-pass configuration, as depicted in Figure 2.16(a), where only one bus waveguide couples to the ring. This can be contrasted with the add-drop filter shown in Figure 2.16(b), where two bus waveguides are coupled to the ring. This particular configuration can be used to route photons of a specific wavelength from one bus waveguide to the other, whilst photons with wavelengths not on resonance will pass through without coupling to the ring. Other methods of coupling to a ring resonator can involve vertical coupling, where the bus waveguide is above or below the ring resonator [131–133], but will not be considered further in the discussion. The geometry of the ring itself is not limited to being circular. For example, the racetrack resonator shown in Figure 2.16(c) is an alternative design where the coupling region involves a parallel waveguide [134–136]. The next section will describe the theoretical operation of these devices.

2.1.4.1 Theory

The theory of the ring resonator used here is taken from [137]. There is also an alternative derivation by Bogearts with other relevant quantities which can be found in [138]. This analysis is valid only for an all-pass ring resonator. The basic schematic of the ring resonator is shown in Figure 2.17. There are fields defined in the bus waveguide (labelled E_{i1} and E_{t1}) and within the ring itself (labelled E_{i2} and E_{t2}). The coupling coefficients between the bus waveguide and the ring are labelled t and κ, with power conservation requiring that $|t|^2 + |\kappa|^2 = 1$. The matrix representing the relationships between input and output fields is:

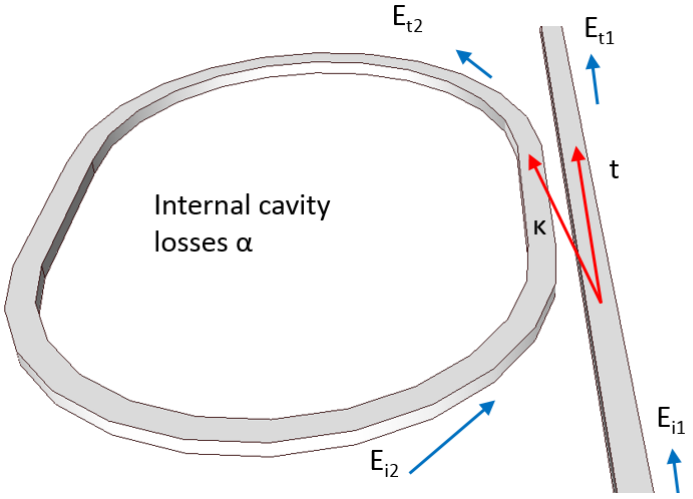

Figure 2.17: Basic diagram of a ring resonator in the single-bus configuration. Blue arrows are for the electric fields, whilst red arrows show the coupling coefficients to the ring (t and κ).

$$\begin{pmatrix} E_{t1} \\ E_{t2} \end{pmatrix} = \begin{pmatrix} t & \kappa \\ -\kappa^* & t^* \end{pmatrix} \begin{pmatrix} E_{i1} \\ E_{i2} \end{pmatrix} \tag{2.40}$$

The electric fields in the ring are related by:

$$E_{i2} = \alpha e^{i\theta} E_{t2}, \tag{2.41}$$

where α is the round trip transmission (i.e. $\alpha = 1$ indicates a lossless ring). θ is related to the waveguide parameters (wavelength λ, group index n_g) and cavity length L_c through:

$$\theta = \frac{2\pi}{\lambda} n_g L_c, \tag{2.42}$$

using the above relationships and that the transmitted power is proportional to the square of the electric field i.e. $P_{out} \propto E^2$, the transmitted power out of the bus waveguide is:

$$(\frac{P_{out}}{P_{in}}) = (\frac{E_{t1}}{E_{i1}})^2 = \frac{\alpha^2 + t^2 - 2\alpha t cos(\theta)}{1 + \alpha^2 t^2 - 2\alpha t cos(\theta)}, \tag{2.43}$$

on resonance $\theta = 2\pi m$, where m is an integer. Under this condition, the power transmitted through the bus waveguide is:

$$(\frac{P_{out}}{P_{in}}) = (\frac{E_{t1}}{E_{i1}})^2 = \frac{(\alpha - t)^2}{(1 - \alpha t)^2}. \tag{2.44}$$

Examining Equation 2.44, three different regimes can be observed. The first regime is when $t > \alpha$. In this regime, the loss per round trip is greater than field travelling through the bus waveguide. This is known as under-coupling. In the under-coupled regime, demonstrations involve manipulation of fast and slow light [139]. Furthermore, the under-coupled regime has a smaller resonance linewidth and resistance to thermal broadening effects, which has found advantages in sensing applications [140, 141].

The second regime occurs when $t < \alpha$. In this case, more light is being coupled into the ring than is being lost. This is known as over-coupling. Since more light is being coupled into and out of the cavity, a signature of over-coupling is a larger linewidth. This is desirable for applications such as single-photon sources which were briefly discussed in Chapter 1. Other applications of over-coupling include filtering schemes [142] and improvements to on-chip squeezing [143]. In the latter example, a squeezing level of 2 dB was reported when operating in over-coupling, whereas 0.5 dB was obtained when operating in under-coupling. This particular implementation had

active control of the coupling region, enabling the same optical cavity to be used for comparison.

Finally, the last regime is unique to when the bus propagation coefficient $t = \alpha$, resulting $E_{t1} = 0$. In this case, there is an equal amount of light coupling to the cavity to what is lost. This is known as critical coupling. As a result, the light coupling out of the ring is out of phase with the light in the bus waveguide, undergoing destructive interference. Critical coupling is most desirable for filtering applications where high extinction of desired wavelengths are required. As far as I am aware, the best extinction obtained on a single chip with ring resonators is 95 dB [46]. This particular implementation used four stages of second-order rings. Critical coupling is an important concept for the work in Chapters 4 and 6. However, the next important concepts to understand are the transmission spectra that occur in a ring resonator and their features which result from Equation 2.43.

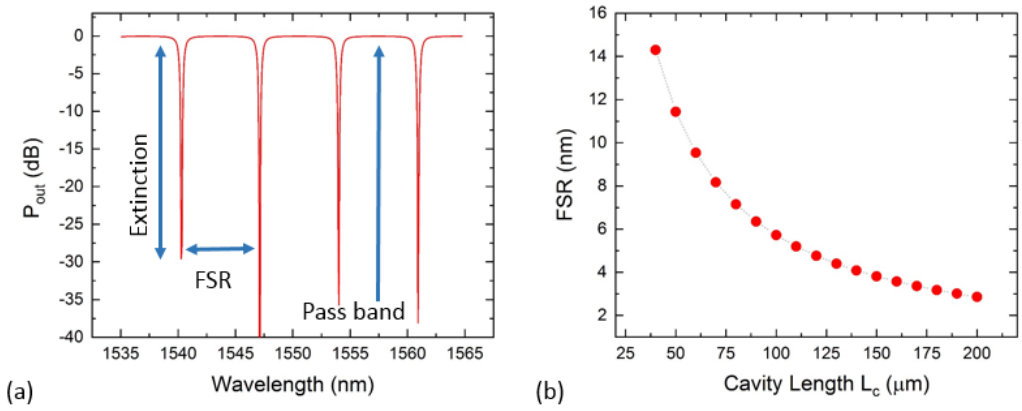

Figure 2.18: (a) Typical ring resonator transmission spectrum. Relevant features of the spectrum are labelled. (b) Calculated FSR as a function of L_c for n_g = 4.2 and λ = 1550 nm.

An example of a ring resonator transmission spectrum is shown in Figure 2.18(a), which is calculated using Equation 2.43 for L_c = 83 μm, n_g = 4.2, α = 0.932 and t = 0.93, therefore operating very close to critical coupling. Four resonance dips are observed where the wavelength of the light satisfies the boundary conditions for travelling in the cavity. These resonance wavelengths will now be labelled λ_{res}. The spacing between these resonances is called the free spectral range (FSR). The FSR depends on λ_{res} and the cavity length L_c by:

$$FSR = \frac{\lambda_{res}^2}{n_g L_c}. \tag{2.45}$$

The spacing between resonances (where P_{out} is near 0 dB) is called the pass band, whilst resonances are referred to as the stop band. The pass band to stop band contrast defines the extinction of the resonance and is usually quoted in dB. The full width at half-maximum (FWHM) describes the linewidth of the resonance and can be related to α, λ_{res} and t through:

$$FWHM = \frac{(1-t\alpha)\lambda_{res}^2}{\pi n_g L_c \sqrt{t\alpha}}. \tag{2.46}$$

Thus, the tuning of the ring FWHM and FSR can be tailored for high performance in various applications through tuning of parameters such as L_c. As an example, Figure 2.18(b) shows the calculated FSR using Equation 2.45 for λ_{res} = 1550 nm and n_g = 4.2. These considerations will be important for tasks such as filtering pump photons whilst allowing signal and idler photons to pass through without coupling to the ring as was discussed in Chapter 1. A sensible approach for this consideration is to design the filter with an FSR twice the size of the spacing between the pump and the signal (idler) photons, so that the signal and idler photons lie on the maximum of the pass band, whilst the pump signal is on resonance with the filter [46, 144]. Another important parameter describing the photons lifetime in the cavity is the loaded Q-factor Q_L, which is defined as:

$$Q_L = \frac{\lambda_{res}}{FWHM} = \frac{\pi n_g L_c \sqrt{t\alpha}}{\lambda_{res}(1-t\alpha)}. \tag{2.47}$$

Equation 2.47 describes the Q-factor of the cavity with the coupling of the bus waveguide - as evident by the inclusion of t. This is the Q-factor that can be experimentally determined from the transmission spectrum through measuring the FWHM and λ_{res}. There is also an unloaded Q-factor Q_U, which describes the losses that are intrinsic to the ring itself. These originate from mechanisms described in Section 2.1.1.4. An approximate expression for the unloaded Q-factor is [110, 145]:

$$Q_U \approx \frac{2\pi n_g}{\alpha \lambda_{res}}. \tag{2.48}$$

Thus, with knowledge of L_c, the propagation loss in the ring resonator can be extracted from using Equation 2.48.

2.1.4.2 Relevance to this work

Ring resonators are targeted for use as the spectrally selective element for the filters and the detectors in a detector chip. Ring resonators were fabricated in Chapter 3, and are a key component for the work in Chapters 4 and 6. Typically, we chose rings of 83 μm, since they could be accommodated by 10 μm bend radii to reduce unwanted losses. These lengths originate from work previously carried out [51] which describe an ideal high performance detector using a racetrack resonator.

2.1.5 Multi-Mode Interference Waveguides

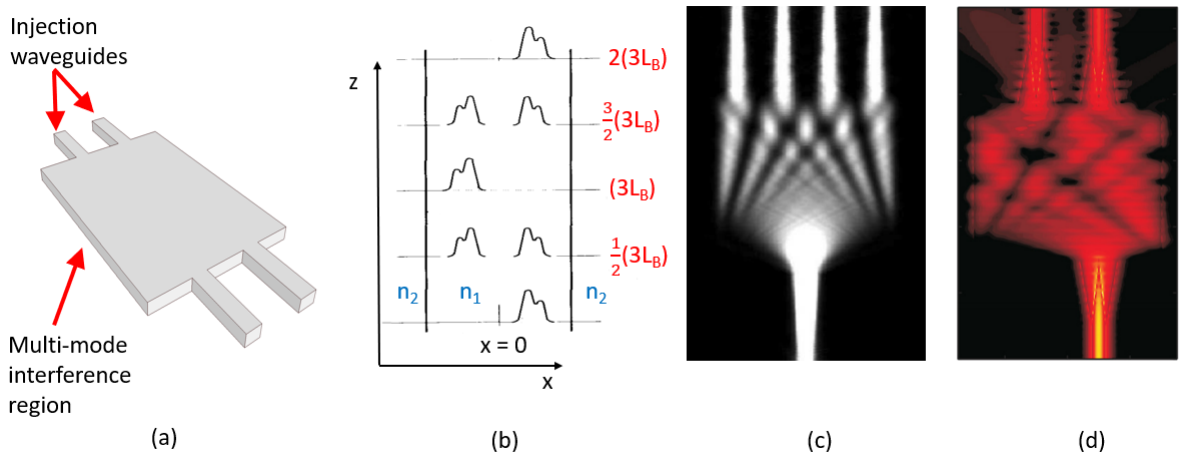

Figure 2.19: (a) Schematic of an MMI device. (b) Field evolution in the multi-mode interference region. n_1 and n_2 are refractive indices of the waveguide material and the cladding respectively. Figure adapted from [146]. (c) and (d) are electromagnetic simulations of 1 x 4 and 1 x 2 MMI devices respectively [147, 148].

Multi-mode interference (MMI) waveguides can be considered an integral part of the silicon photonics toolbox. A schematic of an MMI waveguide is shown in Figure 2.19(a). In general, an injection waveguide enters the multi-mode waveguide either directly or through expanding adiabatically by using a taper. In the multi-mode waveguide, many waveguide modes are supported due to the large waveguide width. These modes interfere with each other as they travel through the multi-mode waveguide. This principle can be exploited in various ways to realise useful integrated photonic components such as beam splitters, waveguide crossings and polarisation filters.

2.1.5.1 Theory

The theory for MMI devices is described well by Soldano and is used in this section [146]. Consider a multi-mode waveguide of width W_M. The centre of this waveguide denotes x=0, and the multi-mode waveguide extends in the z direction (as in Figure 2.19(b)). The waveguide supports m guided modes, each with their own unique n_{eff} for a wavelength λ according to the principles of Section 2.1.1. The evanescent fields of these modes mean that they extend beyond W_M, which necessitates introduction of an effective width W_e to compensate for the penetration of the field into the cladding:

$$W_e = W_M + (\frac{\lambda}{\pi})(\frac{n_2}{n_{eff}})^{2\sigma}(n_{eff}^2 - n_2^2)^{-\frac{1}{2}} \tag{2.49}$$

where σ is 0 for TE modes and 1 for TM modes. It should be noted that in high index contrast waveguides such as SOI, the penetration depth is not very large (due to the confinement) and therefore the correction will be less significant relative to lower index contrast material systems. The propagation constant for the jth mode β_j can be deduced from the dispersion equation for the waveguide modes, but the result will just be given here for simplicity:

$$\beta_j = kn_{eff} - \frac{(j+1)^2\pi\lambda}{4n_{eff}W_e^2}. \tag{2.50}$$

An important quantity is the beat length L_B, which is defined in terms of the lowest order modes $j = 0$ and $j = 1$, and can be related to W_e through using Equation 2.50:

$$L_B = \frac{\lambda}{2(n_{eff,0} - n_{eff,1})} = \frac{4n_{eff}W_e^2}{3\lambda}. \tag{2.51}$$

Now to turn attention to the excitation of the multi-mode region. Consider an input field profile $F(x,z)$. Injection at $z = 0$ and all modes contained within the effective width W_e means that the field profile can be written as a superposition of all the guided modes:

$$F(x,0) = \sum_{j=0}^{m-1} c_j\phi_j(x) \tag{2.52}$$

where c_j is the field excitation coefficient for the jth mode and $\phi_j(x)$ is the field distribution of the jth mode. At a distance z away from the injection, the field profile can be written as:

$$F(x,z) = \sum_{j=0}^{m-1} c_j\phi_j(x)e^{i(\omega t - \beta_j z)}, \tag{2.53}$$

where i = $\sqrt{-1}$. By considering the spacing of an arbitrary mode j relative to the fundamental $j = 0$ from Equation 2.50 and inserting into Equation 2.53 for a distance z=L yields:

$$F(x,L) = \sum_{j}^{m-1} c_j\phi_j(x)e^{i\frac{j(j+2)\pi}{3L_B}L}. \tag{2.54}$$

Equation 2.54 is important for the MMI device. Analysis of the exponential term yields various field profiles formed at various multiples of L_B as shown in Figure 2.19(b). For example, $F(x,0) = F(x,L)$ occurs when the following condition is satisfied:

$$e^{i\frac{j(j+2)\pi}{3L_B}L} = (-1)^j, \tag{2.55}$$

which describes replicas of the input field, since the phases of the modes along L differ by an integer multiple of 2π. The alternation of phases result due to varying j. These result in mirror images of the input field (as shown in Figure 2.19(b)). Since the multi-mode waveguide can be longer than L and the integer multiples of 2π can be satisfied for larger distances, these conditions are satisfied for:

$$L = p(3L_B), \qquad p = 0, 1, 2.... \tag{2.56}$$

where p is an integer which denotes the periodicity of the imaging. It is also possible to find multiple images within the evolution of the field. For example, considering the two-fold images in Figure 2.19(b), these occur under the condition:

$$L = \frac{p}{2}(3L_B), \qquad p = 1, 3, 5... \tag{2.57}$$

which can be used to design devices such as 3 dB beamsplitters and early demonstrations on SOI were shown in 2001 for the 1 x 2 and 2 x 2 cases [149, 150]. These original designs used straight waveguides for injection and suffered large losses. This was improved upon later by implementing tapers for the input and output waveguides, reducing the device loss from 1.2 dB (without tapers) to 0.1 dB for a 1 x 4 MMI device [147]. Figure 2.19(c) shows an electromagnetic simulation of this device. This is to be contrasted with Figure 2.19(d), where the excitation port is off the centre of the multi-mode waveguide [148]. This is due to restricted interference regimes that are possible which depend on the excitation of the multi-mode waveguide. One of these is called paired interference. In a paired interference regime, the multi-mode waveguide region is excited from the position $x = \pm\frac{W_e}{6}$, as in Figure 2.19(d). Under paired interference, the distance for single image and N-fold images are pL_B and $\frac{pL_B}{N}$ respectively, representing a reduction in the required multi-mode region length relative to the general interference excitation conditions. Due to the different c_j for paired interference, a different field profile results, which can be observed in Figures 2.19(c) and 2.19(d) before the field exits the multi-mode waveguide.

Based on the physics of multi-mode interference and self-imaging, the characteristic dependence of L_B on λ is weaker than it is for the directional coupler, meaning 50:50 splitting can be realised over a larger bandwidth. As an example, the power splitting ratio C of an MMI device I measured for another project is shown in Figure 2.20. The splitting ratio changes by less than 2% over 80 nm. When comparing conventional designs, the MMI coupler is more resilient to changes in wavelength relative to the directional coupler. However, this is generally met at the expense of larger insertion losses, which originate from various mechanisms such as non-perfect imaging in the multi-mode waveguide and finite sized tapers to maintain a reasonable device footprint. In 2013, Maese-Novo et al. proposed a sub-wavelength multi-mode interference waveguide structure

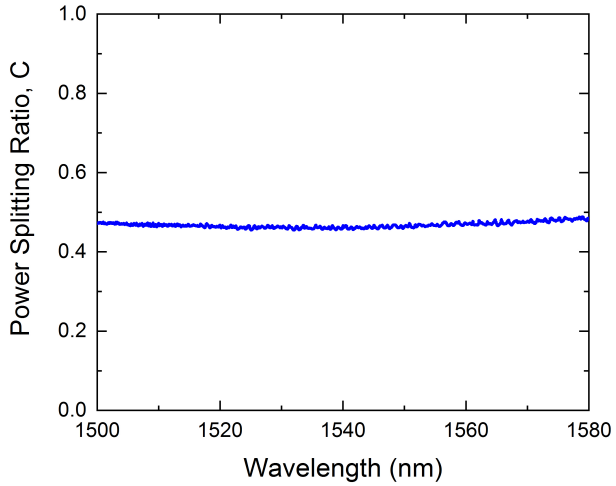

Figure 2.20: Experimentally determined power splitting ratio of an 3 dB MMI coupler.

[148]. In this work, the modes are dispersion engineered in the multi-mode waveguide and injection waveguides through the use of sub-wavelength structures. The work shows a reduction in device length of half and a fivefold increase in bandwidth relative to a conventional MMI waveguide device, although this was not experimentally demonstrated.

2.1.5.2 Demonstrations

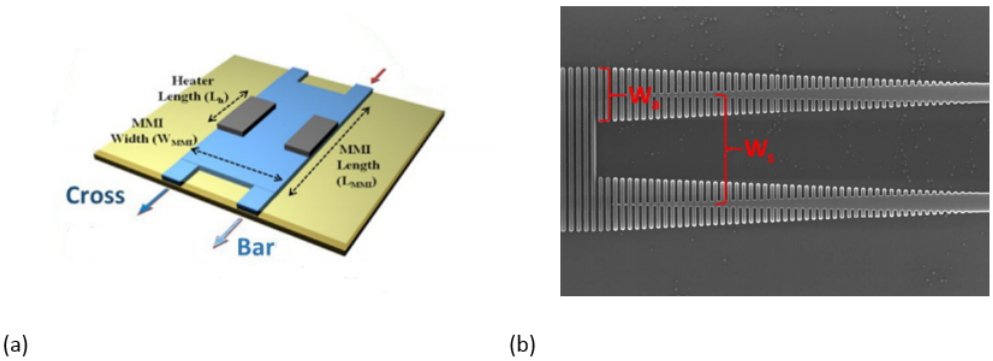

Figure 2.21: Examples of MMI waveguides exploited as (a) optical switches [151] and (b) polarising beam splitters [152].

The fabrication tolerance of the MMI device can be exploited for various applications such as optical switching. An example is by Rosa et. al in 2016 [151], where thermo-optic phase shifters were implemented within the MMI region (as opposed to MZI-based approaches with

MMI devices as in [153]). The switching occurs in this device by inducing a π phase shift on one of the self-images which are located underneath one of the electrodes (centred half way along the multi-mode interference region as shown in Figure 2.21(a)). As a result, the interference pattern after the electrode is changed. This switch operates with a power consumption of 24.9 mW and a switching time of 1.19 μs, whereas the MZI-based architecture has a power consumption of 235 mW and a switching time of 60 μs.

Polarisation can be manipulated - for example, the ability to produce an MMI that has similar transmission properties for both input TE and TM light can be done through matching a common beat length for both modes i.e:

$$nL_{B,TE} = mL_{B,TM} \tag{2.58}$$

where n and m represent integer quantities. Conversely, it is also possible to design the MMI such that one of these modes gets rejected i.e. does not self-image at the output. This allows realisation of an integrated photonic polarising beam splitter, which has been demonstrated in SOI with TE/TM extinction ratios better than 10 dB [154, 155]. Expanding on this application further, a sub-wavelength MMI was experimentally demonstrated by Xu et al. in 2018 [152]. This particular structure also uses sub-wavelength gratings to engineer the modes in the multi-mode interference region and injection waveguides, as shown in Figure 2.21(a). In particular, the multi-mode interference region is engineered to produce $L_{B,TM} = 2L_{B,TE}$. The input waveguide is off-centre, so that if TM is desired in one port, the TE polarised light will be the mirror image and found in the other port. This principle resulted in measured extinction ratios of > 20 dB at 1550 nm whilst retaining a device length shorter than 100 μm. The sub-wavelength MMI structure demonstrated here was smaller by at least a factor of 3, whilst having a larger bandwidth than the conventional designs [154, 155].

2.1.6 Waveguide Crossings

The waveguide crossing is a structure where two waveguides cross, enabling efficient routing of photons. This structure is used in dense photonic integration and has an appeal to classical photonics. Waveguide crossings have been implemented in conjunction with micro-electro-mechanical systems (MEMs), microring resonators and MZI structures to form optical switches networks of up to 128 x 128 ports and reconfigurable multiplexers [156–160]. The waveguide crossing allows a larger density of components to be built on-chip due to its small (typically < 50 x 50 μm^2) footprint. It can circumvent problems associated with routing waveguides around other structures on-chip such as leakage due to evanescent field coupling with another waveguide when their separation is small (as described by coupled-mode theory in Section 2.1.3). This is very apparent for large networks of structures such as that shown in Figure 2.22(a). There are some figures of

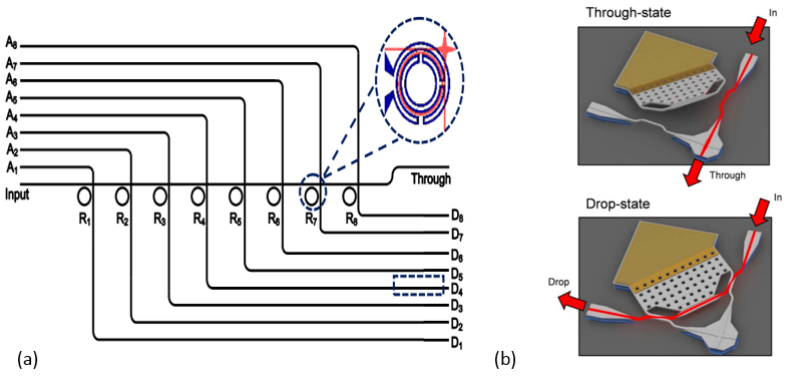

Figure 2.22: Waveguide crossings used in (a) reconfigurable optical add-drop multiplexers (see inset) [156] and (b) MEMs based switches [157].

merit for the waveguide crossing that are very important for realising optimal performance in these applications. The general purpose of the waveguide crossing structure is to be able to guide photons straight through the structure with minimal loss, crosstalk (defined as the amount of power that is measured in undesired waveguides) and backscattering. As an example, consider the MEMs based switch in Figure 2.22(b). When the switch is in the through-state, the beam propagates through the waveguide crossing. If the crosstalk of the waveguide crossing is large, then light will leak into the drop port, limiting the extinction ratio of the switch and degrading its performance. Also, for the reason that many waveguide crossings may be connected in series (as in [157]), this will effect multiple ports, whilst the overall loss of the device may quickly increase if the waveguide crossing is not optimised. To the best of my knowledge, the largest number of crossings implemented on a silicon photonic chip is 16 x 10^3 [160].

There are several types of architectures for a waveguide crossing, including simply overlapping two perpendicular waveguides to make a right-angle crossing [161], using sub-wavelength waveguiding structures [162] and multi-mode waveguides similarly to Section 2.1.5 [156, 157, 163, 164]. The multi-mode waveguide crossing works in the symmetric interference regime, where only even modes in the multi-mode waveguide are excited through injection on the centre. Under this condition, the first single-image occurs at $\frac{3L_B}{4}$ and N-fold images occur at $\frac{3L_B}{4N}$. The design of a waveguide crossing using multi-mode interference relies on self-imaging of the input field at the ouput of the multi-mode waveguide. As far I am aware, the best performance waveguide crossing in terms of device loss that has been demonstrated was by Dumais et al. in 2017 using a staged taper to synthesise a Gaussian beam at the centre of the waveguide crossing [163]. This device had a loss of 7 mdB and a crosstalk of -40 dB, although the device footprint was fairly large at 30 x 30 μm^2. This design and the performance of other multi-mode interference based designs are compared in Chapter 5.

2.1.6.1 Relevance to this thesis

Various types of waveguide crossings are investigated in Chapter 5. The optimised design was then adapted in Chapter 6 for considering practicalities associated with racetrack cavity-enhanced SNSPDs.

2.2 Superconducting Nanowire Single-Photon Detectors

The SNSPD is a single-photon detection technology renowned for its high efficiency coupled with low dark counts, low timing jitter and low dead times. The first demonstration of an SNSPD was performed by Golt'sman in 2001 [35, 165] with the niobium (Nb) material platform. The high efficiency at low photon energies of 1550 nm owes to the low superconducting band gap of these materials which can create an avalanche effect orders of magnitude higher than typical semiconductors. Since the inception of the SNSPD, the technology has found use in a variety of applications such as detection of time-energy entangled photons from SFWM [166], implementation in light detection and ranging (LIDAR) systems where sub-cm spatial resolution has been demonstrated [167–169], quantum key distribution (QKD) experiments [170], quantum computing-based experiments [24, 171] and more.

Typically, the SNSPD consists of a superconducting material such as niobium nitride (NbN), tungsten silicide (WSi) or others (see Section 2.2.3). The nanowire is patterned into a resist and then this pattern is transferred to the superconducting material through etching. Since SNSPD's are patterned are generally between 50 nm - 150 nm wide, they facilitate the requirement for electron-beam lithography. The thickness of the nanowire tends to be on the order of 3.5-7 nm thick, which creates a quasi-2D system, whilst they can be designed on the order of microns to hundreds of microns in length. This can be in a single line in the case of a waveguide-integrated detector, or with multiple bends as a meandering nanowire, typically used for normal-incidence detectors. These types of SNSPD will be discussed in more detail in Section 2.2.2. When an SNSPD is biased with a high enough current, upon absorbing a photon, the Cooper pairs are broken and a voltage spike is created on the electrical circuit. This is detected and registered as a photon count. The device has to operate at a low enough temperature to be superconducting. Typically, NbN SNSPD's operate at 4.2K, whereas WSi is required to operate below 2K. The difference between these two temperatures results can facilitate greater expenses in cryogenic technology for operation. In the fabrication process, the SNSPD is connected to contact pads. The electrical circuit involves read-out from the detector, but also allows biasing of the detector. An SNSPD will have a current (denoted switching or critical current) I_{sw} or I_C for which values of current that satisfy $I_B > I_{sw}$ cause superconductivity to perish in the detector. Therefore, detectors are typically biased at $I_B \leq xI_{sw}$, where x is typically around 0.9 to 0.99. The bias current is important because it affects detector performance metrics such as efficiency of detection,

timing jitter and dark counts, all of which will be explored in Section 2.2.1.

2.2.1 Quantities and Figures of Merit

The relevant characteristics of a given SNSPD can be characterised as follows, with all the quantities discussed in greater detail below.

- **Detection Effficiency**. The probability of detecting a photon given that a photon was incident i.e. p(n | n). This can be defined in terms of a system detection efficiency or a device detection efficiency (see Section 2.2.1.1).

- **Timing Jitter**. The timing jitter can be considered as the deviation of the measured electrical response from an ideal single-photon response. It can be considered as the timing delay between output voltage pulses and the incident photons. The timing jitter can be separated into extrinsic components (those not related to the nanowire) and intrinsic components (those that exist within the nanowire). These will be discussed in detail in Section 2.2.1.2.

- **Dead Time**. The dead time is the time during photon absorption where the detector is unable to detect another photon - this is due to the breaking of superconductivity caused by the previous photon and therefore the detector has to wait until the superconducting state is restored before another photon can be detected.

- **Dark Counts**. Dark counts characterise detection events that have triggered the detector but are not caused by incident single-photons. This can be due to other events such as black body radiation from an improperly shielded cryostat, or aspects inherent to the detector itself such as the vortices. Suppression of dark counts is important for high signal to noise performance.

The next sections will now look at some of these relevant quantities and show some signature behaviours from SNSPDs.

2.2.1.1 Detection efficiency

As discussed in Section 2.2.1, there are two ways of characterising the efficiency of an SNSPD. These are the system detection efficiency (η_{SDE}) and the device detection efficiency (η_{DDE}) and are given by:

$$SDE = \eta_{SDE} = \eta_c \eta_{abs} \gamma, \tag{2.59}$$

$$DDE = \eta_{DDE} = \eta_{abs} \gamma, \tag{2.60}$$

where η_c is the efficiency of coupling, η_{abs} is the probability of the detector absorbing a photon and γ represents an internal probability that an absorption event leads to a voltage pulse. It can therefore be observed in Equations 2.59 and 2.60 that the SDE and DDE are equivalent if and only if $\eta_c = 1$, corresponding to coupling to a detector without any losses. In reality this is not possible to achieve due to considerations such as fibre-to-chip coupling (grating coupler losses must be accounted for) and waveguide losses as discussed in Section 2.1.1.4. η_{abs} can be controlled from the geometric considerations of the detector i.e. the width, thickness and the material used for the SNSPD itself. γ is a factor that depends on the operating conditions - the incident photons wavelength λ and therefore energy E_{ph}, the bias current I_B and the operating temperature T. A signature curve to show the performance of an SNSPD is typically shown by plotting the SDE as a function of I_B. An example is given in Figure 2.23 by Marsili et al. [172]. The behaviour of the SDE follows a sigmoidal behaviour. For low values of I_B, the SDE is very low - this can generally be explained by the biasing not being great enough to form a resistive spike large enough to measure a count. This is referred to as the probabilistic regime, since $\gamma < 1$. In the probabilistic regime, an increase in I_B results in an increase in SDE due to a rise in γ. Eventually, at larger values of I_B some absorbed photons lead to detection events - registering as a rise in the SDE. For high values of I_B the SDE does not appear to increase and stays approximately constant. This is known as saturation and represents the deterministic regime, where $\gamma = 1$. A saturated SDE marks the regime where $\eta_{SDE} = \eta_c \eta_{abs}$. If coupling losses are accounted for, then the deviation is due to η_{abs}. The deviation from expected absorption may arise from fabrication errors from lithography or etching which cause a mismatch in dimensions, or imperfect knowledge of the detectors absorption characteristics. For example, with NbN the refractive index at 1550 nm is quoted as $\eta_{NbN} = 5.23 - i5.82$ [173], but recent studies on grown films suggest that the absorption coefficient may be much lower [174]. η_{abs} is an important consideration for the device investigated in Chapter 6.

In terms of trends, there is a large parameter space to be explored. Here the discussion of efficiency trends will be limited to operational temperature and wavelength. An old study in 2005 investigated NbN SNSPDs and their quantum efficiency (which will be referred to as QE and is equivalent to SDE in Equation 2.59) at the visible to the infrared wavelength range [175] and two of their results are shown in Figures 2.24(a) and 2.24(b). They found an exponential decrease in the QE as a function of wavelength and for all bias currents between

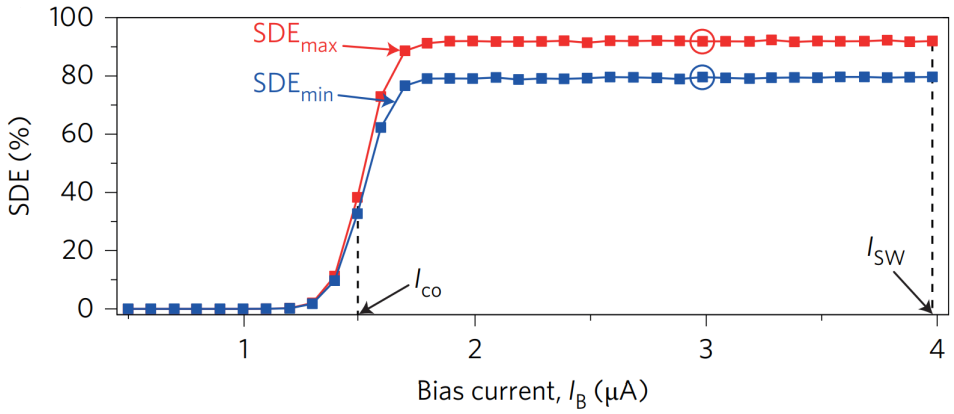

Figure 2.23: Typical SDE curve for an SNSPD detecting $\lambda = 1550$ nm photons from [172]. I_{sw} is the switching current as described previously in this section. In this particular example. SDE_{max} and SDE_{min} correspond to different input light polarisations. It can be observed in both cases that a flat profile is observed for $I_B > 2\mu$A.

$0.778I_c \leq I_B \leq 0.943I_c$. Since longer wavelength photons have less energy, the trend of Figure 2.24(a) can be explained in terms of these longer wavelength photons not being able to overcome an activation energy barrier for breaking Cooper pairs, which depends on the superconducting band gap Δ. Since $\Delta(T = 0) = 1.765k_BT_c$ according to BCS theory [176], this suggests that the superconducting material needs to have a small band gap in order to detect infrared photons efficiently. In terms of QE vs I_B shown in Figure 2.24(b), it can be seen that saturation is reached for the 560 nm photons at T = 2K. For the same wavelength but at T = 4.2K it can be observed that the same QE is reached but at a larger bias current. This most likely is due to Δ having a larger value at higher T, but within the range where saturation can still be reached. This observation also explains the other data at λ = 1550 nm, although saturation is not reached in this case.

Practically, to measure the SDE of a given detector, characterisation is usually carried out through using a single-photon source or an attenuated bright-light source such as a laser. Generally the incident photon flux can be inferred from the power, a measure of the energy per unit time. The SDE can then be calculated as the ratio of the photons counted by the detector after the dark counts are subtracted from the incident photon flux.

2.2.1.2 Timing jitter

Timing jitter is defined as the deviation of a signal from its ideal single-photon response [169]. Typically, timing jitter is taken from measuring the detectors instrument response function based on acquiring statistics from the time bins of detector counts. This forms a Gaussian distribution and the FWHM of the distribution is used to quantify the jitter, as shown by the red fit in Figure

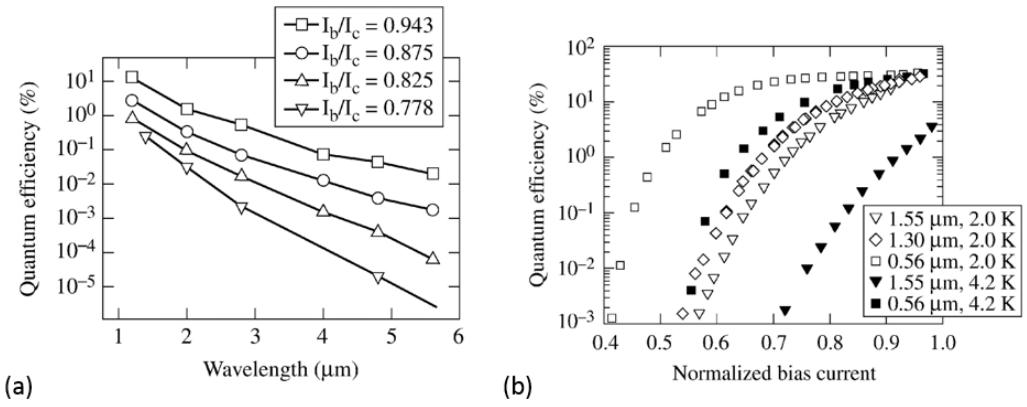

Figure 2.24: (a) Quantum efficiency as a function of wavelength. Data was taken at T = 3K. (b) Quantum efficiency vs I_B for various wavelengths and temperatures. Both graphs were taken from reference [175].

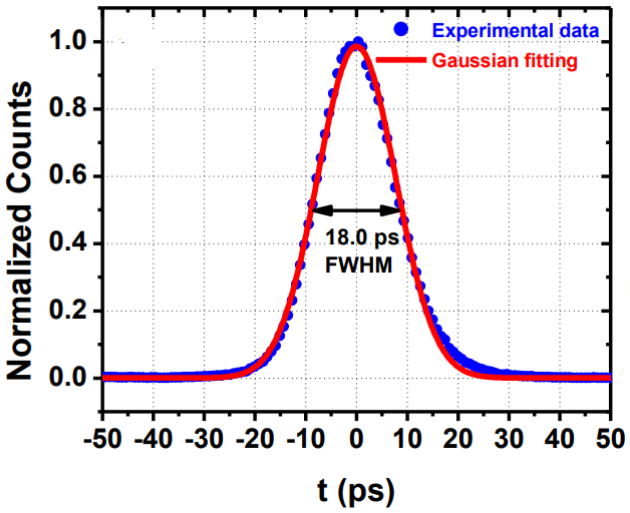

Figure 2.25: Example of an experimentally determined jitter. Figure taken from [169].

2.25. The origins of the timing jitter j come from various sources and can generally be separated in terms of intrinsic j_{in} and extrinsic j_{ex} contributions:

$$j = \sqrt{j_{in}^2 + j_{ex}^2}. \tag{2.61}$$

Intrinsic jitter can come from mechanisms in the SNSPD itself, such as the location which a photon impinges upon the nanowire [177]. Furthermore, the length of the nanowire also in-

creases the intrinsic jitter due to kinetic inductance based on the inertia of the electrons [178]. Extrinsic jitter can come from various sources such as the electronics readout, the laser used in characterising the detector and the presence of cavities if applicable. The latter case is relevant in this thesis and features in Chapter 6.

As far as I am aware, the best timing jitter was reported in 2018 by Korzh et al. on a small meander SNSPD structure [179]. This was demonstrated on 7 nm thick NbN nanowires and was solely focused on trying to demonstrate the smallest possible overall jitter. 3 ps jitter was demonstrated through a combination of a small SNSPD with a low-noise cryogenic amplifier (to reduce electronic jitter). This work suggests that it may be possible to realise sub-picosecond jitters in the future.

2.2.1.3 Dark Counts

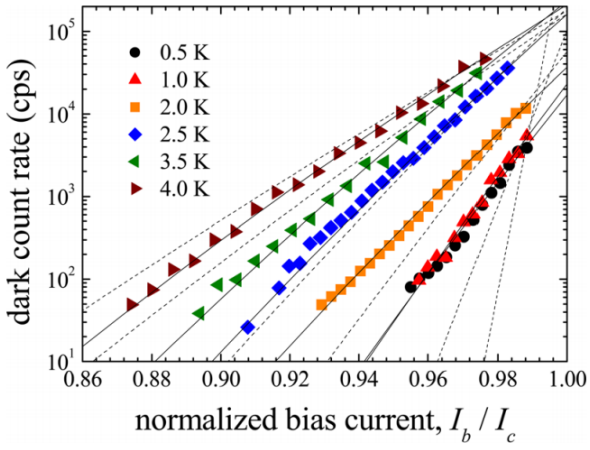

Figure 2.26: Characteristic dependence of the dark count rate on the bias current. Figure from [180].

Dark counts determine the false detection events in the detector. The contributions to dark counts can be separated into two categories. The first are intrinsic dark counts and originate from the detector itself. In this case, they can be associated with mechanisms such as increases in I_B, as shown in Figure 2.26 [180]. The characteristic exponential dependence indicates that the dark count rate is dominated by the device (as opposed to extrinsic contributions) [181]. For this reason, electrical biasing of the detector plays a substantial role in the dark counts and also expresses the requirement for a saturated SDE curve. Operation at I_B very close to I_C results in high dark count rates and therefore reduces the signal to noise ratio of the SNSPD. It is desirable in some applications to operate the SNSPD at an I_B where a high DDE is maintained but at a low DCR. The second category are extrinsic dark counts and these originate from mechanisms

such as black body radiation and stray light, which can be blocked by filtering and packaging techniques.

2.2.2 Optically Coupling to an SNSPD

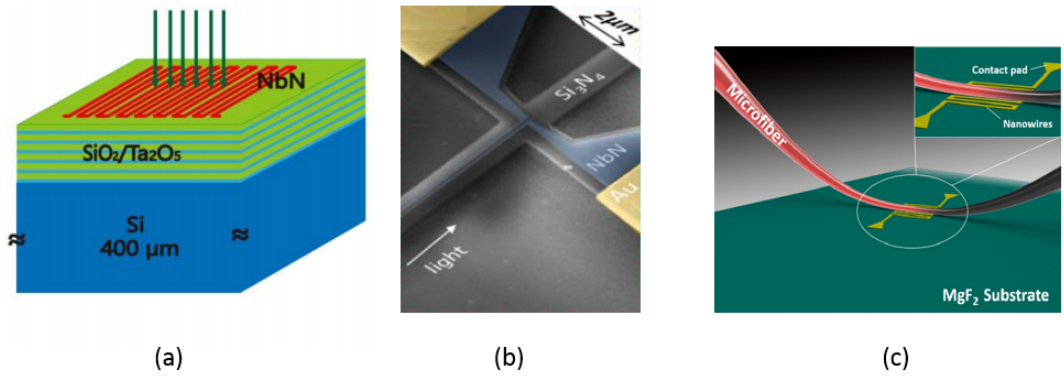

Figure 2.27: Methods for optically coupling to an SNSPD. (a) Normal-incidence [182] (b) Waveguide-integrated [183] (c) Microfibre [184].

There are three different methods of optically coupling to an SNSPD. The earliest demonstrations of optically coupling to an SNSPD used light from either above or below the substrate propagating towards the SNSPD. These are usually referred to as normal-incidence detectors. Other approaches such as waveguide-integrated detectors followed in the early 2010's (See Chapter 1) and are now commonly exploited. Another method has only been demonstrated once and holds promise. Figure 2.27 shows an example of each of these methods. In the following paragraphs I will explain each of the methods in more detail.

The normal-incidence detector involves a top-down approach (depicted in Figure 2.27(a)), consisting of an optical fibre incident on a detector [182, 185, 186]. Since these fibres have fairly large mode diameters (> 10 μm) it is required to pattern meanders of nanowires over a large area to obtain good absorption for high efficiencies. However, as a trade-off, this can increase the timing jitter through a larger kinetic inductance. Furthermore, although the meander may be patterned over a large area, the light will propagate through the film thickness, giving a very small interaction length for coupling to the detector. Section 2.2.3 shows how a cavity can be implemented with these types of detectors to improve the absorption properties.

The second method of optically coupling to an SNSPD is via evanescent coupling with a waveguide mode. This is referred to in the literature as a waveguide-integrated detector [34, 41, 183]. An example is shown in Figure 2.27(b). The waveguide-integrated approach offers a greater

interaction of the light with the nanowire, since the nanowire can be patterned for a certain length and the mode will evanescently couple to the nanowire along this length. Furthermore, spot-size issues with normal-incidence detectors are solved due to the inherent optical input and output devices (such as the grating coupler in Section 2.1.2). This allows for the SNSPD to be fabricated shorter, which can improve performance aspects such as the timing jitter. However, the η_{SDE} of a waveguide-integrated detector is more prone to external issues (for example, insertion losses of the grating couplers). This is coupled with the extra fabrication steps involved relative to a normal-incidence detector, which could cause extra issues with the device performance.

The third approach involves the use of microfibre [184, 187]. This has been motivated in circumventing the requirements for external insertion loss elements such as grating couplers, whilst still having a large region of interaction with a nanowire. A schematic of the design is shown in Figure 2.27(c). This SNSPD takes the same structure as a normal-incidence detector, but a microfibre is bound to the SNSPD material using an adhesive cladding. This approach uses evanescent coupling to the nanowire, like in the waveguide-integrated case. So far, the design and initial demonstrations have been shown, but there have been challenges that have to be considered. For example, the microfibre has to be fabricated from tapering down a standard optical fibre. Furthermore, microfibre based losses limited the SDE of this device to around 50%. The mechanism for this loss was attributed to the change in adhesive cladding index at 4K, which changed the waveguiding properties of the microfibre.

2.2.3 Demonstrations of Cavities and High Performance Metrics

High SDEs have been demonstrated and proposed through the use of cavity structures [39, 51, 172, 188]. Cavities can take on various geometries. For example, Figure 2.28(a) shows a cavity based on normal-incidence excitation [188]. A 5 nm NbTiN nanowire in a meander geometry is separated by two silicon oxide layers (SiO_2 and SiO) whose thickness has been designed to be equal to a quarter of the wavelength (λ = 1550 nm). These act as anti-reflection coatings, meaning that the reflection of the 100 nm gold mirror acts to reflect any light scattered upwards (away from the substrate) back towards the detector, whilst the cladding films act to reduce backscattered light at the NbTiN layer. This particular system reached 77% SDE. Cavities can also be present for waveguide-integrated detector geometries [39, 51]. Two examples are shown for SOI (Figures 2.28(b) and 2.28(c)). Nicola Tyler et. al proposed a cavity design for an SNSPD in a racetrack ring resonator geometry whose schematic is shown in Figure 2.28(b). The ring resonator operates in the critically coupled regime. The design is based on the 220 nm x 500 nm Si strip waveguide platform. In this proposal, detection efficiencies exceeding 99% were promised for NbN nanowires as short as 1 μm. The work also explores important parameters such as the cavities geometric size contribution to the extrinsic jitter. This was shown to be on the order of 5 ps based on the number of round trips a photon has to make in the cavity before there is a 70%

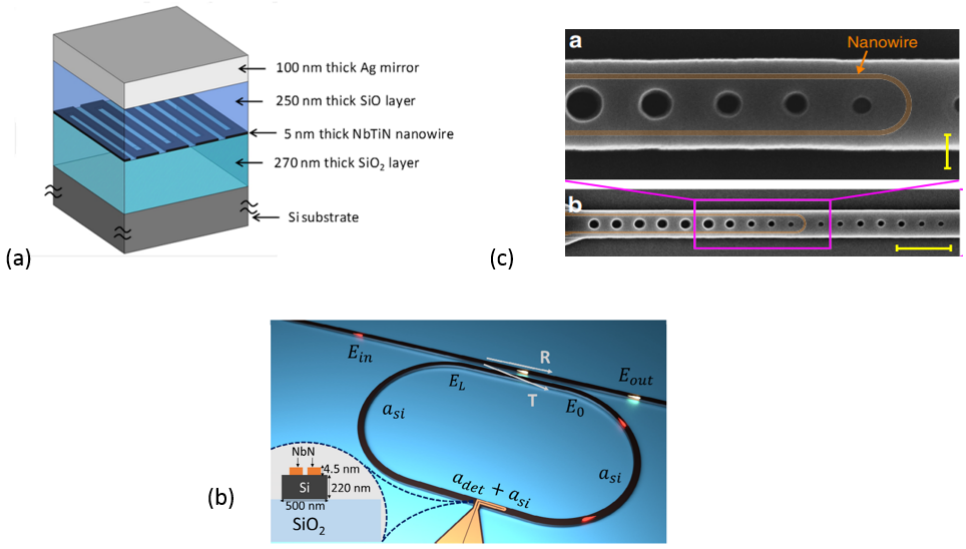

Figure 2.28: Three examples of cavity structures for enhancing detector efficiency performance. (a) is a film stack cavity for a normal-incidence SNSPD [188]. (b) and (c) are waveguide-integrated cavity SNSPD structures using SOI ring resonators and photonic crystals respectively [39, 51].

confidence in the probability a photon has been detected. This particular design will form the basis of the discussions in Chapter 6. Figure 2.28(c) is an SEM image of an SOI photonic crystal cavity SNSPD from Akhlagi et al. in 2015. In this work, a NbTiN nanowire is patterned in a U shape around photonic crystal holes designed for a front and back-reflector. These devices were experimentally demonstrated with high on-chip detection efficiencies above 95% at 1545 nm.

2.3 Conclusions

This chapter outlined the theoretical principles necessary to understand the content in the remaining chapters of this thesis. The field of silicon photonics is young and there are many reasons why this material system is promising. The integration of electronics with photonic structures and clever design enables a new generation of components with improved performances. Furthermore, as shown in this chapter, many key components for manipulation and detection of light on-chip have been developed. The remaining chapters will now focus on the simulation and fabrication of some of these devices in the direction of realisation of a detector chip. As noted in the waveguide section, Lumerical is a simulation tool that utilises the finite-difference time domain (FDTD) method developed by Yee [189]. FDTD allows electromagnetic simulations to be performed through discretisation of Maxwell's equations and calculating the electromagnetic field at each time step. FDTD analysis is very important for predicting the performance of any of the photonic components discussed in this chapter. Two Lumerical packages are used in this thesis.

The first package is MODE solutions, which was used in Chapters 4 and 6 for ring resonator structures and Chapter 5 for initial parameter sweeping. The advantage of MODE solutions is that simulations are faster due to its 2.5D effective index method. The 2.5D FDTD (also known as varFDTD) method involves collapsing the z dimension into an effective index whilst retaining full information in 2D, speeding up simulation times at the expense of accuracy. The other package is the full 3D FDTD, which was used in Chapter 5 due to the small structure footprint, enabling reasonable simulation times. The eigenmode solver of MODE was also used to model and calculate effective indices of modes for various analyses that feature in Chapters 4, 5 and 6. The next chapter looks at the development of in-house fabrication processes for these SOI components.

CHAPTER 3

FABRICATION AND EXPERIMENTAL METHODS

The fabrication carried out in this thesis was all performed in the University of Bristol clean room. Since the clean room has only been open for three years at the time of the writing this document, many of the processes have been developed during the course of my PhD. There is still much room for improvement on these processes and their implementation within the detector project. The main fabrication processes used here for the concepts shown in the succeeding chapters are electron beam lithography and dry fluorine-based reactive ion etching which are discussed in detail. The experimental setup used for experimental measurements is also shown. Finally, the story of the fabrication process is presented for the SOI platform. The story shows how errors have been overcome, resulting in fabricated waveguides and grating couplers with > -10 dB fibre-to-fibre transmission. Furthermore, racetrack resonators with Q-factors on the order of 10^3 have been demonstrated. To declare contributions, My project student Friederike Johlinger assisted in taking measurements and analysis of the data from the chips SOI Chip-1 and SOI Chip-2. I credit Pisu Jiang for providing a fabrication process flow with XR1541-006 resist that I could use when the FOx-14 resist became defective. The work with the XR1541-006 process flow is at the end of this chapter.

3.1 An Overview of the Fabrication Process

An overview of the general fabrication process is given in Figure 3.1. The materials used in this thesis are SOI with a 220 nm Si device layer and a 2 μm BOX layer beneath the device layer, resting on top of an Si substrate. Often, wafers are prepared with a protective layer (as in Figure 3.1(a)), which helps to prevent damage to the device layer during wafer dicing or cleaving and prevent further contamination from moisture when not in use. The protective layer is often photoresist, which is spin coated onto the sample. To remove the protective layer, the

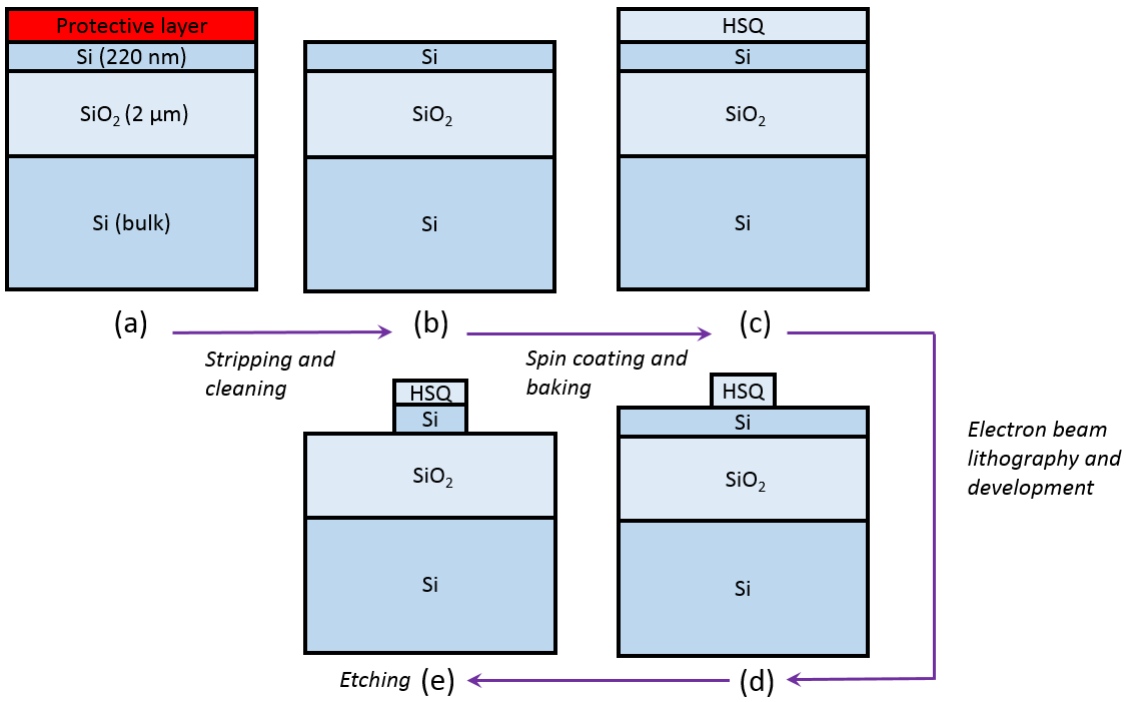

Figure 3.1: Schematic of the fabrication process for SOI waveguides in five steps. The dimensions of the relevant SOI layers are shown in (a). The fabrication steps resulting in SOI waveguides in (e) are discussed in this chapter.

samples were immersed in acetone after cleaving for two minutes. To avoid residual acetone from remaining on the sample surface after stripping the protective layer, the samples were then immersed into isopropyl alcohol (IPA) followed by water and then blown dry with N_2. This sequence of steps were used for the sample preparation stage of the process flow given from Figure 3.1(a) to 3.1(b). The cleaning of the sample prior to processing is important to ensure a clean surface free of contaminants which could otherwise result in non uniformities in resist thickness from the spin coating processes. The succeeding steps will now be discussed in order of their place on the process flow.

3.1.1 Spin Coating and Baking

Spin coating and baking are the first steps in the fabrication process. A spin coater consists of a chuck, which is usually circular and has a hole in the centre. The chuck sits on a spindle which has a vacuum line through its axis and is controlled by an electronic motor. The process starts by placing the sample on top of the hole and activating vacuum. Then, deposition of a given volume of liquid - usually called a resist - is carried out onto the centre of the substrate. This is usually carried out with a pipette, and is followed by spinning. During spinning, the liquid experiences centrifugal forces that causes it to spread across the sample. The resist is composed

of the molecules that have the properties required for lithography and the carrier solvent. The carrier solvent is pushed off of the sample whilst the resist molecules remain. The resulting thickness is dependent on the balance between surface tension and centrifugal forces.

The spin speed ω is typically set to values between 2000 and 5000 revolutions per minute (RPM). The reason for this range is for achieving a film thickness as uniform as possible over the sample. Slower spin speeds may be used to achieve thicker films at the expense of non-uniformity. The range of speeds is important because it determines the resulting film thickness. In the most basic sense, the thickness h of a resist varies as:

$$h \propto \omega^{\frac{n}{m}}, \tag{3.1}$$

where $-1 < \frac{n}{m} < \frac{-1}{2}$. In general, Equation 3.1 suggests that a faster spin speed will result in a thinner resist layer. On a basic level of theory, a dependence of $\omega^{-\frac{1}{2}}$ is predicted, whilst more advanced theories consider the rate of evaporation of the solvent during the spinning process and predict stronger inverse dependencies of ω^{-1} [190, 191]. These considerations are important in a fabrication process. For example, they can limit the resolution of features that can be defined with a given lithographic process (for example, EBL in Section 3.1.2). They may also be important for etching processes. This will be discussed in the context of Si etching in Section 3.1.3.2. Since Equation 3.1 implies that the rate of change of h depends on $\omega^{(\frac{n}{m}-1)}$, the resist thickness tends to a regime where large increases in spin speed result in small reductions of thickness. An alternative way of achieving a thinner thickness of resist can be accomplished through dilution of the solution with more carrier solvent.

3.1.2 Electron Beam Lithography

Electron beam lithography (EBL) is a technique for writing high resolution (sub 10 nm) features onto chips. Implied by the name, the writing is achieved through electrons - to be contrasted with light. This immediately highlights the resolution advantage, since the resolution of features which can be written using optical lithographic methods are diffraction-limited, with a dependence on the wavelength of light [192]. The principle behind EBL involves the generation of electrons from a source through thermionic emission. This is typically achieved through heating of a filament, in the same manner as scanning electron microscopy (SEM). The electrons are guided by sets of electromagnetic lenses through an aperture onto the sample. After the aperture, electromagnetic lenses are also used to deflect the beam within a certain area called a writefield. EBL systems can have mechanical (low resolution) or interferometer (high resolution) based stages to track the position of the beam. In this case, if a design is larger than a writefield, the beam has to move to the next writefield to pattern, which introduces some spatial error when attempting to join the structure at the boundaries of the writefields. This is known as a writefield stitching error. With

electron beam lithography, the resolution of features that can be written is determined through the following parameters:

- **Accelerating Voltage**. The accelerating voltage of the EBL system determines the energy (momentum) of the electrons that are fired towards the sample. In this case, it is particularly important to have an accelerating voltage of 50 kV or higher. The result is that the forward penetration is much greater. Furthermore, since more energy equates to a larger velocity for the electrons, the beam size is reduced relative to a lower voltage system due to the a shorter interaction time of electrons in the beam to scatter in the plane perpendicular to their propagation.

- **Type of Resist**. The type of resist limits the resolution through its molecular size. The structure of the molecule that makes up the resist determines its scattering properties. Furthermore, the chemistry of the molecule determines the type and how it will behave under exposure. This is explored in Section 3.1.2.2.

- **Resist thickness**. As an extension from the resist type, for all resists the thickness resulting from the spin process and resist type can limit the resolution of features that can be defined. The mechanism that hinders the resolution can be thought of in terms of having to penetrate through a thicker amount of material, increasing the probability of scattering.

The system used for EBL in this work is the Raith VOYAGER 50 kV system. Structures were generally patterned with a step size of 2 nm using a 30 μm aperture mode resulting in a beam current of approximately 120 pA. To avoid stitching errors, all designs were contained within 500 μm by 500 μm writefields. Contamination dots were burned into the sample for focusing the beam onto the surface for optimal writing performance.

3.1.2.1 Electron Beam Dose

In an EBL process, the beam dwells for a certain time when exposing a structure, depending on the current that depends on the aperture mode selected and the step size, which is the spacing between exposure shots. However, a very important parameter is the exposure dose, which is quoted in μC cm^{-2}. The exposure dose is a measure proportional to the number of electrons incident on the target area. In terms of the physics for low doses, not enough electrons are incident on the resist to induce a significant chemical change in the structure being exposed, resulting in most of the structure disappearing in the developer. This leads to a measured thickness that is very small. As the dose is increased, more chemical change is induced in the resist which cannot be removed by the developer, resulting in a thicker film. Eventually, when the dose reaches a sufficiently high value, there are enough electrons incident on the area to penetrate and induce chemical change through the full thickness of the resist layer. This critical value is called the clearance dose. Figure 3.2 shows an example of the clearance dose measurement in this work for

the FOx-14 resist spin coated at 5000 RPM. It can be inferred from the dose factor and the base dose that the clearance dose occurs at a dose factor of around 600 μC cm^{-2}, since increasing the dose further has little effect on the thickness.

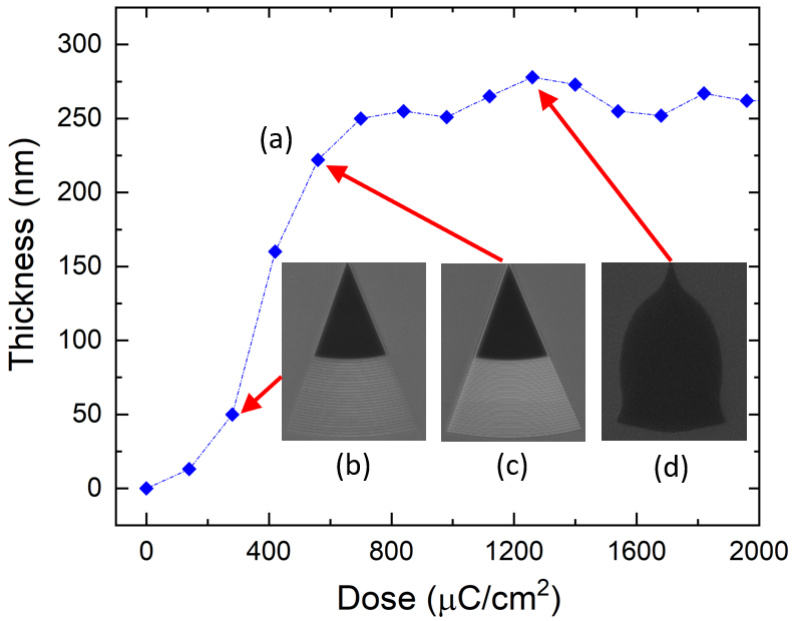

Figure 3.2: (a) Thickness curve of FOx-14 spin coated at 5000 RPM as a function of dose. This data was measured with contact profilometry on 500 nm waveguides. (b), (c) and (d) are SEM images of a grating coupler design representing underdosing, satisfactory dosing and overdosing respectively. The doses used for each structure are shown by the red arrows.

In general, Figure 3.2(a) can be used to infer dosing regimes. Dosing below the clearance dose is generally the regime of underdosing. For a structure with a specific dimension, underdosing will often result in structures with smaller dimensions than intended. At the clearance dose, there is an acceptable dose range which can be used before overdosing occurs for higher values. Overdosing can result in greater proximity effects (regions near the area exposed receiving a dose, even if they are not intended to be dosed). Figures 3.2(b)-(d) show the various dosing regimes that were explored when testing the FOx-14 resist for writing a grating coupler. At the low dose regime, there is high contrast in the colour of the gratings due to the variation in thickness - this is likely because the clearance dose has not been hit as in Figure 3.2(a). Dosing near the clearance dose results in a uniformly coloured grating. Higher dosing starts to induce proximity effects which can be observed in the tapering region, compromising the original structure. The black appearance of the grating region suggests overdosing.

More complex structures such as grating couplers can require more advanced EBL treatment. The clearance dose for a resist can be different for a different structural dimension, as will be made clear in Section 3.3. Figure 3.3 shows tilted SEM images of a grating consisting of a bigger

(260 nm) grating with a smaller (80 nm) grating in its periodic structure. It can be observed that on the lower dose structure, there is appreciable depth to the bigger grating, but the smaller grating does not appear visible. In the case of the higher dose structure, the presence of the smaller grating can be seen much more easily. However, care should be taken and a dose should be chosen such that minimal overdosing can be observed. This can also be reduced by proximity effect correction (PEC) but unfortunately PEC structures did not appear to pattern well during this stage in the development of the clean room processes. The relative thicknesses of the resist layer for these structures should be the same to avoid issues with the etching process (described specifically in Section 3.1.3.2).

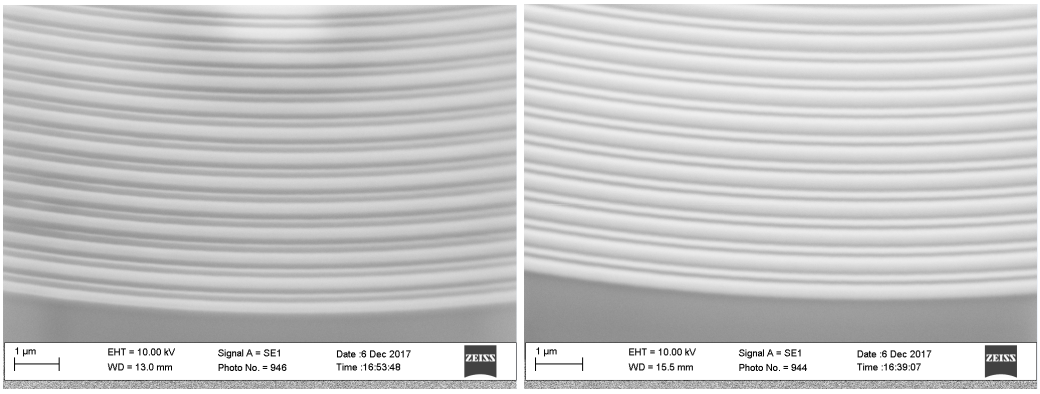

Figure 3.3: Two examples of grating couplers written in HSQ and imaged with SEM at a 45 degree angle to illustrate the dependence of clearance dose on structural dimension. The structure on the left is exposed with a dose of 350 μC cm^{-2}, while the structure on the right is exposed with a dose of 525 μC cm^{-2}.

3.1.2.2 Resists

Resists are the chemically active compounds that enable transfer of patterns in the EBL process. Resists generally come in two types, positive and negative. The terms describe the direction of the chemical change on electron beam exposure - the change in solubility of the molecule in the developer solution. For a positive resist, the area that is exposed becomes soluble in the developer, meaning that the unexposed areas remain after development. This results in trenches in exposed areas. On the contrary, a negative resist starts out soluble in the developer and then becomes insoluble on immersion in the developing solution. In terms of chemical change, the descriptions above are linked to polymerisation (negative resist) or breaking down polymers into soluble monomers (positive resists).

Positive resists include poly-methyl methacrylate (PMMA) and ZEP520A, whereas negative resists include hydrogen silsesquioxane (HSQ) and ma-N. Generally, resists will have various properties. PMMA and HSQ are high resolution EBL resists and are capable of patterning very

small (10 nm) features whereas the ZEP520A resist has shown excellent etch resistance, which provides great selectivity for etching (more on this will be discussed in Section 3.1.3).

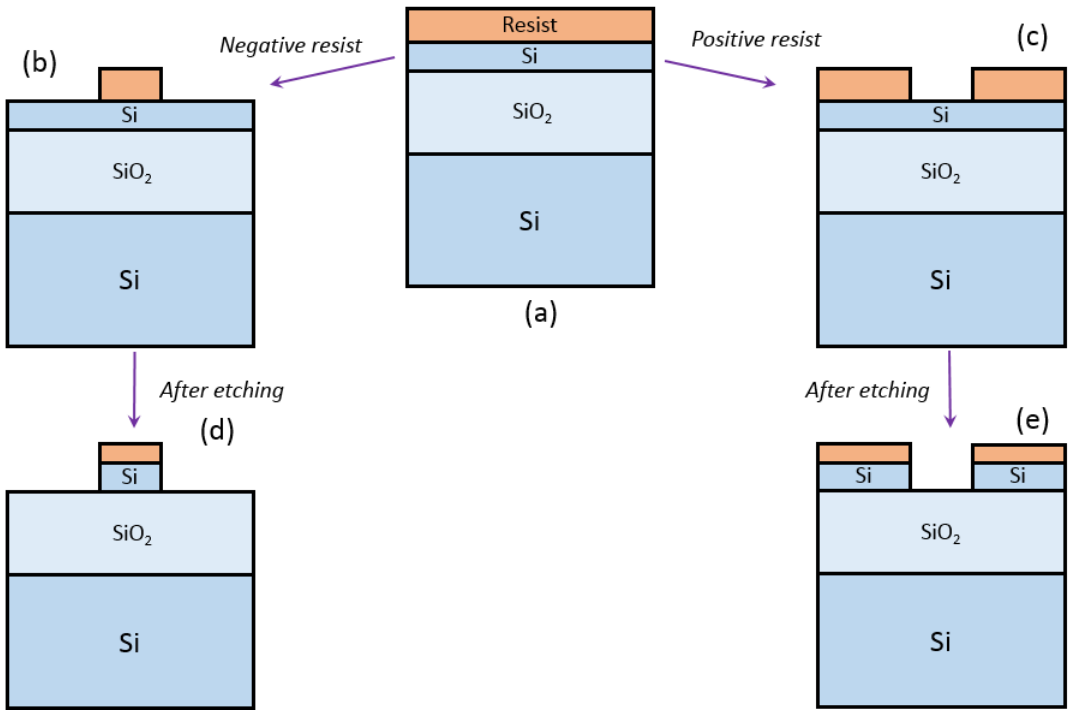

Figure 3.4: Schematic to show the contrasting responses of positive and negative tone resists when creating an etch mask with EBL. (a) is the initial resist after spin-coating and baking. (b) and (c) show the resulting structure obtained after EBL and development for negative and positive resists respectively, whilst (d) and (e) show the structures that are obtained with the etch masks of (b) and (c) after etching.

3.1.2.3 Development

In development, the EBL compound is immersed in a solution which effectively etches away the soluble resist from the film. It is important to emphasise that the structural change induced from EBL does not ensure total insolubility. For example, continued immersion in the developer will result in all of the structures disappearing. There is a time window for optimal development, with sensitivity to structural quality depending on the dilution or chemical properties of the developing solution. For example, cold development of PMMA resulted in higher resolution and the ability to fabricate lines with resolution as high as 4 nm [193]. For the SOI waveguides in this work, the developing solution was tetra-methyl ammonium hydroxide (TMAH), with all development carried out at room temperature.

3.1.3 Reactive Ion Etching

Reactive ion etching (RIE) is a technique that can be used for transferring patterns on a sample (for example, structures that are written with with EBL) to a film. The etching process enables the fabrication of waveguides, grating couplers and other integrated photonic devices shown in Chapter 2. The principle behind etching is the creation of a plasma - a state of matter that involves gaseous phase neutrals and ionised species in a non-equilibrium. To generate a plasma, electric fields are required. This is generally achieved using two parallel-plate capacitors. The ions are then directed by an electric field towards the sample. Etching mechanisms can involve both chemical and physical mechanisms. RIE has some advantages in that anisotropic etches can be achieved (in contrast to wet etching approaches which are generally isotropic).

3.1.3.1 Important quantities for RIE Processes

A given RIE recipe has some important quantities to consider in processing and they are described here:

- **Etch rate.** This is the speed at which a given process etches through a film of material. For RIE processes, this is usually on the order of 10s to 100s of nm/min.
- **Selectivity.** The selectivity S is the ratio of etch rates of two materials. Selectivity is often used to compare the etch rates of the film to the mask.
- **Anisotropy.** Anisotropy the favouring of etching in one direction over the other, usually defined in terms of the relative etch rates.

The etch rate R_x, where x denotes the material (Si, HSQ, PMMA etc) is a function of the various gas flow rates and RIE power. For a given material and etch recipe, there will be a unique etch rate. To determine the etch rate, there are two methods that can be used. Firstly, many samples can be etched with the same process, but varying the etching time per run. This is demonstrated in Section 3.1.3.2. Secondly, interferometry can be used to determine the etch rate. Interferometry was used in this thesis but not for etch rate determination. In the context of this chapter, the selectivity S can be defined as:

$$S = \frac{R_{Si}}{R_{HSQ}}. \tag{3.2}$$

The etch selectivity is very important for a process flow, since it can force constraints. An example in this work is the critical thickness of HSQ required to mask a 220 nm Si etch. If the selectivity is not favourable in terms of etching Si, it will require a thicker HSQ, which may compromise resolution in the mask from the EBL process in Section 3.1.2. For Si, there have been studies on the etch selectivity as a function of power and gas flows. For more information,

the reader can refer to the references [194, 195].

The anisotropy of an etch process, A, can be defined as:

$$A = 1 - \frac{R_{lat}}{R_{vert}}, \tag{3.3}$$

where R_{lat} and R_v characterise the etch rate in the plane of the film and in the vertical direction respectively. Often associated is an angle of the side wall. For example, an etch where $A = 1$ would have a side wall of 90 degrees. For the waveguides in integrated photonics, and particularly the designs presented in this work, they are generally based upon structures which satisfy $A = 1$. Referring to Equation 3.3, this would involve a reduction in R_{lat} or increasing R_{vert}. The lateral etching rate depends on various parameters such as the gaseous phase mean free path, which is inversely proportional to pressure [196]. Physically, a lower pressure means a lower amount of gaseous neutrals or ions in the chamber, reducing the probability of a collision. Furthermore, gas phase chemistry in the plasma can result in polymer formation on the sidewalls, which then act as an inhibitor to the lateral etching. For more information on these processes and their mechanisms, see the references [197, 198].

3.1.3.2 Characterising a Silicon Etching Recipe

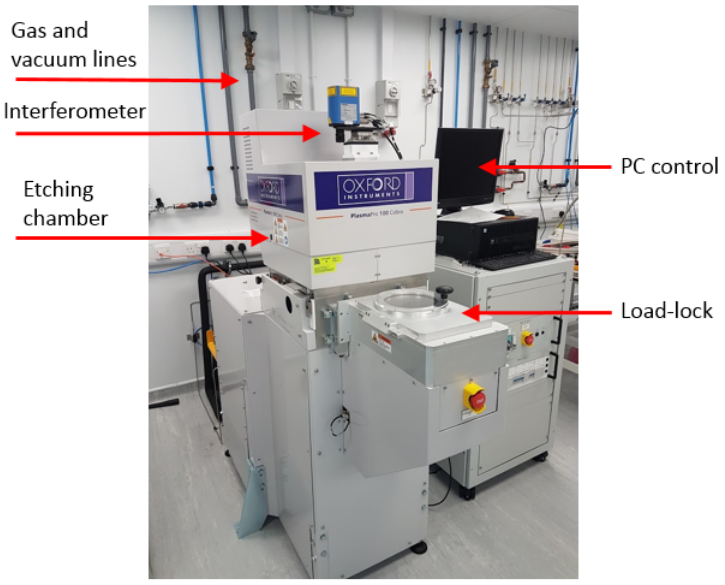

Figure 3.5: Image of the RIE-ICP system used for etching the devices presented in this work. The system is controlled electronically through a computer and has a laser interferometer for etch tracking.

The RIE etching in this work was carried out with a Oxford Instruments PlasmaPro 100 Cobra RIE-ICP system. An image of the system is shown in Figure 3.5. The system is loaded with a laser interferometer for etch tracking which is discussed in terms of etching SOI in Section 3.1.3.3. The system came with a silicon etch recipe that was tuned by Oxford Instruments for QETLabs purposes. This meant that characterisation of the etch rate and the selectivity was necessary for processing. The etch recipe uses an RIE forward power of 30W with 14 sccm (cubic centimetres per minute) CHF_3 and 56 sccm SF_6.

To proceed with the characterisation, Si samples were used instead of SOI for two reasons. Firstly, Si wafers are much cheaper than SOI and therefore are appropriate for process development purposes. Secondly, since HSQ effectively turns into SiO_2 during development, it is more difficult to remove with methods such as O_2 plasma cleaning. Hydrofluoric acid (HF) shows no appreciable etching of Si whilst stripping HSQ. With SOI, this convolutes the measurement because HF can attack the BOX layer. To characterise the process, 50 μm x 50 μm block structures were patterned with EBL into 250 - 265 nm thick HSQ onto a parent Si sample that was cleaved into five different samples. Each sample was then etched in its own process for a unique time, ranging from two minutes to eight minutes. In order to calculate the etch rates of HSQ and Si, three measurements of the structures height must be made for each etch time. These are:

- **Measurement 1:** Measuring the height of the structures patterned into the resist layer i.e. the initial HSQ thickness t.
- **Measurement 2:** Measuring the height of the structures straight after the etching process, yielding the quantity t_{obs}. Refer to Figure 3.6.
- **Measurement 3:** Measuring the height after removing HSQ with HF. This yields t_{Si}.

Since Measurement 3 directly yields the Si thickness t_{Si} then R_{Si} can be extracted from Measurement 3 alone. To extract R_{HSQ}, it is necessary to perform Measurement 2 and measure t_{obs}, which is the sum of the two layers:

$$t_{obs} = t_{Si} + t_{HSQ}. \tag{3.4}$$

Since the original thickness of resist t is known from Measurement 1, it is possible to calculate the amount of HSQ that has been etched from $t - t_{HSQ}$, since knowledge of t_{Si} is obtained from Measurement 3. Measurement 2 is important because the measured thickness is related to S. Figure 3.6 shows the various observations that can be made from thickness measurements for a given etch time depending on the relative material etch rates (and therefore the selectivity) of the

process. Figure 3.6(a) corresponds to highly Si-selective etches, characterised by a much quicker etching speed relative to resist, whilst (c) corresponds to the opposite case where the etch process is selective to the mask. In this case, the mask is likely to be depleted quickly. This generally will mean little etching of the pattern into Si, requiring a thicker etch mask. It was discussed in Section 3.1.1 that this is highly undesirable for nanostructures due to resolution reasons. Typically, most processes will fall into (b), where the etch rates are comparable. When the etch rate of the mask is slightly greater than the film as shown in (b)-(ii), there may be mask present after the etch, but generally this is undesirable although to a lesser extent than part (c). If a measurement of the thickness t_{obs} is made after the etch in this regime, it will be thinner than the original thickness t before etching. On the other hand, when the etch is favoured towards the film as in (b)-(i), generally the mask will have etched by a certain amount by the time the desired thickness of the film to be etched has elapsed. For film-selective etches, t_{obs} will be larger than t.

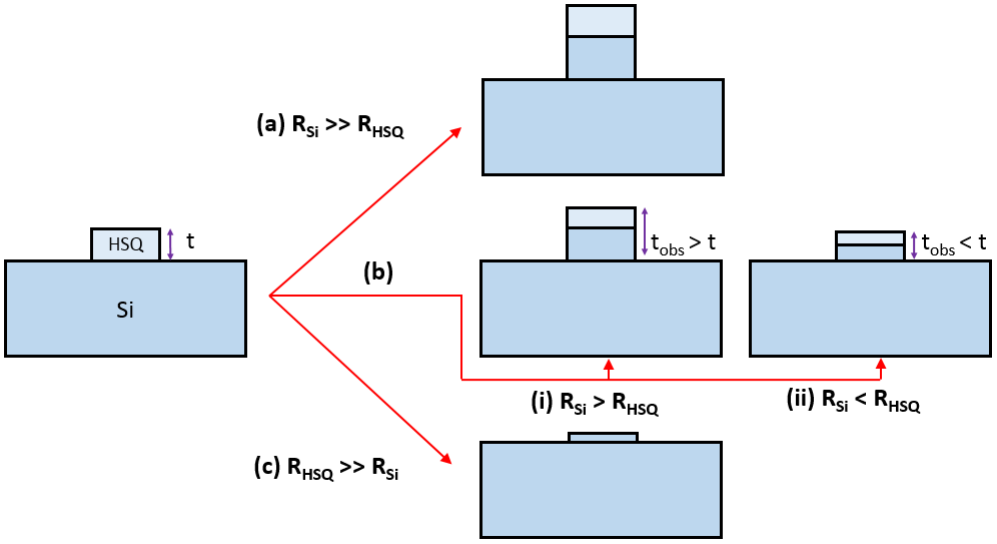

Figure 3.6: Description of the various etch regimes. (Left) is the structure in the resist layer after EBL and development, with a given thickness t. The regimes (a) through (c) on the right are discussed in the text.

Figure 3.7 shows the results of the analysis. The data is displayed in terms of the measured Si thickness and the thickness of HSQ that has been etched as a function of time. For each sample, ten measurements of the height were performed for each etch time using contact profilometry to obtain statistical significance. There are observed linear trends for the Si and HSQ thicknesses, which is expected for an etch process with stable powers and gas flows. Linear fits to the data yield the etch rates R_{Si} = 33.14 ± 0.13 nm/min and R_{HSQ} = 18.05 ± 0.72 nm/min. The larger error bar for R_{HSQ} can be linked to the variation of t due to the thickness profile of the resist after spinning. The smaller error bar for R_{Si} is therefore reflective of Si thickness measurements not

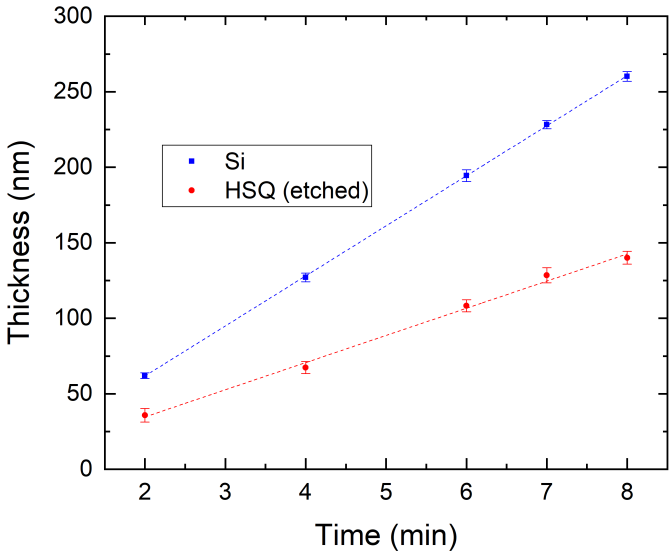

Figure 3.7: Characterising Si etching recipe through multiple etches. Blue squares are Si data points and red circles are HSQ data points. The dotted lines represent linear fits through the data sets. The fits can be used to extract the etch rates, yielding the S value for the process.

requiring any prior measurement of the structures with the resist layer. These values were used to calculate S, resulting in $S = 1.836 \pm 0.07$, where the error ΔS here has been calculated by standard error propagation methods:

$$(\frac{\Delta S}{S})^2 = (\frac{\Delta R_{Si}}{R_{Si}})^2 + (\frac{\Delta R_{HSQ}}{R_{HSQ}})^2. \tag{3.5}$$

The significance of the Si-favoured etch for this work is very important. Since the required device layer thickness is 220 nm, the selectivity can be used to calculate the critical thickness of HSQ required to mask this process, yielding a value of 120 nm. This provides a lower bound for the required thickness of resist, although to be safe from variations and fluctuations in the process there should be an excess in thickness of at least 40-50 nm. HSQ in the form of FOx-14 and FOx-16 proprietary resists are available in the University of Bristol cleanroom. FOx-14 spin coated at 5000 RPM resulted in a thickness between 250-260 nm, whilst FOx-16 resist was found to spin a 90 nm thick layer at 2000 RPM. Based on the measured etch selectivity, FOx-14 could etch through the 220 nm Si device layer, leaving a capping layer of roughly 130-140 nm. It should be noted that the measurements shown here were carried out in the timescale of less than a week. For longer timescales, the etch rate is prone to fluctuations. This makes interferometry a more appealing choice when performing full etches on the device layer and will now be explored.

3.1.3.3 Etching Si with Interferometry

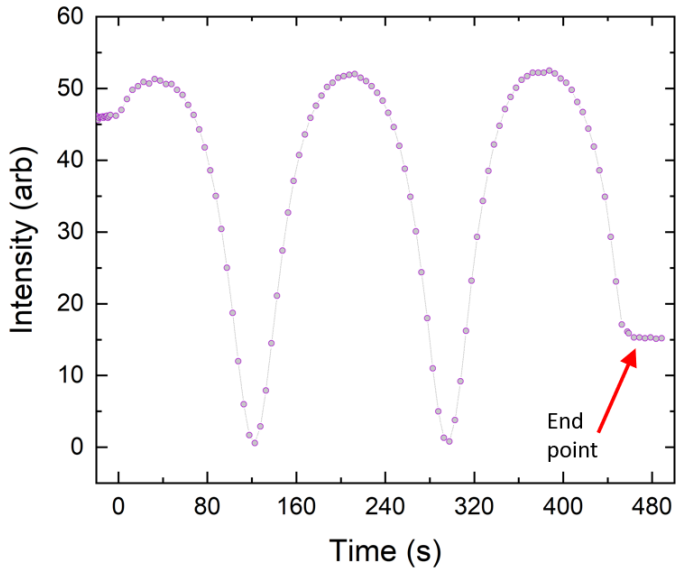

Figure 3.8: Tracking the progression of an SOI etch. Periodic fringes are observed, whilst the end point is also observed by the presence of a flat line - or a suppression of the fringe periodicity.

Interferometry is an important aspect of RIE, which allows in-situ tracking of the etching process. This tracking offers the ability to perform end-point detection, which is important for being able to determine when a film has been fully etched. This method has a large advantage over the timed method that was used to characterise the etch recipe given in the previous section because the fluctuation of the etch rate does not matter - the end point will remain an indication of when to stop etching. A description of the process is as follows. Light from the laser is incident on the film. A fraction of the light is reflected from the film surface and a fraction is transmitted through the film according to the Fresnel equations described in Section 2.1.1 of Chapter 2. The light that is transmitted through the film proceeds to travel through the layer until it reaches the lower interface. At this point there is also a reflection and transmission. The reflected signal from the top and the bottom interfaces interfere, which results in a periodic signal as a function of time. The periodic signal has a period that depends on the materials refractive index and the etch rate. The change in periodicity is an indication that the device layer has been fully etched. If the etch is continued beyond this point, the next layer will start to etch and generally fringes with a different periodicity corresponding to the new material will be observed. For the 220 nm SOI used in this work, only the Si layer was etched using this process, so the end point is important. Figure 3.8 shows an example of an SOI device that was etched using end point detection with the etching recipe characterised in 3.1.3.2. The interferometry for the RIE system here uses a 635 nm red laser. Before etching, the camera is used to focus the laser onto the sample to achieve as large a signal as possible. It is essential for the camera to be aligned to the Si (as

opposed to being focused on the structures written in HSQ), otherwise the end point will occur according to depleting the mask. Whilst a high signal to noise is desirable, too much signal can flood the detector, meaning that the peaks may not get resolved. This results in a step-function like response, which can mask where the true endpoint of the etch is. In this work, care was taken to avoid flooding the detector signal, resulting in clear sinusoidal behaviour being observed repeatedly from run to run.

3.2 Measurements

3.2.1 Automated Testing Station

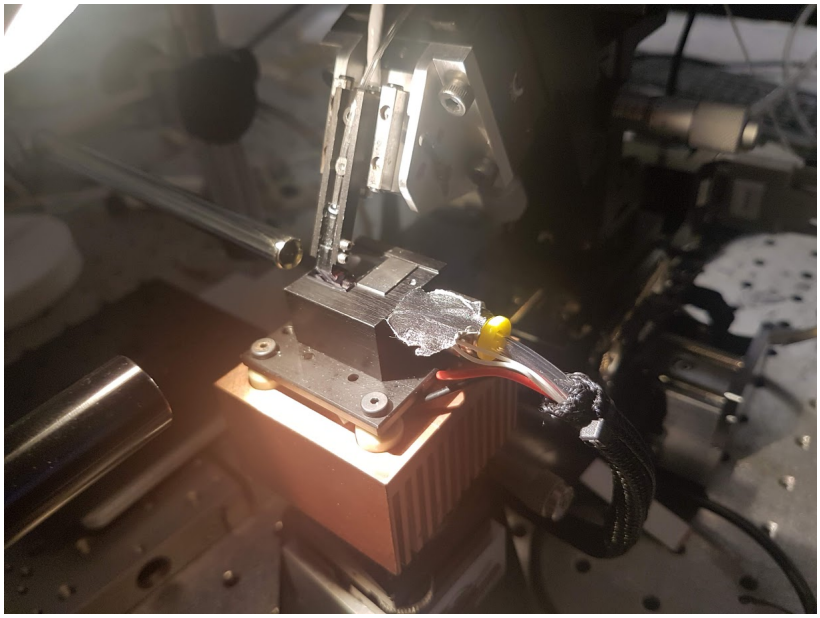

Figure 3.9: Image of the sample stage. The sample rests on a block with four vacuum holes. There is a blank sample to the right which can be used to line up a sample with the lip at the back.

The measurement setup used in this work is an automated photonics testing station made by the company Maple Leaf Photonics and is designed to be compatible for coupling to integrated photonic circuits via grating couplers. A picture of the setup is shown in Figure 3.9. The sample rests on a stage which has four vacuum holes for securing a chip to prevent any movement that may arise during operation from mechanisms such as touching the chip with the fibre array/stray turbulent air flow. Although not used in this work due to the passive nature of device operation, the stage has a water cooled copper block for maintaining a constant temperature. Also, there is a raised lip at the back which the chip can rest against and can be used for alignment. Not shown on the figure are screws that can be used for fine tuning rotation and sample levelling adjustments.

The stage is separated from the fibre array, which is controlled by electrically driven motors through Maple Leaf Photonics software with a precision of 1 μm, whilst the X and Y (horizontal plane) degrees of freedom have an adjustment range of 50 mm and the Z (vertical) degree of freedom has an adjustment range of 30 mm. In this work two fibre arrays were used initially - one which was polished at a 10 degree angle and the other which was polished for a 25 degree angle. The fibre array itself sits in a glass fibre holder as seen in Figures 3.10 and 3.11, with a fibre spacing (pitch) of 127 μm. The mount for the fibre array holder is adjustable, allowing incident angle adjustment between $\pm$5 degrees. There are three goniometers that can adjust the fibre array pitch, yaw and roll, resulting in six degrees of freedom available to the user. Also attached to the stage controlling the fibre array is an Edmunds camera with 2x magnification and 65 mm working distance which is fixed by screws. This camera is coupled to the main setup, meaning that it moves with the fibre array. The Edmunds camera provides a plan view of the sample, which helps for locating structures and aligning the fibre array to a particular structure for coupling. Finally, there are two additional cameras used in the setup. One is positioned perpendicular to the fibre array which allows the user to check the fibre array angle and height above the chip, whilst the final camera is positioned to image the fibre array itself which is very important for a better visualisation of how close the fibre array is to the chip and therefore potentially avoiding damage due to crashing. Examples of the views and information that can be obtained from these cameras are shown in Figures 3.10 and 3.11 respectively.

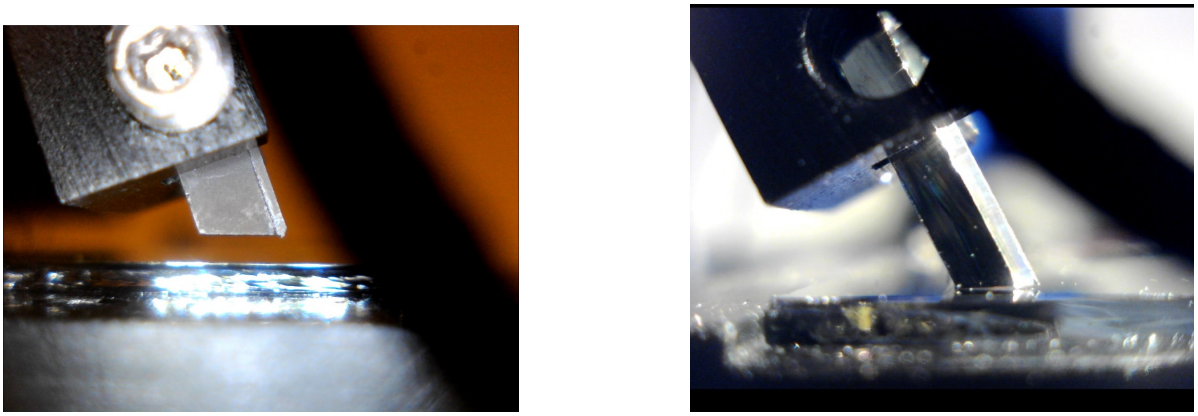

Figure 3.10: Side view camera image of the fibre holders with fibre arrays polished for incident angles of 10 (left) and 25 (right) degrees respectively.

3.2.2 Coupling to a Photonic Chip

There are two methods of coupling to a photonic chip that can be carried out with the Maple Leaf Photonics setup. One utilises the automatic nature of the setup whilst the other is manually operated. In both cases there are some common steps to be followed. This section will discuss

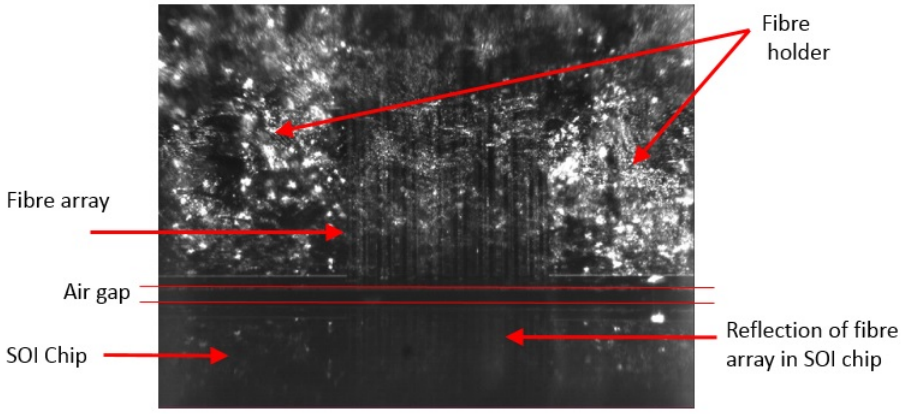

Figure 3.11: View from the camera facing the fibre array head-on. In this image the fibre array can be observed to be close to the chip, since the reflection of the fibre array from the chip can be observed.

how to couple into a chip using the automatic functions available on the setup. Firstly, the chip must be placed onto the sample stage with tweezers in the correct orientation. This is due to the optimal coupling angle for a desired wavelength that is required when using grating couplers for optical coupling (given in Section 2.1.2 of Chapter 2). If the grating coupler has a positive incident angle, the fibre array should be pointing in the direction of the focusing for the gratings. In the opposite case of a negative incident angle, the chip must be rotated 180 degrees. Once the chip is mounted, the rotation is the first important degree of freedom to align. This is the relative angle between the fibre array and the grating couplers. Fabrication of devices on the chip should be carried out in a way that devices are spaced apart by a multiple of 127 μm to match the fibre spacing in the fibre array but lie on the same coordinate for one of the axes.

The plan-view camera can be used to understand the situation as shown in Figure 3.12. The degrees of freedom available are the rotation of the sample stage, the placement of the chip itself and the pitch and yaw of the fibre array. Generally, adjusting the roll can be carried out using the camera as in Figure 3.11 and a reference such as a line on the PC software or a block object on the sample stage. The use of a line is generally preferable since adjustment of the fibre array yaw and the chip rotation can be carried out at the same time. This step is important because it improves the coupling efficiency due to the better matching of the light injected and emitted in and out of the waveguides.

Once the rotation is aligned, the fibre array should then be moved towards the desired structure to couple light into. Firstly, the fibre array should be moved down so that it is 20-50 μm above the sample surface, or close enough that its reflection can be observed (as identified in

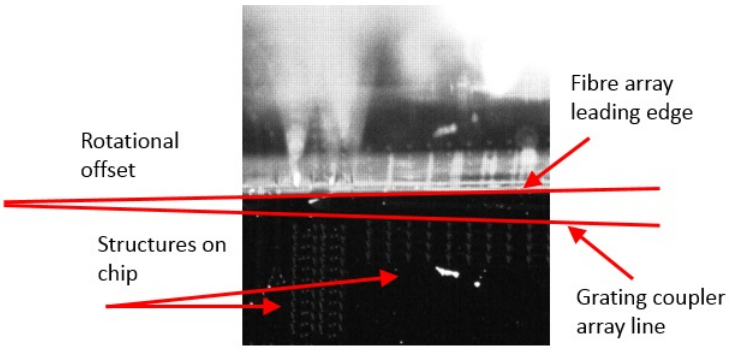

Figure 3.12: Example of chip rotation misalignment. The fibres are visible although not in focus due to the difference in height between the chip and the fibre array.

Figure 3.11). After achieving this height the next step is to move towards the desired structure. Since the wavelengths of light used are in the infrared, this step is tricky due to the inability to see the beam. In order to align with a structure on the chip, visible laser light should be injected into the optical fibres as shown in Figure 3.13. The fibre array should be then moved in the appropriate direction to align with the grating coupler. If this is achieved with good sample rotation, the optical coupling effectively becomes a 1D problem.

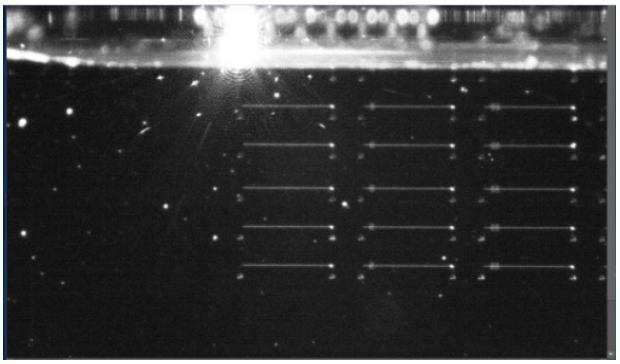

Figure 3.13: Observation of red laser light on the chip surface used for optical alignment.

At this point the manual and automatic methods for coupling diverge. In the manual case, coupling would be achieved by disconnecting the red laser and connecting the infrared laser. Then through moving along the axis of the grating coupler until coupling is found. Generally there is an offset which needs to be accounted for. Once this offset is found, it is possible to line up the fibre array with a grating and then move along the grating axis by the offset to find coupling quickly. For this thesis, the automatic method was used. The testing station has a built-in raster scan function, which can bypass the requirement of using a visible laser entirely. On the other hand, it can be used in conjunction with a visible laser. A rastering window can be defined with a

length for each translational axis, which determines the size of the scan area. Figure 3.14 shows the result of the raster scan. The fibre array can move to a desired coupling port directly through the software or by reading the distances and moving in each axis respectively.

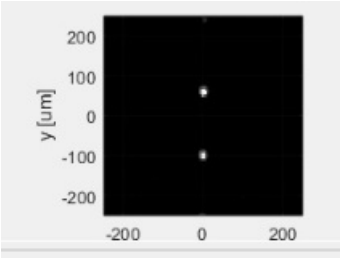

Figure 3.14: Result of raster scanning a 500 μm x 500 μm window. Coupling ports show up as bright white spots. The brightness of the spot is proportional to the coupled power.

Once coupling to the first structure is found, it becomes a matter of identifying the structure. Since a chip generally has many structures on it, a regularly repeating spacing can make structures hard to disambiguate. To avoid issues with identification, it can be beneficial to deliberately design features in ways that warrant distinguishability. This can include patterning groups of three structures in a writefield with a common spacing, but have a different spatial separation to the next writefield. These designs allow easier disambiguation when raster scanning over the chip.

Finally, when coupling was not found using the methods above, other methods were attempted to obtain coupling. Since the incident angle and the peak wavelength of a grating are related by Equation 2.30, changing the wavelength might result in coupling due to a change in the grating coupler dimension or period, resulting in the coupling wavelength being within the gratings bandwidth for that given incidence angle. For parameter sweeping in EBL this can be important since changes in exposure dose will result in varying size features, which will shift the peak wavelengths of grating couplers.

3.2.3 Optical Measurement Setup

The measurement apparatus used with the automated testing station is shown in Figure 3.15. Light is injected from a Yenista Tunics S-100HP tunable diode laser with a wavelength range of 1500 - 1630 nm and an adjustable power from 0-12.5 dBm. Light propagates through single-mode fibre into a polarisation controller which is used to maximise the coupling of TE-polarised light. After the polarisation controller, the light propagates through single-mode optical fibre and is guided into and out of the chip by grating couplers. The light which is guided out of the waveguide is coupled to another single-mode fibre in the array which is connected to a Keysight N7747A detector with a dynamic range of -100 dB. The detector has two available channels, which is

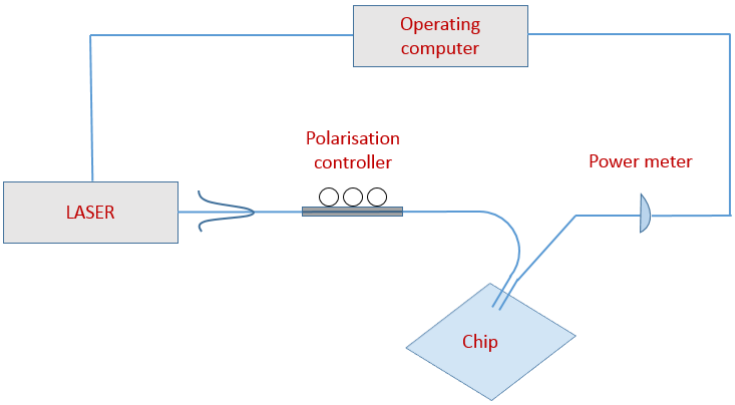

Figure 3.15: Diagram of the experimental setup used for optical measurements.

useful for analysing quantities such as crosstalk from a waveguide crossing in Chapter 5. Unless stated otherwise, measurements were taken at a wavelength of 1550 nm and a laser power of 0 dBm.

3.3 Characterisation of SOI Waveguides

SOI waveguides were fabricated using negative tone HSQ resist. Electron beam exposure was carried out at 50 kV with a step size of 2 nm, a base dose of 350 μC cm^{-2} and adjusted using a dose multiplier. The initial structures that were fabricated were cutback measurements designed for extracting the propagation losses. The following section will guide through the process of fabrication and measurements of waveguides and how problems were solved. The process flow is given below:

1. Wash sample (acetone, followed by IPA and then washing with DI water)
2. Spin FOx-14 HSQ resist at 5000 RPM, 5000 RPM/s, 30s
3. Bake for two minutes at 150 ^oC, followed by two minutes at 220 ^oC
4. Expose with EBL with 50 kV accelerating voltage, 110 pA beam current, 2 nm step size
5. Develop for two minutes in TMAH
6. Etch with interferometer to determine the end point as in Figure 3.1.3.3
7. Measure with automated testing station setup shown in Section 3.2

3.3.1 Choosing a Grating Coupler Design

In QETLabs, we commonly use a shallow etched uniform grating coupler for foundry produced devices with $\Lambda = 630$ nm, $W = 315$ nm, therefore $FF = 0.5$ and an etch depth of 70 nm with an incident angle of 10 degrees. Since the clean room processing at the University of Bristol is new and many parameters need to be adjusted from run to run to improve performance of devices, the complication of a two-step etching process is undesirable and slower. For this reason, two different types of fully etched grating were investigated in this work. The first is a fully etched version of the grating mentioned above. The second is the sub-wavelength grating which has Λ = 560 nm with a major grating width of 260 nm and a subwavelength grating of width 80 nm with a coupling angle of -25 degrees [90]. Firstly, the fully etched grating was tested for various doses (525, 560, 595 and 630 μC cm^{-2}), with simple waveguides connecting two grating couplers. Only coupling was found at 595 and 630 μC cm^{-2}, but coupling levels at 595 μC cm^{-2} were found to be more than -10 dB worse at peak wavelength and were discarded. Figure 3.16 shows behaviour from two different devices that were fabricated with a dose of 630 μC cm^{-2}. The spectra of first device (labelled Device 1) was not observed on any other of the devices in this dose. The peak wavelength was at 1550 nm with a 10 degree incidence angle, achieving a peak transmission of -12.5 dB. It is believed that this device was overdosed in a way that mimicked a two-step etch, reproducing the behaviour of a shallow etched grating - which is why it has a very small oscillation ripple, unexpected for a process which should yield a fully etched grating. Device 2 shows a more characteristic signature of a fully etched uniform grating that was observed on multiple structures - it has a large oscillation ripple of amplitude of approximately 3-4 dB. This is expected due to the large differences in η_{eff} in the grating teeth and the gap regions, leading to large reflections as discussed in Chapter 2. As a consequence, the coupling level is much lower (-25 dB at peak wavelength), with a peak wavelength blueshift of $\approx$ 50 nm relative to Device 1. The chip was cladded with 2 μm of SiO_2 and retested to attempt to observe better performance. Device 2 with 2 μm SiO_2 resulted in relatively worse coupling performance relative to air (-28 dB at peak wavelength). However, the peak wavelength looks similar to Device 2, but with a much smaller oscillation ripple of amplitude 1-2 dB. In this case, the best explanation for the result is that depositing SiO_2 has reduced the reflection due to reducing the relative difference in effective indices in the grating region because $\eta_{SiO2} = 1.44$ whereas $\eta_{air} = 1$. However, the quality of the SiO_2 is rough, with particle-like regions that may cause scattering or absorption, resulting in worse transmission.

The result of this initial test was that coupling was possible with the fully etched uniform grating. However, the sub-wavelength grating should also be attempted, since it is posited to reduce reflections and increase coupling efficiency due to its sub-wavelength grating creating effective index regions. This was investigated on the next chip.

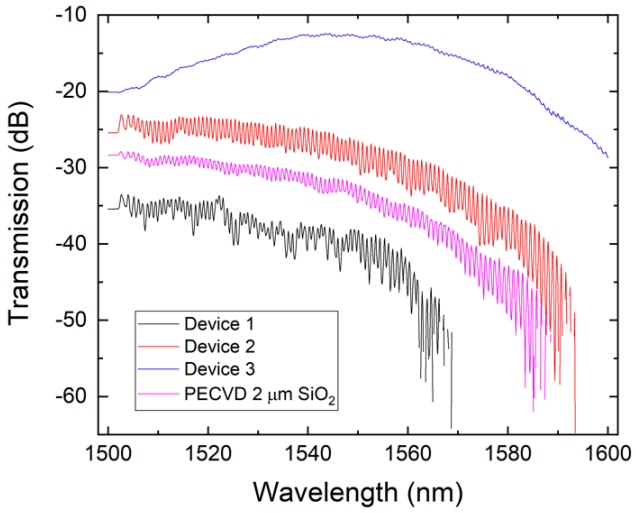

Figure 3.16: Grating coupler transmission spectra for the uniform fully etched grating.

3.3.2 SOI Chip-1

The first chip that was fabricated with a full set of structures using the sub-wavelength grating was SOI Chip-1. On this chip, the first objective was to characterise the loss through the cutback method and find a working dose range. Also, a sweep of the ring resonator coupling gap between 100 nm and 300 nm in steps of 50 nm to observe all the coupling regimes was employed. The purpose of the ring sweep is to obtain knowledge of where the critical coupling point occurs, so that the gap can be determined for over-coupling, which is necessary for the concept discussed in Chapter 4. The loss measurements range from 285 μm to 1085 μm in four different measurements, with nine repeats for the shortest waveguide and 6 for all of the other structures due to writefield consideration. It should be noted that 6 different waveguide lengths were meant to be exposed but the same structure was repeated in three columns by accident.

Figure 3.17: Mask used for Chip-1. The dotted lines represent writefield boundaries. Port spacing for all devices is 254 μm .

Initial measurements of Chip-1 found no coupling for doses 525 μC cm^{-2} and 560 μC cm^{-2}, whilst measurements of dose 595 μC cm^{-2} were around -35 dB fibre-to-fibre at 1550 nm. Struc-

tures patterned with a dose of 630 μC cm^{-2} showed promising results, with the best coupling of -16.5 dB at a peak wavelength of 1530 nm as shown in Figure 3.18(a). Cutback measurements were carried out with this wavelength and are shown in Figure 3.18(b). Unfortunately, the low yield of Chip-1 meant that many devices did not couple (and in the worst case no coupling was observed in all six devices for one of the measurements). Fitting through the data yields a waveguide loss of 14.44 dB/mm and a coupling loss of 13.27 dB, meaning the loss per grating is > 6.5 dB.

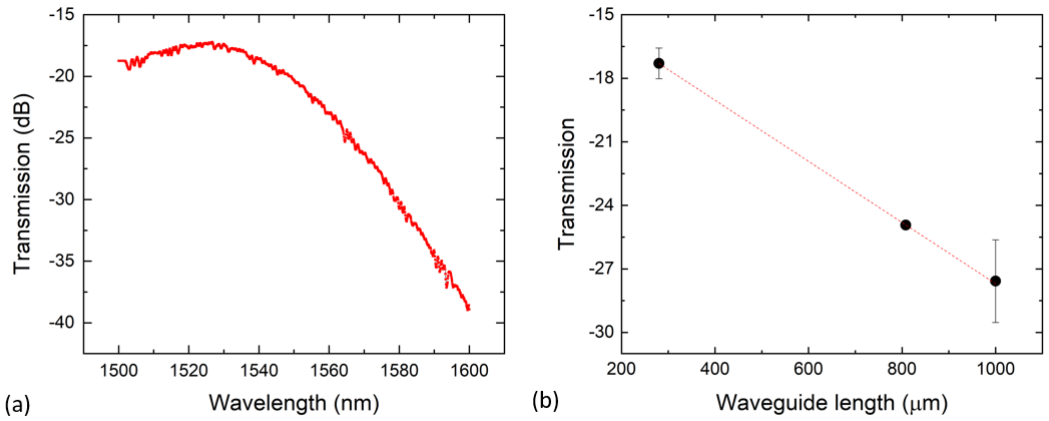

Figure 3.18: (a) Example grating spectrum from Chip-1 measurements. (b) Cutback measurements from SOI Chip-1. Red line is a linear fight through the data.

A ring resonator sweep is shown in Figure 3.19(a). It can be observed that there are steep resonances at a gap of 150 nm, indicating critical coupling. For gaps of 250 nm and 300 nm, the ring is under-coupled. In the former case, this is apparent at lower wavelengths, whereas in the latter case it is true across the spectrum. The data was analysed by choosing resonances within 2 nm of 1520 nm and then calculating the Q-factor by measuring the peak FWHM and using Equation 2.47. This was carried out after baseline subtraction to avoid convolution with the grating coupler envelopes. The results are given in Figure 3.19(b). Since only two devices with the same gap were measured, the error bar for these measurements are also large. The FWHM appears to follow an exponential decay, which is expected for the racetrack resonator.

3.3.3 SOI Chip-2

Given the results of Chip-1, a second attempt at the loss measurements was made. Firstly, the doses on Chip-2 started from 630 μC cm^{-2} and were increased in increments of 10 μC cm^{-2}, to a dose of 672 μC cm^{-2} because of the observation of improving transmission from Chip-1. Also, since the results from Chip-1 had a low yield and covered a small range of waveguide lengths, new loss measurements were made similar to those shown on Figure 3.17, but extending the range to 4.8

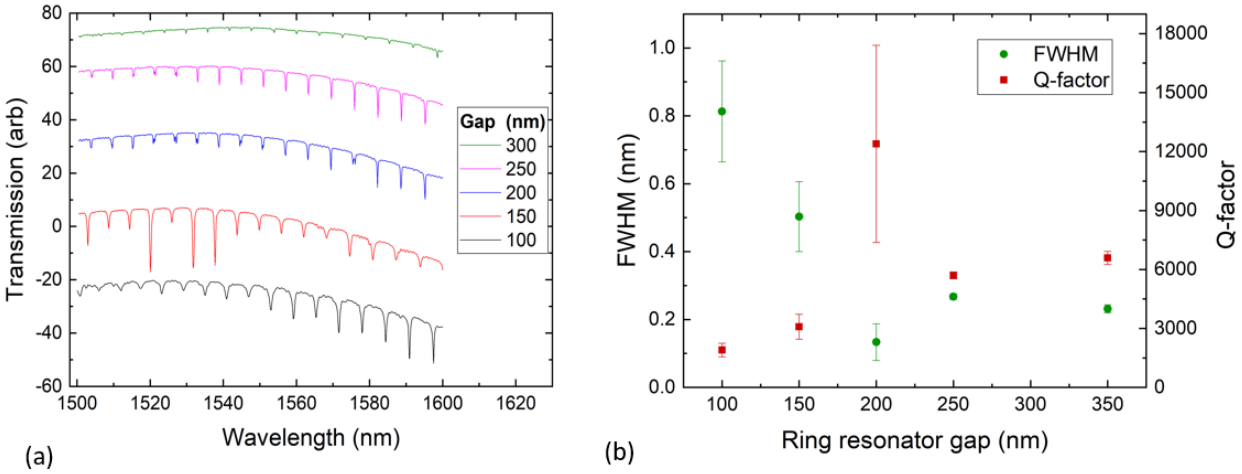

Figure 3.19: (a) Gap sweep for ring resonator measurements. (b) Q-factors and FWHM for resonances calculated near 1520 nm.

mm waveguides. The ring sweep was altered to be between 160 nm and 220 nm, in steps of 20 nm according to the observations of critical coupling. Also, the coupling region was extended to allow for the structure discussed later in Chapter 6 to be implemented into the resonator. Furthermore, the number of repeat devices for each gap was increased to 9. For the devices on this chip, we achieved coupling. There were a variety of devices, and some experimental results from this chip are shown later. This includes ring resonators with and without a multi-mode interference region (Chapter 6). However, we still had similar issues to Chip-1 for loss measurements. The only extra observation we had on the fibre-to-fibre transmission was that the peak wavelength of the grating coupler shifted to 1520 nm for larger doses, which can be attributed to a change in the period and dimensions of the subwavelength grating. The next section describes investigations into why we were observing poor propagation losses in the waveguides.

3.3.4 Working out the Issues with SOI Chips 1 and 2

The optical microscope and SEM were employed to study Chip-1 and Chip-2. Figures 3.20(a) and (b) show optical microscope images for doses 1.8 and 1.5 respectively. From the insets, it is clear in both cases that there are issues at the bending sections from the contrast observed between these sections and the straight waveguides, indicating that this is a design issue rather than a dosing issue. For dose 1.5, the effect is pronounced, with bends appearing very feint under the optical microscope. For dose 1.8, there is a visible change of colour at the bend sections and one of the straight regions. Other issues involved broken waveguides (particularly for dose 1.5) and damage to the grating couplers.

SEM was then employed to look at the bending sections and to measure the waveguide

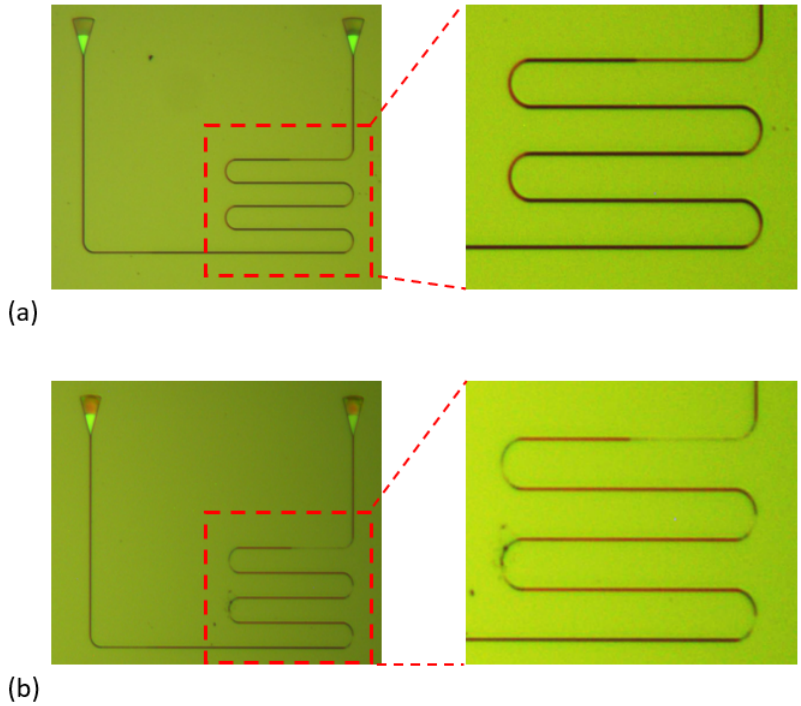

Figure 3.20: Optical micrographs of waveguide structures from SOI Chip-1 at a dose multiplier of (a) 1.8 and (b) 1.5. Insets for both figures zoom in on the meandering section of the waveguide.

structural dimensions. A bend and a waveguide are shown in Figure 3.21. It can clearly be seen from the measurement that the waveguide width at the bend is significantly narrower than the straight waveguides. From Section 2.1.1.4 in Chapter 2, the narrow waveguide means a larger fraction of the mode is distributed outside of the Si core. Furthermore, at the bend region, the combination of the mode being pushed to the outer edge with this narrow core is believed to be a large source of loss. In terms of systematic errors, the waveguide widths on the straight sections were measured to be around 435 nm. This is expected to increase the propagation loss [80], but also the coupling losses due to the sub-wavelength grating coupler design being optimal for tapering into a 500 nm waveguide.

3.3.5 Solving the Problems

In order to solve the problems, boosting the dosing at the waveguide sections was attempted but SEM measurements still yielded widths that were off by about 40 to 50 nm on straight waveguides and 50 nm on the bends with clear overdosing. It was noted that the bend was not a regular bend but an Euler bend. It is suspected that the VOYAGER system has issues with interpreting the structure when writing, leading to effectively underdosing the structure. To attempt to solve the problem, instead of increasing the waveguide dose, the waveguide width in the GDS design was increased to 530 nm and regular bends generated by the EBL software were

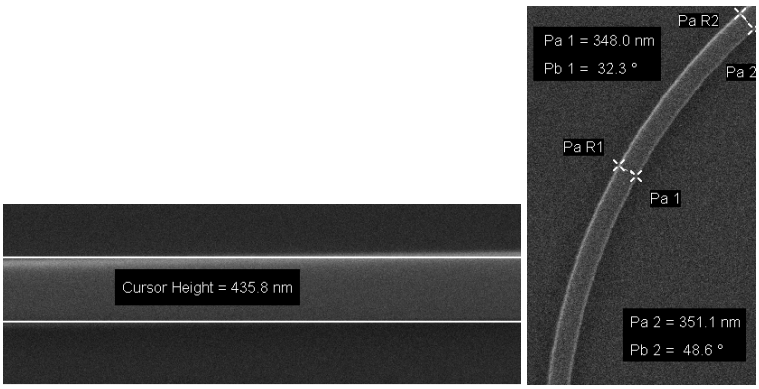

Figure 3.21: Measured widths of straight and bent waveguides fabricated on SOI Chip-2 by SEM. The white lines on the straight waveguide represent measurement cursors.

used. For the grating coupler, the same tapering angle was preserved by using the vertices of the taper to work out the line equation and solving for a width of 530 nm. A chip was tested, however, since it was patterned with the high grating coupler dosing, the peak wavelength blueshifted a significant amount out of the range of the laser. This meant to shift the peak wavelength back to 1550 nm, the fibre array angle of the setup would induce coupling losses due to the fibre holder touching the chip at an angle which is much different than the polished angle. These observations conclude that the waveguides should be dosed higher than the gratings, so that the target dimensions can be achieved but with grating couplers allowing access to a 1550 nm peak wavelength for the polished angle of the setup. However, the dimensions of the waveguides patterned in the resist layer could still be imaged. These are shown in Figure 3.22. It can be observed that the waveguide widths in the bending sections are more than 100 nm larger than those observed in Figure 3.21, resulting in being less than 21 nm offset from the target value. The straight waveguide width was observed to be 5-10 nm larger than expected.

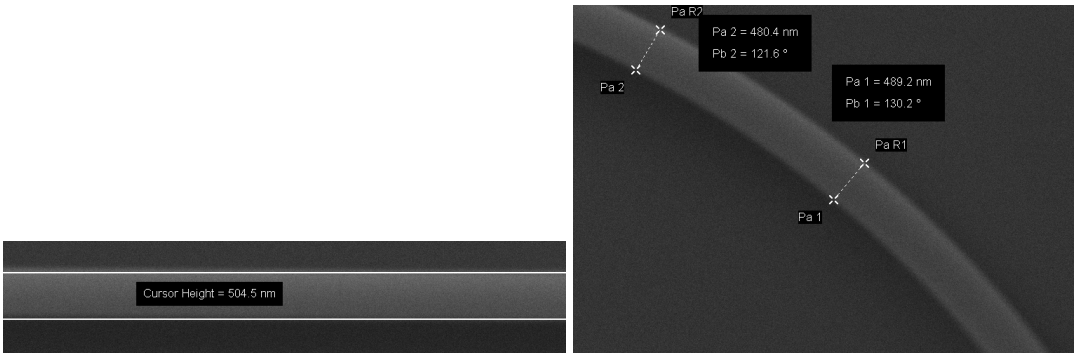

Figure 3.22: Measured widths of straight and bent waveguides fabricated on SOI Chip-5 by SEM. The white lines on the straight waveguide represent measurement cursors.

3.3.6 Moving on to Photonic Crystal Grating Couplers

Towards the end of my project, I experienced issues with the process flow based on FOx-14 resist - after the analysis on the chips above, subsequent spin coats would result in 500 nm thick resist under the same conditions. It was noted that the resist had well-surpassed its use-by date and had been exposed to room temperature frequently, which is suspected to be the reason for the defective performance. Pisu Jiang, a colleague at the University of Bristol also worked on SOI structures. He had developed a process flow with negative tone XR1541-006 resist (which is also similar to HSQ). I started to adapt the use of XR1541-006 resist. The devised process flow is:

1. Prepare samples by dicing an SOI wafer into 8.7 x 8.7 mm samples
2. Wash sample (acetone, followed by IPA and then washing with DI water)
3. Spin XR1541-006 resist in two steps. First step: 1030 RPM, 1000 RPM/s for 60s. Second step: 1100 RPM, 1000 RPM/s, 30s
4. Bake for two minutes at 150 ^oC, followed by two minutes at 220 ^oC
5. Expose with EBL with 50 kV accelerating voltage, 1.9 nA beam current, 5 nm step size. Base dose was 1000 μC cm^{-2}, with a dose multiplier of 1
6. Develop for two minutes in TMAH
7. Etch with interferometer to determine the end point as in Figure 3.1.3.3
8. Measure with automated testing station setup shown in Section 3.2

where the spin coat step results in a thickness of 170 nm. Structual parameters were extended in the GDS. For example, the waveguide width was extended to 540 nm on linear and bending regions. This was important to ensure 500 nm waveguides resulted after fabrication. After etching through the full device layer, there is a capping layer of 20-40 nm. Furthermore, we implemented the fully-etched, apodised photonic crystal grating described in Chapter 2 onto our material system [97]. We contacted Yunhong Ding (the lead author) regarding this design. The design was simulated on our platform and coupling losses of 4.5 dB at 1550 nm were expected, with most of the loss due to reflection into the substrate. The reason for the loss is due to the 2 μm BOX used in our process flow not being optimal for satisfying constructive interference of reflected waves. The photonic crystal design has an incident angle of 10 degrees, which is desirable for future prototyping and compatibility with fibre arrays in the cryogenic setups at the University of Bristol. Figure 3.23(a) shows the fabricated grating coupler. Since the photonic crystal design does not have parabolic focusing gratings, the taper has to be much longer to accommodate mode matching, resulting in a length > 100 μm. Figure 3.23(b) shows the photonic crystal holes in the grating region. Furthermore, the apodisation can be observed. The larger holes to the bottom of

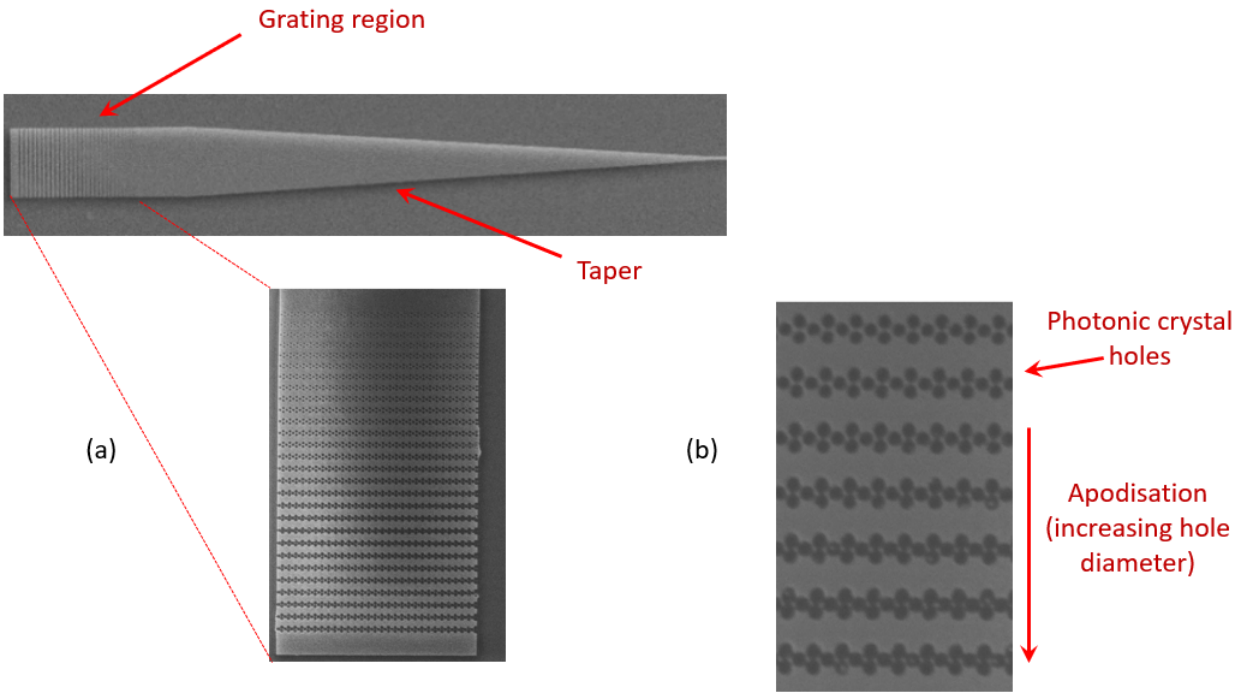

Figure 3.23: (a) Full SEM of the fabricated photonic crystal grating coupler. Inset shows the grating region (b) Higher magnification zoom into the photonic crystal holes of the grating.

the image appear to be overdosed. In terms of dosing in for this design, the structure was split into four regions which had different dose multipliers (this optimisation was performed by Pisu Jiang).

Since the use of this process flow occurred towards the end of the project, I focused on fabricating structures to characterise a waveguide crossing, which are described fully in Chapter 5. SEM images of the waveguides fabricated with this recipe can be found there. The crosstalk measurement waveguides can be used to test the fibre-to-fibre transmission performance, since the loss of the waveguide crossing is negligible in comparison. For these measurements, the 10 degree fibre array was used, with the polished angle being parallel to the chip for maximising coupling. Overall, twelve structures of this type were fabricated and nine worked, resulting in a 75% yield. Figure 3.24 shows three of the best performing devices. All three of these devices achieved a fibre-to-fibre transmission better than -10 dB, with the best case being device 2, obtaining -9.71 dB at 1530 nm. From this we can estimate the grating coupler loss as about 4.85 dB per coupler, under the assumption that the waveguide loss is negligible for this calculation. This is not far from the simulated target of 4.5 dB per coupler, where the discrepancy could be due to dosing effects (as observed in Figure 3.23(b)).

Figures 3.25(a) and 3.25(b) plot the fibre-to-fibre transmission and peak wavelength of every device tested. Besides two devices with < - 30 dB coupling, all devices show performances better

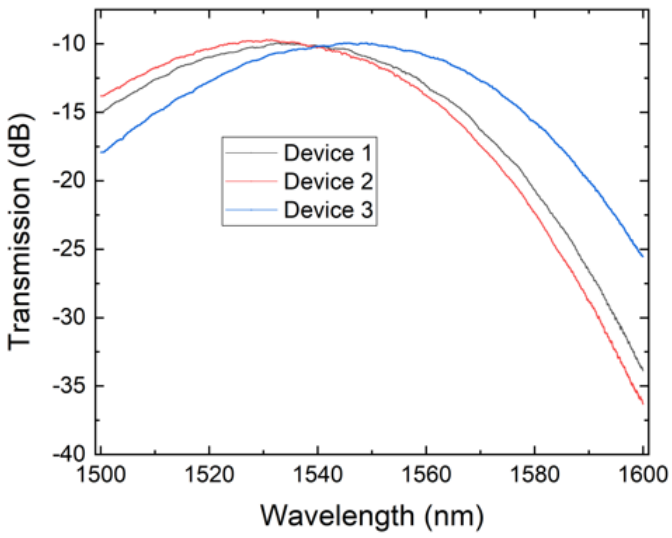

Figure 3.24: Grating coupler transmission spectra for the best three devices.

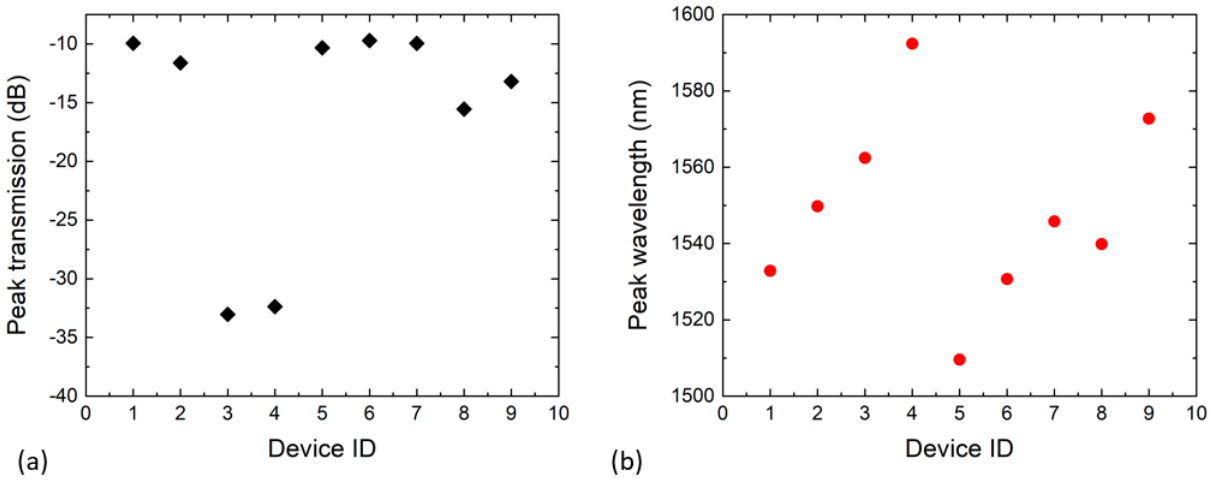

Figure 3.25: Peak (a) fibre-to-fibre transmission and (b) wavelength for the tested devices.

than -15.5 dB, with four devices with > -11.6 dB. On the other hand, the peak wavelengths range from 1500 nm to 1600 nm. This is most likely caused by fabricating the devices in various areas of the chip (changes in resist profile) and deviations in photonic crystal hole dimensions. It is stated in the associated paper for the photonic crystal grating that a ± 4 nm hole diameter results in a ± 10 nm peak wavelength shift [97].

3.4 Conclusions and Suggestions

The development of a process flow for a given material system is very difficult, potentially involving the tweaking of many parameters. As a result, it takes time to develop the processes required for developing silicon photonic components. This chapter focused on the photonic device layer fabrication, a crucial element for the detector chip, since the structures required for a detector chip are all based on waveguides and fibre-to-chip grating couplers. Etching processes were characterised to ensure that the 220 nm Si device layer can be fully etched without depleting the etch mask. For FOx-14 resist, this was easily satisfied, leaving > 100 nm of capping layer. However, poor performances such as 14 dB/mm propagation losses and < -16 dB fibre-to-fibre transmission were observed. Investigations led to conclude that the high propagation losses were caused by poorly fabricated Euler bends, which were not foreseen (this is attributed to an improper fracturing of structures during the EBL process). Despite this, racetrack resonators with Q-factors on the order of 10^3 were fabricated, similar to other works [199]. Due to resist aging issues, a new process flow had to be used. Although not shown here, both me and Pisu were unable to get the sub-wavelength focusing grating performance better than -24 dB fibre-to-fibre when fabricating structures with the XR1541-006 resist. We suspect that the 25 degree fibre array used for these measurements became damaged, which may also be a cause of loss. Moving on to the photonic crystal grating, fibre-to-fibre transmissions of > -10 dB were experimentally observed. However, it was found that peak wavelength shifts across the chip ranged from 1509 nm to 1592 nm. This is attributed to non-uniform spin coating on the 8.7 mm x 8.7 mm samples. The photonic crystal grating coupler used here is very sensitive to changes in hole dimensions, which can be affected by changes in dosing (mechanisms include fluctuations in beam current and resist thickness). Further work would involve fabricating a chip with a set of structures for extracting the bending and linear propagation losses. These values could then be used to predict the performance of racetrack resonator structures, which could be then tested and verified. This will determine if further optimisation of the losses are required. If the losses are already satisfactory, then the focus will turn to developing a lift-off recipe (using bi-layer PMMA) for metal nanowires, which are used for the component shown in Chapter 4. Also, a reliable recipe for contact pads needs to be devised for being able to experimentally realise the work in Chapter 6. Other directions for future work include improvements to the reproducibility of structures. This can be achieved by dicing larger samples (> 1 cm x 1 cm), tweaking various parameters in the spinning process and performing beam current stability tests to ensure satisfactory performance in the lithographic process. For the following chapters, the work with XR1541-006 resist was used to fabricate the structures shown in Chapter 5, whilst extra ring resonator structures were fabricated on SOI Chip-2 with the FOx-14 process flow and feature in Chapter 6.

CHAPTER 4

Low Q-factor Racetrack Resonators for Optical Filtering

Nanowires of superconducting material or metal may be placed on top or within a certain distance of a waveguide, allowing the nanowire to absorb light confined in the waveguide via evanescent coupling. This concept was shown in Chapter 2 as the working mechanism of the waveguide-integrated SNSPD. However, the concept may find applications for on-chip filtering of pump light, which is an essential element of a detector array circuit. In this chapter, the concept of a nanowire on top of a waveguide is explored in a SOI optical cavity for filtering. The combined use of a nanowire implemented in an SOI optical cavity approach allows spectral selectivity based on the dimensions of the cavity. The absorption caused by the nanowire can be exploited to realise critical coupling in the low Q-factor regime, opening the opportunity to target desirable pump filtering characteristics such as linewidth (FWHM) and high extinction. Furthermore, the scheme reduces the build up of electric field in the cavity due to the presence of the absorber. This absorbs unwanted signal and idler photons generated from pump light propagation in these optical filters as well as pump light, which in turn reduces the number of potential photons that can reach the detectors and register as dark counts. This is particularly important for quantum photonic experiments, where more than 90 dB of pump extinction is required for insuring high signal to noise ratios when counting coincidences of signal and idler photons [144], as opposed to classical applications where up to 60 dB is sufficient [200–202]. The nanowire used in the absorber uses the same thickness and material as used in an SNSPD, which means that it can be fabricated in the same step for simplicity. To realise critical coupling, the coupling coefficient of the ring must be considered. If the coupling coefficient is determined, then the scheme also finds application in post-processing of photonic circuits for improving filtering performance. This work starts by exploring the parameter space for a nanowire on a waveguide and then explores the concept of

the racetrack resonator for realising low Q-factor filters along with a detailed consideration of their advantages and disadvantages. Pump extinctions of 50 dB can be achieved in a cascaded N=3 ring configuration.

4.1 Principles and Origin of the Concept

To initiate the chapter, the relevant theoretical principles for understanding the concepts are presented here. Also, the initial ideas behind the concept are presented to provide some context and how the idea was conceived.

4.1.0.1 Absorption and the Beer-Lambert Law

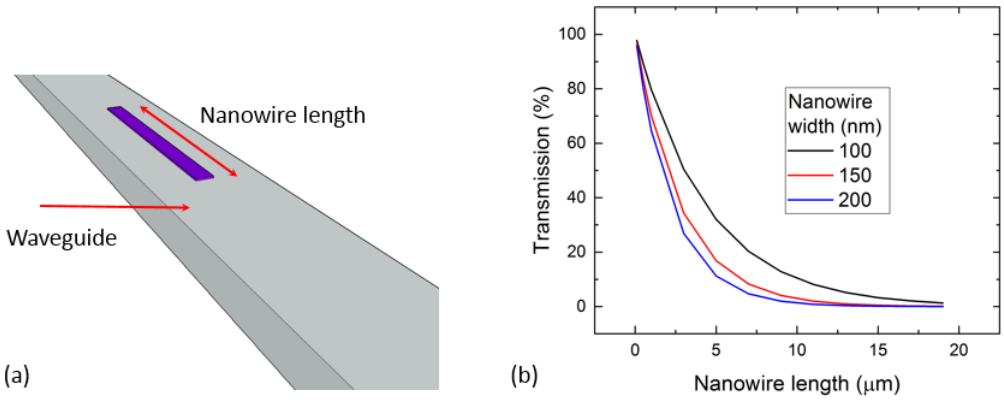

Figure 4.1: Demonstration of the Beer-Lambert law. (a) shows the design geometry - a 5 nm thick NbN nanowire directly on top of a 220 nm x 500 nm SOI waveguide. As light travels through the absorptive medium (the nanowire) it encounters loss through absorption as shown in (b), which depends on the nature of the absorber. In this example, the nanowire width is changing the absorption properties.

The Beer-Lambert law of absorption is applied in many contexts such as chemistry - in particular UV-Visible spectroscopy for characterisation of solutions [203–206]. It is applicable to absorption in bulk solids, which is relevant for waveguide-integrated SNSPDs. The Beer-Lambert law for the case of a solid is given by:

$$I = I_0 e^{-\alpha L}. \tag{4.1}$$

Where I is the intensity of the signal after absorption, I_0 is the intensity of the signal before reaching the nanowire region, α is the absorption per unit length (often known as the attenuation coefficient) and L is the length of the absorption region which is sometimes referred to as the

path length. Equation 4.1 is relevant for the design of waveguide-integrated detectors, where α is related to the geometry of the absorption region (or the geometry of the nanowire). For this application, the approach should be to minimise I for given constraints. Figure 4.1(a) shows a relevant situation in the present work, applying Equation 4.1 for three different NbN nanowire widths which will be investigated later in Section 4.2. Figure 4.1(b) shows the calculated decay according to Equation 4.1 as the light travels through the nanowire region. It can be observed that wider nanowires are more absorptive, causing the signal to decay more rapidly. For the work in this chapter, Equation 4.1 serves as an underlying principle and the cavity will behave according to the ring resonator equations in Chapter 2 and will be subject to the modifications given in Section 4.3.1. Generally, α will be material-dependent, based on the refractive index $\tilde{n}$ which has a real and an imaginary component:

$$\tilde{n} = n - ik, \tag{4.2}$$

where n is the real part and is associated with the speed of light propagation (and therefore governs effects such as reflection and refraction which were discussed in Chapter 2), and k is the absorption coefficient. k is related to α in Equation 4.1, which is discussed in terms of power, through the equation:

$$\alpha = \frac{4\pi k}{\lambda_0}, \tag{4.3}$$

where λ_0 is the free space wavelength. It should be noted from dimension analysis that the units of α in Equation 4.3 are in inverse meters i.e. μm^{-1}. To convert to dB μm^{-1} the result must be multiplied by 4.34.

4.1.0.2 Backscattering

The second quantity that is important to characterise in this work is the backscattering. Backscattering affects the ring resonance lineshape [207, 208]. In terms of this chapter, the backscattering is a coherent property (as opposed to backscatter than originates from mechanisms such as surface roughness) which originates from two physical regions creating an interface. The first region is the bare SOI waveguide and the second region has the SOI waveguide with the nanowire on top. These regions have effective indices n_{eff} and $n_{eff,abs}$ respectively. Since the waves propagate within a waveguide, they can be considered at normal incidence from the SOI waveguide to the nanowire region, making no distinction (invariant) of polarisation and the reflectance R becomes:

$$R = |\frac{n_{eff} - n_{eff,abs}}{n_{eff} + n_{eff,abs}}|^2. \tag{4.4}$$

In this case, the magnitude of $n_{eff,abs}$ and therefore R is determined from the geometry of the absorber. Section 4.2 explores this in detail for a variety of parameters.

4.1.0.3 Origin of the Concept and Distinguishing Factors of this Work

The idea for this concept originally started from the SNSPD in a racetrack cavity that was discussed briefly in Chapter 2 (with the design and necessary modifications for an SNSPD are discussed in Chapter 6) [51]. It was discussed in QETLabs that a detector chip could be realised with its own filtering stage. It is important to note here that this is possible as a separate chip (as initially conceived) or as part of a fully integrated circuit. The idea for filtering was to use a passive approach with critically coupled ring resonators. However, as was found from previous members of QETLabs, high Q-factor critically coupled ring resonators have very sharp critical coupling points and are sensitive to fabrication imperfections. As a result, a high number of rings are required ensure high extinction which can take up precious space on a chip. Instead, it would be desirable to be able to fabricate rings and extract their coupling and loss coefficients. From here, post-processing critical coupling through the metal deposition process for the nanowire onto these rings can form low Q-factor, high performance filters since the desired amount of absorption can be calculated given a particular absorber design. In terms of a detector circuit, the thickness is a constraint set by the design of the SNSPD. Therefore, to keep simplicity in the fabrication, the main parameters to control are those that can be controlled in the EBL process. This is different from the detector design due to the extra design freedom available when fabricating a passive structure (no bends to contact pads for example). Also, there are considerations such as trying to maximise extinction. A filtering stage implemented in a detector array should provide 50 dB or more complementary extinction to filtering already present in the experiment chip. The need for extra filtering in the detector array was contextualised by Piekarek et al. [47], who suggest that 130 dB of pump filtering is required to attenuate the signal down to the detector noise level (given an input power of 1 mW and a dark count rate of 1 kHz). This is to be contrasted with critical coupling levels of 20-30 dB, resulting in trapping 99 to 99.9% of the light to the cavity, which is satisfactory for a cavity-enhanced detector.

Also, the absorption medium itself does not need to be an SNSPD material such as NbN which is simulated here. This process can also be realised with metals that are foundry compatible such as chrome (Cr), titanium (Ti) and nickel (Ni). In terms of their differences, they will have different α and R due to their material indices from Equation 4.2. Therefore, the corresponding design will need to be adapted to the materials natural absorption. In terms of application of the materials, a recent study in 2017 showed 60+ dB of filtering from a 3-ring configuration, where NiCr heaters were placed 1 μm above the ring resonator waveguides [45]. In this case, the NiCr heaters were used both as a resonance tuning element and to absorb unwanted TM light that may be present from various mechanisms, although the propagating mode was TE. In effect, the cavities are still high Q-factor. This was enabled by the evanescent field of the TM mode being larger than the TE mode, allowing a resistive heater at 1 μm to have a large absorption of TM and negligible absorption for TE. In this work, the absorber is used to tune the absorption on the propagating

waveguide mode (TE) and can then be used to realise filter stages with larger linewidths that can be desirable for various applications. For example, the purity of ring resonator single-photon sources can be improved by increasing the spectral pump width, which will naturally requires a larger linewidth filter for reliable filtering [209].

4.2 An Absorption and Backscatter Analysis for Nanowires on a Waveguide

The parameter space for designing a nanowire onto a waveguide is in general very broad. For instance, TE and TM propagations have very different field profiles for a 500 nm wide SOI waveguide, as was shown in Figures 2.6(a) and 2.6(b) of Chapter 2. For this reason, a certain nanowire may favour TE absorption over TM absorption or vice versa. For this work, the TE mode is predominantly considered. However, this method is completely general and can also be used to design low Q-factor critically coupled filters for the TM mode. The attenuation coefficient and the coherent reflection (or backscatter) R will be looked at in terms of relevant design parameters as listed below:

- **Nanowire width**
- **Nanowire position**
- **Nanowire thickness**
- **Nanowire material index**
- **Nanowire height above waveguide**
- **Waveguide width**

All the data in the following sections were obtained via Lumerical MODE Solutions' eigenmode solver. For these simulations, unless stated otherwise, NbN was used with a refractive index of η_{NbN} = 5.23-5.82i and a thickness of 5 nm, typical for an SNSPD. The Si waveguide width W_{wg} was 500 nm and the waveguide height was 220 nm, whilst the lower BOX SiO_2 layer was 2 μm.

4.2.1 Nanowire Width

The width of the nanowire is a good starting point for analyses. For these studies, the nanowire is resting directly on top of the waveguide and in terms of lateral position, the centre of the nanowire is in line with the centre of the waveguide. In terms of the range of nanowire widths that are accessible, the structures vary from 50 nm and the lower limit depends on two factors. Firstly, a structure that is too small will lead to smaller attenuation coefficients. This can potentially limit the range of Q-factors that can be achieved with a cavity of a given length. Secondly, if

the processing is to be compatible with EBL or optical lithography, it will need to adhere to the resolution limits of these methods. In terms of EBL, this depends on the system used to perform the exposure, but generally the resolution of this technique is better than 50 nm. For optical steppers, the feature size depends on the diffraction limit of the light, and generally the dimension of the nanowire may need to be > 150 nm. The upper limit for the dimension of the nanowire is realistically set by the size of the waveguide, since patterning a nanowire larger than the waveguide will result in metal either side of the waveguide that is fixed above the BOX SiO_2 layer. This will deviate from the simplicity of the design, and may contribute to extra amounts of backscattering and unwanted absorption.

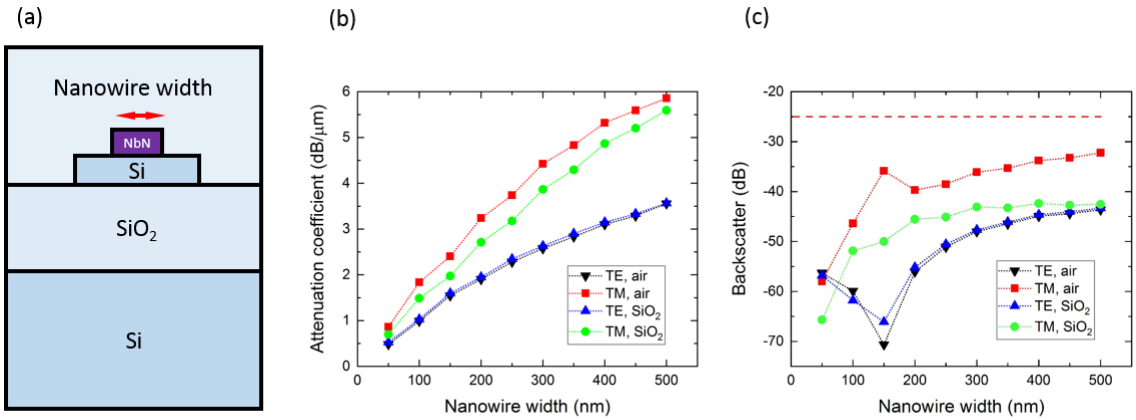

Figure 4.2: Nanowire width analyis. (a) is the design schematic. The upper box is the cladding modelled both as air and SiO_2. (b) attenuation coefficient as a function of nanowire width for TE and TM modes. Black and red represent data for air cladding whilst navy blue and light green represent data for SiO_2. The dashed red line is the threshold for observing a split resonance according to [207].

Figure 4.2 shows how the absorption and backscatter changes for the TE and the TM modes when the nanowire width is changed from 50 nm to 500 nm, with air and SiO_2 cladding. It can be observed in all cases of Figure 4.2(b) that a larger width of nanowire results in a greater absorption. The TE modes reach a peak absorption of approximately 3.5 dB/μm whilst the TM modes peak above 5.5 dB/μm. The reason for the difference in absorption can be explained in terms of the TM mode possessing a larger fraction of its field profile on top of the waveguide, whereas the TE mode is generally confined with its maxima in the Si waveguide core. The presence of air and cladding has very little effect on the TE mode absorption, whereas it is more pronounced for the TM mode. In terms of backscatter shown in Figure 4.2(c), a similar trend is produced, with backscattering reaching levels of up to -32 dB for the TM mode in air. This is suppressed to -42 dB in SiO_2. However, for the TE mode which is of interest in this work,

the level does not exceed -43 dB for nanowire widths of up to 500 nm. For this case, a 100 nm nanowire gives a backscattering level of -58 dB for the TE mode. There is a drastic reduction in backscattering observed for the 150 nm nanowire, which originates from $n_{eff,abs}$ originally starting lower than n_{eff} and passing through it and then continuing to rise for nanowire widths above 150 nm. The trend for larger nanowire widths is expected since more high index NbN material is being added (increasing the difference between $n_{eff,abs}$ and n_{eff}). For this reason, the point at 150 nm nanowire width may be a simulation issue. However, since the backscatter level is better than -50 dB for nanowire widths smaller than 200 nm, this is deemed no problem. If the backscatter exceeds -25 dB, then the presence of the nanowire will cause the resonance lineshape to split into a doublet, even in the absence of other backscattering mechanisms such as surface roughness or point defects [207] when implemented in a ring resonator (in Section 4.3).

4.2.2 Nanowire Position

The position of the nanowire on the waveguide is particularly important since the absorption can change depending on the profile of the particular mode propagating along the waveguide. The nanowire position is also important for various other reasons such as layer alignment in multiple exposure processes. The alignment accuracy of the Raith VOYAGER system used in this work is 30 nm. Since often Au markers are fabricated for use in multiple layer exposures with their own associated errors, the best case error of nanowire misalignment with the waveguide can be taken to be 60 nm as the markers are used for both waveguide and nanowire fabrication. This means that if a 60 nm width block is patterned with its centre 30 nm away from the waveguide edge, the alignment error can result in a similar situation to what was discussed in Section 4.2.1, where the exposure results in some of the nanowire being patterned off the edge of the waveguide. In general, this sets a bound for the range of translational positions for the nanowire. For a nanowire of width W_{nw}, the distance of the centre of the nanowire to the edge of the waveguide (i.e. $x = \pm W_{wg}/2$) and the alignment error can dictate how much tolerance is available.

Figure 4.3 shows the absorption and backscatter of the allowed modes as a function of the nanowire placement on the waveguide, where an offset of zero corresponds to the nanowire being centred on the waveguide. It can be observed that the behaviour is Gaussian in all cases, which is consistent with the mode profiles shown in Figure 2.6 of Chapter 2. Therefore, the observations in Figures 4.3(b) and 4.3(c) can be interpreted as improving the overlap with the modes. Since there is a stationary point at the centre of the waveguide, this suggests that the best position for the nanowire for these modes is on the centre. It should be noted here that for the 500 nm Si waveguide, the TM mode is most prone to alignment errors due to its larger rate of change in absorption across the waveguide. Although extra backscatter is induced when the nanowire is centred on the waveguide, the level is already sufficiently low from considering smaller nanowire widths as was shown in Figure 4.2. Furthermore, similar trends were observed for the different

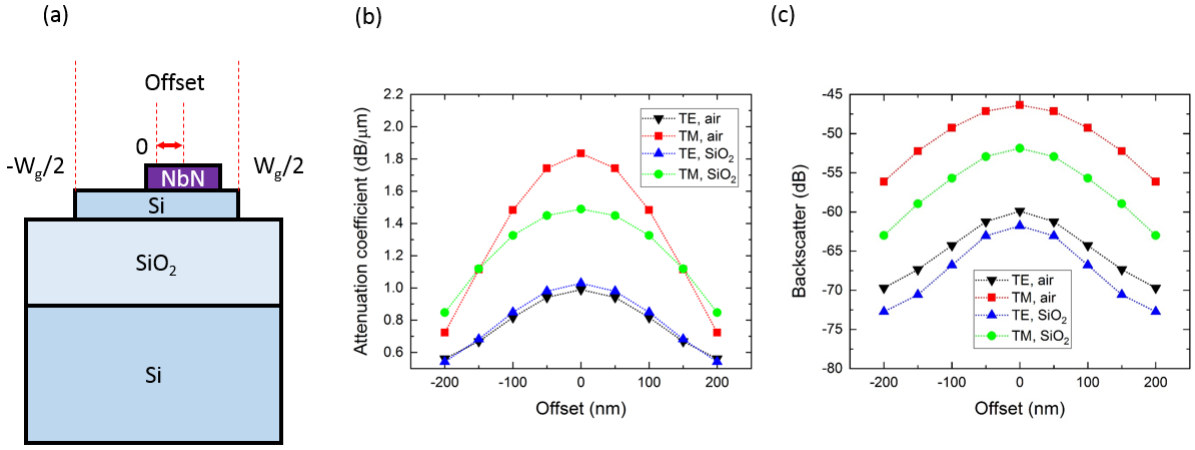

Figure 4.3: Nanowire offset analyis for 100 nm wide NbN on an SOI waveguide. (a) is the design, showing the waveguide edges and the offset. Cladding has been omitted for clarity. (b) and (c) shows how the attenuation coefficient and backscatter respectively change when the nanowire is moved across the waveguide. Black and red represent data for air cladding whilst navy blue and light green represent data for SiO_2.

modes and claddings as was observed in Figure 4.2.

4.2.3 Nanowire Thickness

Although this parameter was fixed at 5 nm for the succeeding work shown in this chapter, it is tuned in this section to investigate its effect. The first investigation that should be considered is within the range of thicknesses of the SNSPD materials itself, which can also be considered as a fabrication tolerance study of the sensitivity of the fabrication process for the nanowire. Figure 4.4(b) shows that an increase in thickness leads to an increase in absorption and backscatter in all cases. For the TM mode, the linear trends result in increases of 0.29 dB/μm and 0.24 dB/μm for air and SiO_2 cladding respectively, for every nm of nanowire thickness. The TE mode shows slight non-linear behaviour but with lower rates of change. Similarly to the results of Figures 4.2 and 4.3, the trends of Figure 4.4(b) can be thought of in terms of modal overlap, since the addition of material is on top of the waveguide, this has a stronger overlap with the TM mode than the TE mode. Since the TE mode is mostly confined in the core, it can be expected to decay away rapidly outside of the waveguide, which explains the slight non-linear behaviour relative to the TM modes. A linear fit was still applied to the data, yielding 0.15 dB/μm and 0.165 dB/μm for air cladding and SiO_2 respectively per nm of nanowire thickness. This trend is similar for the backscattering in Figure 4.4(c). However, further analysis was not necessary due to the low levels (below -40 dB in all cases).

The thickness of the nanowire is important from an experimental point of view. Films of

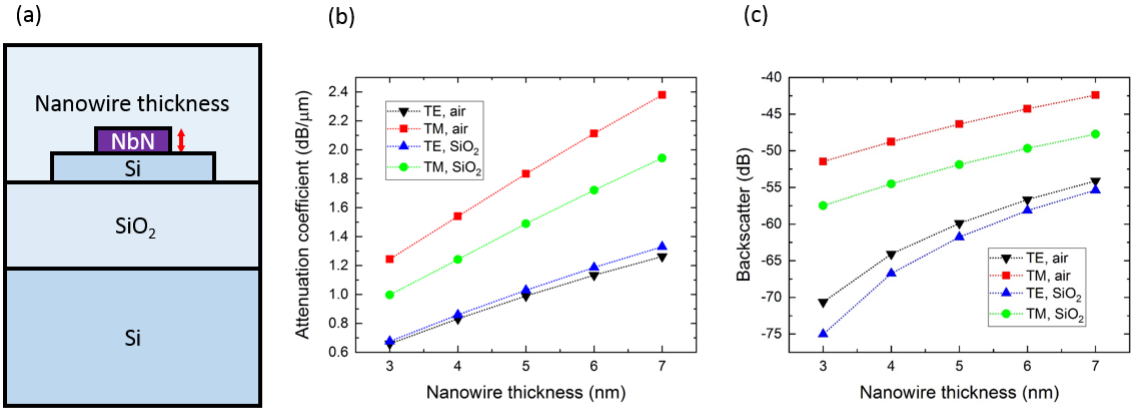

Figure 4.4: Nanowire thickness analysis for 100 nm wide NbN on an SOI waveguide. (a) is the design schematic. (b) and (c) shows how the attenuation coefficient and backscatter respectively change when the nanowire thickness is changed from 3 nm to 7 nm. Black and red represent data for air cladding whilst navy blue and light green represent data for SiO_2.

superconducting material are generally grown by sputtering, which targets a particular thickness with knowledge of the sputtering rate and time. The sputtering process is prone to similar fluctuations that were described with etching in Chapter 3 which can cause sample to sample variations and result in a thickness different to what is designed. The results of Figure 4.4 suggest that TM light is much more susceptible to these variations than TE mode light, although all results show more than a 0.1 dB/μm change in attenuation per nm of film thickness. Therefore, considerations to minimise the error in these processes are very important. Furthermore, the etching process associated with the nanowire should be considered. If the absorber is under-etched, a film remains on top of the waveguide, which will significantly contribute to the absorption and can be expected to result in larger attenuation coefficients (relatively more significant for the TM mode given the results of Figure 4.4(b)) and backscattering. On the contrary, if the film is over-etched, the pattern will transfer into the BOX layer. Given that a fabrication process for an SNSPD may start with the nanowire first, over-etching can be expected to be less damaging, since the nanowire itself is already on top of the Si waveguide, which is then patterned by EBL and RIE in a successive step.

4.2.4 Nanowire Material Index

For the rest of Section 4.2, all simulations use NbN. However, various different materials with their respective refractive indices as represented by Equation 4.2 can be used. Generally, a desirable feature for a material is to possess a relatively high k meanwhile having an n similar to the effective index n_{eff}. However, the adhesive properties of the material will also need to be

considered. For example, if the nanowire is to be fabricated through a lift-off process then the interface between the nanowire and the waveguide will need to be considered. Since Ti and Cr are materials commonly used for adhesion layers in processing metal contact pads, they can also be used as absorptive material. Figure 4.5 shows how the real and complex indices affect the backscatter and absorption respectively. The TE absorption trend in Figure 4.5(b) is fairly shallow, indicating that other parameters such as the nanowire width and thickness are more important for designing larger absorptive mediums. The backscattering is also expected to increase but does not exceed -40 dB for the TE mode for n as large as 10. However, when considering the TM mode, a much larger range of absorptions can be accessed for k between 2 and 10. The compromise is that this is met with larger backscatter, with Figure 4.5(c) showing backscattering levels of -29 and -33 dB at n = 10 for air and SiO_2 cladding respectively. The drop in backscatter at n = 4 for the TM mode in SiO_2 is assumed a similar simulation issue to the result in Figure 4.2(c).

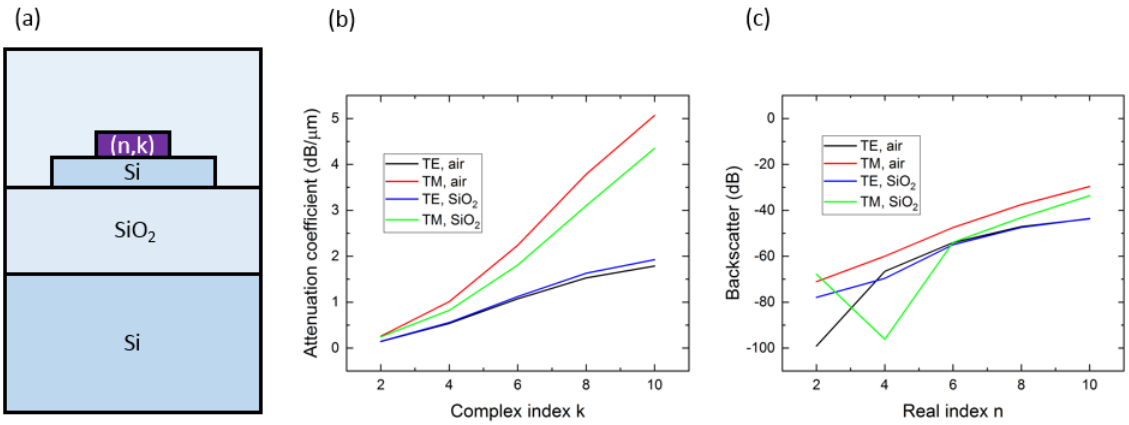

Figure 4.5: Material index analysis for a 100 nm wide (n,k) material centred on an SOI waveguide. (a) is the parametrisation. (b) and (c) show how the attenuation coefficient and backscatter respectively change when the real and complex indices of refraction for the absorptive material change for a range of typical values. Black and red represent data for air cladding whilst navy blue and light green represent data for SiO_2.

To complement the results of Figure 4.5, the n and k of various foundry compatible materials are tabulated in Table 4.1. These values were obtained using the Lumerical materials database. It should be noted that metals processed through different methods (such methods include thermal evaporation, electron beam evaporation and sputtering) may result in different absorptions from variations in parameters such as grain size and roughness, meaning it will be important to quantify the loss of the absorption medium through cutback measurements with different lengths of absorber. Metals such as aluminium (Al) show large k values, meaning that large ranges of absorption can be realised if desired.

Material	n	k
Cr	4.13	5.03
Al	1.44	16
Ag	0.446	10.1
Ni	3.38	6.82
Ti	4.04	3.82

Table 4.1: List of material index data for metals at 1550 nm. Data taken from Lumerical.

4.2.5 Waveguide Width

As well as parameters relating to the nanowire, the SOI waveguide through which the light propagates can be changed. In essence, the mode is subject to the considerations discussed in Chapter 2 (for example, n_{eff} will change due to the change in confinement). In this section, the thickness will be kept to 220 nm and only the width will change. However, it should be noted that moving to different thicknesses of SOI, such as 260 nm and 340 nm commonly used in integrated photonics can also be used for the scheme presented in this chapter. Furthermore, if 500 nm are the main working waveguides in a circuits, then tapers will be required to connect to the new waveguide width with minimal induced losses and backscatter.

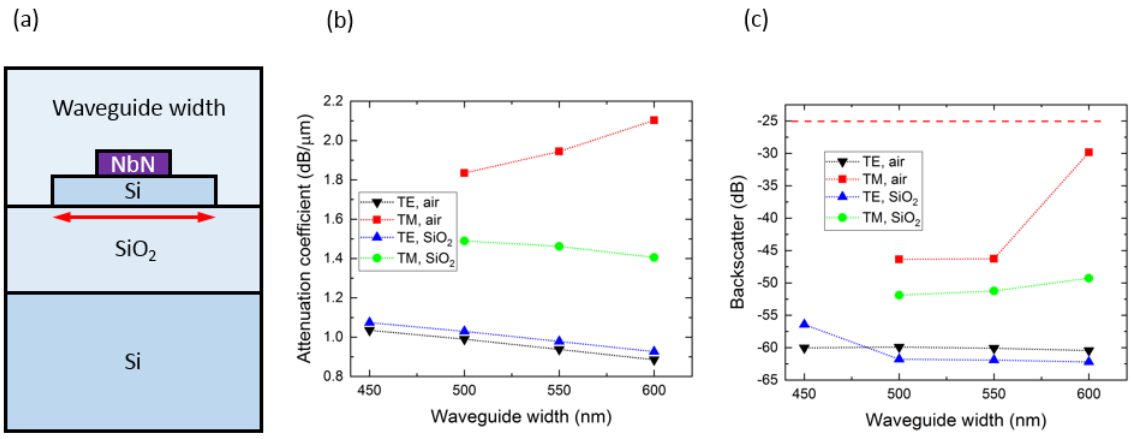

Figure 4.6: Changing waveguide width for 100 nm wide NbN centred on top of the SOI waveguide. (a) is the schematic. (b) and (c) shows how the attenuation coefficient and backscatter respectively change when the Si waveguide width is changed from 450 to 600 nm. Black and red represent data for air cladding whilst navy blue and light green represent data for SiO_2.

For this analysis, the important consideration is the extent to which the mode is confined in the core (and the fraction which is in the cladding). This effectively controls the overlap of the nanowire with the field concentration and similar positional offset dependencies can be expected

like those shown in Figure 4.3. The results are given in Figure 4.6. For this study, only the centre (peak) absorption and backscatter are shown. The missing datapoint for the TM mode in air is due to its n_{eff} being close to the cut-off in a 450 nm waveguide. For the TE modes, Figure 4.6(b) shows the absorption decreasing as the waveguide width increases. This can be thought of as the mode becoming more confined within the waveguide core, which reduces the amount of field that extends out into the cladding. The peak absorption changes from 1.07 dB/μm to 0.9 dB/μm for a range of 150 nm. This indicates that dimensional offsets in fabricated devices from lithographic errors such as dosing will need to be considered. However, a wider waveguide will require a longer absorption medium to achieve the same desired absorption as a narrow waveguide. Similarly, backscattering levels shown in Figure 4.6(c) for the TE mode are reduced at a larger waveguide width, achieving levels of -60 dB with the exception of the 450 nm wide waveguide in SiO_2. The TM mode in air behaves differently, with an increase in absorption as the waveguide width increases. This may be a result of more of the mode being distributed centrally for larger TM waveguides with air cladding. However, it is also accompanied by high levels in backscattering, where at 600 nm the backscatter level is greater than -30 dB and close to the resonance splitting level. It is also important to consider that reducing the waveguide width is generally unfavourable due to the discussions in Chapter 2, where experimental results showed significant increases in propgation losses for SOI waveguides smaller than 500 nm [80].

The results of this analysis suggest that for the TE modes, which are of interest in this work, the attenuation coefficient is less sensitive to changes in the waveguide width when compared to parameters relating to the nanowire itself. The decrease in attenuation coefficient can be counteracted by patterning an absorber of a longer length. The choice of waveguide width then depends on application and factors such as alignment accuracy.

4.2.6 Special Case with Cladding - Height Above Waveguide

It is not simple to fabricate the absorptive nanowire at a height z above the SOI waveguide when there is no cladding. However, if a cladding such as SiO_2 is chosen, then it is possible to deposit a cladding layer and fabricate a nanowire a certain distance above the waveguide, similarly to fabricating resistive materials for thermo-optic phase shifters. Figure 4.7 shows how the absorption for the TE and TM modes change as a function of z for various placements in the cladding layer. In Figure 4.7(b) it can be observed that the TE mode absorption falls off rapidly whilst the TM mode falls off at a relatively slower rate due to its further field extension into the cladding. This is consistent with the work performed by Cantarella et al. [45]. However, for the purposes of designing low Q-factor ring resonators, this is not desirable. The backscatter is not shown in this analysis, since levels were no greater than -60 dB, and were found to be < -100 dB when the nanowire is placed 600 nm above the waveguide or greater.

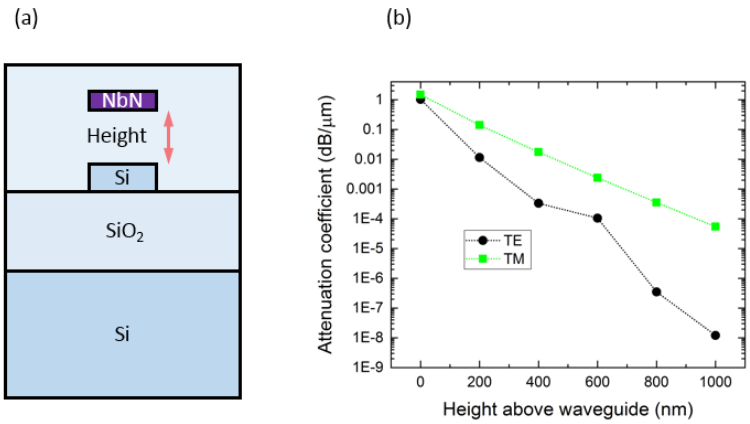

Figure 4.7: Changing the nanowire height above the waveguide. (a) is the schematic, defining height as the distance from the top of the Si waveguide to the bottom of the nanowire. (b) shows the absorption for the TE and TM modes from 0 to 1000 nm above the waveguide.

4.2.7 Concluding the Analysis

The chosen design for implementation was a 5 nm thick, 100 nm wide NbN nanowire placed on the centre of a 500 nm Si waveguide. The attenuation coefficient for this configuration was 1.03 dB/μm with a backscatter of -60 dB for the TE mode. In general, the attenuation coefficient and backscatter were quantified for a large range of realistic parameters that can be realised in a fabrication run given the many degrees of freedom that are available. Certain parameters such as the nanowire width and the nanowire thickness showed larger sensitivities than other parameters such as the waveguide width. Optimal performance can be achieved by choosing appropriate dimensions to ensure coherent reflection is not a major contributor to the ring backscatter. Tuning the absorption of the propagating mode is important for being able to realise various levels of absorption, which enables the ability to realise larger ranges of Q-factors (as will be evident in the next section). With the analysis of this section, the length of the nanowire can be adjusted to tune the required absorption, which is simple to implement with EBL techniques.

4.3 Implementation into a Ring Resonator Cavity

The ring resonator from Chapter 2 is a relevant integrated photonic structure commonly used in optical filtering. In terms of interplanar structures, a circular ring and racetrack with one or two bus waveguides are available. The racetrack is a very natural choice for implementing an absorptive nanowire for several reasons. Firstly, the racetrack structure possesses two linear regions and two bends. For this particular work, both linear regions are important. For the absorptive nanowire region, the absorption can be accurately predicted by the simulations given

in Section 4.2. This is not true for implementation in a standard circular ring structure, since a bent nanowire would need to be designed to function as the absorptive medium. Furthermore, as given in Section 2.1.1.4 in Chapter 2, the propagating mode in the SOI waveguide is pushed to the waveguide edge in a bending region, meaning to attain adequate absorption, a large bend radius is required, or fabricating a structure which overlaps with the modes position in the waveguide. This is likely to show greater sensitivity to alignment errors when compared to simply designing the absorber on a linear waveguide. Secondly, the advantage of the linear regions are for creating a well defined coupling region to a bus waveguide, as described in Chapter 2. This will become more apparent in the succeeding sections. For these reasons, the design discussed in this chapter opts to use a racetrack structure with two 180 degree bends and two linear regions, being suitable for a single-bus waveguide configuration as shown in Figure 4.8.

4.3.1 Modification of the Ring Equations

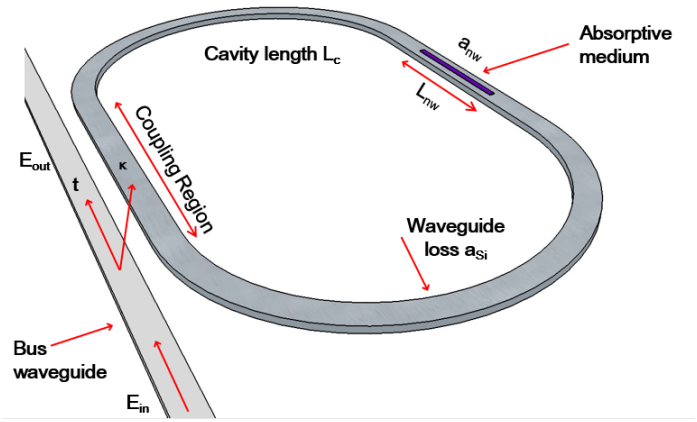

Figure 4.8: Example of a racetrack cavity with an absorptive medium. t and κ are transmission and cross-coupling coefficients of the coupling region respectively, L_c is the cavity length and the waveguide loss is a_{Si}. The absorptive medium is a nanowire with length L_{nw} and attenuation coefficient a_{nw}.

Considering the schematic given in Figure 4.8, the first aspects to consider before proceeding are how the equations in Section 2.1.4 of Chapter 2 change when the absorptive medium is present in the cavity. Firstly and most importantly, the absorptive nanowire can effectively be considered as an additional term contributing independently to the round trip transmission α, which is now given by:

$$\alpha = 10^{-(\frac{a_{Si}L_c + a_{nw}L_{nw}}{20})}, \tag{4.5}$$

where a_{Si} represents the losses present in the Si waveguide, expressed as dB per unit length, which originate from mechanisms such as those given in Chapter 2 and exist regardless of the

nanowire. L_c is the length of the cavity, α_{nw} is the absorption per unit length of the region with the nanowire, which was quantified in Section 4.2 and L_{nw} is the length of the nanowire. The factor of 20 on the denominator is present due to α being defined for electric field in the ring resonator equations (as opposed to power or intensity).

The second modification comes from the perturbation of the nanowire on the travelling waveguide mode. Although discussed in Section 4.2 in the context of coherent backscattering, an extra consideration is required. Since the mode has to propagate through this region of $n_{eff,abs}$ for a length L_{nw}, this will modify the ring resonator equations also by a small amount. For example, the $cos(\theta)$ term in Equation 2.43 that depended on n_{eff} now changes to:

$$\theta = \frac{2\pi(n_{eff}(L_c - L_{nw}) + n_{eff,abs}L_{nw})}{\lambda}. \tag{4.6}$$

It is possible to consider the perturbation of the nanowire in Equation 4.6 as changing the overall effective index of the mode to a weighted average (for example as $n_{eff,avg}$ with a single term). However, since the perturbation is relatively small, this analysis is deemed not necessary due to other important factors taking precedence. Although the FSR and FWHM depend on n_{eff} and therefore they will be modified by Equation 4.6, the change will not be appreciable compared to the modification of another parameter (for example, a change in L_c). Furthermore, other parameters such as the natural dispersion of the SOI waveguide can also convolute the cavity shift that originates from Equation 4.6.

4.3.2 Implication of the Modifications and Applications

The implications of Section 4.3.1 are that the two independent loss mechanisms contribute to α. α_{Si} is the natural waveguide loss parameter, which in a photonic circuit should be as minimal as possible. Thus, by tuning the round trip transmission using α_{nw} and L_{nw}, lower values of α can be obtained. This is in contrast with reducing α from other mechanisms such as larger α_{Si} which is undesirable (increased waveguide losses), or an increase in L_c for fixed α_{Si}, which would limit the wavelength tunability of the scheme. The use of the absorptive medium to control α is the most important concept for the chapter - a standard SOI resonator without a nanowire operating in the critical coupling regime will provide pump suppression. However, if spurious, unwanted photon pairs are generated in this filtering stage through SFWM, those will not be suppressed and free to couple out of the cavity, since critical coupling only applies to the light circulating in the ring and destructively interfering with the pump light in the bus waveguide. The presence of the absorptive medium reduces the power build up in the cavity (lower α), but also can function to absorb photon pairs generated in the ring, which contrasts to other schemes [45]. The on resonance critical coupling equation describing the power out of the bus waveguide is restated here:

$$(\frac{P_{out}}{P_{in}}) = (\frac{E_{out}}{E_{in}})^2 = (\frac{\alpha - t}{1 + \alpha t})^2, \tag{4.7}$$

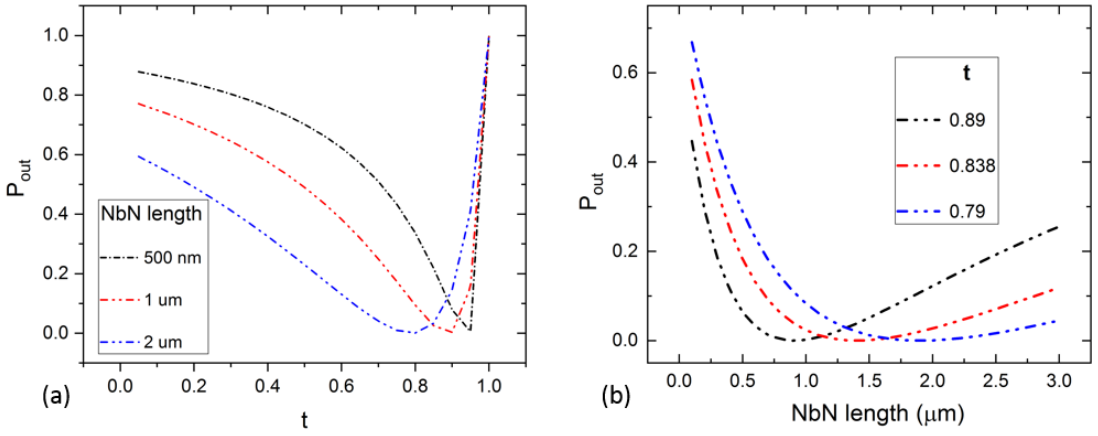

Figure 4.9: Plotting the on resonance equation for the bus waveguide output power as a function of (a) the coupling coefficient t for fixed lengths of NbN and (b) NbN length for fixed t.

where $0 \leq \alpha \leq 1$ and $0 \leq t \leq 1$. As discussed in Chapter 2, there are three regimes to which the terms over-coupling, under-coupling and critical coupling are ascribed. For the purposes of on-chip filtering applications, critical coupling is desired and is of interest here. To achieve critical coupling with the post processing of an absorptive nanowire, an SOI resonator must be fabricated in the over-coupled regime prior to the nanowire fabrication, to satisfy $t < \alpha$. Then metal can be fabricated onto the ring resonator, lowering the value of α, with the aim to target the condition of $t = \alpha$. However, by being able to tune α through a wider range of values using the absorptive nanowire, the realisation of more critical coupling regimes that correspond to lower Q-factor resonators are evident. In terms of the fabricated structure, since over-coupling is required (corresponding to lower t), the coupling region requires a smaller ring-bus waveguide separation. If the gap size becomes too small for resolution of equipment, it is possible to redesign the ring with a larger coupling length, so that the gap can be increased. Figures 4.9(a) and 4.9(b) plot Equation 4.7 to explore these concepts. It can be observed that the transmission out of the bus waveguide P_{out} tends to 0 at the critical coupling regime. It is also interesting to note that for lower Q-factor resonators (characterised by lower values of α as a result of larger NbN nanowire lengths) the region for critical coupling has shallower gradients - indicating that they are more tolerant to changes in α and t. This is highly desirable for passive filtering stages (as considered in the detector array chip) and can be expected from low Q-factor cavities. However, it should also be noted that this scheme is compatible with active schemes such as thermo-optic phase shifters for tuning. This can occur in a couple of forms. For example, heating a region of the

ring waveguides to enable active cavity wavelength shifting. Alternatively or in conjunction with wavelength tuning, heating of the coupling region enables control of t. This has been used in the high Q-factor regime for filtering purposes [45]. The shallower gradients shown in Figure 4.9 suggest that active tuning may also beneficial in the low Q-factor regime on improving the critical coupling level, particularly in cases where precise tuning of t would otherwise be voltage resolution-limited. This was cited as a limitation in achieving beyond 60 dB spatial extinction in other work [112]. Since fabricating the absorptive medium onto the ring resonator is a separate step, an application of this method is that it can be used to post-process a ring resonator to improve extinction for improved filtering performance. Figure 4.10(a) depicts the post-processing concept. In the initial stage, the SOI resonator has a typical a_{Si} on the order of 3 dB/cm, leading to $\alpha = 0.997$. The blue spectra in Figures 4.10(b), 4.10(c) and 4.10(d) show different coupling coefficients which are physically realised through changing the bus-ring waveguide gap in the case of an SOI resonator with no nanowire. A narrower gap means more light couples to the ring, resulting in a reduced fraction of field passing through the bus waveguide. This results in an increased degree of over-coupling. After post-processing of the absorptive medium as depicted in Figure 4.10(a), they can all be turned to critically coupled cavities through fabricating an appropriate size absorptive medium to satisfy $t = \alpha$. The different critically coupled structures have varying FWHM as shown in Figures 4.10(b)-(d). The process shown in Figure 4.10 can be used to target various FWHM filters. This is shown in Figure 4.11, where FWHM is shown as a function of the waveguide loss for various lengths of metal absorber. It can be seen that the FWHM for each L_{nw} does not increase greatly with waveguide loss, which emphasises the range of FWHM that are available as a result of the absorption medium.

4.4 Simulations of Single Ring

This section represents the simulation results obtained for this concept using Lumerical MODE solutions. Three different racetrack cavities were used whose attributes (coupling region length, cavity length and bend radius) are given in Table 4.2. Since the pulse injected into the waveguide was normalised, this corresponds to $E_{in} = 1$. Furthermore, all simulations in this chapter have $a_{Si} = 0$ with an injected TE mode. A non-zero a_{Si} is expected to induce a change in the critical coupling points, which will be different when considering different L_c. However, these can be interpreted as offsets. Two of the cavities have the 10 μm bend radius for practically realising minimal waveguide losses, although an extra cavity with 5 μm bend radius was also considered due to the smaller achievable cavity size. In this case, an FSR of 18 nm is achieved. These choices are to test if tuning of the cavity parameters with the absorption medium are coupled and to how much extent. Furthermore, the range of FSRs given here are generally appropriate for satisfying the conditions of filtering pump photons whilst allowing signal and idlers to propagate in the pass band [29, 30, 144]. In QETLabs, fellow colleagues use single-photon sources with separations of

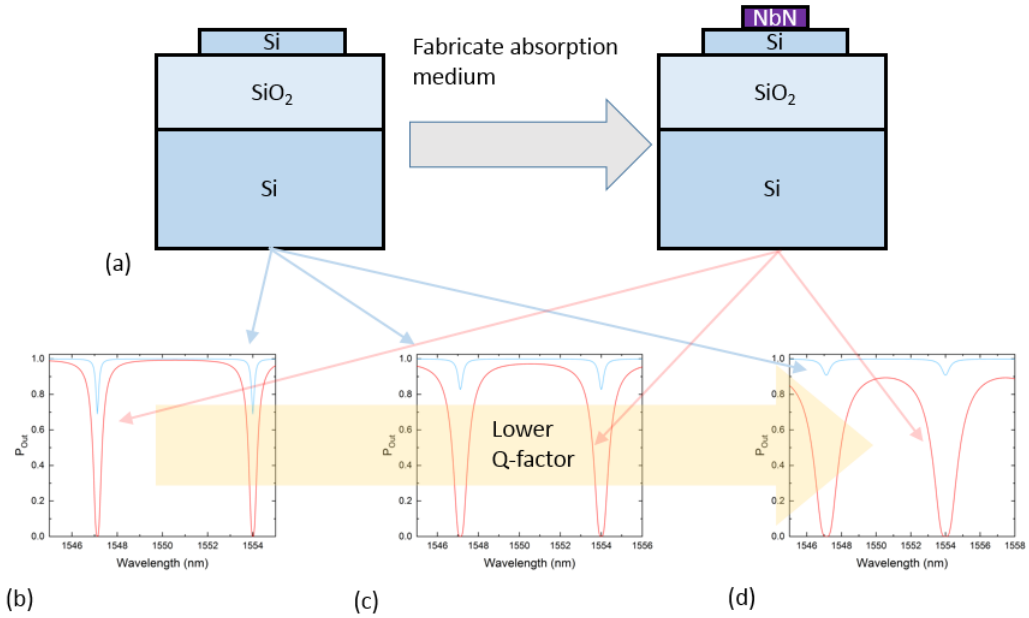

Figure 4.10: (a) Post-processing step. (b), (c) and (d) are calculated spectra. Blue spectra are of the SOI resonator with 3 dB/cm waveguide loss and coupling coefficients of 0.94, 0.886 and 0.7877 respectively. Red spectra show the wavelength response after α is post processed to satisfy $\alpha = t$.

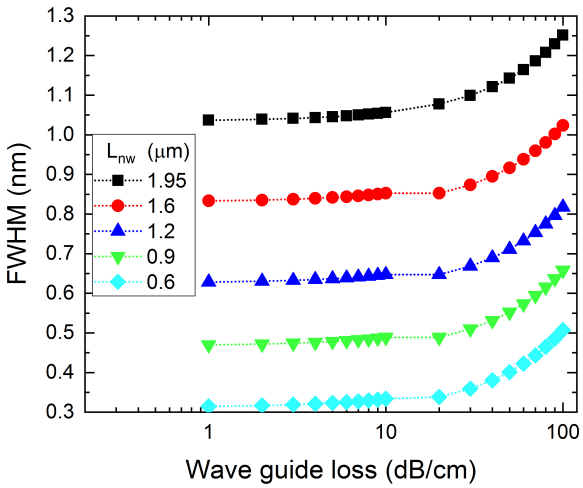

Figure 4.11: FWHM for various low Q-factor cavities calculated with Equation 2.46 in Chapter 2. Critical coupling is assumed for a waveguide loss, a_{Si}, of 0 dB/cm. This implies that the linewidth of a single critically coupled ring can be tuned through the metal properties (a_{nw} and L_{nw}).

Cavity Length (μm)	Bend Radius (μm)	Linear Region length (μm)	FSR (nm)
43	5	5	18
73	10	10	8
83	10	10	6

Table 4.2: Designs of various SOI racetrack cavities.

2.5 nm. The 83 μm cavity here has a suitable FSR of 6 nm for these purposes.

The nanowire was placed on top of the SOI waveguide in the linear region as per the scheme in Sections 4.2 and 4.3 and meshes were applied to accurately resolve the absorption medium and coupling regions. The method and results will now follow in the succeeding sections.

4.4.1 Method

The results in the next section are obtained by keeping the dimensions of the absorptive nanowire constant and then the bus-ring waveguide separation was adjusted to obtain critical coupling at wavelengths near 1550 nm. In this case, since critical coupling is taken to mean a minimum in transmission for a given wavelength, the cavity with the maximum extinction (pass to stop band contrast) for a given metal can be considered the most critically coupled. Simulations were carried out with the varFDTD solver in Lumerical MODE solutions. Some examples of critically coupled spectra are shown in Figure 4.12.

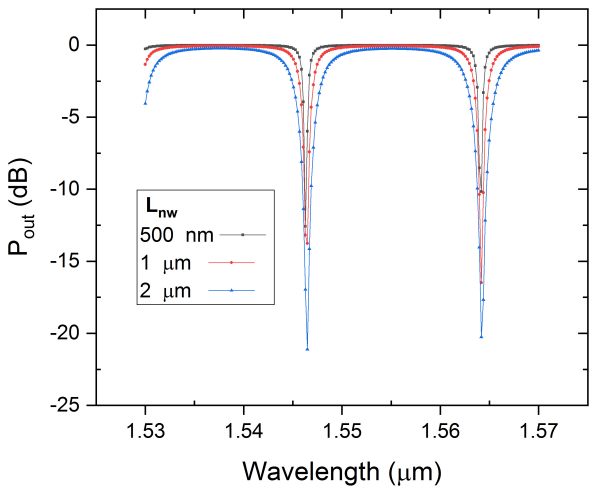

Figure 4.12: Simulated spectra from 1530 to 1570 nm for a L_c = 43 μm, low Q-factor SOI cavity with various L_{nw}.

4.4.2 Extinction and FWHM

Figure 4.13(a) shows the extinction and FWHM obtained for the three cavities listed in Table 4.2. In terms of extinction, it can be noted in all datasets that the lower Q-factor (higher L_{nw}) designs tend to obtain higher extinction, with 15 dB or greater being shown for L_{nw} above 500 nm. It appears that lower Q-factor cavities obtain greater extinction independent of L_c, which is commensurate with shallower critical coupling points shown in Figures 4.9(a) and 4.9(b). The best case shown here is 33 dB for L_c = 83 μm and L_{nw} = 2 μm. It is suspected that the low extinction of 4.5 dB observed for L_{nw} = 200 nm with L_c = 83 μm may be a simulation issue, since even in the high Q-factor case (no nanowire), ring resonators with higher extinctions have been fabricated (Chapters 3 and 6). Figure 4.13(b) shows the respective FWHM for the cavity parameters in Table 4.2. The trends are as expected and in accordance with Equation 2.46 in Chapter 2; cavities with smaller L_c have greater FWHM and for fixed L_c and larger L_{nw}, the FWHM increases due to the increased absorption. FWHMs between 0.6 to 2.5 nm can be realised for L_{nw} between 400 nm and 2000 nm for L_c = 43 μm. The implications of these results will be discussed in Section 4.4.4.

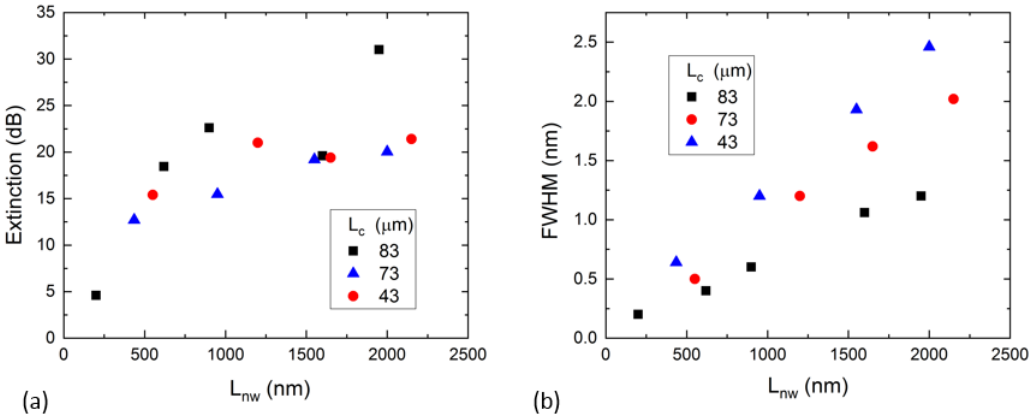

Figure 4.13: (a) Extinction and (b) FWHM for various critically coupled racetrack cavities.

4.4.3 Pass Band Loss

One disadvantage of low Q-factor cavities arises from the loss in the pass-band. These are the wavelengths that do not couple into the cavity. For example, considering the spectra shown in Figure 4.12, with a normalised input pulse, a high Q-factor critically coupled ring resonator can be expected to give close to unity transmission on the pass band. However, when considering low Q-factor critically coupled resonators, there is an observable reduction in P_{out} for wavelengths that are not on resonance. Figure 4.14 characterises the pass band loss in dB for all of the

critically coupled cavity designs. It can be observed that with lower Q-factor (longer lengths of metal) that the pass band loss increases, reaching a maximal value of 0.35 dB for L_c = 43 μm and L_{nw} = 2 μm. In the single ring case, the pass band loss itself can be considered independent of L_c and is mainly controlled by α. Very reasonable pass band loss levels below 0.15 dB can be realised for designs with $0.5 < L_{nw} < 2$ μm.

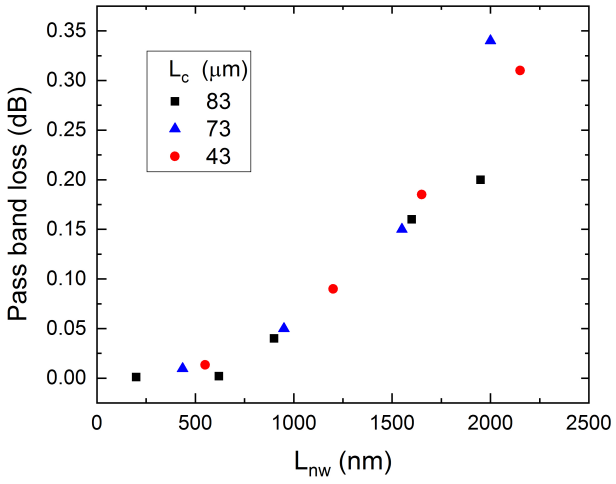

Figure 4.14: Characterising the pass band loss for various critically coupled, low Q-factor SOI racetrack cavities.

4.4.4 Discussion and Other Effects

Since linewidth is an important aspect of filtering, the ability to realise critical coupling in low Q-factor ring resonators through the methods of this chapter opens an option for realising various FWHM for a single-bus ring resonator using a post-processed loss mechanism for an SOI resonator fabricated using usual methods. The magnitude of the loss for photons in the pass band also need to be considered, since this affects the photons in an experiment that are desirable for detection, such as signal and idler photons passing through to the detectors.

The low Q-factor single-bus rings shown here also has some advantages compared to the two-bus mechanism, where both bus waveguides can be tuned to increase the FWHM. The exponential dependence of the gap poses a great challenge for matching coupling coefficients, which in turn leads to requiring thermal tuning of the coupling regions for reliable operation. Matching critical coupling is more simple for this case, since only one coupling region has to be considered.

4.4.5 Cavity Shift

The resonant wavelengths λ_{res} in a ring resonator can shift through a change that can be ascribed to a change in η_{eff}. One mechanism unique to the shift in the low Q-factor resonators based on absorption shown in this Chapter comes from heat dissipation. Since the mechanism involves absorption of the guided light from a pump laser, it can be expected that the absorptive medium will rise in temperature, with a change in properties. These properties can involve changes in refractive index through heating the local region near the absorption medium, changing the η_{eff}, leading to a resonance shift. For the context of an SNSPD detector array, this is balanced to some extent by the cooling power of the cryogenic apparatus. For room temperature, water cooling solutions or heat dissipation using materials such as copper are often used to deal with active components and this scheme is not suspected to require greater cooling solutions. However, the change in material properties with temperature may effect the critical coupling level and this will need to be tested experimentally. One intrinsic advantage of the low Q-factor system is the larger linewidth, which if sufficiently larger than the resonance, can maintain reliable filtering in the presence of material based cavity shifts.

4.4.6 Cavity Stability from Non-Linear Effects

Non-linear effects such as those based on the Kerr effect (where the refractive index of the material changes as a function of the intensity of the light propagating through it) can be important since they may shift the rings resonance off of the desired pump light wavelength. As discussed in the previous paragraph, the low Q-factor system also protects against these shifts due to the reduced build up of electric field in the cavity. Furthermore, non-linear effects that depend on pump power such as SFWM are also important to consider in a filtering circuit. For example, SFWM pair generation rates depend quadratically on the pump power due to two photons being required for the process [210, 211]. For both a detector chip and a fully integrated photonic chip, the production of spurious SFWM photon pairs is undesirable and will lead to errors in quantum computing applications if they are detected. The low Q-factor cavities in this chapter through absorption are able to limit the lifetime of pump photons in the ring resonator, which is expected in turn to attenuate the production of photon pairs relative to other filtering schemes such as standard SOI critically coupled ring resonators.

4.4.7 Dispersion

The parameters α and t are symmetrical in the ring resonator equations, with particular emphasis to Equation 4.7. The biggest notable difference is their variation with wavelength [212]. Without the absorptive material, typically α is not expected to vary with wavelength as the only loss mechanisms present are associated with the Si waveguide. However, with an absorptive medium, the material indices $\eta(\lambda)$ and $k(\lambda)$ are important since any significant variation will

result in large changes in α and thus in performance due to deviations from critical coupling. Although relatively lower Q-factor rings are more resilient to this problem as was shown in Figure 4.9, it is still desirable to use a material with slowly varying $k(\lambda)$.

The variation of t with wavelength for the racetrack resonator design here is ubiquitous for both high and low Q-factor regimes. The coupling region for the symmetric directional coupler used in this work is the convential design, which has a large dependence on wavelength as was shown in Section 2.1.3 of Chapter 2. To obtain more reliable broadband operation to open up these low Q-factor ring resonator filters for use in other applications, the structure should utilise a flat-profile directional coupler [213, 214].

4.4.8 Cascaded Rings

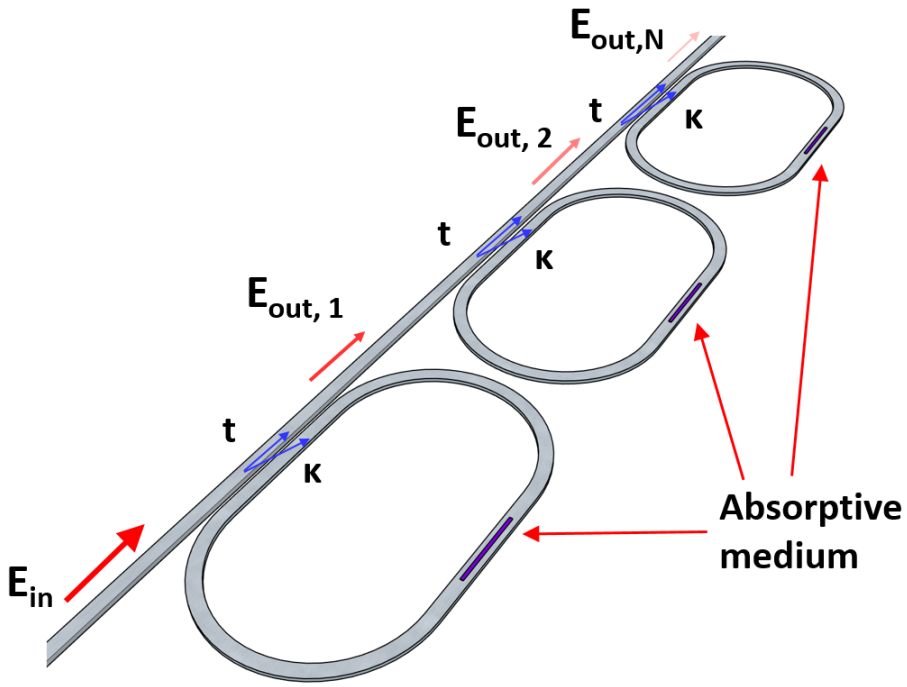

Figure 4.15: Schematic of a linear cascade of racetrack resonators. The design considered has the same absorber and ring parameters for each ring.

The preceding results have been for a single ring resonator. This section looks at the case where the low Q-factor rings can be serially connected to the bus waveguide in a linear cascade configuration. This can be used to improve extinction performance of the filtering circuit. In this case, Equation 4.7 represents the field out of the bus waveguide after passing through the first ring resonator. When entering the next ring resonator the new E_{in} will correspond to the E_{out}

that was calculated using Equation 4.7. These correspond to $E_{out,1}$ and $E_{out,2}$ in Figure 4.15. Since Equation 4.7 originates through the transfer matrix method, it can be considered that a cascaded ring scheme is multiple applications of the transfer matrix. Ergo, it can be inferred that in a cascade scheme, the on resonance critical coupling equation when considering low Q-factor rings with the same α and t is:

$$P_{out} = \left(\frac{\alpha - t}{1 + \alpha t}\right)^{2N}, \tag{4.8}$$

where N denotes the number of rings. Considering the pass band losses from the single ring case shown in Figure 4.14 and footprint of the filtering stage, it was decided that a N=3 cascade would be the maximum limit. Figures 4.13(a) and 4.13(b) show the extinction and pass band loss for the low Q-factor designs with L_c = 83 μm with L_{nw} = 1600 nm and 1950 nm respectively. It can be observed that extinctions above 40 dB are observed in both cases, with the best case being greater than 52 dB for N = 3 and L_{nw} = 1600 nm, representing a viable filtering level in the purely passive regime. As with the single ring case, this level can be expected to increase with active tuning of the coupling region through more accurate matching of the coupling coefficients to achieve critical coupling in each ring. The extinction may also improve with extra rings. However, the pass band loss would then exceed 0.5 dB even in the best case, which can start to be of significant detriment to photons passing in the pass band which are desired for detection. Figure 4.16(b) shows the pass band loss as a function of N. The results are additive in dB, suggesting that there is a trade-off between the extinction and the loss induced in the pass band.

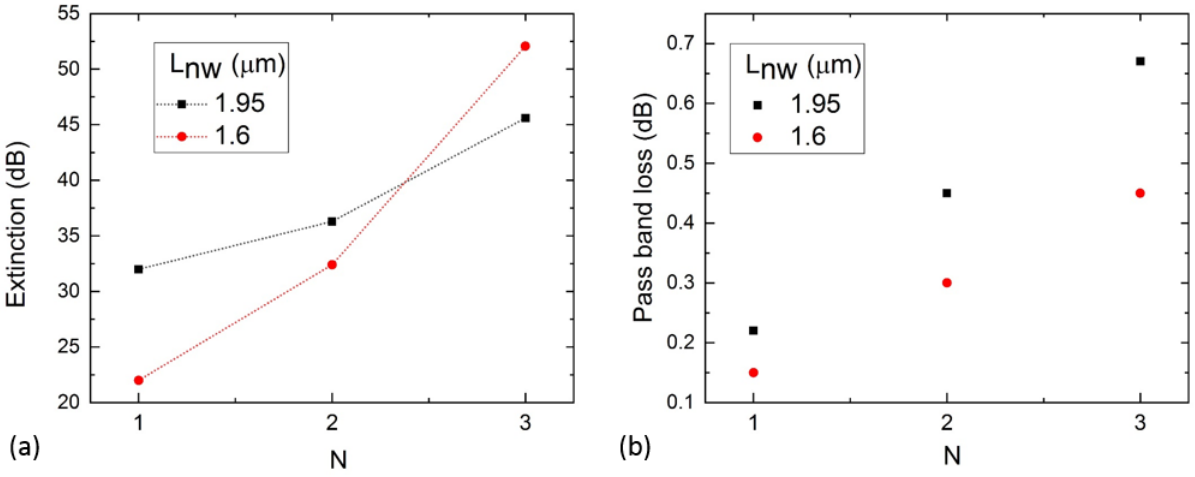

Figure 4.16: (a) Extinction and (b) Pass band two different low Q-factor cavities with L_c = 83 μm.

As a final note : I made a mistake in taking data of simply recording the extinctions and the pass band loss only. It should be noted that as N equivalent absorption based rings increase, the overall FWHM also increases. As a result, this reduces the bandwidth in the pass band, since each ring has the same FSR, but the overall FWHM is larger. This motivates the use of a smaller cavity for a larger FSR if only filtering of the pump wavelength is desired, since a reduced pass band bandwidth will induce more stringent requirements on the single-photon sources (in particular, signal and idler separation tuning) in a quantum information circuit. I believe the optimal performance (with respect to maximising extinction against pass band loss and FWHM) will be from choosing an absorber with $800 < L_{nw} < 1200$ nm and repeating it up to N = 3 rings.

4.5 Experimental Study of Reproducibility of Ring Resonators

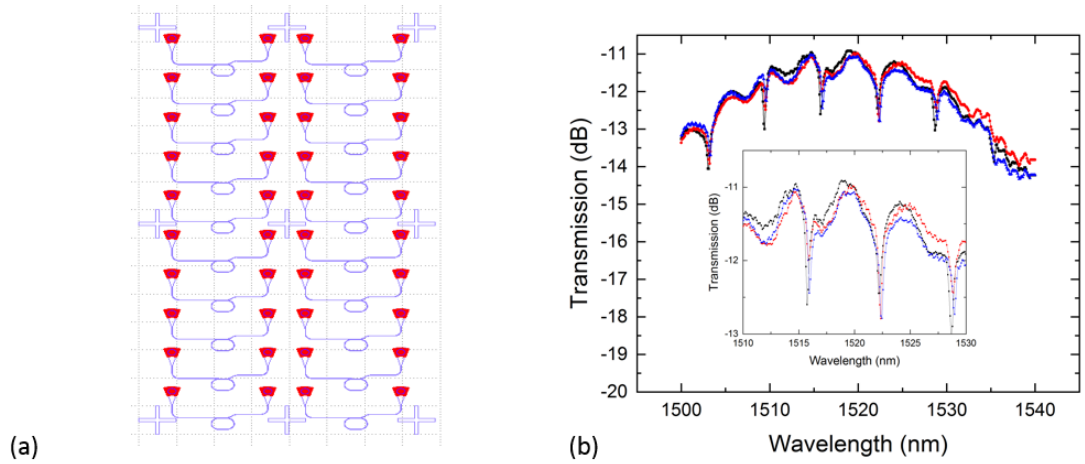

Figure 4.17: CORN02 fabrication run (a) GDS of designs submitted. (b) Experimental spectra for three different devices. Inset shows three resonances between 1510 and 1530 nm.

A design was submitted to a foundry run provided by the CORNERSTONE service based at the University of Southampton. These designs were submitted to the run titled CORN02. The foundry fabricates SOI chips with a 220 nm Si device layer and a 2 μm BOX layer. Also, there is a 2 μm upper SiO_2 cladding, which would need to be opened locally in the area of the designs to remove the SiO_2 so that a nanowire could be post-processed on top of the waveguide according to the analysis in Section 4.2. Unfortunately, we received a small number of chips (relative to the number of different designers' designs, meaning that we could not proceed with this work). However, measurements were carried out with the cladding on to be able to quantify the reproducibility of the fabrication process. The designs are shown in GDS form in Figure

4.17(a). There are N = 20 identical designs, split over two columns. Each design consists of two grating couplers spaced by 127 μm, connected by a waveguide with a racetrack ring resonator in the centre. The ring has a length of 83 μm, consisting of a 10 μm coupling region and 10 μm bends. The bus-ring waveguide gap was designed to be 150 nm to operate in over-coupling with $t = 0.6624$ calculated using coupled mode theory. Experimental measurements were carried out using the automated test station in Chapter 3. Figure 4.17(b) shows the coupling level of -11 dB at 1520 nm, and all devices were observed to perform within 0.5 dB of this value. The FSR was calculated based on the three peaks observed within the range of $1510 < \lambda < 1530$ nm and was found to be 6.6 nm. This result agrees with the analytical equation when using $\eta_g = 4.2$. The peak at $\lambda = 1522$ nm was then chosen to study the performance of all of the devices. All spectra were baseline subtracted and peaks were fitted to compute the FWHM and extinction. The results are shown in Figure 4.18(a). It can be observed that the extinction varies between 0.6 and 1.5 dB, with most of the devices appearing to have peaks with 0.9 dB extinction. On the other hand, the FWHM varies between 0.2 nm and 0.6 nm and appears to fluctuate more. The average of N = 20 devices were computed, with a mean FWHM of 0.42 $\pm$ 0.08 nm and a mean extinction of 1.03 $\pm$ 0.25 dB. Linear waveguide losses and spiral waveguide losses were calculated from cutback measurements (performed by other members of QETLabs) and were found to be 7 dB/cm and 13 dB/cm respectively. Using the ring resonator equations with a weighted average α (based on the relative lengths and measured propagation losses) with the theoretical value of t predicts a resonance with 0.946 dB extinction, which is within the experimental error of the measured value. Also, the resonance wavelength λ_{res} was recorded for all devices and is shown in Figure 4.18(b) with the wavelength shift from the average for each device. The mean λ_{res} was calculated to be 1519.97 $\pm$ 0.5 nm. The FWHM and the λ_{res} positions in this high Q-factor study motivate the improved stability of low Q-factor racetrack resonators for filtering applications.

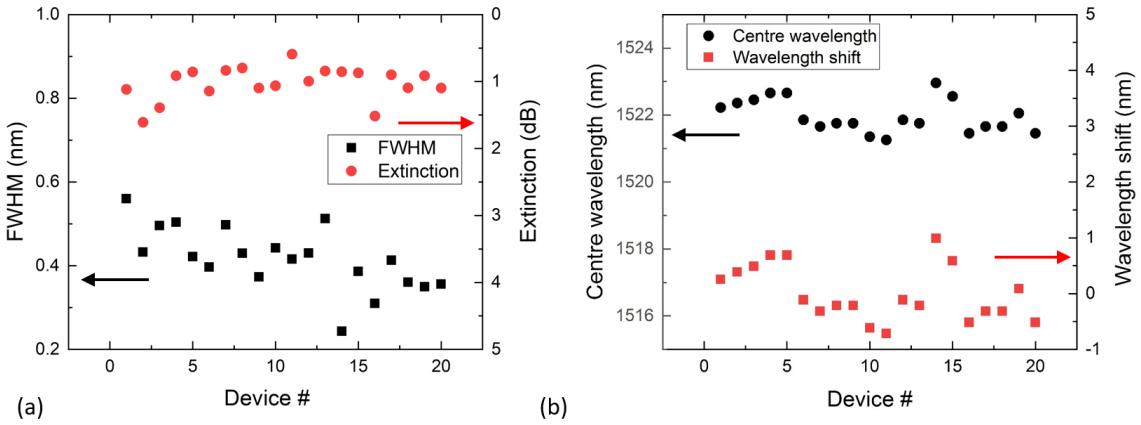

Figure 4.18: Testing the fabrication tolerance of the CORN02 process. (a) shows the extinction and FWHM of a resonance peak, whilst (b) shows the centre wavelength and the associated wavelength shift from the average for all 20 devices.

4.6 Summary

This chapter demonstrates the ability to modify a ring resonator for filtering applications through fabrication methods. The ability to realise reliable performance on-chip filters as a passive structure is desirable due to freeing up electric connections to be used for active circuit components, or to reduce heat dissipation in a cryostat. Designing an absorptive nanowire with dimensions that can be realised through typical fabrication methods such as EBL, which is used in SNSPD fabrication can enable low Q-factor filters to be produced with no added complication. Futhermore, the dimensions of the absorptive nanowire when fabricated with tools such as EBL lead to very little backscatter, which is desirable for avoiding deleterious effects such as resonance splitting, or mitigating backscattering back into a photonic circuit in the fully integrated case. A full analysis of the absorption and backscatter for a nanowire on a waveguide was presented with NbN on SOI for both air and SiO_2 cladding in order to quantify the effects on guided modes. For a 500 nm SOI waveguide supporting TE and TM modes, the analysis suggests that the TM mode is more absorptive and with greater backscatter due to its field profile, whilst the TE mode could still achieve absorption on the order of dB/μm with shallower changes with respective to the given parameters. However, for the case of moving the nanowire into the cladding layer, the TE mode absorption decays much faster than the TM mode, which formed the basis of recent ideas for on-chip filters. This work utilises the absorption of the waveguide mode to realise low Q-factor ring resonators. Using the ideas discussed, the Q-factor can be tuned through the length of the absorptive medium, which can be realised very easily with EBL. Through doing this, applications such as post-processing circuits to improve filtering performance is possible. The concept was shown using FDTD and various critically coupled designs were presented in the single-ring case with extinctions of up to 33 dB and FWHM of up to 2.5 nm. The disadvantage of the scheme is the pass band loss, which was shown to reach levels of 0.35 dB in the worst case. Using an in-series cascaded configuration, extinctions of up to 52 dB in a purely passive case with N = 3 rings were shown. The pass band loss appeared to be additive (0.15 dB for N = 1 ring to 0.45 dB for N = 3 in the best case) for the low Q-factor ring designs shown, indicating that concatenating smaller absorptive low Q-factor rings will give the best overall performances when all aspects are considered. A detailed discussion of the parameters and modifications to the basic design shown here are given to enable more reliable broadband operation, whilst other aspects such resonance wavelength shifts have been considered.

4.7 Guidance for Experimental Realisation

Since during the time of my PhD, I was not able to get to the experimental demonstration of this work, I will present a guidance for the experimental approach to realisation of the structures. In the simulation sections, the bus-ring waveguide gaps were not given due to the errors induced in the 2.5D FDTD method, so that absolute values are likely wrong with experiment (particulary

as a_{Si} was chosen as 0), but the trends are expected. The first two important parameters to get a grasp on are the loss of the nanowire and the variation of the coupling coefficient when sweeping the bus-ring waveguide gap. The former can be carried out through fabricating straight waveguides and then post-processing the absorptive nanowires with EBL using layer alignment techniques such as gold marks to obtain high (10's of nm) accuracy, depositing metal with a method such as thermal evaporation or sputtering, followed by metal lift-off. There should be repeat measurements on various L_{nw}, to represent a reasonable cut back measurement. Plotting the transmission as a function of L_{nw} then yields a_{nw} in the gradient. This first set of measurements yields the a_{nw}, whilst the other contribution to α can be characterised by changing the waveguide lengths and measuring their transmission properties without a nanowire, as was shown in Chapter 3. Determining the coupling coefficients requires fabricating multiple ring resonators with the same dimensions but sweeping the bus-ring waveguide gap in a certain range. This range should be such to identify the region where no interaction with the ring is present (i.e. where $t = 1$) and the various regimes. The critical coupling point is important to find in the high Q-factor case since it is the point where $t = \alpha$, and α in the high Q-factor case will be based on the results from a_{Si} in the prior measurements. These two points for t coupled with the exponential dependence of the gap for the racetrack resonator can yield can be combined with simulations to determine the dependence of t as a function of the bus-ring waveguide gap. For the filters in this work, the bus-ring waveguide gaps which correspond to critical coupling point can be expected to be smaller than those found in the high Q-factor case, since an over-coupled SOI ring resonator without the nanowire is a pre-requisite for realising the low Q-factor rings.

The interesting experiments would then involve sweeping L_{nw} for rings with various gaps corresponding to $t < 1$ to find critically coupled designs. Once these are found, then the same should be applied to cascade designs. The reproducibility of the method should also be considered - for example, the error bar for the average extinction for a given L_{nw} should be smaller for lower Q-factor cavities due to the nature of the critical coupling curves given in Figure 4.9. This would demonstrate the viability of the approach for post-processing photonic circuits. Furthermore, the designs (both single-ring and cascade) should also be tested with active tuning, to see if pump extinctions > 60 dB can be realised with this scheme. If this is achievable, then the performance is competitive with existing schemes [44, 45, 215].

CHAPTER 5

Design and Characterisation of a Multi-Mode Interference Waveguide Crossing for the 220 nm SOI Platform

Waveguide crossings are important structures for dense photonic integration, allowing many more structures to be packed on-chip due to circumventing any re-routing problems associated with bending waveguides around to avoid other waveguides. Instead, the crossing can be used at a small loss penalty, which if designed with a sufficiently low loss, is a preferred option to free up on-chip real estate. This is important in quantum photonic demonstrations where signal and idlers are required to be swapped for achieving path entanglement [216]. Furthermore, these devices are used in large numbers (> 100 in a recent multi-dimensional quantum entanglement demonstration [20]) and more can be expected when these experiments reach larger scales. In this chapter, the multi-mode interference theory is used to design a waveguide crossing on the 220 nm SOI platform, with a device foot print smaller than 15 x 15 μm^2, with a device loss of 0.042 dB at 1555 nm and a crosstalk better than -45 dB between 1525 and 1570 nm, with a best case of -50.2 dB at 1550 nm. Devices were fabricated and experimentally measured to quantify the relevant figures of merit of the crossing. Extra simulations are also presented to show the effects of a capping layer on device performance as well as showing the evolution of the crosstalk signal as it propagates away from the crossing region. The fabrication tolerance of the device is also investigated whilst further simulations are provided to give insight to the backscattering signatures found in these devices.

5.1 Introduction

The work in this chapter came out as a by-product to the main elements in the detector array (covered in Chapters 4 and 6), with its own applications relevant to classical photonics. The section starts out by presenting initial designs that were tested and explaining their advantages and why they were discarded. The section then proceeds to discuss the relevant architecture and shows the steps that were taken to optimise the structure. Unless stated otherwise, all simulations were carried out using Lumerical 3D FDTD and experiments were fabricated according to the XR1541-006 recipe that was given in Chapter 3. All designs considered in this chapter use SOI with a 220 nm Si device layer and 2 μm BOX. The upper cladding is air.

5.2 Initial Designs

In the initial design phase, the main attributes to the crossing are as were described in Chapter 2 and are repeated here. The relevant parameters for a waveguide crossing are:

- **Transmission:** This quantity should be maximised, because any reduction in transmission (from a normalised, ideal transmission of 1) is loss. Loss can occur through a variety of mechanisms including leakage into perpendicular waveguides (crosstalk), backscatter (through discontinuities in n_{eff}, leading to Fresnel reflections) and other mechanisms such as TE/TM conversion and diffraction [217].

- **Crosstalk:** This quantity should be minimised to avoid signal leakage into the perpendicular waveguide of the crossing. This is particularly important for implementation as part of larger integrated photonic networks.

- **Backscatter:** This quantity should be minimised. Since the n_{eff} takes on different values when considering the fundamental propagating mode in the waveguide and the crossing region, these should be treated as interfaces like the considerations given in Chapter 4 for a nanowire on top of a waveguide. Since backscatter in these waveguide crossing systems is not usually discussed (see Table 5.1), there may also be other mechanisms present.

- **Broadband:** The variation of the quantities above should minimal over a wide range of wavelengths to allow greater functionality and flexibility.

5.2.1 Right-Angle Crossing

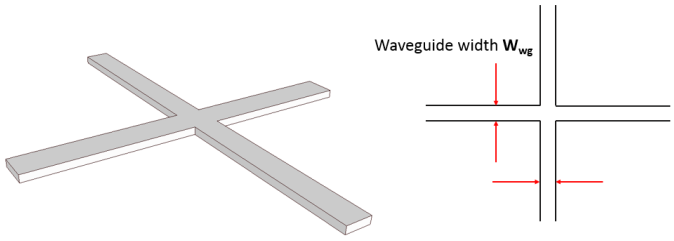

Figure 5.1: Schematic of a right-angle crossing (device only) and parametrisation. The waveguide width W_{wg} is the only parameter controlling the right-angle crossing.

Figure 5.1 gives a schematic of a right-angled waveguide crossing. Given that the input into the crossing is a straight waveguide, the simplest design that can be conceived is to route two waveguides of equal width W_{wg} into each other at 90 degrees. This creates a square crossing region of size W_{wg} x W_{wg} where W_{wg} is in the single-mode regime (between 400 nm to 800 nm as shown in Section 2.1.1 of Chapter 2). The right-angled crossing has the advantage of being very small, with a device foot print smaller than 1 x 1 μm^2.

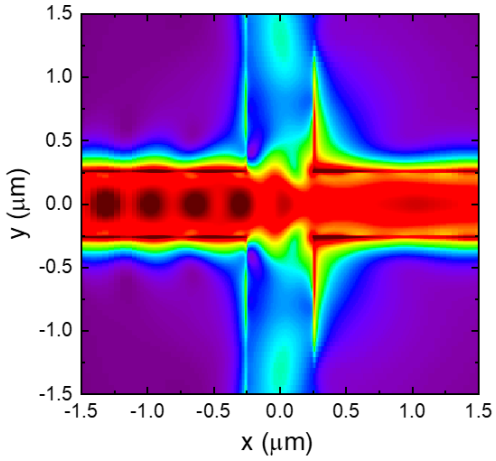

Figure 5.2: Electromagnetic simulation of the pulse travelling through the right-angled waveguide crossing with W_{wg} = 500 nm.

Figure 5.2 shows the evolution of the pulse through the crossing. It can be observed that the upon entering the crossing region, the field expands radially in the direction of propagation due to diffraction [217]. On the right-hand sidewall of the perpendicular waveguide it can be observed that some of the field is not able to pass through to the output waveguide, which is a mechanism of loss since it is not guided through the crossing region. This can be observed by the amplitude

of field that passes through to the straight waveguide relative to the injection waveguide.

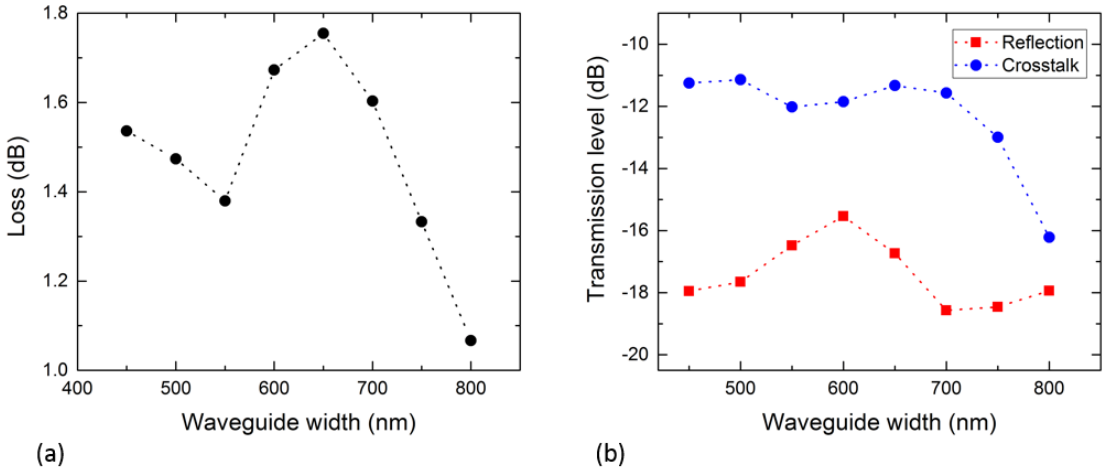

Figure 5.3: (a) Loss, (b) crosstalk and backscatter levels for a right-angle crossing of varying waveguide width at 1550 nm.

Figure 5.3(a) shows the forward propagation loss through the crossing as a function of the waveguide width between 500 nm and 800 nm. The right-angled crossing has a very high transmission loss of 1.47 dB per crossing for W_{wg} = 500 nm. Whilst increasing W_{wg} beyond 650 nm can alleviate some of the loss, the overall level is still greater than 1 dB. Figure 5.3(b) shows the corresponding crosstalk levels for the device, which are significant at -11 dB for W_{wg} = 500 nm, reducing to -16.5 dB in the best case of W_{wg} = 800 nm. For a reasonable performance waveguide crossing, the device loss needs to be better than 0.2 dB per crossing and as low as possible for other purposes (See Chapter 6).

To further investigate the dynamics of the right-angle crossing, the n_{eff} was swept across the crossing region for various W_{wg}. The results are shown in Figure 5.4. It is evident that for all W_{wg}, there is a discontinuous jump when the field enters the crossing region (where the perpendicular waveguides meet). From the point of view of the pulse, entering the crossing region resembles entering an infinitely wide waveguide of thickness 220 nm. The crossing region has n_{eff} = 2.826, corresponding to the fundamental TE slab mode for SOI.

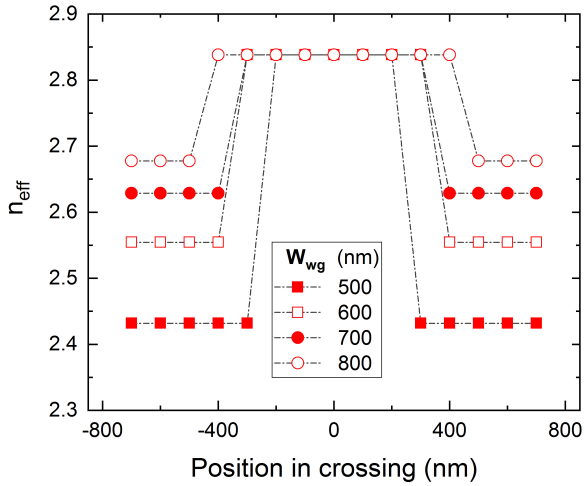

Figure 5.4: Effective index as a function of position in the crossing. Zero denotes the crossing centre. The crossing width is equal to the waveguide with W_{wg}.

5.2.2 Tapered Crossings

To reduce the discontinuity Δn as shown in Figure 5.4 of Section 5.2.1 and retain the ability to use 500 nm width waveguides, the first step taken to improve the crossing performance can be to raise the n_{eff} of the TE mode in the waveguide before it reaches the crossing region. In this case, it would involve raising the n_{eff} gradually to a larger waveguide width whose dimension forms the crossing centre. Tapering is used to minimise insertion losses by evolving the field adiabatically, which is in contrast to the schemes in Section 5.2.1 which have abrupt changes in n_{eff}. This is also important for evolving the field back down to W_{wg} = 500 nm, since results with smaller W_{wg} for the right-angled crossing in Section 5.2.1 show parts of the field touching the sidewalls of the perpendicular waveguide - necessitating the requirement for a wider injection waveguide to be able to capture all of the field after it is injected into the crossing and collect it in the output waveguide with minimal loss. The tapered structure is shown in Figure 5.5. The parametrisation for the tapered crossing structure consists of the ordinary waveguide width W_{wg} as before, with the inclusion of new terms: the taper length L_T, taper angle θ_T and the waveguide width at the crossing W_c. From trigonometry, W_c is related to L_t, θ_T and W_{wg} through:

$$W_c = W_{wg} + 2L_T tan(\theta_T). \tag{5.1}$$

For the tapered crossings, L_T and θ_T were considered, resulting in a different W_c according to Equation 5.1. To perform the optimisation for a structure, a fixed L_T was chosen and then θ_T was swept from $0 < \theta_T < 15$ degrees. Figure 5.6(a) shows the results from sweeping θ_T for L_T. It can be seen for each L_t there is an optimal θ_T for which transmission through the crossing

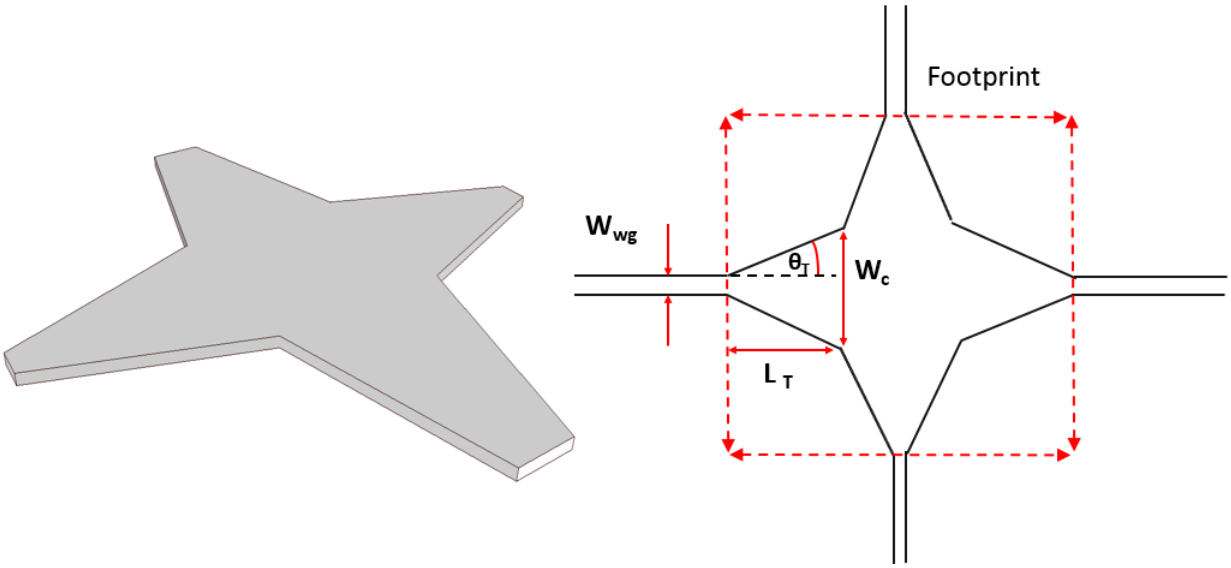

Figure 5.5: (Left) 3D Schematic of the tapered crossing (device only). (Right) Relevant parameters in the tapered crossing. The black dashed line is to show where the angle θ_T is measured.

is maximised. This corresponds to the most adiabatic-like condition for the given L_T. Figure 5.6 plots the transmission as a function of L_T, given the optimal transmission value found from sweeping θ_T. It can be observed that longer tapers result in lower crossing losses. This can also be explained through longer tapers expanding the field more adiabatically. However, this comes at a cost of footprint. The structure consists of two tapers, and the results of Figure 5.6(b) and extrapolation of the data for $L_T > 20$ μm suggests that L_T should be at least 30 μm to achieve a crossing loss of 0.2 dB, meaning that the overall structure is larger than 50 μm (also, the value of W_c that is obtained from the optimal L_T and θ_T will contribute to the footprint). The tapered crossing structure therefore requires a large footprint, undesirable for a CMOS integration device and for this reason no comprehensive crosstalk or backscatter analysis was performed. However, the optimal design with L_T = 15 μm had a reflection of -36 dB and a crosstalk of -42 dB at 1550 nm.

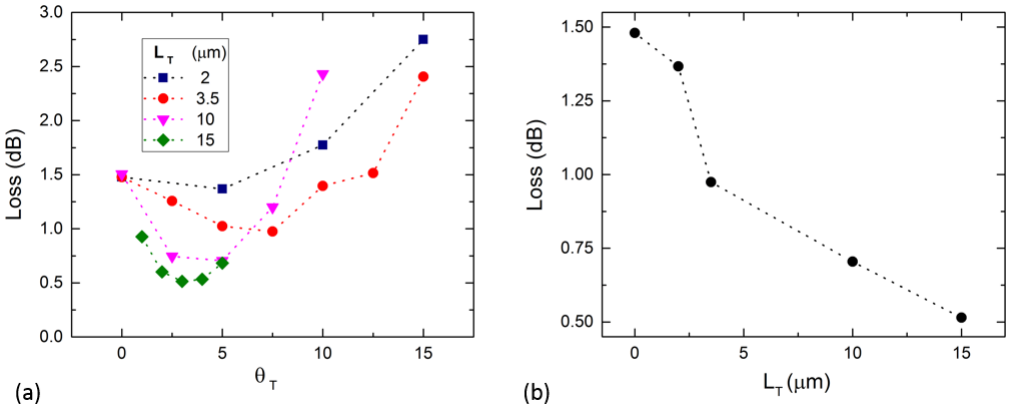

Figure 5.6: Calculated loss from (a) sweeping θ_T for various L_T and (b) the lowest loss (at optimal θ_T for each L_T).

5.3 Multi-Mode Interference Waveguide Based Design

The multi-mode waveguide structure discussed in Chapter 2 can be used to design N x M beam splitters. The waveguide crossing is a special case, where self-imaging of the field at the output port enables low loss devices, desirable for dense photonic integration. The multi-mode waveguide crossing is easily contrasted to the approaches shown in Sections 5.2.1 and 5.2.2. The right-angle and tapered crossings involve single-mode operation and preserve single-mode operation through the crossing. The multi-mode waveguide crossing instead expands to a larger waveguide which can support many modes of propagation. The beating between the lowest two order modes L_B (see Equation 2.51 and Section 2.1.5 in Chapter 2) is an important quantity as multiples of L_B correspond to imaging of these two modes, and is often referred to as a multi-mode interference (MMI) waveguide crossing. A multi-mode waveguide crossing device and its parametrisation are shown in Figure 5.7. The usual waveguide width W_{wg} and the taper length L_T are defined as before. W_c as defined in Equation 5.1 now becomes the width of the multi-mode waveguide i.e. W_{MMI}, and L_{MMI} is the length of the multi-mode waveguide interference region (between the taper section and the crossing region). This means that the total length of the structure in one direction is $2L_T + 2L_{MMI} + W_{MMI}$. For this structure, similar optimisations have to be made as before (such as optimising L_T as was carried out in Section 5.2.2).

5.3.1 Initial Approach - Coarse Sweeping and Constraints

As discussed earlier, there is a relatively large parameter space that has to be explored. The method that was used to find the optimal structure involved coarsely sweeping parameters in Lumerical MODE solutions with the varFDTD solver initially, since the simulation times are quicker than in Lumerical full 3D FDTD. The dimensions obtained from these results can then be

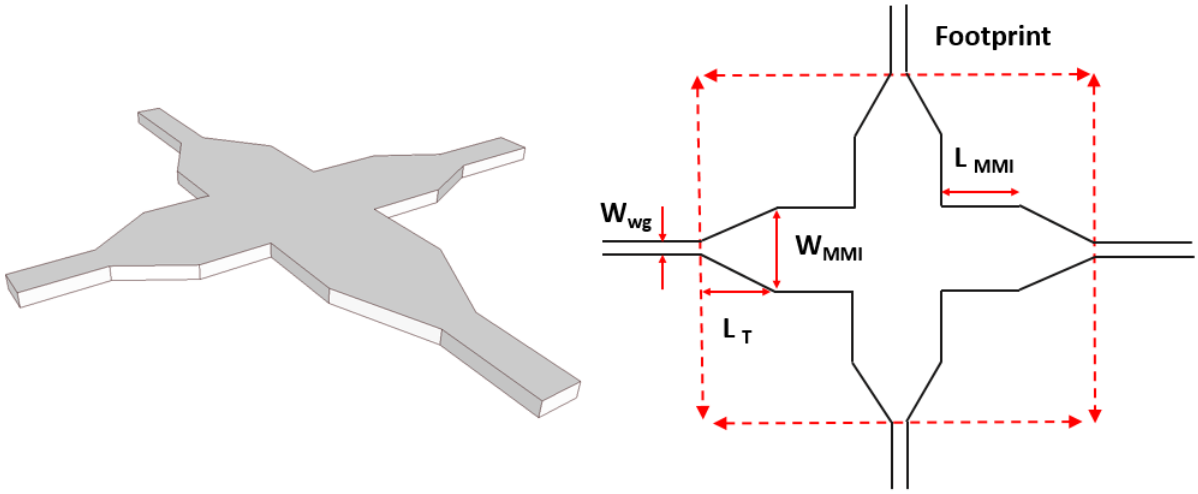

Figure 5.7: (Left) 3D Schematic of the multi-mode waveguide crossing (device only, although input waveguides are shown). (Right) Relevant parameters in the tapered crossing. The width of the waveguide after tapering is W_{MMI}, and before reaching the crossing region there is a length of multi-mode waveguide L_{MMI}.

used to guide the starting point for optimisation in the full 3D FDTD software. For a waveguide crossing, it is desirable to have a small footprint (for example of less than 20 x 20 μm^2). This number was chosen based on some considerations which also carry over to Chapter 6 and will be explained in their relevant context there. This gives an upper bound on the length of the crossing, although there are no specific constraints on L_T, W_{MMI} or L_{MMI}. The results in Figure 5.8 are obtained using the varFDTD solver under a low-resolution mesh with L_T = 3 μm at 1550 nm. The parameter of choice to sweep was W_{MMI} for various L_{MMI}. The full range of data is shown in Figure 5.8(a). It can be observed that for $W_{MMI} < 1.2$ μm, the performance is fairly similar to the tapered crossing in Section 5.2.2. In general, all data sets show some level of periodicity but with a general decrease in loss, which becomes apparent for $W_{MMI} > 1.5$ μm. In particular, each L_{MMI} has a unique W_{MMI} that gives an optimal performance and is shown clearly in Figure 5.8(b). Three designs have performances lower than 0.1 dB. The best performance device has 0.06 dB, with W_{MMI} = 1.9 μm, L_{MMI} = 4 μm, and L_T = 3 μm. The general high performance of devices with $W_{MMI} > 1.7$ μm from these simulations can be taken as the starting point for the optimisation given in the succeeding sections.

5.3.2 Analysis of Modes in the Multi-Mode Waveguide

Given the results of Figure 5.8, it suggests that W_{MMI} should be greater than 1.5 μm for best loss performance in nearly all the cases. This width means that the multi-mode waveguide region can support many modes of propagation. Figure 5.9(a) shows effective index data for the range

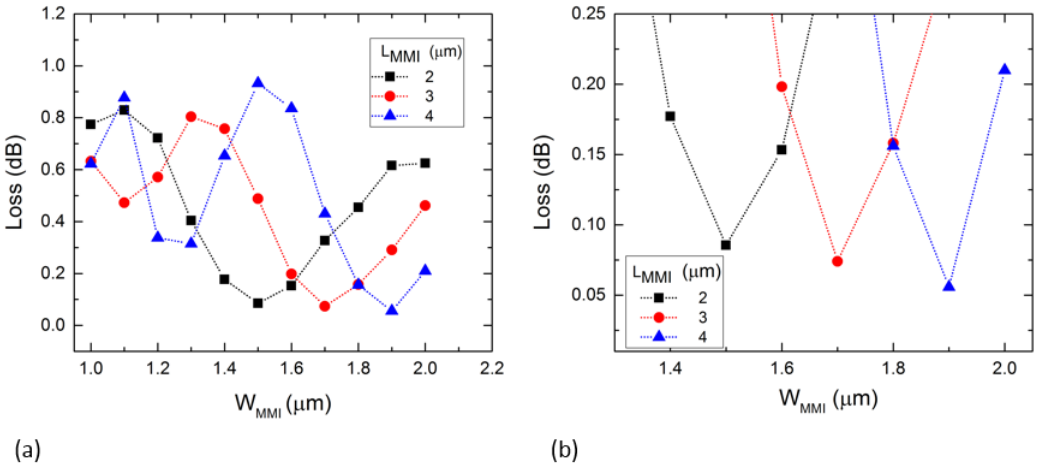

Figure 5.8: Coarse sweeping parameters for a multi-mode waveguide crossing in MODE solutions. (a) is the full dataset whilst (b) shows the best performance devices.

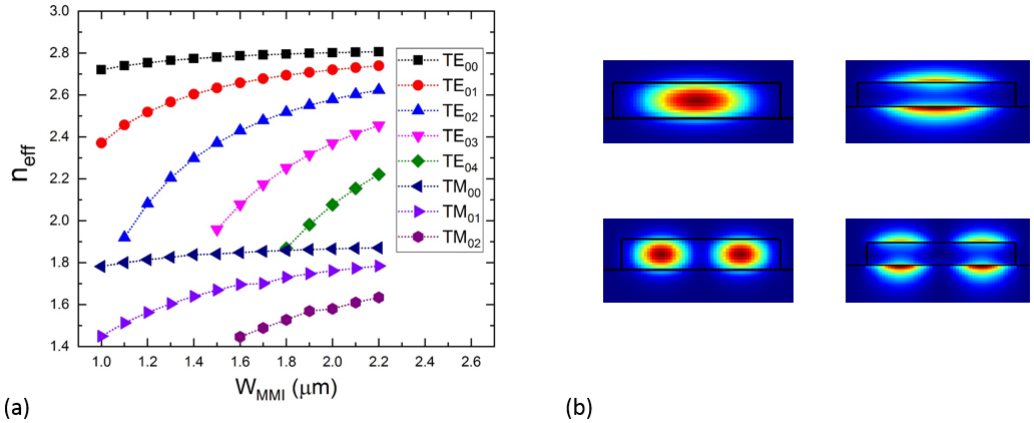

Figure 5.9: (a) Full mode data for $1 \leq W_{MMI} \leq 2.2$ μm. (b) shows the relevant modes for the device. Left column are TE, Right column are TM. First row shows the fundamental modes (TE_{00} and TM_{00}) whilst the second row shows TE_{01} and TM_{01}.

of W_{MMI} sweeped in Figure 5.8. The modes can be distinguished through their field profiles as shown in Figure 5.9(b). It can be observed that the fundamental modes (TE_{00} and TM_{00}) are concentrated in the centre of the multi-mode waveguide whilst the first order modes (TE_{01} and TM_{01}) have two equidistant regions of field concentration from the centre. At W_{MMI} = 1.9 μm, there are modes which have three, four and five peaks, whilst for the TM mode there is one with three peaks. These higher order modes (TE_{02}, TM_{02} or higher) are not of interest for the multi-mode waveguide crossing structure as they are not excited due to operation in the

symmetric interference regime [146]. More details on the first two TE modes are given in Section 5.3.3.5 for the context of field evolution through the waveguide crossing, whilst TM propagation is considered later in Section 5.5.2.

5.3.2.1 Calculated Beat Lengths

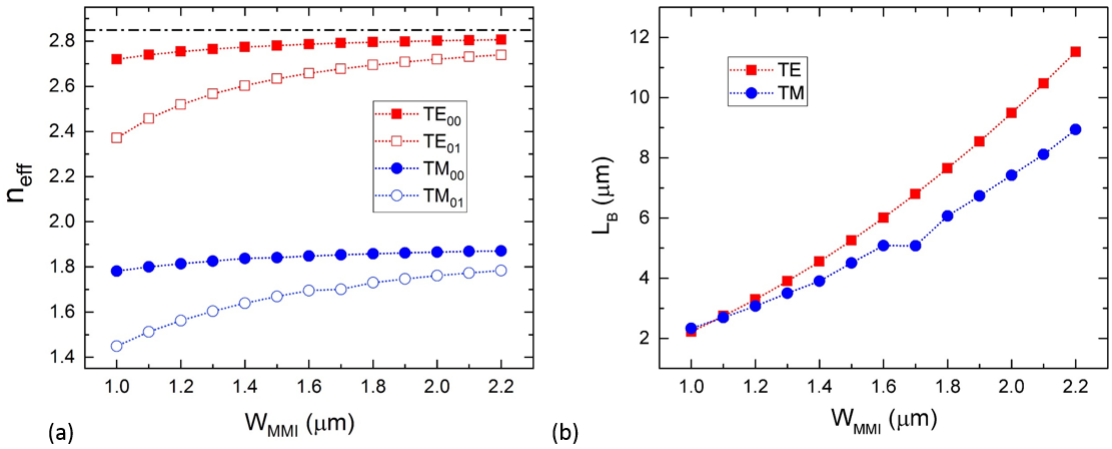

Figure 5.10: (a) Effective indices of the relevant modes used in the calculation of L_B. These are utilised in (b), where L_B is calculated for each W_{MMI}. The dashed grey line represents the slab mode for Si with n_{eff} = 2.826 and a thickness of 220 nm.

Since L_B depends on both $n_{eff,1}$ and $n_{eff,0}$ whose mode profiles were shown in Figure 5.9(b), it is necessary to quantify L_B for the relevant W_{MMI} used in the coarse sweeping. Figure 5.10(a) shows the effective indices of these modes for both TE and TM polarisations whilst Figure 5.10(b) shows the resulting L_B. It can be observed that L_B grows larger due to the n_{eff} of the fundamental and first order modes becoming closer with increasing W_{MMI}. The kink for the TM mode at W_{MMI} = 1.7 μm is believed to be due to the mode conversion between the TM_{00} and TE_{04} mode (shown in Figure 5.9(a)) owing to their similar n_{eff}, although the general trends of L_B for the TE and TM mode throughout the range of W_{MMI} are similar, it is noted here that this design is optimised for TE mode propagation. For polarisation-insensitive operation (similar performance for TE and TM injection), then Figure 5.10(b) suggests that W_{MMI} should be 1.1 μm for beat length matching.

5.3.3 Optimisation of the MMI Crossing

5.3.3.1 Parameters : Multi-Mode Waveguide Width and Length

Given the results of Figure 5.8, the starting point for design optimisation was performed by sweeping various L_{MMI} and W_{MMI} within a constrained range using full 3D FDTD simulations

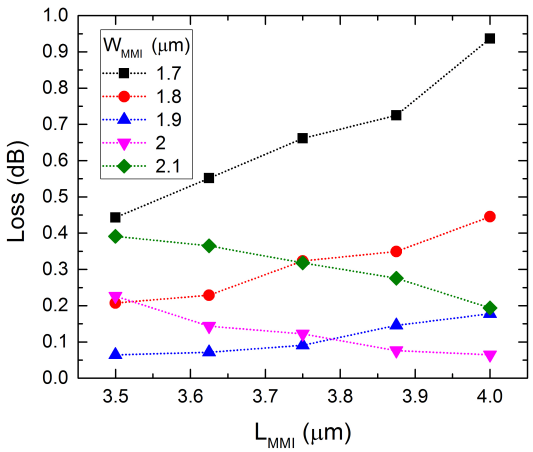

Figure 5.11: Sweeps for various W_{MMI} and L_{MMI} at 1550 nm with L_T = 3 μm. The mesh accuracy for these simulations were 20 nm in the z direction (height of the waveguide) and 35 nm along the waveguide width.

with a finer mesh accuracy. The results are shown in Figure 5.11. There are two W_{MMI} that achieve very good loss properties as good as 0.05 dB. These occur at 1.9 μm and 2 μm. To choose the suitable W_{MMI}, the footprint was considered. Given that the device footprint depends more strongly on L_{MMI}, it is more desirable to choose W_{MMI} = 1.9 μm given that the lowest loss device occurs at L_{MMI} = 3.5 μm. On the other hand, W_{MMI} = 2 μm has the lowest loss at L_{MMI} = 4 μm, adding 1.1 μm of extra length. For this reason W_{MMI} = 1.9 μm was chosen.

5.3.3.2 Parameters : Taper sweep

Up until this point, L_T had been fixed at 3 μm. Since a sub-optimal taper structure can result in high losses as was observed for tapered crossings in Section 5.2.2, it is necessary at this point to optimise the taper to ensure efficient mode conversion when exciting the multi-mode waveguide. Given the choice of parametrisation for crossing, W_{MMI} is fixed at 1.9 μm, meaning that changes in L_T can also be interpreted as optimising the taper angle. L_T was sweeped from 2 μm to 3.5 μm in steps of 0.25 μm. Figure 5.12(a) shows the corresponding device loss. It can be observed that for L_T = 2 μm, the device loss is comparable to a right-angled crossing. The mechanism for this loss is evident in Figure 5.12(b), where the reflection is -5.56 dB. However, this can be avoided and L_T can be chosen between 2.25 μm and 3.5 μm, resulting in backscattering levels between -33 and -42 dB. The inset of Figure 5.12(a) shows that the device loss does not exceed 0.06 dB for L_T between 2.25 μm and 3.5 μm. The best case occurs at L_T = 2.5 μm with a device loss of 0.046 dB at 1550 nm. L_T = 2.5 μm was chosen based on best performance and exhibiting a reasonable fabrication tolerance with respect to L_T.

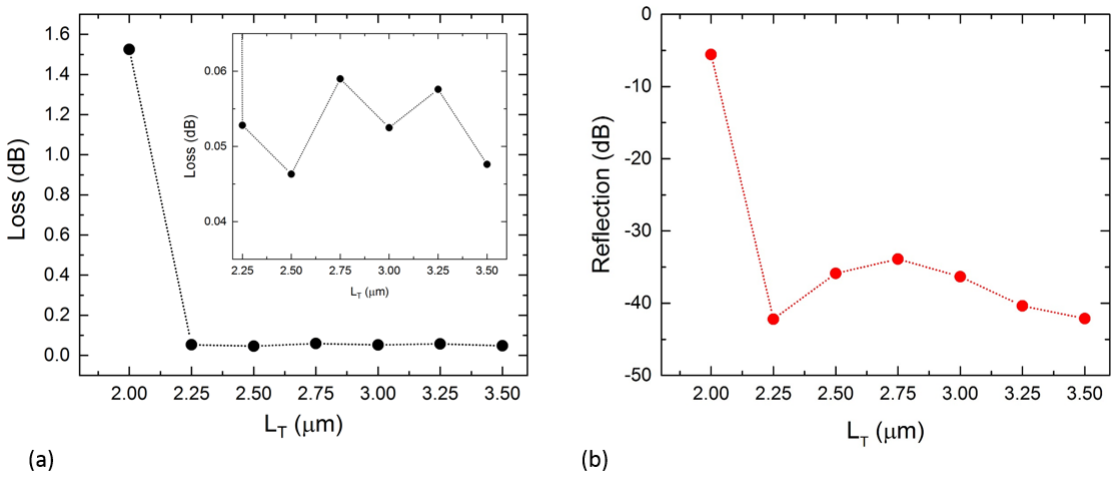

Figure 5.12: Sweeping L_T for optimisation of device loss. (a) shows the forward transmission loss and (b) shows the reflection. The inset in (a) shows the low loss region in finer detail for clarity. Simulations are performed with 20 nm resolution in all dimensions.

5.3.3.3 Parameters : Finer Detail Sweeps

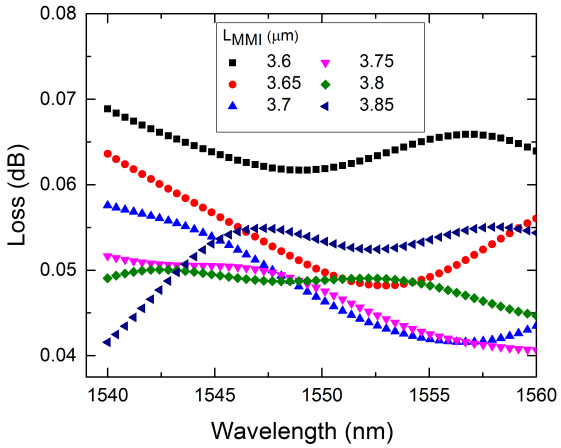

Figure 5.13: Sweeping L_{MMI} in the wavelength range of 1540-1560 nm. Data is taken with 20 nm resolution in all dimensions, with L_T = 2.5 μm and W_{MMI} = 1.9 μm.

Wavelength spectra were recorded between 1540 and 1560 nm for various L_{MMI} in steps of 50 nm and are shown in Figure 5.13. The best results were obtained for $3.6 < L_{MMI} < 3.8$ μm. With the exception of L_{MMI} = 3.6 μm (which may be optimal for a wavelength above 1560 nm), the loss is between 0.042 and 0.058 dB on all devices. This can be interpreted as a robustness to fabrication since the corresponding datasets are in a 200 nm range. The best performance at

1550 nm is the light blue dataset corresponding to L_{MMI} = 3.7 μm. For the design, L_{MMI} = 3.7 μm was chosen given that it has the best performance at 1550 nm, with the minimum also being closest to 1550 nm. It can be observed that some other structures achieve 0.04 dB loss at other wavelengths away from 1550 nm, meaning there may be further potential reach this value for λ = 1550 nm.

5.3.3.4 Broadband Response of Optimised Structure

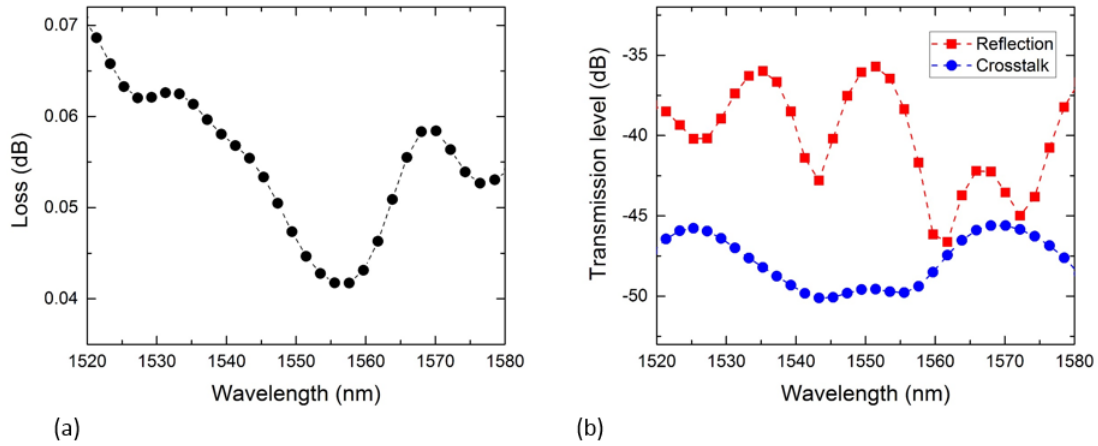

Figure 5.14: Broadband response of the optimised multi-mode waveguide crossing. Figure of merit are (a) device loss and (b) backscatter and crosstalk.

The parameters for the optimised structure are W_{MMI} = 1.9 μm, L_{MMI} = 3.7 μm and L_T = 2.5 μm, resulting in a device footprint of 14.3 x 14.3 μm^2. The wavelength response of the optimised structure is shown between 1520 nm and 1580 nm in Figure 5.14. The lowest loss level of 0.042 dB occurs at λ = 1555 nm, with 0.045 dB at 1550 nm. Generally, the loss is better than 0.07 dB over a 80 nm range - between 1520 nm and 1600 nm. Crosstalk levels of -50 dB are observed between 1540 and 1560 nm, with the worst case of -45 dB. The backscatter level is higher, ranging between -36 dB in the worst case and -46 dB in the best case. Since one mechanism for backscattering can originate from discontinuities in n_{eff}, the best explanation to offer for the observed periodicity is considering two reflections - the first contribution is from entering the crossing region from the multi-mode region, whilst the second comes from exiting the crossing region and entering the multi-mode region. Since the sign of n_{eff} is inverted, there is a π phase shift between the reflections. This particular effect coupled with destructive interference from the reflections may explain the minimum value of -46 dB.

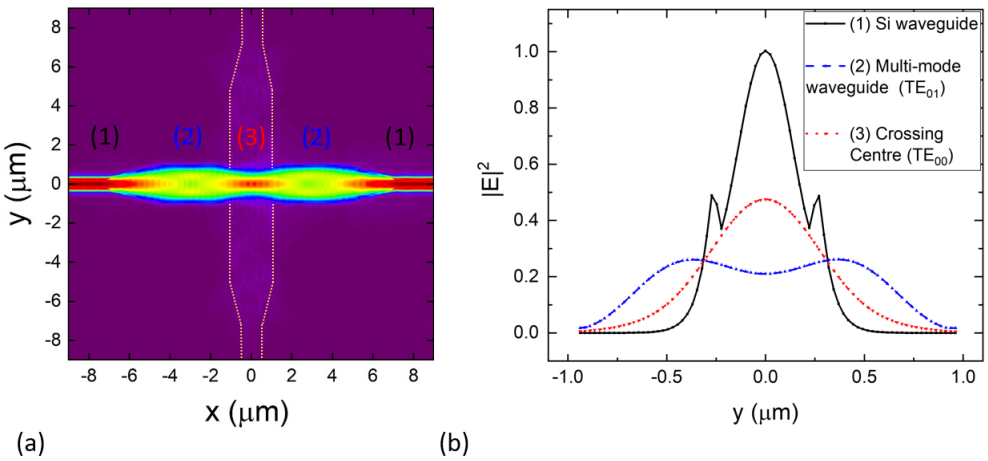

Figure 5.15: (a) Electromagnetic simulation of the pulse travelling through the multi-mode waveguide crossing from left to right. The different regions are labelled (1), (2) and (3) and are characterised by their electric field distributions in (b).

5.3.3.5 Electromagnetic Simulation and Forward Field Evolution

Figure 5.15(a) shows the evolution of the field as it is injected from the Si waveguide region marked (1) for the TE polarisation, travelling in the positive x direction. The electromagnetic simulation shows that the field expands into the multi-mode region and then oscillates between the TE_{00} and TE_{01} modes whose profiles are shown in Figure 5.9(b). The crossing can be considered to have two self-imaging points for the fundamental TE_{00} mode, one of which lies in the crossing centre and is marked (3), whilst the other is on the exit waveguide marked (1). There are two self-imaging points for TE_{01} mode which occur inbetween the start of the tapering and crossing regions (in the centre of the multi-mode waveguide). The imaging points for the TE_{01} mode are marked (2) on Figure 5.15(a).

Figure 5.15(b) shows the field profiles at various points in the crossing structure and in the injection waveguide. Comparatively, it can be observed that the self-imaging point of the fundamental TE mode in the crossing centre has a shallower slope relative to the injection waveguide with a lower central amplitude than when it is contained in the 500 nm Si waveguide - with the trade-off that the field concentration is spread out across a wider space. This particular aspect is taken advantage of in Chapter 6 when considering implementing the multi-mode waveguide crossing structure in a ring resonator for an SNSPD. Half way between the first self-imaging point for the TE_{00} mode and the injection point into the taper, the field evolves into TE_{01} which is characterised by the electric field amplitude having two peaks, commensurate with the field profiles shown in Figure 5.9(b).

In comparison to the previous crossing designs shown in Sections 5.2.1 and 5.2.2, there is still a discontinuity in n_{eff} that exists between the multi-mode region of width W_{MMI} and the crossing centre, which the field propagating through can be considered to be a slab mode as discussed in Section 5.2.1. However, in the previous cases, the mode would just propagate in a standard manner through the waveguide (albeit evolving to a wider waveguide in the case of a tapered crossing) and experience diffraction and backscatter in the crossing region. Since the multi-mode crossing is designed to self-image at the crossing centre, the field evolution from the first order TE mode to the fundamental TE mode occurs as it is passing through the interface of the multi-mode region and the crossing region. It is expected that this inward (evolution of the field back to the centre of the waveguide) results in a suppression of the diffraction, which explains why the transmission loss is improved in an multi-mode interference based crossing relative to a right-angle or tapered crossing. As an extra note, the design here uses strip waveguides. For further reduction of the index continuity, 60 nm partial etched rib waveguides of width 2.5 μm have been implemented into a multi-mode waveguide crossing, achieving a loss of 0.011 dB and a crosstalk of -70 dB [218]. However, the device had a large footprint > 30 x 30 μm^2. For some further suggestions about potential improvements, see Section 5.7.2.

5.4 Experimental Measurements

5.4.1 Fabricated Devices

Structures were fabricated in XR1541-006 resist using EBL and transferred to Si through RIE using the recipe given in Chapter 3. Figure 5.16(a) shows an SEM image of the fabricated device as part of a measurement structure for crosstalk characterisation, as shown in Figure 5.16(b). For this particular measurement, three grating couplers spaced apart by 127 μm were used for characterisation. To extract the crosstalk of the device, light must be injected through the port labelled 'Input', whilst detectors measure the gratings in the ports labelled 'Cross' and 'Through'. The difference between the resulting spectra can be used to quantify the crosstalk. Figure 5.16(c) and (d) are part of a set of measurements used to characterise the device loss. These are part of a set of cutback measurements. The distance between grating couplers in this case is 381 μm, corresponding to the largest port spacing that can be accommodated in a 500 μm x 500 μm writefield area. The waveguide which connects the gratings is 3.8 mm long, consisting of 8 straight sections with bends. In these straight sections, waveguide crossings are added from the centre outwards, as can be observed in Figure 5.16(c) for 40 crossings to Figure 5.16(d) for 160 crossings. The increment for the cutback measurement was 40, meaning that structures with 0, 40, 80, 120 and up to 160 crossings were fabricated. The reason for this choice was to be able to accurately extract the insertion losses above other sources of error. From Figure 5.14(a), we can observe that for a single crossing, the loss is between 0.04 and 0.05 dB for $1550 \leq \lambda \leq 1560$ nm. This means that for an increment of 40 crossings, we can expect 1.6-2 dB of loss. All measurements on these

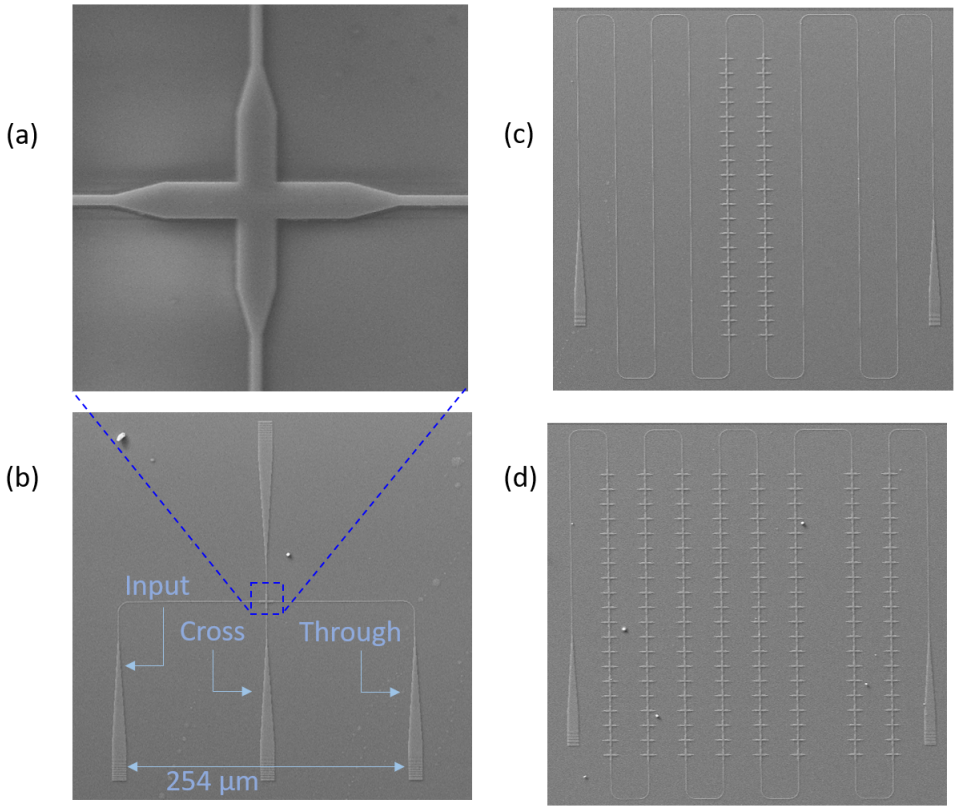

Figure 5.16: (a) SEM image of a fabricated crossing. (b) Crosstalk measurement. (c) and (d) are waveguides with 40 and 160 crossings respectively as part of the cutback measurement set.

fabricated devices were carried out using the setup in Chapter 3.

5.4.2 Insertion Losses

Various insertion loss measurements for characterisation of the waveguide crossing are shown in Figure 5.17(a). These raw grating spectra highlight some sources of error in the fabrication. For example, it can be observed that the grating peak of the 120 cross measurement is at λ = 1570 nm, whereas it is nearer to 1560 nm for the other measurements. This introduces some error when considering the use of grating couplers for characterising an on-chip device. Although not shown, for zero crossings it is possible to consider the best case fibre-to-fibre transmission regardless of λ in the band considered, since the efficiency of the grating does not change significantly if the peak wavelength shift occurs due to small changes in period [87]. The crossing here is wavelength-dependent, which means that the observed spectra are a convolution between the gratings and the crosser. For characterisation of the insertion loss, we considered the measurement to be taken at 1560 nm whilst taking account for errors introduced in the fabrication. The resulting plot is shown in Figure 5.17(b). From this plot, we can observe a change in fibre-to-fibre transmission

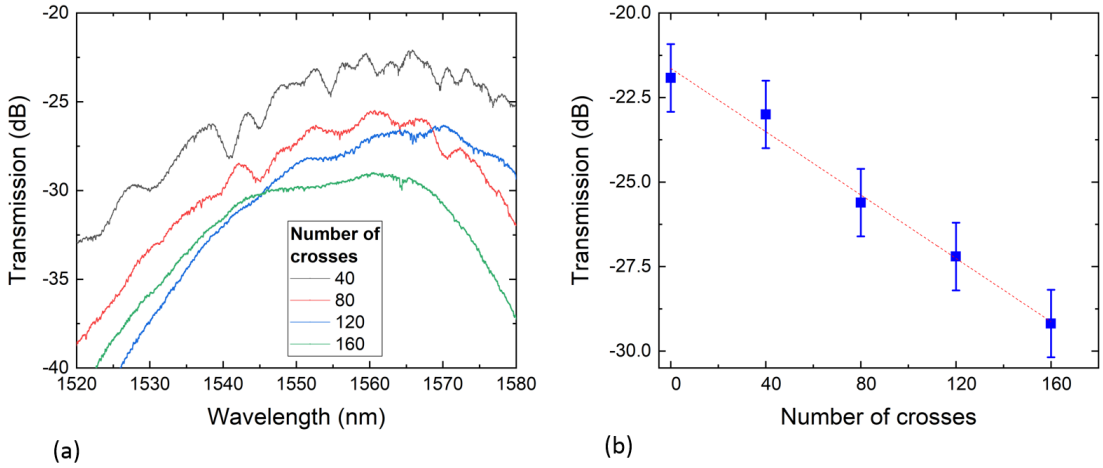

Figure 5.17: (a) Wavelength spectra for four various cutback structures. (b) Example of a plot to extract the insertion loss at 1560 nm.

of around 8 dB when considering the loss of 160 crossings. A linear fit was applied to this data, yielding a loss per crossing of 0.044 ± 0.002 dB.

5.4.3 Crosstalk

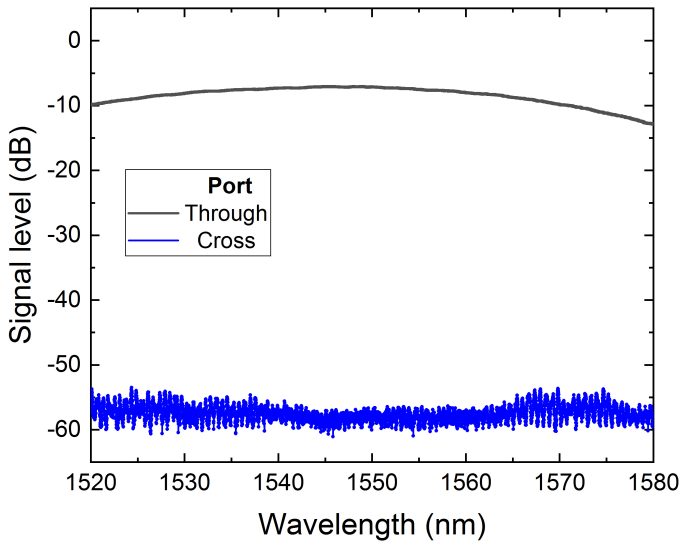

Figure 5.18: Experimental measurement for extraction of the device crosstalk.

The device crosstalk was measured using a crosstalk structure shown in Figure 5.16(b). The result is shown in Figure 5.18. For accurate extraction of this quantity, the noise floor of the

detector must be considered. To be able to determine whether the signal of the cross port is the noise floor or device crosstalk, the laser power has to be increased, monitoring both the through and cross ports for various detector dynamic ranges. It was found that the detector range could only be set to -60 dB or -50 dB. The -60 dB noise floor was chosen, since it was not possible to distinguish the crosstalk signal with a -50 dB noise floor with the maximum laser power available. The crosstalk was found at 3 dBm laser power as shown in Figure 5.18. In terms of the through port, this structure has the grating peak at λ = 1550 nm. The fibre-to-fibre transmission for this measurement is -7.3 dB at 3 dBm laser power. Fast noise can be observed in the cross port at λ = 1530 nm and λ = 1570 nm, whilst between 1540 and 1560 nm the amplitude of the noise appears to be decreased. This is due to the device crosstalk performing better at this wavelength, in accordance with the simulated crosstalk given in Figure 5.14(b). At 1550 nm, the signal at the crosstalk port is -57.5 dB, resulting in a crosstalk of -50.2 dB.

5.4.4 Backscatter

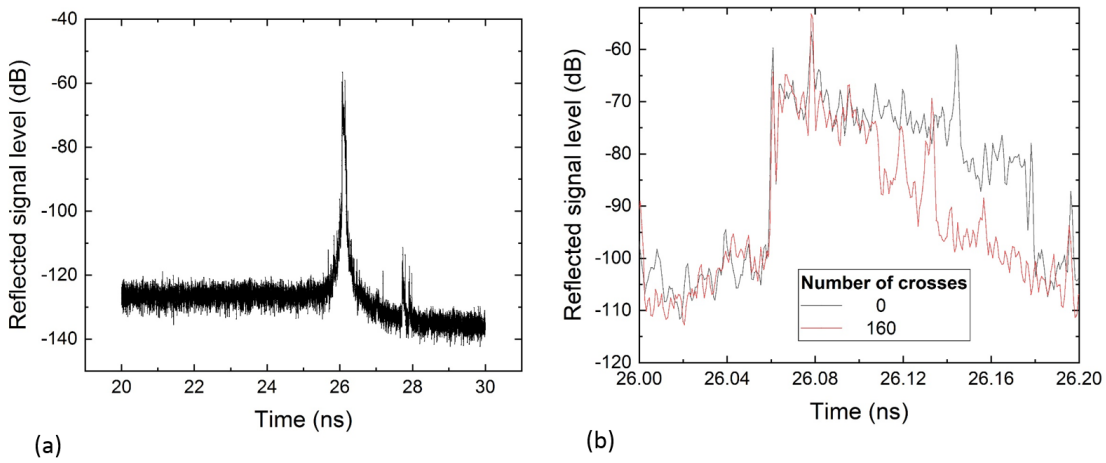

Figure 5.19: Time-domain backscatter measurements. The scan in (a) is the full range whilst (b) is zoomed in on the time interval corresponding to signal propagation in the chip.

The backscatter was investigated using a Luna OBR 4600 white light reflectometer. This tool has its own source and for experimental measurements the OBR effectively replaces the laser. The operational principle is based upon wavelength-swept interferometry, which has been explored in various contexts [219–221]. For measurements, the laser was used to optimise coupling for a structure. Afterwards, the laser was replaced with the OBR and measurements were taken. The resulting data from this device is in the time domain, allowing spatial resolution of reflections from various structures in the device under test. The best spatial resolution of this instrument is 7 μm, which result from scanning the instrument in its largest wavelength range of 1529 - 1571 nm. Figure 5.19(a) shows the time domain response in the interval of 20 to 30 ns for one of the

cutback measurement waveguides with zero crossings. The data outside of this interval was cut off due to its correspondence to features not relating to the chip such as fibre connectors, etc. It can be observed that there is a large peak with a reflection of -59 dB at 26 ns. This shoulder was investigated more closely in Figure 5.19(b). Two waveguides were compared - the zero crossing waveguide and the waveguide with the largest number of crosses, 160. Two aspects of the plot confirm that this interval does indeed correspond to the chip are as follows. Firstly, the calculated time to propagate in the 3.8 mm waveguide can be estimated by:

$$\Delta t = \frac{\eta_g \Delta L}{c}, \tag{5.2}$$

where Δt is the relevant time interval, c is the speed of light, η_g is the group index of the SOI waveguide and ΔL is the waveguide length. Using Equation 5.2 with η_g = 4.2 (corresponding to a 500 nm SOI wire waveguide), we obtain Δt = 0.05 ns. Note that for the Luna OBR system, the pulse is sent from the device and returns to the device, meaning that the total time for propagation in the chip is $2\Delta t$, meaning the relevant interval should be on the order of 0.1 ns. From Figure 5.19(b), the start of the peak is at 26.06 ns and continues to approximately 26.18 ns. This is a rough calculation, and does not account for some aspects of the measurement such as the change in index at bends, or in the crossing regions. The second aspect stems in the performance when considering two different waveguides with 0 and 160 crossings. It can be observed from Figure 5.19(b) that the waveguide with 160 crossings has a faster decay in signal relative to the 0 crossing waveguide. This can be explained from the waveguide crossing having a larger loss than a simple waveguide and that the signal has to pass through these crossings twice - corresponding to effective propagation through up to 320 waveguide crossings. From these measurements, we observe no significant reflection peaks from a waveguide with 160 crossings relative to the 0 crossing waveguide, suggesting that the backscatter contribution from the crossings is not any more significant than the contributions from other components such as the grating couplers. Finally, measurements were taken on the crosstalk waveguide and inverse Fourier transforms were taken to characterise the spectral response of the waveguide crossing, which is shown in the next section.

5.4.5 Comparison to Simulation

In this section the measured experimental results are compared to the simulations. Figure 5.20(a) shows the device loss as a function of wavelength and compared to the simulation. Three points were taken at 1555, 1560 and 1565 nm (an example of such a measurement was shown in Figure 5.17). The best agreement is found at 1555 nm, yielding 0.043 ± 0.004 dB, although the other wavelengths are also within experimental error of the simulation. Figure 5.20(b) shows the comparison of the residual crosstalk spectrum (subtracting the through port and cross port in Figure 5.18) and the backscatter of the single crossing from a crosstalk waveguide with their

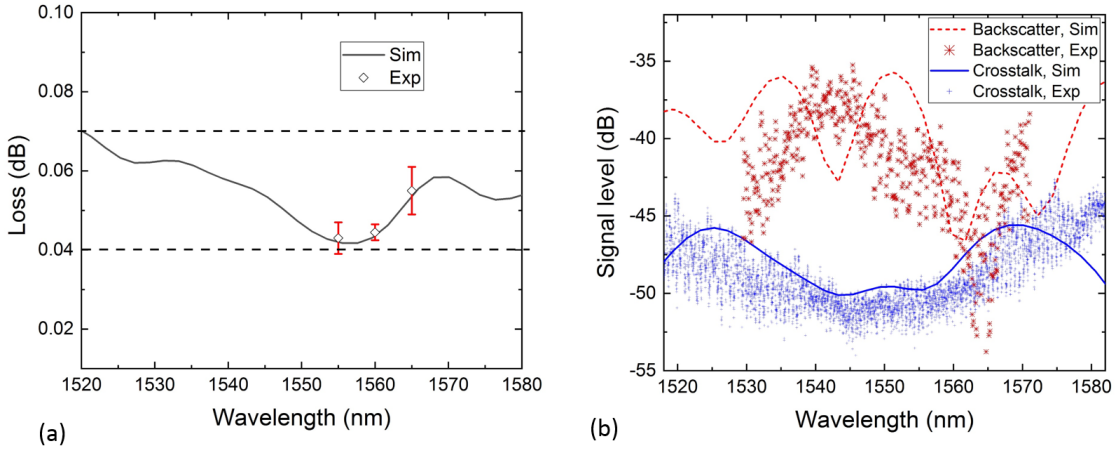

Figure 5.20: Comparison of measured (points) with the simulations (lines) for (a) device loss and (b) backscatter and crosstalk.

simulated counterparts. In terms of crosstalk, there is excellent agreement between 1525 nm and 1565 nm. The worse experimental performance outside of this range can be attributed to the limited bandwidth of the grating couplers, which can be observed by the decrease in through-port coupling from Figure 5.18. In terms of backscatter, the device is offset in wavelength. This can be explained as a combination of two aspects. Firstly, the sensitivity of the interference condition will depend on dimensions - which could change the interference conditions in the experimental structure relative to ideal dimensions. This is investigated in Section 5.5. Secondly, the reflected spectra is obtained by using a Lumerical monitor placed behind the source in a fixed position. From this monitor, interference fringes can be expected from the two reflections in the crossing region [222] and proportional to:

$$I = I_1 + I_2 + 2\sqrt{I_1 I_2}\,cos\delta \tag{5.3}$$

where I_1 and I_2 are the intensity of reflections from the first and second interfaces in the crossing region and δ determines the periodicity of the fringes. In the experimental measurement, it is believed that there may be a phase offset relative to the simulation, which stems from the additional propagation length back through the chip, grating coupler and fibres. Although the backscatter is offset, similar performance was extracted in the range of 1530 nm to 1570 nm. The worst case backscatter experimentally was -35 dB. The -55 dB signal level that occurs at 1565 nm has been observed in simulation when changing the structural dimensions (see Section 5.5). For this reason, we believe this superior backscatter performance is real and not due to other factors originating from the measurement setup.

5.5 Further Simulations

5.5.1 Understanding the Backscatter

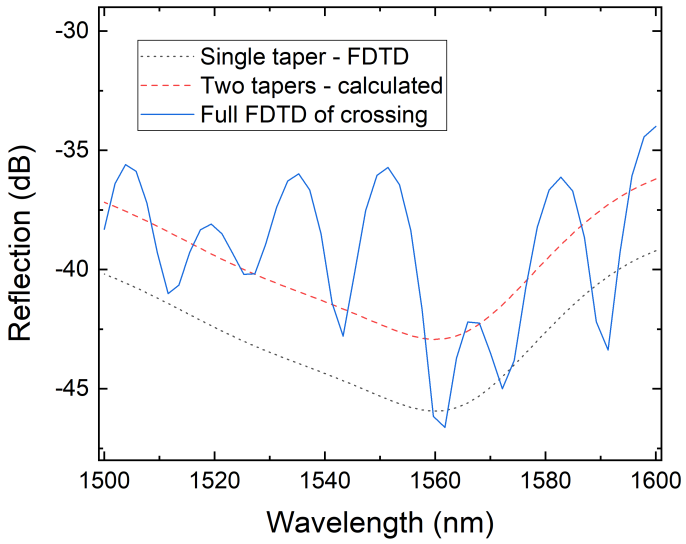

Figure 5.21: Decomposing the full reflection spectrum of the waveguide crossing to understand its components.

Some further simulations were performed to gain insight into the backscattering. Figure 5.21 shows three datasets. One corresponds to the full FDTD of the crossing which is the same as Figure 5.20(b) and is used for comparison. The other datasets correspond to the wavelength response of the taper, which was achieved by simulating the fundamental TE mode propagation through the first taper and placing a transmission monitor at the start of the multi-mode waveguide. It can be observed that the single taper response is the envelope to the overall performance of the crossing, with the best performance of < -45 dB near 1560 nm. This propagation through the taper represents a performance limitation for this waveguide crossing with respect to backscattering. The largest values are -40 dB and -39 dB at the respective wavelengths of 1500 and 1600 nm respectively. No periodicity is observed from the taper which is expected, since the simulation does not include the crossing region. The overall response of two tapers is calculated and also shown, under the assumptions that the backscatter response is equal for both tapers and the signal from the second taper does not experience loss in the crossing region. As a result, the signal level rises by 3 dB. When compared to the full simulation, there are regions where the backscatter signal is greatly increased with respect to the tapers due to the constructive interference from reflections in the crossing region. These are most noticeable at the wavelengths of 1505, 1535 and 1555 nm respectively. The FSR of the constructive interference peaks is 18 nm, which is likely to

follow a similar form to the FSR for ring resonators (Equation 2.45), with the cavity length being given by the width of the crossing region (i.e. W_{MMI}) and the corresponding group index for the slab TE_{00} mode in the crossing region. There is likely to be an angular dependence due to the nature of the diffraction when the forward propagating mode expands into the crossing region. The analysis above is the most that was investigated for this aspect of the backscatter.

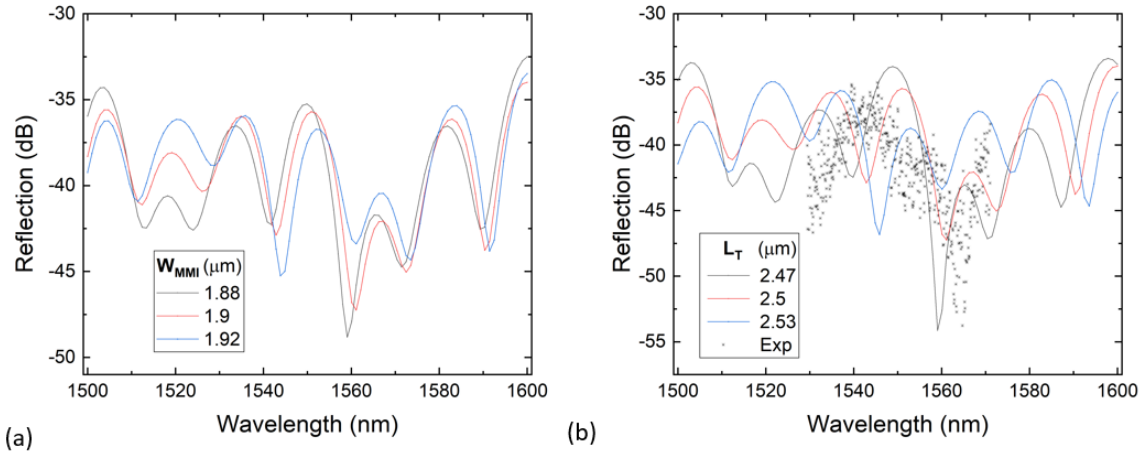

Figure 5.22: Investigating the effect of structural bias on the backscatter for (a) W_{MMI} and (b) L_T.

To attempt to verify the -55 dB performance at 1565 nm observed in Figure 5.20(b), simulations with offset structural parameters were performed to determine if deviations in structural parameters had large effects. For this, the full crossing was simulated and structural biases were given to one of the parameters (W_{MMI}, L_{MMI} and L_T) whilst the others were kept constant. Figure 5.22(a) shows the effect of biasing W_{MMI} by ± 20 nm. It can be observed that the periodicity of the peaks remains similar, although certain regions of the spectra can vary by as small as 1 dB (for the peaks at 1573 nm) to as large as 6 dB (for the peaks at 1520 nm). This would have to be verified further by simulating the taper sections only, to see if similar envelopes are observed to that of Figure 5.21. Similar spectra were observed when biasing L_{MMI} by the same amount. This leads to the conclusion that the backscatter of these devices are sensitive to fabrication errors. It should also be noted that the wavelength for minimum backscatter may not necessarily contribute to the wavelength that minimum forward loss is attained. As an upper bound, the largest backscatter observed for the optimised structure is -35 dB, which accounts for 0.0017 dB loss (4% of the total loss for the waveguide crossing). The forward propagation dynamics are based on self-imaging, with the majority of loss caused by diffraction in the crossing region. However, the dynamics for the reflected waves are not fully understood at present. Figure 5.22(b) shows that -55 dB backscatter is obtained near 1560 nm in simulation as a result of biasing L_T by -30 nm. This gives more credence to the notion that the -55 dB backscatter observed in Figure

5.20(b) is real. The 5 nm offset in wavelength between the simulation and the experimental data may be possible to resolve by biasing all of the structural parameters in the crossing, which is a realistic condition for the fabricated devices.

5.5.2 Capping Layer Study

In this section, the effect of the capping layer (according to the experimental considerations given in Chapter 3) may play a role in device performance and therefore should be discussed for practical contexts. To model the effect of the capping layer, an identical multi-mode waveguide crossing structure was placed on top of the Si device layer with refractive index 1.44 and with a thickness varying between 50 and 150 nm (according to the considerations of the capping layer with FOx-14 resist given in Chapter 3). For this study, both TE and TM modes were injected to study their behaviour. Figure 5.23(a) shows that the loss performance in TE polarisation is not reduced beyond 0.05 dB when considering up to 150 nm of HSQ capping layer. On the other hand, the TM mode shows a larger variation up to 0.98 dB (no HSQ) and in the best case of 0.63 dB for a HSQ thickness of 100 nm. The general discrepancy between the loss performance for TE and TM mode stems from Figure 5.10(b), since $\Delta L_B = L_{B,TE} - L_{B,TM}$ appears to grow as W_{MMI} grows. The variation within the TM dataset may be from two contributions. More HSQ should raise the effective indices of the modes with a net result that $L_{B,TM}$ becomes closer to $L_{B,TE}$ with no HSQ - hence, a stronger self-imaging condition is met, which could explain the improvement in crosstalk observed for the TM mode in Figure 5.23(b). The second contribution is from the taper optimisation. The optimal taper length was considered for the TE mode only and therefore may not be optimal for the TM mode, resulting in stronger amounts of loss and backscatter (which is observed in Figure 5.23(b) with roughly 6 dB difference). When considering the trends observed for the TE mode, the results of Figure 5.23(b) suggest that a small capping layer improves the crosstalk by 2 dB and backscatter by 6 dB. When considering Figure 5.14(b), the backscatter changed by 10 dB between 1550 nm to 1560 nm. This result in the present context suggests that the capping layer is changing the interference condition between the reflections in the crossing through changing n_{eff} as expected.

5.5.3 Crosstalk Evolution

To study the crosstalk, the TE mode was injected through the optimal structure at 1550 nm with transmission monitors placed from -0.95 μm, which corresponds to the entrance from the multi-mode region into the crossing region, and swept towards the 500 nm waveguide in steps of 2 μm. Figure 5.24 shows how the crosstalk varies. The crosstalk level is around -26 dB at the crossing region boundary. The crosstalk at this particular region is discussed in more detail in Chapter 6. There are two large decays of different strength when passing through L_{MMI} and L_T. The resulting coherent crosstalk then tends to the value found in Figure 5.14(b) when in the Si waveguide.

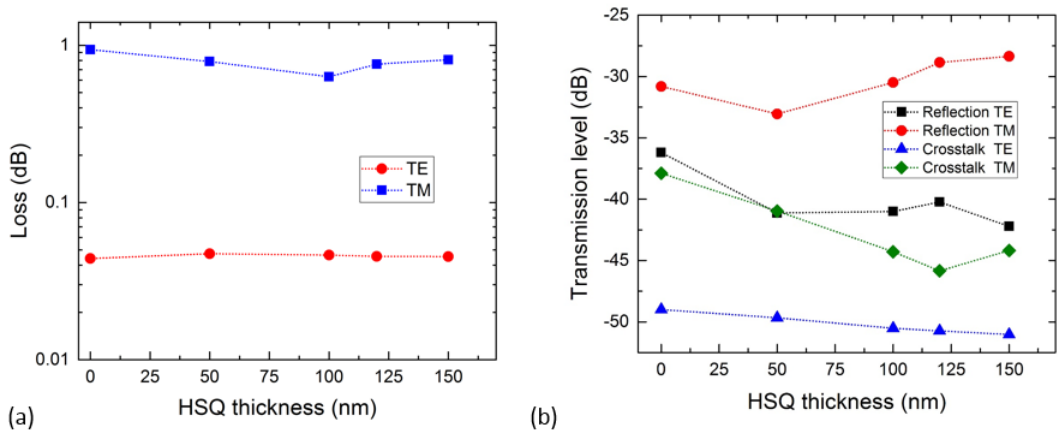

Figure 5.23: Capping layer effect on (a) loss and (b) backscatter and crosstalk of the optimised crossing device at 1550 nm.

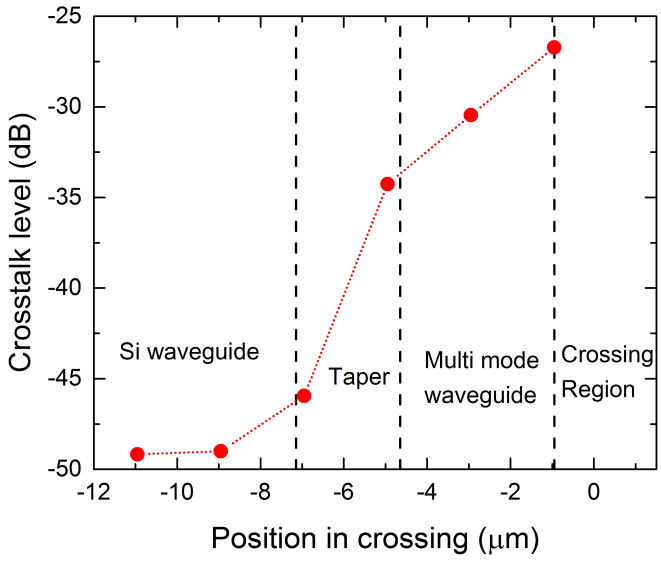

Figure 5.24: Studying the crosstalk level as it propagates through the multi-mode crossing device. The dashed lines separate the various regions of the structure and are labelled.

5.5.4 Fabrication Tolerance

In this section, the tolerance of the multi-mode waveguide crossing is explored in terms of structural parameters. For this study, only the forward loss is considered. To perform this study, one parameter in the crossing (L_{MMI}, W_{MMI} and L_T) is changed whilst the others are kept constant.

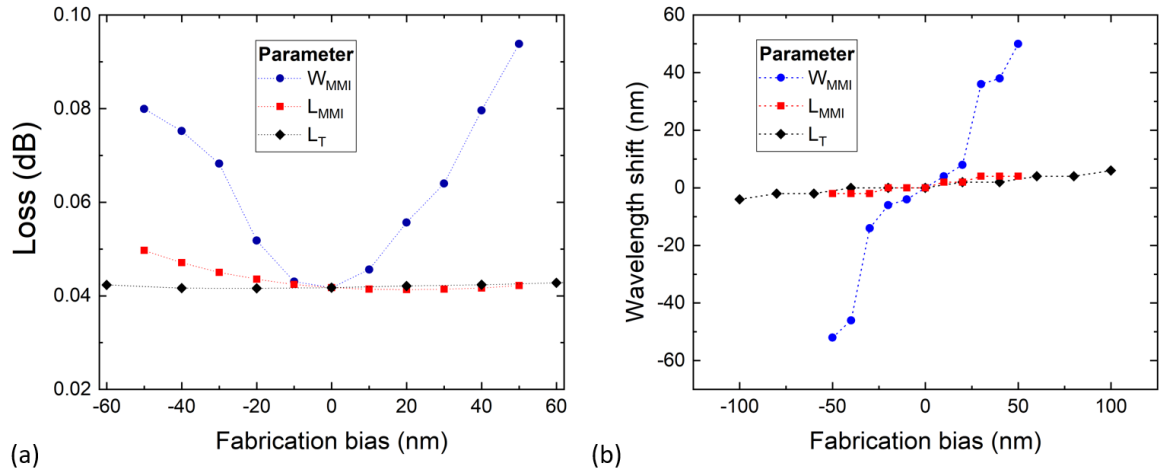

Figure 5.25: Fabrication bias of the multi-mode waveguide crossing. (a) examines the device loss, whilst (b) examines the optimal wavelength shift.

Figure 5.25(a) shows the forward device loss as a function of fabrication bias (change in spatial dimension) for the various structural parameters. All losses are recorded at λ = 1555 nm, corresponding to the optimal wavelength for the designed structure. It can be observed that L_{MMI} and L_T induce small changes in loss, reaching 0.05 dB for a bias of -50 nm on L_{MMI} in the worst case. On the other hand, W_{MMI} largely effects the loss, rising up to 0.1 dB for a bias of +50 nm, and 0.08 dB for a bias of -50 nm. The asymmetry for this parameter is believed to be related to the taper. A smaller W_{MMI} for a constant L_T can be expected to perform better than a larger W_{MMI} due to being more adiabatic (slowly changing n_{eff}). The dominant reason to why changes in W_{MMI} are much less tolerant than changes in L_{MMI} and L_T is because of the change in self-imaging properties based on Equation 2.51. The beat length is dependent on W_{MMI} due to the change of n_{eff} that occurs for the fundamental and first order modes. From Figure 5.10(b), a change in W_{MMI} of -100 nm results in a change in L_B of -0.9 μm for the TE mode. To maintain high performance at 1555 nm, a large change in L_{MMI} would therefore be required. As a result, W_{MMI} is the least tolerant parameter with respect to loss because it is shifting the optimal wavelength of the device. This is confirmed in Figure 5.25(b), where large shifts in wavelength are observed. A fabrication bias of ± 50 nm shifts the optimal wavelength by ± 50 nm. For a fabrication bias of ± 20 nm, wavelength shifts below 20 nm are observed, whilst maintaining good performance < 0.052 dB as shown in Figure 5.25(a). It should be noted that the peak device performance at shifted optimal wavelengths are similar to the zero-bias device (0.042 dB). L_{MMI} and L_T have a negligible contribution to shifting the optimal wavelength, which is expected, since L_T only functions to inject and output the TE mode efficiently, whilst the structural biases explored for L_{MMI} are insignificant compared to the changes in beat length that result from differences in W_{MMI}.

5.6 Comparison with Existing Designs

Crossing designs						
Reference	Insertion loss (dB)	Reflection (dB)	Crosstalk (dB)	Footprint (μm^2)	Fabrication	Material
This work	0.043 (1555 nm)	-35 (Best case -55)	-50	14.3 x 14.3	Single step	SOI, 220 nm Si, 2 μm BOX, air cladding
Celo (2014) [223]	0.11 (1540 nm)	N/A	-45	6.5 x 6.5	Single step	SOI, 220 nm Si, 2 μm BOX, 2.3 μm SiO_2 cladding
Bogaerts (2007) [217]	0.16 (1550 nm)	N/A	-40	6 x 6	Two step	SOI, 220 nm Si, 2 μm BOX, air cladding
Dumais (2017) [163]	0.007 (1550 nm)	N/A	-40	30 x 30	Single step	SOI, 220 nm Si, 2 μm BOX, air cladding
Ma (2013) [224]	0.028 (1550 nm)	-28	-37	9 x 9	Single Step	SOI, 220 nm Si, 2 μm BOX, 2.3 μm SiO_2 cladding

Table 5.1: Comparison of various figures of merit for the device in this work with existing devices. N/A means not quantified.

The optimised design in this work is compared with some existing works in Table 5.1. These include multi-mode interference based designs [223, 224], two-step etched designs using parabolic tapers [217] and 3D gaussian beam synthesis [163]. It can be observed that the crosstalk of the device presented in this chapter performs better than the existing devices. Its insertion loss is only higher than the devices by Dumais and Ma. However, the device by Dumais requires multiple taper structures to efficiently synthesize a Gaussian beam, resulting in a large footprint, and the device by Ma performs worse in backscatter and crosstalk, though it is smaller. It also performs worse in bandwidth, rising to 0.09 dB in a 60 nm range. It is believed that the ultra-low

crosstalk, low loss and large bandwidth performance of the device presented in this work will be necessary for a variety of applications, whilst not being too large to restrict dense integration.

5.7 Conclusions and Suggestions

5.7.1 Conclusions

There are many ways to design a waveguide crossing that can find applications in classical and quantum photonics, enabling the large-scale integration of components. This chapter tells the story of how a low loss waveguide crossing was developed which will be implemented for cavity integrated SNSPDs in Chapter 6. The initial designs show that direct right-angle crossings with SOI strip waveguides possess small footprints, but are accompanied with large loss, crosstalk and backscatter that occur due to waveguide expansion into the crossing region. The associated mode mismatch results in diffraction and reflection. Tapered crossings can reduce the loss but they necessitate large lengths of taper for efficient performance, much akin to the early 1D grating couplers. The large footprint is undesirable for the application of high-density waveguide crossings. The multi-mode interference theory was then used to develop a self-imaging crossing through a set of constraints defined for implementation into a cavity structure for an integrated quantum photonic application. Parameters were swept coarsely in the initial phase to guide to structures that showed promising losses. Then full 3D FDTD was implemented to optimise the structure. It was found that the optimal structure had a footprint of 14.3 x 14.3 μm^2. The structure has 0.042 dB loss at 1555 nm with < -50 dB crosstalk at 1550 nm and -35 dB reflection. The bandwidth of the device is characterised with a worst case loss of 0.07 dB between 1520 and 1580 nm. The device was fabricated and characterised experimentally. The loss of the crossing was measured to be 0.043 ± 0.005 dB at 1555 nm, whilst the best crosstalk was -50.2 dB at 1550 nm. Finally, white light reflectometry was used to characterise the backscatter of the device. In the time domain, no significant observable signals were found when considering 160 waveguide crossings relative to a reference waveguide. In the frequency domain, the wavelength response of a single crossing was characterised to be no worse than -35 dB, whilst showing exceptional performance of -55 dB at 1565 nm. These performance metrics offer high transmission performance when implemented in quantum photonic experiments (to ensure signal and idler photon coincidence count rates are not compromised). The low crosstalk is also important for ensuring a high degree of isolation between signal and idler modes, leading to improved entanglement, whilst the low backscatter will be important for mitigating any counter propagating signals exacerbating unwanted effects in other areas of an experiment such as the single-photon sources. Furthermore, the footprint of this crossing is suitable for implementation in a racetrack cavity, which forms the content of the following chapter.

5.7.2 Suggestions for Further Work

Since sub-wavelength structures have already been discussed in this work for reducing backscatter and reflection in grating coupler structures (Section 2.1.2 of Chapter 2) through creating effective index regions. In addition to this, a sub-wavelength crossing structure has achieved a loss of 0.02 dB, although it is necessary to taper into the sub-wavelength crossing from a standard Si waveguide, inducing losses > 0.2 dB [162]. For the optimal crossing device in this chapter, it appears that the main mechanism for loss in the crossing comes from the crossing region. The index discontinuity from the multi-mode waveguide to the crossing region causes forward transmission losses from backscatter, crosstalk and diffraction. This is explored in a slightly different context in Chapter 6 through changing the size of the perpendicular arm (which for the present discussion can be interpreted as reducing the distance the field propagates in the slab mode before re-entering the multi-mode waveguide region. The present design uses a large multi-mode waveguide region. Figure 5.10(a) suggests that the index discontinuity can be reduced by increasing the width further. However, this will result in two immediate implications. Firstly, for single-mode operation a longer taper will be required for efficient mode conversion, increasing the device footprint. Secondly, given the results of Figure 5.10(b) this approach is not useful for polarisation-independent operation, since smaller W_{MMI} are desirable for a smaller ΔL_B. Given this compromise, an alternative option is to reduce the index discontinuity through decreasing the slab mode n_{eff}. It may be possible to achieve this through implementation of sub-wavelength structures in the crossing region to make a proposed sub-wavelength multi-mode waveguide crossing. This could be done through the use of a periodic block structure with fully etched regions (denoted as Gaps in Figure 5.26). The specific choice of periodic structure is arbitrary and many designs are possible, but the major constraint is that the structure should be four-fold symmetric to preserve the function of the crossing when excited from any of the four ports. The sub-wavelength structure will need its period and fill factor tuned in order to minimise the loss and crosstalk. Using Equation 2.31 in Chapter 2 that describes the average n_{eff} as a function of fill factor, the gaps need to be sufficiently large to index match the local n_{eff} with the multi-mode waveguide. The structure parameters may need to be altered to ensure that the self-imaging effect is preserved. As a confirmation that the introduction of fully-etched regions can improve performance, a right-angle crossing with a footprint of 1 x 1 μm^2 recently experimentally demonstrated insertion losses of 0.3 dB and a crosstalk of -30 dB through using etched holes in the crossing region to create lens-like structures on the order of 100 nm [161]. It should be noted that this structure came out of an inverse design algorithm and the employed design physics is different to this proposal, since their structure is employed for focusing and not index matching. The main drawback of these approaches are that improvement in the performance of the device is met with a high resolution fabrication requirement. It must be noted that a sub-wavelength multi-mode waveguide crossing cannot be utilised with the concept in the next chapter, because it requires a nanowire to be fabricated on top of the crossing.

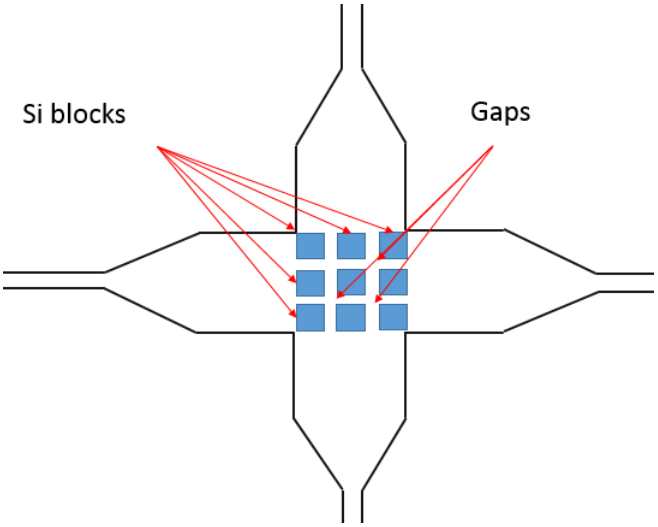

Figure 5.26: Proposed sub-wavelength crossing structure.

CHAPTER 6

Bridging Structures for a Superconducting Nanowire Single-Photon Detector in a Racetrack Cavity

The optimised multi-mode waveguide crossing featured in Chapter 5 is a relatively small device with a low forward loss and crosstalk that can be used for applications in classical and quantum photonics photonics. The work in this chapter shows how this structure can be adapted for use in a specific quantum photonic application. In particular, solving a practical issue with the SNSPD in a racetrack cavity. The multi-mode waveguide crossing is implemented into an SOI racetrack structure, replacing one of the linear regions of the ring resonator. As a result, considerations such as where to place contact pads are considered given constraints such as spatial dimensions from waveguides. Furthermore, the crossing design is modified from the four-fold symmetric design shown in Chapter 5 to be fit for purpose with an SNSPD. This work allows the racetrack SNSPD to be practically realised with no additional fabrication steps to the original design [51]. Investigations into the nanowire absorption in the self-imaging region of the multi-mode waveguide crossing is studied with FDTD and critically coupled designs are presented. Finally, analytics are carried out to quantify the efficiency of the detector in the presence of the crossing. The loss induced by the modified crossing design (0.0125 dB at 1550 nm) does not deteriorate the detection efficiency drastically. Values of over 99% DDE can still be achieved when assuming operation at a saturated I_B (all absorption events lead to detection). Finally, discussions of potential modifications for the ring resonator with a crossing structure that involve manipulation of the multi-mode region for polarisation filtering/insensitivity are discussed. These structures are fabricated and experimentally tested, showing a critical coupling extinction of 24 dB, which is necessary for a high performance detector. It is believed that the structure fabricated on SOI with no nanowire may also have applications in reducing the effects of unwanted polarisation conversion on-chip which originate from various sources such as waveguide bends [225, 226].

6.1 Original Design and Issues

The initial concept and analytics for the SNSPD in a racetrack cavity were carried out by a previous PhD student at QETLabs [51]. As mentioned in Chapter 1, the racetrack cavity is an appealing cavity for the SNSPD, since it is structurally formed from SOI strip waveguides (therefore it can be fabricated in the same step, to contrast with cavities utilising more complex multi-layer fabrication processes such as optical stacks [172, 188]). Similar to the optical filters and work in Chapter 4, the FSR of the cavity can be modified by changing the cavity length, which enables the detector to exhibit various spectral selectivities. This cavity is highly motivating for a detector chip due to its multi-pass nature. When the ring is critically coupled, the light is trapped in the ring on a resonance wavelength. As a result, the photons may make several round-trips in the cavity, enhancing the probability of detection. This particular concept allows high detection efficiencies to be achieved with short nanowires, which is important for improving device yield and performance. The motivation for short nanowires stems from a study that showed degregation in NbN nanowire critical currents as a function of nanowire length, with inhomogeneities existing for length scales as small as 100 nm [53]. Therefore the nanowire should be as small as possible to avoid unwanted performance degradation. The concept is similar to Chapter 4 with some exceptions. For example, only a single ring is considered for the detector, whereas the filter stage can contain multiple rings. Furthermore, the SNSPD nanowire has to be made of superconducting material and whose design has to satisfy various constraints - for example, two nanowires need to be connected by a bend and addressed electrically.

The analytics that were performed in the conceptual paper for the SNSPD consider two 100 nm NbN nanowires of 4.5 nm thickness with a spacing of 100 nm [51]. Critical coupling is investigated and detector efficiencies are quantified in terms of parameters such as the cavity length, pulse width and waveguide loss. The presence of the cavity was found to contribute a geometric jitter and this was studied for various nanowire lengths. However, what was not considered in the work was the practical consideration of routing the nanowire to contact pads, which is essential for the realisation of experimental devices. This motivates the work featured in the rest of this chapter.

6.2 Introducing a Bridging Structure

Generally, since the loss introduced by the electrical connection needs to be minimised, one solution is to use a waveguiding structure (such as a crossing). The crossing enables guiding of the nanowire out to electrical connections that are sufficiently far enough away as to not absorb the propagating mode. It is also important to note that other performance aspects of the detector such as the jitter may also be effected due to the extra size when incorporating the crossing structure. As discussed in Chapter 2 and investigated in great detail in Chapter 5, waveguide

crossings can exist in a variety of geometries. For this chapter, the waveguide crossing is still an in-plane structure like the design in Chapter 5 to retain simplicity of fabrication. Although the implementation of a waveguide crossing is one method of routing out nanowires to contact pads, there may be more ways to achieve it with the racetrack structure. However, only the waveguide crossing implementation is considered in this chapter.

6.2.1 Multi-Mode Waveguide Crossing for an SNSPD

The attributes of a waveguide crossing were listed in Section 5.2 of Chapter 5 for a classical photonics device. These included minimisation of the device loss, crosstalk, backscatter whilst exhibiting broadband operation and small device footprint. These quantities will be compared in the context of classical photonics and an SNSPD in the following paragraphs.

A low device loss is very important for a single-photon detector. As discussed in more detail in Section 6.5, the detection efficiency in the racetrack structure depends on critical coupling, the absorption of the nanowire and loss mechanisms such as scattering and bending losses. The waveguide crossing will have its own loss contribution which will need to be as small as possible. For example, considering the initial investigations into crossing structures, the right-angled crossing shown in Section 5.2.1 of Chapter 5 has a large device loss, making it undesirable for an SNSPD structure. This is shown clearly in Section 6.5.

In the SNSPD it is not necessary for the crosstalk in the waveguide crossing to be minimised if and only if it is at no detriment to the device loss (and therefore the detection efficiency). For comparison, a classical photonic crossing may be part of a switching network [157, 160, 215, 218] or for densely packing structures and therefore low levels of crosstalk are essential if multiple operations are to be addressed simultaneously. In the case of the SNSPD, the waveguide crossing structure is simply for routing nanowires and therefore considerations involving four port device symmetry are relaxed. This is utilised in Section 6.3.

Backscatter will include the contributions from the multi-mode waveguide crossing and the nanowire (which follows similar considerations to Chapter 4). To investigate if resonance-splitting is observed, simulations of the modified cavity structure are shown in Section 6.4.2.

Broadband operation is similarly desirable for quantum photonic applications as it is for classical applications. It is noted that the addition of a multi-mode waveguide crossing will have an effect on aspects of the SNSPD performance such as critical coupling over a broad wavelength range, since the loss term α for the ring resonator will become wavelength-dependent.

Finally, small device footprint is also clearly an important quantity. If this structure is to be

implemented into a racetrack ring resonator then it is essential for the structure to be small enough as to not increase the cavity length drastically. This is the most significant drawback of the tapered crossing design in Section 5.2.2 of Chapter 5. The most clear consequence of an extended cavity is that the losses due to absorption and scattering from the silicon waveguide will be larger, meaning that the efficiency will also be compromised. Furthermore, as was investigated in the original paper, the geometric jitter may also be larger when considering larger cavity lengths.

6.2.2 Considering Contact Pads

In waveguide-integrated SNSPDs without a cavity, the nanowires sit on a linear waveguide with a certain length, designed for maximal absorption subject to constraints such as fabrication defects (specifically NbN) and timing jitter. At the end of the waveguide, the nanowires are connected to contact pads. If the racetrack cavity structure is to be modified to incorporate a waveguide crossing region for routing, the first consideration should consider the dimensions of the racetrack. There are two possibilities for routing structure. The first option is to use both perpendicular arms and route the nanowires out to a contact pad both ways. In other words, one of the nanowires is routed towards the empty space in the centre of the cavity. The size of this region is determined largely by the bending radius. For SOI, an optimal bending radius is 10 μm for minimising losses in this region. With 10 μm bend radii in the cavity, the empty space in the closed loop is constrained to roughly 20 μm. This area of 20 x 30 μm^2 is not large enough to support a contact pad, which usually needs to be on the order of 60 x 60 μm^2 to support a ball bond. For this method of routing to work, a very large coupling region and bend radius of SOI waveguide would be required, which would result in a large device footprint with the disadvantages that were given in Section 6.2.1. The alternative is to route both nanowires out of the same port as shown in Figure 6.1. This means the contact pads can be fabricated in the outer region of empty space with no constraints given by the cavity. Two contact pads can be fabricated either side of the waveguide and the nanowire can be tapered to provide sufficient contact. This approach is suitable to get at least one structure per EBL writefield (based on the VOYAGER writefield size of 500 x 500 μm^2) and to enable flexible tuning of the cavity dimensions to suit the resonance properties required. Although not shown in the figure, extra considerations may be required to avoid latching (an issue where the SNSPD fails to restore superconductivity) [227]. Other works have addressed this issue through the addition of a resistor in parallel [228], or a series attenuator [229] in the electrical circuit.

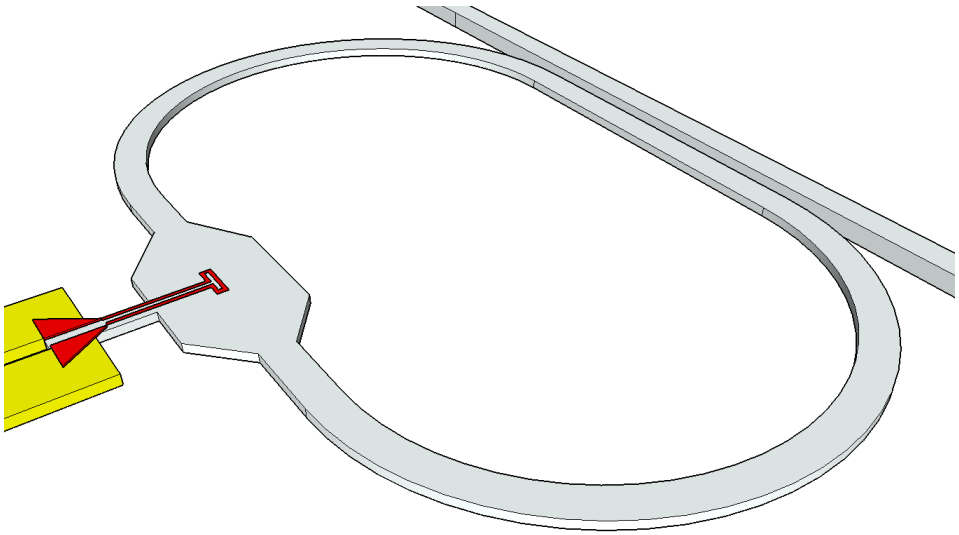

Figure 6.1: Schematic of the modified SNSPD structure. The waveguide crossing structure is three ports, and routes the nanowires (red) to gold contacts.

6.3 Modifications to the Multi-Mode Waveguide Crossing Design

6.3.1 Reducing Vertical Arm Length

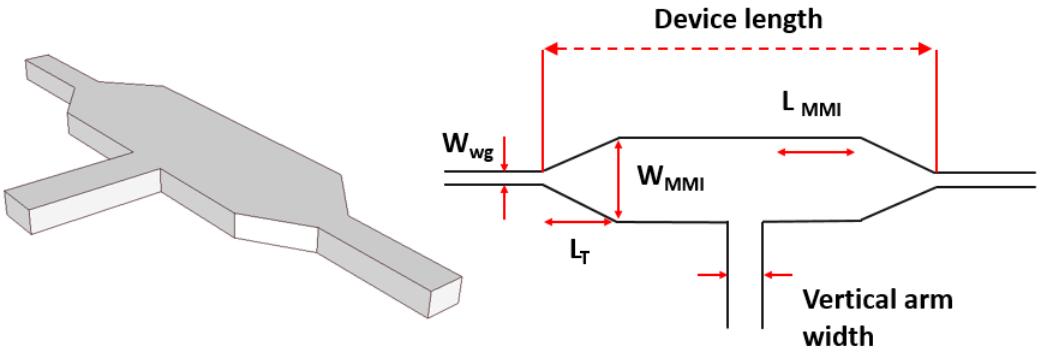

Figure 6.2: (Left) Schematic of the SNSPD waveguide crossing (device only). (Right) parameters relevant to the modified SNSPD crossing.

As discussed in Section 6.2.2, the best approach is to utilise a three port MMI waveguide crossing, shown in Figure 6.2. In Chapter 5 the crosstalk evolution was shown to change from -28 dB to less than -47 dB when travelling through the perpendicular waveguide through a distance > 10 μm, corresponding to the length of the crossing. As discussed in Section 6.2.1, a compromise in crosstalk for reduction in the length of the perpendicular waveguide (now referred to as the vertical arm according to the parametrisation in Figure 6.2) is favourable. Since this arm does not have to be symmetric, it can be reduced down to a small length (1 μm from the original 14.3 μm) which should result in a large reduction in the timing jitter contribution from kinetic inductance. The vertical arm width remains the same as was given for the optimised multi-mode waveguide crossing device in Chapter 5 i.e. W_{MMI} = 1.9 μm. In terms of fabrication considerations such as alignment of nanowires onto a waveguide, this leaves a large region where an SNSPD can be patterned. Specifically, for two 100 nm wide nanowires separated by 100 nm, there is more than 1.5 μm of alignment tolerance if the nanowires are patterned centrally. Given the alignment accuracy specifications of the VOYAGER system in Chapter 3, this can be made much smaller, which leads on to the next modification.

6.3.2 Reducing Perpendicular Waveguide Width

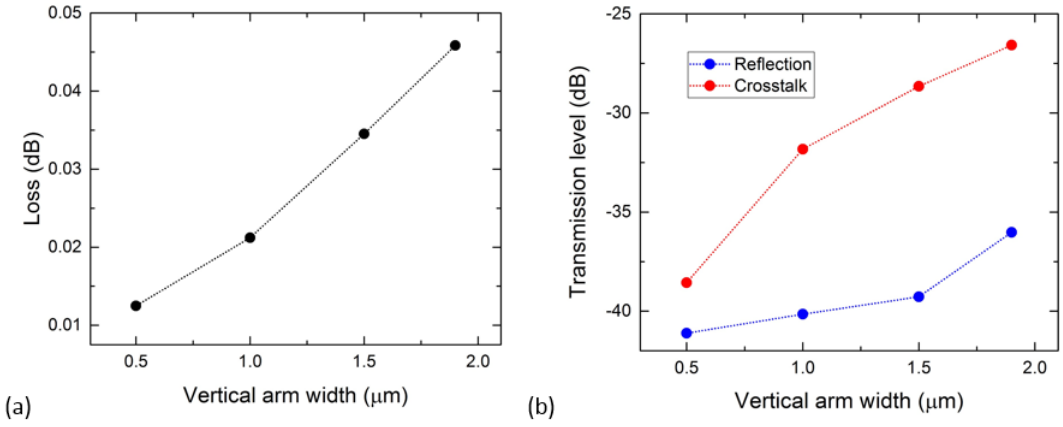

Figure 6.3: Influence of the vertical arm width on (a) device loss and (b) reflection and crosstalk of the crossing device.

Since the vertical arm in the crossing region is not being used to route photons, it is possible to reduce its size from the previously considered structure whilst maintaining sufficient alignment tolerance for fabrication. The results of reducing the vertical arm width are shown in Figure 6.3. These results are optimised - after reducing the vertical arm width, the multi-mode length L_{MMI} was swept to find the lowest loss at 1550 nm. As a result, the device length increased, with the largest device length being 14.8 μm with a vertical arm width of 500 nm. This is explained in

terms of the crossing dynamics changing when the vertical arm width is made smaller. As a result, the field spends less time in the slab mode because it travels a shorter distance in this mode. As a result, the self-imaging point changes and has to be re-optimised for 1550 nm operation. In Figure 6.3(a) it can be observed that a reduction in the vertical arm width results in a reduction of the device loss, reaching 0.0125 dB at a wavelength of 1550 nm when the vertical arm is reduced to 500 nm. Vertical arm widths below 500 nm were not considered due the alignment tolerance. For example, a vertical arm width of 500 nm gives 140 nm of alignment space given the typical values for nanowires already considered. However, in the case that a 500 nm vertical arm is also too small, it can be made larger at the expense of extra device loss (i.e. 0.021 dB with a vertical arm width of 1 μm). From Figure 6.3(b) it can be observed that the crosstalk also improves as expected from the slab mode propagation distance argument, from a level of -28 dB to a level of -38 dB with a 500 nm vertical waveguide when measured 1 μm into the vertical waveguide region. As a side note, this suggests that a large fraction of the loss in the MMI crossing comes from the crossing region, motivating the incorporation of an index-matched region in the crossing region which was suggested in Chapter 5.

6.4 Investigation of the Absorption and Critical Coupling

The theory of self-imaging in the MMI waveguide crossing is well known [146]. However, the use of the MMI crossing region to design a detector is to my knowledge a concept that has not been explored. In Chapter 5, Figure 5.15(a) showed the evolution of the field through the crossing region whilst Figure 5.15(b) showed the electric field profile in the crossing centre. This provides a good place to begin discussion of where the nanowire should be placed. From the absorption analysis for nanowires on a waveguide shown in Figure 4.6 of Chapter 4, it was observed that a larger waveguide width results in a lower peak absorption (corresponding to placement of the nanowires in the centre of the waveguide), but with a greater tolerance to alignment, since the electric field of the TE mode is distributed over a larger width and has shallower gradients. The reduced absorption at the peak is also desirable for the racetrack cavity from the aspect of being able to design critically coupled detectors with various FWHM. The main aspect of designing absorption in the self-imaging region that needs to be considered (relative to the designs for low Q-factor filters using nanowires in Chapter 4) is the evolution of the field as it is propagating in the crossing. It is not possible to model the absorption simply as a $\eta + ik$ material, resulting in a loss coefficient per unit length i.e. a_{nw} and then multiplied by a length i.e. L_{nw} because the absorption coefficient is changing as a function of position in the crossing region. The next section shows how modelling the absorption was achieved when using 5 nm NbN with the refractive index given in Chapter 4.

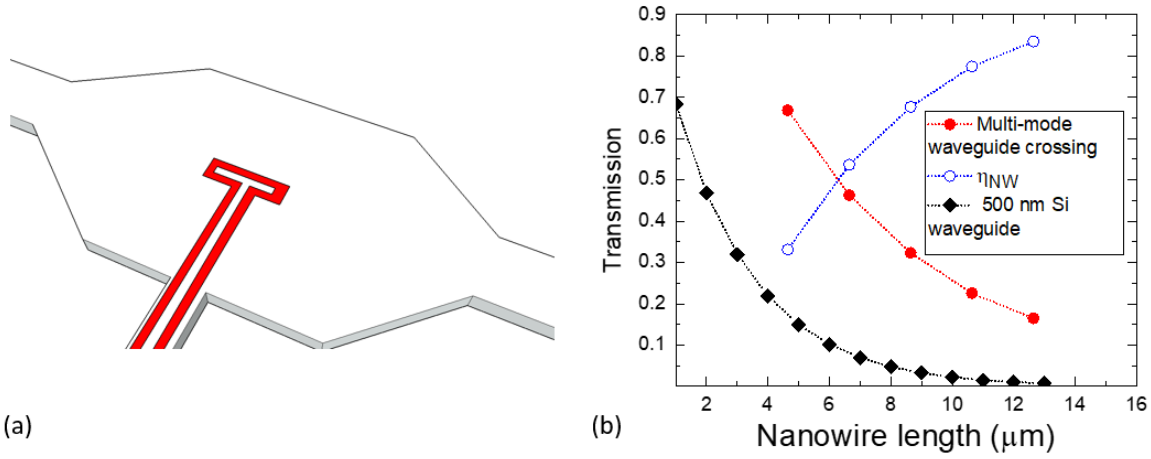

Figure 6.4: (a) Simulated structure. Red represents the nanowire. (b) absorption analysis for various nanowire lengths.

6.4.1 Absorption

Since the vertical arm is placed at the self-imaging point of the fundamental TE mode, the shortest nanowires can be placed here. The design that was conceived is shown in Figure 6.4(a). It must be noted at this point that the schematic is representative of what is modelled due to issues with Lumerical software in constructing 100 nm bend radius for the nanowires. Although this results in an offset, it is not expected to be significant to the result given that the straight sections of the nanowire are relatively much longer and therefore contribute much more to the overall absorption. Two nanowires come from the vertical arm and travel straight towards the crossing centre. There are 90 degree bends for both nanowires with 100 nm bend radius that extend in both directions of the multi-mode waveguide region before reaching a 180 degree bend of radius 100 nm to make a nanowire on the crossing centre. The nanowire length on the crossing centre was varied from 1 μm to 5 μm, whilst the extent of the nanowires into the vertical arm was 300 nm to capture any extra absorption contributions from the field when travelling in the slab mode. This resulted in nanowires with lengths between 4.7 μm and 12.7 μm. Given the field profile is broad, it is also possible to design shorter nanowires in this region. For example the two nanowires can come into the crossing region and connect by a simple 180 degree bend. However, all considerations in this work are based on the design given in Figure 6.4(a).

Full 3D FDTD was used to study the absorption through the crossing region. Like in Chapter 4, the introduction of a nanowire on the waveguide results in a local perturbation of n_{eff} which will have a small effect on the overall native MMI transmission properties. However, this was not considered in this study. Four different lengths of nanowire were studied and their absorption is plotted in Figure 6.4(b). It can be observed that there is an exponential decay in transmission,

similar to what would be expected in a case with a constant loss coefficient like in the Beer-Lambert law. The transmission values with this structure range from 0.66 for the smallest nanowire (4.7 μm) to 0.16 for the largest nanowire (12.7 μm). The probability of absorption by the nanowire n_{NW} can be deduced simply as the transmission through the crossing in the absence of a nanowire (i.e. considering the 0.0125 dB loss which is equivalent to a transmission of 0.997) minus the loss caused by the nanowire. This quantity will be important later in Section 6.5. For comparison, modelling results for two 100 nm wide, 5 nm thick NbN nanowires placed equidstant from the centre of a standard 500 nm silicon waveguide are included. The absorption in this case is much greater due to the confinement of the mode. For example, 2 μm long nanowires on athe 500 nm Si waveguide have similar absorption to a 6.7 μm nanowire placed on the multi-mode waveguide crossing.

6.4.2 Critical Coupling

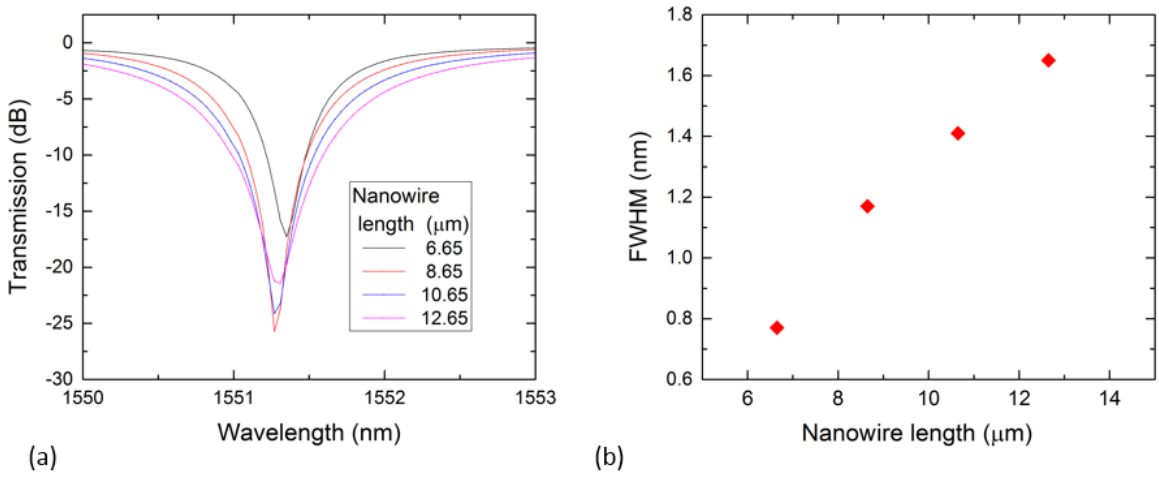

Figure 6.5: Critically coupled SNSPD designs. (a) shows the critically coupled resonance and (b) shows the associated FWHM.

The crossing structure was implemented into a racetrack cavity for simulation in MODE solutions. To achieve this, the length of the structure needs to be considered. Given the footprint of the modified crossing is 14.8 μm, this means that the coupling region has to also be increased. For the originally proposed cavity with 10 μm bend radii with a 10 μm coupling region, the presence of the crossing structure increases the cavity by 9.6 μm, resulting in a cavity length of 92.5 μm. The nanowire designs from Section 6.4.1 were used and the bus-ring waveguide gap was swept to find critical coupling. Figure 6.5(a) shows the critically coupled spectra beyond 15 dB extinction for various nanowire designs. It is suspected that the smallest nanowire design had similar issues with critical coupling in simulation to the small nanowires used in Chapter 4

for the low Q-factor filters where low extinctions were observed. The best observed extinction was 27 dB for the longest nanowire and the worst case was 16.8 dB, whilst the other two designs achieved > 20 dB. An associated range of FWHM from 0.8 nm to 1.8 nm were calculated from the resonances and shown in Figure 6.5(b). This observation is also expected according to the ring resonator equations in Chapter 2.

6.4.3 Geometrical Jitter

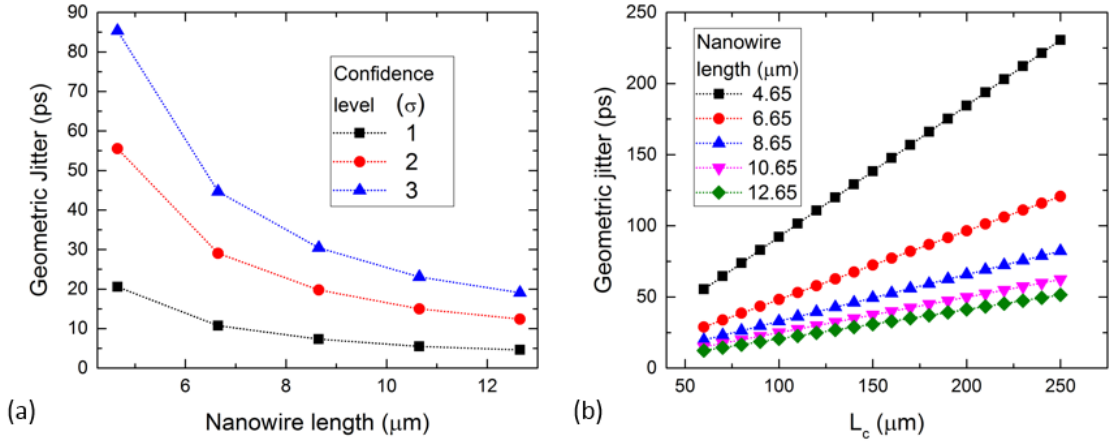

Figure 6.6: Jitter calculations. (a) shows the geometrical jitter for the designs considered in Section 6.4.1 for a fixed 92.5 μm cavity. (b) shows the effect of increasing cavity length for the nanowire designs considered in this chapter and are calculated for 3σ confidence interval.

A study of the geometrical jitter contribution from the racetrack resonator was carried out based on the modified SNSPD structure. This contribution can be considered as the number of round trips made to reach a certain confidence level σ of absorption with the time taken for a round trip and is given by:

$$\Delta t = N(\sigma)\frac{< n_{eff} > L_c}{c}. \tag{6.1}$$

Where N is the number of round trips the pulse makes in the cavity, c is the speed of light, $< n_{eff} >$ represents the weighted average of the effective index of the waveguide mode in the ring (considering that the pulse travels through the crossing region and in the 500 nm SOI waveguide at different effective indices) and L_c is the length of the cavity as defined previously. $< n_{eff} >$ is considered first by considering effective index in the crossing region $n_{eff,c}$. A value of 2.64 is calculated through considering the weighted average of the effective index in each section. Since a linear taper was used, the average of the effective index in the Si waveguide (2.38) and the

start of the multi-mode waveguide (2.8) were considered, yielding a value of 2.59 in the taper section. The slab mode was considered as 2.82. Using these n_{eff} with the respective distances in each section yields $n_{eff,c}$ = 2.64. It is noted that this calculation does not take into account the field evolution between TE_{00} and TE_{01} in the multi-mode waveguide and its effect on $n_{eff,c}$ in this region, but instead considers the field as TE_{00}. This overall is slightly unfavourable, since TE_{00} has a larger effective index than TE_{01}. To calculate $< n_{eff} >$ another weighted average was used according to:

$$< n_{eff} >= \frac{(L_c - L_{cross})n_{eff} + L_{cross}n_{eff,c}}{L_c}, \tag{6.2}$$

where L_{cross} is the crossing device length (14.8 μm). For L_c = 92.5 μm, this yields $< n_{eff} >=$ 2.42. Considering this value relative to n_{eff}, the resulting increase is less than 1.7% and therefore the crossing structure itself does not contribute significantly to the geometrical jitter according to Equation 6.1. Although it is neglected in this work, the presence of the nanowire will also modify $< n_{eff} >$, which could explain the cavity shifts of the peaks given in Figure 6.5(a). Figure 6.6(a) shows the geometric timing jitter calculated with Equation 6.1 for one to three σ probabilities (representing 66%, 95% and 99% confidence intervals) that the photon has been absorbed for each length of nanowire considered in Section 6.4.1. It can be observed that larger nanowires induce a smaller contribution to the geometric jitter. This observation is explained by considering that the ring round trip transmission coefficient is α and the number of round trips to reach a certain transmission level T (which is related to the confidence interval) is therefore given by α^N. α considers the loss of the crossing and the absorption of the nanowire per round trip. However, the crossing loss is constant and α is reduced with a longer nanowire, meaning that T is reached faster for larger nanowires. This is equivalent to making the statement that a larger nanowire results in a lower Q-factor cavity, which is interpreted as a reduction in the photon lifetime in the cavity. As shown in Figure 6.6(a), the geometric jitter increases when considering higher confidence intervals, but reaches no larger than 90 ps with the shortest nanowires. The values differ compared to the results in the original paper (the values calculated here are larger) and this is due to a combination of factors such as the change in n_{eff}, the increase in cavity length as a result of placing the crossing region into the racetrack and most importantly the difference in absorption when using the self-imaging region of the MMI relative to a placing the nanowires on top of a 500 nm Si waveguide. Figure 6.6(b) is shown to emphasise the effect of the cavity length on the jitter and is calculated with a 3σ interval. The trends for various nanowire lengths can be explained by previous arguments of increased absorption resulting in less round trips. However, if L_c is changed for a particular application (for example, to tune the ring FSR and the FWHM) then the cavities contribution to the timing jitter also needs to be considered.

6.5 Analytics

In the original paper the derivation of the equation which describes the system detection efficiency (SDE) was considered [51]. The use of SDE in this paper is not correct, since the concept is theoretical and does not require consideration of losses associated with fibre-to-chip coupling. The device detection efficiency (DDE) is more appropriate for this work, since the device consists of all on-chip elements (bus waveguide, ring waveguide and detector). For this section, the analytics will only be carried out for considerations from this chapter. The DDE of the racetrack SNSPD when on a cavity resonance peak is given by:

$$DDE = (1-(\frac{\alpha - t}{1-\alpha t})^2)\frac{(1-\eta_{Si,beg})\eta_{nw}}{1-(1-\eta_{nw})(1-\eta_{Si})}, \tag{6.3}$$

where t and α carry their original meanings from Chapters 2 and 4. As noted in Section 6.4.3, the α term now has a contribution from the crossing device loss, which provides a small contribution to the overall cavity losses - and therefore the critical coupling. Equation 6.3 can be considered as two overall factors. The first term is the critical coupling term, which can be considered as the degree to which light is trapped in the cavity, and the second term describes the probabilities of detecting or losing the photon. $\eta_{Si,beg}$ represents the probability of the Si waveguide absorbing the photon on the first round trip from entering the cavity to the detector region. η_{nw} is the probability of the nanowire absorbing the photon per round trip, which was investigated with FDTD in Section 6.4.1, and η_{Si} is the probability of losing a photon from losses in the Si waveguide that occur from fabrication-based mechanisms such as surface roughness as described in Chapter 2. For the structure originally presented by Tyler, this was calculated as $\eta_{Si} = 1 - 10^{-\frac{a_{Si}L_c}{10}}$. However, what must be included for the present design is the loss from the crossing structure, which transforms as:

$$\eta_{Si} = 1 - 10^{-(\frac{a_{Si}(L_c - L_{cross}) + a_c)}{10}}, \tag{6.4}$$

where L_{cross} is the length of the crossing region (14.8 μm) and a_c is the loss from crossing region, as was calculated in Section 6.3. Calculations of the detection efficiency are all performed assuming 100% internal efficiency. This means that all absorbed photons are registered as counts, which is a signature of device operation in the deterministic regime (a saturated detection efficiency). Furthermore, unless stated otherwise, all calculations use the optimised loss crossing (500 nm vertical arm width with 0.0125 dB device loss).

6.5.1 Quantifying the Impact of Crossing Device Loss on Detection Efficiency

To contextualise the importance of crossing device loss optimisation that has been performed in Chapter 5 and Section 6.3 of this chapter (as motivated for this context in Section 6.2.1),

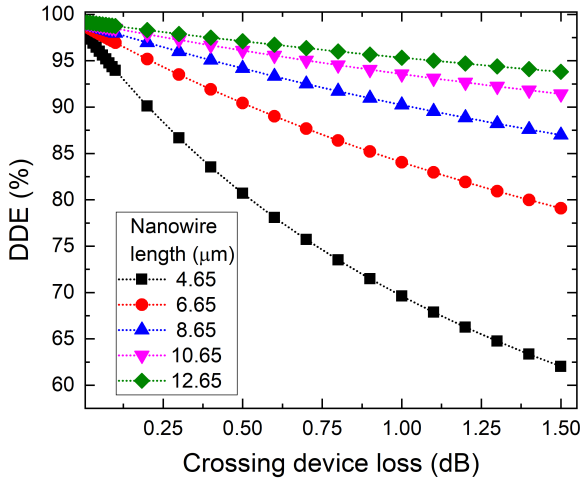

Figure 6.7: Analytically calculated DDE for 25 dB critical coupling and 3 dB/cm waveguide losses for various nanowire lengths.

Figure 6.7 shows the DDE as a function of the crossing device loss plotted from 0.01 dB to 1.5 dB. These calculations were performed with a 25 dB critical coupling level (which has been shown to be achievable in this work and other studies [230]) and waveguide losses of 3 dB/cm based on previous experimental demonstrations with SOI wire waveguides and foundry values [80, 231]. It is clear here that shorter nanowire designs drop off in efficiency much more rapidly than longer nanowires. For a fixed η_{Si} and critical coupling condition, a longer nanowire will have a larger probability of absorption per round trip, which reduces the number of round trips the photon has to make before it is detected. This argument shows the importance of optimising the crossing device for shorter nanowires.

Figure 6.8(a) plots the DDE as a function of nanowire length for the various routing structures that have been investigated in this thesis. The structures that are compared are the 500 nm waveguide width right-angle crossing, the best performing tapered crossing, the optimised multi-mode waveguide crossing (named 4 port crossing) and the modified device in this chapter (named 3 port SNSPD crossing). It is clear that the high losses from the tapered and right-angle crossings restrict the best obtainable DDE to 95%. However, increasing the nanowire length beyond the largest value given here will risk fabrication defects. Also, if the nanowire length is too long, the presence of a cavity becomes less relevant since the majority of the absorption occurs in a single round trip, similarly to a waveguide-integrated detector on a linear waveguide. The multi-mode waveguide designs are shown in Figure 6.8(b) for DDE values between 95% and 100%. Whilst both devices can perform above 96 % DDE with the smallest nanowire, the optimised 3 port SNSPD crossing can obtain an DDE above 99% for nanowires above 10 μm. These results suggest

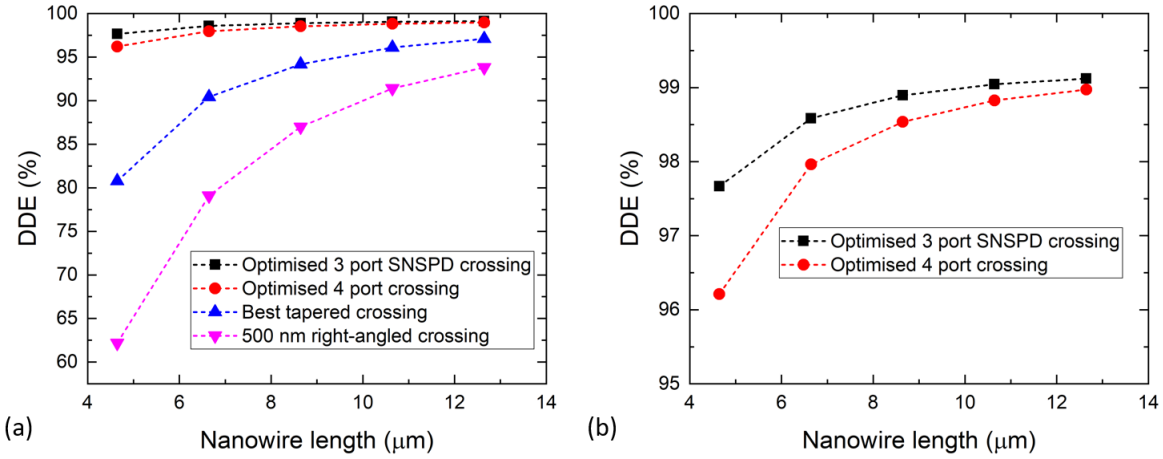

Figure 6.8: (a) DDE as a function of nanowire length for the various designs presented in this thesis. (b) compares the multi-mode waveguide crossing devices in a finer range of 95 % < DDE < 100 %.

that the racetrack SNSPD with a low-loss routing structure can be competitive with other cavities that have demonstrated efficiencies above 90 % [172, 232].

6.5.2 Detection Efficiency with the Optimised Crossing

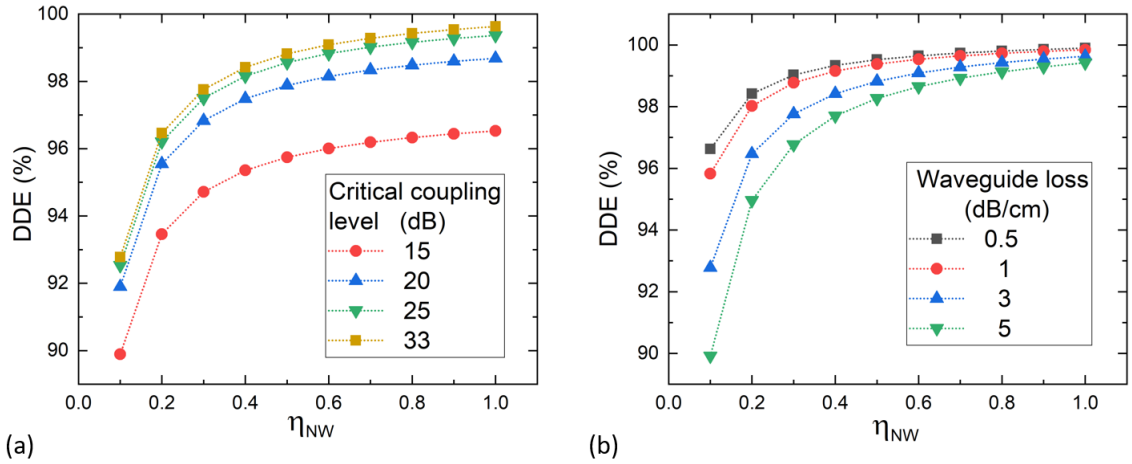

Figure 6.9: DDE as a function of η_{NW} for (a) various critical coupling levels, with a waveguide loss of 3 dB/cm and (b) various waveguide losses with a critical coupling level of 33 dB.

The previous section illustrated the importance of the waveguide crossing device loss by calculating the DDE based on realistic experimental parameters for the various lengths of nanowire and crossing devices presented in this chapter and Chapter 5. In this section, the effects of critical coupling and waveguide losses on the DDE are now studied in the same 92.5

μm cavity. For this section, the optimised 3 port SNSPD crossing is used. A critical coupling level of 33 dB has been experimentally demonstrated [233]. This level was also observed for the low Q-factor filters in Chapter 4, which will now be considered as the upper bound. In terms of waveguide losses, two studies have experimentally demonstrated waveguide losses below 1 dB/cm in SOI wire waveguides [234, 235] and so losses as small as 0.5 dB/cm will be considered for this analysis. Figure 6.9(a) shows how the DDE varies with η_{NW} for critical coupling levels of 15, 20, 25 and 33 dB. η_{NW} is proportional to the geometry of the nanowire. An example of this was demonstrated with the effect of nanowire length on η_{NW} in Figure 6.4(b), but the nanowire width and thickness may also be adjusted, or the design of the absorber in the self-imaging region. It can be observed that for 15 dB of critical coupling, the DDE saturates at around 96 % for $\eta_{NW} > 0.7$. This indicates that the critical coupling level is limiting the DDE. For a given η_{NW}, critical coupling level increases results in an increase of DDE with drastic improvements. For example, at a critical coupling level of 25 dB, an DDE of 99% is achieved for $\eta_{NW} > 0.7$. This reduces to $\eta_{NW} > 0.6$ for a critical coupling level of 33 dB. However, it can be observed that the rate of DDE increase with critical coupling decreases for all η_{NW}, suggesting that at critical coupling levels better than 20 dB, the limitation to the DDE is coming from losses due to the Si waveguide and the crossing. This explains the reason why a 15 dB critical coupling level cannot achieve efficiencies beyond 96 %, since 15 dB of critical coupling results in 3% of the field passing through the bus-waveguide, limiting the detector to seeing 96.8% of the input power. The critical coupling level therefore needs to be greater than 20 dB for achieving DDE better than 99 %. Figure 6.9(b) studies the DDE as a function of the Si waveguide loss for 33 dB critical coupling. For waveguide losses up to 5 dB/cm, detection efficiencies above 95% can be realised for $\eta_{NW} > 0.2$, which would correspond to a smaller nanowires (< 4.5 μm) based on the results of Figure 6.4(b). In terms of high DDE, it is not possible to realise 99% DDE with 5 dB/cm waveguide losses for this 92.5 μm length cavity. For waveguide losses of 0.5 and 1 dB/cm, detection efficiencies over 95 % can be realised for $\eta_{NW} = 0.1$, whilst DDEs over 99 % are obtained at $\eta_{NW} \geq 0.4$. The reduction in waveguide loss decreases the magnitudes of η_{Si} and $\eta_{Si,beg}$, allowing designs with smaller, less absorptive nanowires to still perform with high DDE. However, there will be a trade-off in the overall performance as the geometric timing jitter contribution will become more significant, as was shown in Section 6.4.3.

6.6 Further Considerations

In this section, two manipulations are discussed which involve the use of multi-mode waveguide region adapted from this chapter for filtering applications or a 2 x 2 multi-mode interference waveguide for broadband SNSPD operation.

6.6.1 Multi-Mode Waveguide Crossing in a Racetrack Resonator for Polarisation Filtering

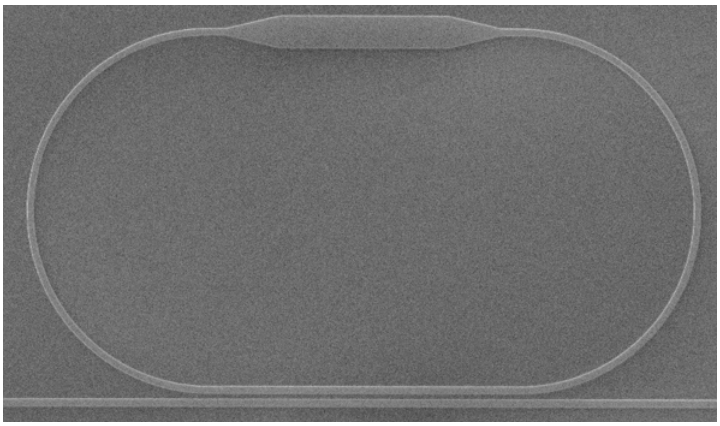

Figure 6.10: SEM image of a high Q-factor MMI all-pass ring resonator

An alternative method to the high Q-factor filtering demonstrated by Cantarella et al.[45] which does not require a heater to be fabricated 1 μm above the resonator is to utilise the waveguide crossing structure developed in this work and to fabricate it similarly to the SNSPD, but without the vertical arm as to minimise device losses. An SEM image of the fabricated device from SOI Chip-2 is shown in Figure 6.10. The concept involves designing the multi-mode waveguide to accept TE and reject TM. When considering the four-port optimised multi-mode waveguide crossing in Chapter 5, the TE loss was 0.045 dB at 1550 nm whilst the TM loss was near 1 dB. The structure therefore can add some polarisation-dependent filtering and provide rejection of TM light. For comparison, in Cantarella's work the TM propagation losses were measured to be 60 dB/cm with the heater above the waveguide. To achieve a TM loss of 1 dB, the heater would have to be 1.66 mm long, or placed closer to the waveguide, which would introduce TE propagation losses. Furthermore, other MMI designs with polarisation extinction ratios above 10 dB have been demonstrated (See Section 2.1.5 of Chapter 2), which suggests that the TM rejection can be improved.

6.6.1.1 Experimental Characterisation

In SOI Chip-2, racetrack resonators with the multi-mode waveguide region were compared to standard racetrack resonators (with no multi-mode waveguide region) with an equal coupling region for comparison. Figure 6.11(a) shows an experimentally measured transmission spectrum for the ring resonator with the multi-mode waveguide region, where critical coupling is observed with a bus-ring waveguide gap of 200 nm. The critically coupled peaks occur in the range of 1535 $< \lambda <$ 1550 nm and are shown in Figure 6.11(b). In this case, both critically coupled peaks show extinctions of 23-25 dB. This justifies the choice of a 25 dB critical coupling level for the DDE

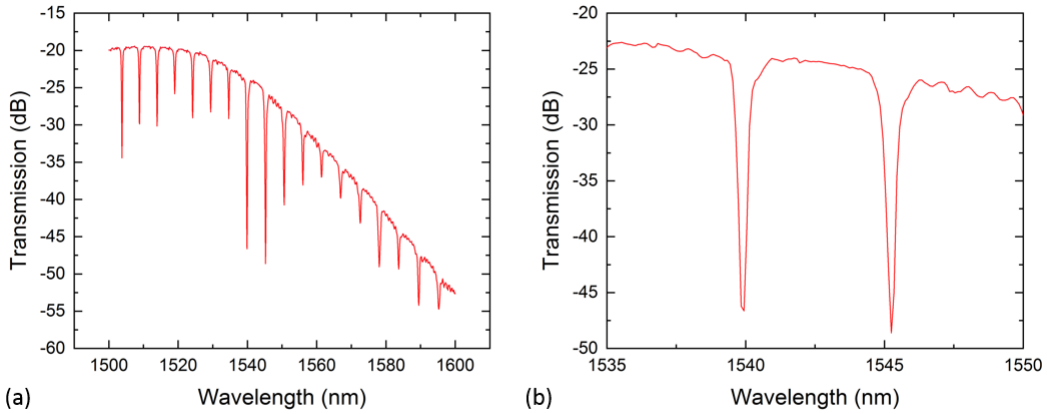

Figure 6.11: Transmission spectrum of racetrack resonator with multi-mode waveguide region. (a) shows the full spectrum whilst (b) shows the two critically coupled peaks between 1535 and 1550 nm.

calculations in Figure 6.5, since the structure is representative of the SNSPD design as shown in Figure 6.1 but without the vertical arm and a nanowire. There is optimism about an improvement in the critical coupling level for two reasons. The first consideration is that the inclusion of a nanowire reduces the Q-factor of the system, which leads to a broader critical coupling curves (as was shown in Figures 4.9(a) and 4.9(b) in Chapter 4). The second consideration is that the bus-ring waveguide gap was swept in steps of 20 nm, which could be made finer. Figure 6.12(a) and 6.12(b) show the FWHM and calculated experimental Q-factor as a function of the bus-ring waveguide gap for a standard racetrack and the racetrack with the multi-mode waveguide respectively. The error bars shown for each bus-ring waveguide gap are from N=9 different devices with peaks close to 1520 nm. In general, the data suggests that the multi-mode waveguide has a small effect on the Q-factor. However, it is difficult to quantify the exact amount given the issues with the chip (discussed in Chapter 3), since there are issues with fabricated Euler waveguide bends having widths below 380 nm, which are thought to be the reason for the large error bars. To improve the analysis, regular bends should be used and the same structures should be fabricated on a new run with the XR1541-006 resist. Furthermore, if possible, extra structures with larger TE/TM polarisation rejection multi-mode waveguide regions should also be compared. In all cases the measurements for these structures should include higher order linear cascades of rings to characterise the high extinction regime performance.

6.6.2 Achieving Broadband SNSPD Response

The addition of a multi-mode waveguide crossing into the SNSPD structure introduces a wavelength-dependent loss contribution to the ring, i.e. $\alpha(\lambda)$. However, as was characterised in

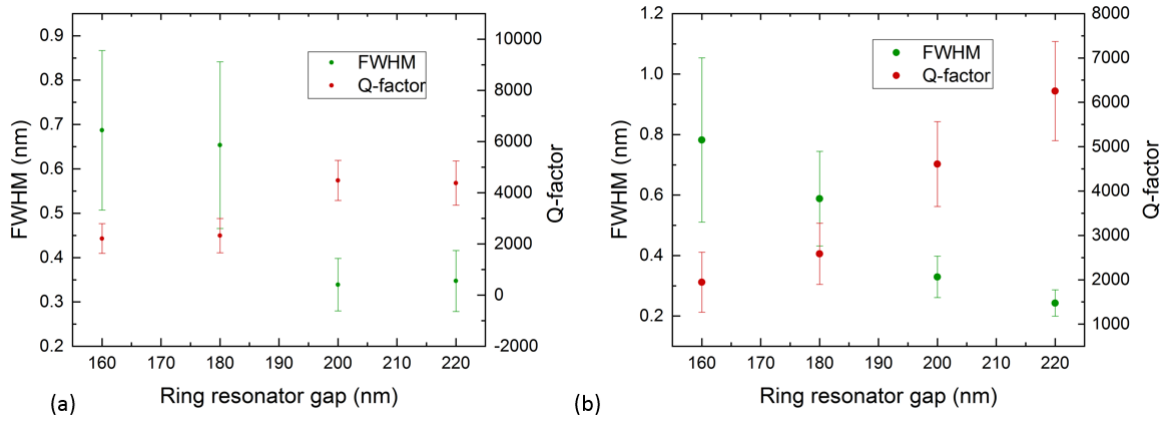

Figure 6.12: Comparing Q-factors of racetrack resonators without (a) and with (b) the multi-mode waveguide region.

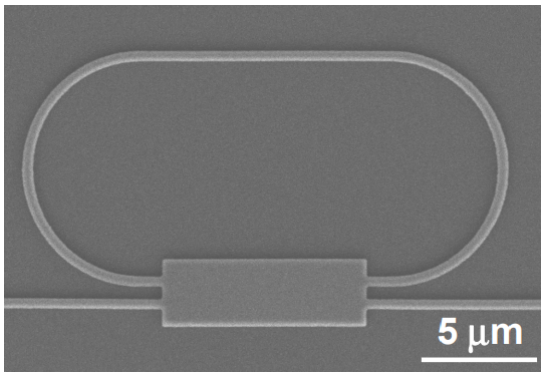

Figure 6.13: SEM image of a racetrack resonator with multi-mode interference region implemented in the coupling region. Originally presented in [230].

Figure 5.14 of Chapter 5, the loss of the crossing showed good operation over a 60 nm bandwidth with a worst case loss of 0.07 dB. The use of an evanescent coupler for the racetrack gives a well defined coupling coefficient t. However, its variation with wavelength is more significant than α, which means that a desired critical coupling level cannot be guaranteed for a given wavelength range. Therefore, reduced performance can be expected when operating away from the originally designed wavelength (to understand the effect in this case, the impact of variation in critical coupling on detection efficiency can be observed in Figure 6.9(a) when considering a fixed η_{nw}). One proposed modification is to use a 2 x 2 multi-mode interference waveguide as the coupling region. This was demonstrated by Xu et al. from the Ottawa group in 2007 [230] and shows that critical coupling can be achieved over a much broader wavelength range. Figure 6.13 shows an SEM image of the fabricated structure, whilst Figures 6.14(a) and 6.14(b) show the experimental transmission spectra of the ring with an evanescent coupler and multi-mode waveguide coupler respectively. It is clear that the critical coupling is satisfied for a much larger

range of wavelengths, which is a valuable addition for the SNSPD presented in this chapter. The only drawback to this implementation is that the efficiency may be compromised if the loss of this device is significant. Like the crossing structure in this chapter, the loss from this coupling region would also have to be considered as an extra term in η_{Si} in Equation 6.3.

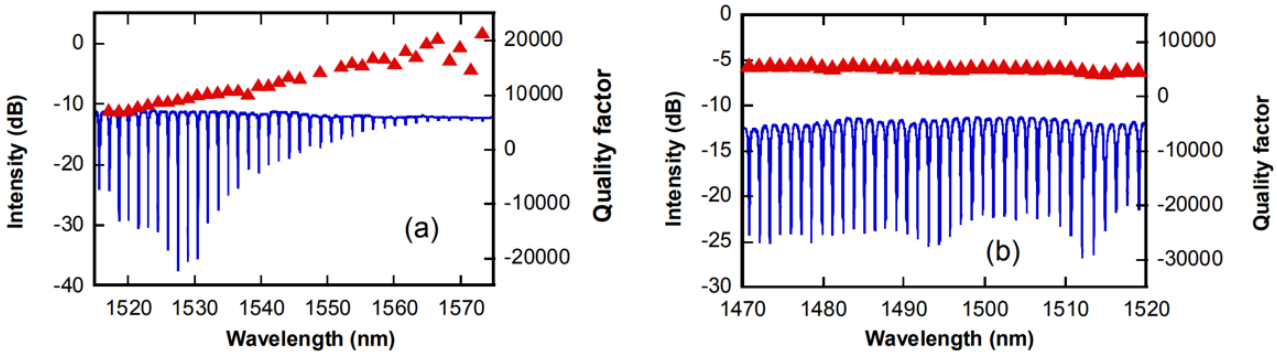

Figure 6.14: Comparing a racetrack resonator with (a) an evanescent coupler and (b) multi-mode interference waveguide for the coupling region. Graphs from [230]. The data in blue is the relevant data for the discussion in the text.

6.7 Conclusions

Whilst the original concept of the racetrack SNSPD is appealing, it came with a problem that needed to be addressed - the routing of a nanowire to contact pads. This can be achieved by using a waveguide crossing structure. However, other considerations also had to be made. One example of such a consideration relates to the steric properties of the cavity and placement of the contact pads. This resulted in a modification of the multi-mode waveguide structure previously optimised for classical applications. The modification consists of removing the four-fold symmetry and closing a port, resulting in a three-port structure. Further modifications were then made based on SNSPD considerations such as reducing the nanowire size (resulting in a reduction in the vertical arm length) and reducing the vertical arm width to improve the loss of the crossing structure. Important concepts such as absorption from the nanowire were revisited, since the inclusion of the crossing structure gives a self-imaging region for designing a detector, functioning differently to the standard situation of a nanowire on a straight waveguide. Due to the larger spatial extent of the electromagnetic field in the multi-mode region, this design shows a greater tolerance with respect to spatial alignment when compared to designing nanowires on a 500 nm Si waveguide. The waveguide crossing was implemented into a racetrack cavity and simulated with FDTD. Critical coupling levels exceeding 20 dB were observed through sweeping the bus-ring waveguide gap, whilst no resonance splittings were observed. Analytics were then considered based on

the waveguide crossing modification and suggest that high detection efficiencies (some of which exceeding 99%) can be achieved with the structure under realistic critical coupling and waveguide losses. The absorption in the multi-mode region is weaker relative to the 500 nm Si waveguide, requiring longer nanowires relative to the original design (although it must be noted that only one meander design was tested in this study). Despite this, detection efficiencies of > 95% can still be achieved with nanowires as small as 4.65 μm. Critical coupling levels > 20 dB were observed on fabricated SOI racetrack resonators with the multi-mode waveguide region. Furthermore, the Q-factors of these structures did not appear to be significantly altered relative to a standard racetrack resonator, which is promising for the realisation of the detector, since these aspects strongly effect the device efficiency. The challenge remains to fully fabricate and experimentally realise a racetrack detector using the modified structure in this chapter, obtaining high detection efficiencies with short nanowires and then implementing the detectors with other schemes.

CHAPTER 7

CONCLUSION

Whilst the realisation of a quantum computer is a desirable technological advancement that promises to transcend our current technologies, it is not without its challenges. For photonic quantum computing, the necessity of high brightness (large numbers of photon pairs produced per second) single-photon sources coupled with low loss circuitry and highly efficient single-photon detectors represents quite a remarkable challenge. Bulk optics could deal with these aspects reasonably well, but at the expense of one crucial and necessary requirement : scalability. Therefore, it is no surprise that the direction of research in this field has steered towards integration on-chip to enable dense photonic integration, packaging and stability with respect to the outside world. Silicon as a material has been a logical and comfortable choice for implementation on-chip, since foundry processes pertaining to silicon electronics can be leveraged, allowing for on-chip electronics, which have been essential for many demonstrations. The progress in integrated photonics has been remarkable in the development and demonstration of on-chip single-photon sources and on-chip single photon detectors, of which some of the latter have achieved detection efficiencies $> 90\%$. In the former case, the limitation of linear and nonlinear loss (such as TPA which was discussed briefly in Chapter 1) can bottleneck the pair generation rate of entangled photons. This already highlights a drawback when using silicon - the limitations of the small band gap. This kind of compromise is common in photonics. As an example, silicon nitride represents a large bandgap material, free from TPA at 1550 nm - which sounds very promising relative to silicon. However, it is a lower index-contrast system than silicon, meaning single-mode waveguides are larger relative to silicon, pertaining to a general size increase across the integrated photonics component toolbox. For this reason, the density of components in a given area is reduced with respect to silicon, decreasing the scalability of this material. It may be possible to implement a scheme where multiple materials are implemented to exploit their respective advantages,

but generally this will add extra complication in fabrication, leading to more sources for error. At the present time, many components have been developed on the SOI platform utilising the benefits outlined above. I will now start to describe challenges relating to the detector aspects of integrated quantum photonics.

Although high efficiency single-photon detectors have been demonstrated, it does not suffice to say the detector aspect of quantum computing is a solved issue. Whilst the performance figures of merit for the SNSPD are already good, they rely on energy to stimulate a phase transition. Since the phase transition is the basis of the detection mechanism in this technology, the SNSPD does not discriminate in wavelength when considering the negligible difference in energy of photons that are spaced apart by 5-10 nm. This highlights a very important requirement in a quantum computer - the requirement of filtering pump light. As described in Chapter 1, 130 dB filtering of the pump is required to bring the pump level down to the level of dark counts in the detector. This is already a large requirement just to ensure the detectors are not flooded with erroneous pump light. Some implementations have achieved 60-66 dB extinction [44, 45], with a recent study achieving 73 dB [215]. Mateusz Piekarek, a colleague of mine, worked on filters for integrated quantum photonics and investigated absorptive carbon paint on the back side of a chip to attempt to suppress scattering [47]. Single-chip improvements in extinction of up to 20 dB were shown by application of carbon paint and using a large spacing between optical ports. Since the crosstalk signal is relative to the input power, this represents a limitation that will need to be overcome to achieve the target of 130 dB pump extinction on a single chip. So far, the best single-chip extinction is 95 dB [46], although the chip was post-processed by removing the silicon substrate [144]. More fundamental understanding of the mechanisms (such as scattering in the substrate) will be required for progress in this area.

A fully-integrated on-chip solution is a long-term goal, but the present direction should be towards concepts that can be demonstrated in the short-term. These function as stepping stones along the path to the long-term goal. This point is where my thesis comes in. Before a fully integrated on-chip solution is possible, there are many other possibilities to explore such as chip-to-chip experiments. In this case, there is a penalty to pay in terms of coupling losses associated with guiding light off and on-chip (to contextualise this, consider the coincidence count rates of 1.16 s^{-1} as a result of approximately 25 dB transmission losses when implementing 100 dB pump extinction in a chip-to-chip experiment [47]). The upside of the chip-to chip approach is its modularity. For example, certain chips can be designed to have specific functionalities. In the case of a detector chip for quantum photonic experiments, this would consist of a method of fibre-to-chip coupling, a pump light filtering stage as well as the detectors themselves. As described in Chapter 1, 100 dB of pump extinction has been achieved in three different chip-to-chip experiments [47, 49, 50], with the extra option of additional off-chip filtering. The chip-to-chip method

could find applications everywhere in quantum photonics, ranging from quantum computation demonstrations to quantum key distribution networks. Some demonstrations have already been performed using the chip-to-chip concept [236, 237].

Chapter 2 provides a detailed showcase of integrated photonic components. The core mechanism for guiding light is described both in terms of a geometrical optics picture and through Maxwell's equations. These concepts are very important for photonic waveguide design, which is a necessary pre-requisite of a quantum engineer for designing integrated photonic platforms. Various integrated photonic components such as grating couplers, directional couplers, ring resonators and multi-mode interference waveguides are discussed. The theory behind their operation is presented, as well as various demonstrations. These tools allow the ability of coupling light on-chip and manipulating it as we desire. Notably, recent grating coupler designs have shown as good as 0.5 dB coupling losses [86, 102], which shows there is excellent potential in chip-to-chip implementations. Other aspects such as sub-wavelength engineering have been explored to reduce footprint, loss and wavelength dependencies in devices [148, 162, 238]. In my opinion, all of these works will push the viability of the technology and add flexibility going forward, since all components need to be considered when meeting the requirements necessary for a photonic quantum computer. Finally, SNSPDs are discussed in terms of their figures of merit, optical coupling methods and cavities. For a detector chip, the waveguide-integrated detector represents an appealing solution due to the confined modes interaction with the nanowire. This allows much greater absorption than a normal incidence detector with a smaller nanowire, which results in smaller jitters and an efficient, high performance on-chip solution.

Chapter 3 discusses the fabrication aspect of the work. Given that the clean room facility at the University of Bristol was not open at the start of this PhD project, this already implied a large challenge. The work in this chapter is not fully reflective of the endless endeavours to develop working process flows. As a personal thought, I would like to think that this was a unique learning opportunity, as opposed to a project where everything was plain sailing (such as getting a chip fabricated by external means). A lot of attention to detail needs to go into the fabrication, and the work here barely scratches the surface of what is required. This is in part due to time, since we received a high quality lithography and etching system towards the second half of the project. If I could continue the work, a proper characterisation of the waveguide losses would be necessary. In the first instance, this was evaluated to be 14.4 dB/mm. It would be interesting to characterise the performance with properly fabricated bends (which I used at the end of the project for characterisation of the waveguide crossing in Chapter 5). Pisu Jiang, a colleague at the University of Bristol, has characterised the waveguides fabricated with the XR-1541 resist and has evaluated them to be on the order of 6-10 dB/cm. I believe that the ring resonators fabricated in both Chapter 3 and Chapter 6 of this work would benefit largely from the XR-1541 fabrication

recipe, or the use of standard bends on the FOx-14 resist but optimised to be 500 nm (through dosing and a larger width design on GDS). Furthermore, I suspect that the performances from these optimised structures will be more reproducible, although they may not reach the level of reproducibility that the CORN02 devices showed in Chapter 4. With time and effort, the maturation of processes in this clean room will lend themselves to high performance circuits for testing and prototyping.

A new type of implementation for ring resonator based filtering on-chip was introduced in Chapter 4. This functions as an extra contribution to filtering pump light on the detector chip end to complement other filtering contributions (for example, a circuit comprising of sources and a Reck scheme may also include its own pump filtering architecture, or off-chip filtering before being routed off-chip). The scheme is based on the use of an absorptive material implemented in a racetrack ring resonator. This functionality is easily contrasted with other existing schemes based on ring resonators. Some approaches simply just utilise critical coupling for pump rejection, whilst others have implementations such as NiCr heaters for TM polarisation rejection [45]. In our group at QETLabs, the grating couplers used in experiments have on the order of 20 dB of polarisation extinction rejection, meaning that TM light reaching off-chip detectors is not usually an issue (although it may be a necessary consideration when considering on-chip detectors, as this will remove the need to direct the signal through a grating). To contrast, this scheme seeks to improve quantum photonic experiments through providing filtering of the pump, but with the added addition of suppressing electric field build up in these cavities. For a quantum photonic experiment, this consideration is desirable, since single-photon source generation rates from SFWM depend quadratically on the input pump power [239]. As a result, the high intensity pump light may also stimulate unwanted pair generation, which would be emphasised in a ring resonator filter. Although the pump light is critically coupled, there is a large build up of electric field (particularly in critically coupled SOI resonators), meaning non-linear processes can occur within the cavity. Signal and idler photons generated here may couple out of the cavity unfiltered and propagate towards the detectors, giving false detection events if they are absorbed. The addition of an absorptive medium within the racetrack provides a reduced build up of cavity (to reduce the cause of the generated photons) whilst also introducing a probability of absorbing the photons themselves on each round trip. Analytically, these low Q-factor filters appear to be more fabrication tolerant with respect to realisation of critical coupling, as observed in Figures 4.9(a) and 4.9(b). This chapter deals with the design of the component - in the context of a detector chip, the absorptive medium is a nanowire of SNSPD material with the same thickness, meaning that it can be fabricated in the same step for simplicity. This was simulated for a variety of parameters, which show how the absorption and backscatter are effected for a variety of realistic situations. Designs were simulated and various FWHM can be realised with the scheme (based on the dimensions of the absorber). Critical couplings of > 15 dB were observed for many different

cavitiy designs. When cascaded in series, > 50 dB extinction was observed. The disadvantages of the scheme are that the pass band loss and bandwidth can be compromised, with a dependence on the size of the absorber. The latter case can be alleviated to some extent by moving to a smaller cavity (for a larger FSR). In two demonstrations, the filters are designed with an FSR twice as big as the source [46, 47]. It could also be possible that only one or two absorptive filters may be required, whilst the rest are simple critically coupled SOI resonators due to the fact that the pump light intensity will be sequentially reduced after passing through each filter. In my opinion, this would be very interesting to work on experimentally although the clean room processes (including sputtering of superconducting material) at the University of Bristol will need to be developed for this work. A demonstration of critical coupling and the various FWHM is a first goal, but the ultimate goal should be to try and prove that unwanted photon pair generation is suppressed in this scheme - highlighting a major advantage over other schemes. This would require comparing a circuit with absorptive low Q-factor ring filters against another filtering architecture which uses standard ring filters. As a possible extra benefit from this scheme, high scattering in SOI circuits has been observed in our group [43]. In the recent 73 dB extinction filtering work, 73 dB was observed whilst 200 dB extinction was predicted [215]. It is possible that the absorptive medium may assist with reducing background noise from scattering. However, extra experiments will need to be performed to verify the stability of resonance shifts (for example, the filter resonances shifting due to the absorber heating). This will need to be examined both at room temperature and at cryogenic temperature to verify the viability of these device when used in practical applications.

The work in Chapter 5 is not an essential component for a detector chip but warrants a large discussion in its own right. Waveguide crossings are important for dense photonic integration and are a crucial part of the integrated photonics toolkit for both classical [240] and quantum applications [43]. In the latter case, waveguide crossings are used in integrated quantum photonics to implement projections of 3D circuits onto 2D planar circuits for linear optical demonstrations [216, 236]. In these demonstrations, path entanglement is achieved by using a waveguide crossing to swap signal and idler photons from independent single-photon sources to bunch them together for performing quantum operations. In a more recent demonstration, more than 100 waveguide crossings were used in quantum information experiments for rerouting signal and idler photons from 16 independent sources for qudit manipulation [20]. For these applications, it is crucial that the loss of the waveguide crossings are low to maximise single-photon count rates. Furthermore, low crosstalk is desirable to avoid unwanted leakages such as signal photons leaking into idler photon channels, reducing the degree of entanglement. Other applications of the waveguide crossing in integrated photonics include neuromorphic computing with photons [241] to enable large-scale routing and photonic fan-out in conjunction with out-of-plane waveguide crossings on many layers [242] that would incur penalties with analogous electrical circuits. Most prominently, they are used in optical switches [158–160, 218, 243]. In the largest case, up to 16 x 10^3 on-chip

waveguide crossings have been implemented in a 128 x 128 port optical switch [160]. In order to obtain full connectivity in an integrated circuit, the required number of waveguide crossings may scale as N^2 [244], where N represents the number of ports. The large numbers of these passive components can have a significant impact on the performance of devices in all of the aforementioned applications. For this reason, the study of waveguide crossings was important, although its main relevance in this thesis was for the work in Chapter 6 (see paragraph below). The multi-mode interference crossing presented here has a footprint of 14.3 x 14.3 μm^2, with an insertion loss of 0.043 dB at 1555 nm and a crosstalk of -50.2 dB at 1550 nm (no worse than -45 dB between 1520 to 1570 nm). To the best of my knowledge, greater performance has only been achieved with crossing structures over 30 x 30 μm^2 [163, 218], which are more than four times larger. On the opposite side of the spectrum, the smallest crossing I am aware of is 1 x 1 μm^2 with an insertion loss of 0.3 dB and crosstalk of -30 dB [161], which is significantly worse performing. As a result, the crossing here represents a middle of the road solution, with good all-round performance metrics. Furthermore, the backscatter was investigated by optical time-domain reflectometry and no significant increase in backscatter was observed with 160 crossings on-chip. This signals good potential in the device, although this was a simple measurement of backscattering on and off the chip. This may not be fully representative of the dynamics of backscattering on the chip itself - which may be important if the backscatter signal returns to an important part of the circuit such as the single-photon sources. This effect may not be prevalent now in smaller demonstrations where the signal propagates through tens of crossings, but may become important in future large-scale experiments. Whilst this thesis investigates the backscattering in more detail than currently existing literature (to the best of my knowledge), more work can be considered on these waveguide crossings. This includes better index-matching of the mode in the multi-mode waveguide to the slab mode, which may improve the performance figures for structures with smaller multi-mode waveguide regions. On the flip side, investigations into longer tapers may be useful for reducing the backscatter further, since this formed the envelope of the backscatter signature from the waveguide crossing in this work. Also, characterisation of the device loss through the full wavelength band should be carried out - it was performed here for a 10 nm wavelength range. This would best be achieved through using optical input and output coupling with a flat wavelength response, such as edge coupling.

Chapter 6 expands on the work of a previous student in QETLabs, who showed a theoretical concept of an SNSPD in a racetrack cavity. The implementation of the cavity warrants spectral selectivity, which enables the cavity to be designed to have the signal and idler wavelengths on resonance whilst the pump wavelength is off resonance, providing further isolation. Whilst high detection efficiencies were shown with this scheme, there was no route to experimental realisation. The purpose of Chapter 6 (as well as the development in Chapter 5) was to design a low-loss bridging structure for the SNSPD which enables the nanowires to be routed out to

contact pads. There were a set of requirements such as low footprint (< 20 x 20 μm^2), low-loss and fully etched into Si, to enable simplicity of fabrication. The multi-mode interference crossing of Chapter 5 is a low-loss, low-crosstalk component with a footprint < 15 x 15 μm^2, providing an excellent solution. Further considerations resulted in a modification of this structure, allowing nanowires to be guided into the racetrack on a 500 nm width waveguide, whilst photons propagate through the multi-mode interference region with only 0.0125 to 0.0135 dB loss between 1540 and 1560 nm. Whilst this crossing structure enables routing of the nanowires to contact pads, there is a compromise in absorption. Whilst the spatial extent of the mode in the wider multi-mode waveguide allows for greater stability with respect to alignment tolerances, the absorption is compromised with respect to the case of a standard 500 nm Si waveguide (as shown in Figure 6.4(b)). In principle, this means one of the advantages of this cavity is reduced when considering an SNSPD material with fabrication defects such as NbN. The nanowire design must be larger to accommodate the same absorption as would be possible on a 500 nm Si waveguide in the racetrack. As a result there will be a larger intrinsic jitter contribution. It should be noted at this point that I only used one design parametrisation and increasing the length of the nanowire in the crossing centre might not warrant the greatest absorption. Further investigation should be made into meandering nanowire designs in the region where self-imaging of the TE_{00} mode occurs, to find the largest absorption with the smallest possible nanowire. The effects of the crossing region and its impact on the detection efficiency were examined analytically. Many cavity effects, such as wavelength shifts due to the change in n_{eff} when considering the addition of the bridging structure were found to be negligible. In terms of detection efficiencies, Figure 6.7 notably shows why the optimisation of a bridging structure is important. With the optimised device, high detection efficiencies above 99 % are possible for a range of nanowire sizes when this scheme is implemented with > 30 dB critical coupling and excellent waveguide losses on the order of 1 dB/cm (as shown in Figure 6.9(b)). The low Q-factor cavities presented in this chapter, like the filtering scheme in Chapter 4, depend on the size of the nanowire, which change the range of FWHM that can be utilised. This may have applications for single-photon spectroscopy, which has been recently a subject of interest in other SNSPD works [245]. The experimental realisation of a racetrack-enhanced SNSPD would make an excellent direction for future work. This was not possible to accomplish at the University of Bristol due to the early nature of the fabrication facilities (aswell as development of cryogenic testing and superconducting film sputtering). However, we were able to show that the modified SOI cavity structure can achieve a critical coupling level of 24 dB, with a Q-factor of comparable to a racetrack resonator of the same length without the multi-mode interference region. I will proceed to outline some possibilities with this scheme. Firstly, the simple (but easier said than done) goal is experimental realisation of a detector with > 95 % DDE. This will require > 20 dB critical coupling, and waveguide losses 5 dB/cm or better on the silicon photonic waveguiding structures. Furthermore, the assumption of all photon absorption events registering as counts will need to be satisfied, meaning there will

need to be significant work on superconducting film optimisation. Further experiments include investigation of the timing jitter, both overall and isolating the geometric contribution. As I show in Figure 6.6(b), depending on the confidence of detection, the geometric jitter can be as low as 4.6 ps for the 1σ case, and as large as 85 ps for the 3σ case. Although this is suppressed to < 30 ps for nanowires > 10 μm, the results obtained with shorter nanowires should be the main interest. The experimental results for the jitter will give an indication of how many round trips the photon is making in the cavity before it is detected. Overall, the analysis will be important in determining if these cavity-enhanced structures are viable for experiments where low timing-jitter is essential (such as LIDAR [167–169]). This would then be followed by implementation in these schemes for real world applications and purposes.

BIBLIOGRAPHY

[1] A. Arons and M. Peppard, "Einstein's proposal of the photon concept—a translation of the annalen der physik paper of 1905," *American Journal of Physics*, vol. 33, no. 5, pp. 367–374, 1965.

[2] J. C. Maxwell, "Viii. a dynamical theory of the electromagnetic field," *Philosophical transactions of the Royal Society of London*, vol. 155, pp. 459–512, 1865.

[3] M. A. Nielsen and I. Chuang, "Quantum computation and quantum information," 2002.

[4] L. K. Grover, "A fast quantum mechanical algorithm for database search," in *Proceedings of the twenty-eighth annual ACM symposium on Theory of computing*, pp. 212–219, ACM, 1996.

[5] D. Deutsch and R. Jozsa, "Rapid solution of problems by quantum computation," *Proc. R. Soc. Lond. A*, vol. 439, no. 1907, pp. 553–558, 1992.

[6] R. Jozsa and N. Linden, "On the role of entanglement in quantum-computational speed-up," *Proceedings of the Royal Society of London. Series A: Mathematical, Physical and Engineering Sciences*, vol. 459, no. 2036, pp. 2011–2032, 2003.

[7] C.-K. Hong, Z.-Y. Ou, and L. Mandel, "Measurement of subpicosecond time intervals between two photons by interference," *Physical review letters*, vol. 59, no. 18, p. 2044, 1987.

[8] C. Gerry, P. Knight, and P. L. Knight, *Introductory quantum optics*. Cambridge university press, 2005.

[9] E. Knill, R. Laflamme, and G. J. Milburn, "A scheme for efficient quantum computation with linear optics," *nature*, vol. 409, no. 6816, p. 46, 2001.

[10] M. Reck, A. Zeilinger, H. J. Bernstein, and P. Bertani, "Experimental realization of any discrete unitary operator," *Physical review letters*, vol. 73, no. 1, p. 58, 1994.

[11] P. Kok, W. Munro, K. Nemoto, T. Ralph, J. P. Dowling, and G. Milburn, "Review article: Linear optical quantum computing," *arXiv preprint quant-ph/0512071*, p. 29, 2005.

[12] J. L. O'Brien, G. J. Pryde, A. G. White, T. C. Ralph, and D. Branning, "Demonstration of an all-optical quantum controlled-not gate," *Nature*, vol. 426, no. 6964, p. 264, 2003.

[13] P. G. Kwiat, A. J. Berglund, J. B. Altepeter, and A. G. White, "Experimental verification of decoherence-free subspaces," *Science*, vol. 290, no. 5491, pp. 498–501, 2000.

[14] S. Schneider and G. J. Milburn, "Decoherence in ion traps due to laser intensity and phase fluctuations," *Physical Review A*, vol. 57, no. 5, p. 3748, 1998.

[15] A. Garg, "Vibrational decoherence in ion trap quantum computers," *Fortschritte der Physik: Progress of Physics*, vol. 46, no. 6-8, pp. 749–757, 1998.

[16] R. Okamoto, J. L. O'Brien, H. F. Hofmann, and S. Takeuchi, "Realization of a knill-laflamme-milburn controlled-not photonic quantum circuit combining effective optical nonlinearities," *Proceedings of the National Academy of Sciences*, vol. 108, no. 25, pp. 10067–10071, 2011.

[17] G.-Y. Wang, Q. Liu, H.-R. Wei, T. Li, Q. Ai, and F.-G. Deng, "Universal quantum gates for photon-atom hybrid systems assisted by bad cavities," *Scientific reports*, vol. 6, p. 24183, 2016.

[18] S. E. Miller, "Integrated optics: An introduction," *Bell System Technical Journal*, vol. 48, no. 7, pp. 2059–2069, 1969.

[19] M. Bruel, "Silicon on insulator material technology," *Electronics letters*, vol. 31, no. 14, pp. 1201–1202, 1995.

[20] J. Wang, S. Paesani, Y. Ding, R. Santagati, P. Skrzypczyk, A. Salavrakos, J. Tura, R. Augusiak, L. Mančinska, D. Bacco, *et al.*, "Multidimensional quantum entanglement with large-scale integrated optics," *Science*, p. eaar7053, 2018.

[21] J. Carolan, C. Harrold, C. Sparrow, E. Martín-López, N. J. Russell, J. W. Silverstone, P. J. Shadbolt, N. Matsuda, M. Oguma, M. Itoh, *et al.*, "Universal linear optics," *Science*, vol. 349, no. 6249, pp. 711–716, 2015.

[22] T. Fangsuwannarak, K. Khunchana, and S. Rattanachan, "Optical band gaps and electrical conductance of si nanocrystals in sio2 matrix for optoelectronic applications," in *Key Engineering Materials*, vol. 545, pp. 134–140, Trans Tech Publ, 2013.

[23] F. Raffaelli, G. Ferranti, D. H. Mahler, P. Sibson, J. E. Kennard, A. Santamato, G. Sinclair, D. Bonneau, M. G. Thompson, and J. C. Matthews, "A homodyne detector integrated onto a photonic chip for measuring quantum states and generating random numbers," *Quantum Science and Technology*, vol. 3, no. 2, p. 025003, 2018.

[24] C. Schuck, X. Guo, L. Fan, X. Ma, M. Poot, and H. X. Tang, "Quantum interference in heterogeneous superconducting-photonic circuits on a silicon chip," *Nature communications*, vol. 7, p. 10352, 2016.

[25] N. C. Harris, G. R. Steinbrecher, M. Prabhu, Y. Lahini, J. Mower, D. Bunandar, C. Chen, F. N. Wong, T. Baehr-Jones, M. Hochberg, *et al.*, "Quantum transport simulations in a programmable nanophotonic processor," *Nature Photonics*, vol. 11, no. 7, p. 447, 2017.

[26] R. S. Jacobsen, K. N. Andersen, P. I. Borel, J. Fage-Pedersen, L. H. Frandsen, O. Hansen, M. Kristensen, A. V. Lavrinenko, G. Moulin, H. Ou, *et al.*, "Strained silicon as a new electro-optic material," *Nature*, vol. 441, no. 7090, p. 199, 2006.

[27] M. Cazzanelli and J. Schilling, "Second order optical nonlinearity in silicon by symmetry breaking," *Applied Physics Reviews*, vol. 3, no. 1, p. 011104, 2016.

[28] A. McMillan, Y.-P. Huang, B. Bell, A. Clark, P. Kumar, and J. Rarity, "Four-wave mixing in single-mode optical fibers," in *Experimental Methods in the Physical Sciences*, vol. 45, pp. 411–465, Elsevier, 2013.

[29] J. E. Sharping, K. F. Lee, M. A. Foster, A. C. Turner, B. S. Schmidt, M. Lipson, A. L. Gaeta, and P. Kumar, "Generation of correlated photons in nanoscale silicon waveguides," *Optics Express*, vol. 14, no. 25, pp. 12388–12393, 2006.

[30] S. Clemmen, K. P. Huy, W. Bogaerts, R. G. Baets, P. Emplit, and S. Massar, "Continuous wave photon pair generation in silicon-on-insulator waveguides and ring resonators," *Optics Express*, vol. 17, no. 19, pp. 16558–16570, 2009.

[31] Q. Lin, O. J. Painter, and G. P. Agrawal, "Nonlinear optical phenomena in silicon waveguides: modeling and applications," *Optics Express*, vol. 15, no. 25, pp. 16604–16644, 2007.

[32] T. Liang and H. Tsang, "Role of free carriers from two-photon absorption in raman amplification in silicon-on-insulator waveguides," *Applied Physics Letters*, vol. 84, no. 15, pp. 2745–2747, 2004.

[33] L. Yin and G. P. Agrawal, "Impact of two-photon absorption on self-phase modulation in silicon waveguides," *Optics Letters*, vol. 32, no. 14, pp. 2031–2033, 2007.

[34] J. Sprengers, A. Gaggero, D. Sahin, S. Jahanmirinejad, G. Frucci, F. Mattioli, R. Leoni, J. Beetz, M. Lermer, M. Kamp, *et al.*, "Waveguide superconducting single-photon detectors for integrated quantum photonic circuits," *Applied Physics Letters*, vol. 99, no. 18, p. 181110, 2011.

[35] G. Gol'Tsman, O. Okunev, G. Chulkova, A. Lipatov, A. Semenov, K. Smirnov, B. Voronov, A. Dzardanov, C. Williams, and R. Sobolewski, "Picosecond superconducting single-photon optical detector," *Applied physics letters*, vol. 79, no. 6, pp. 705–707, 2001.

[36] S. Ferrari, C. Schuck, and W. Pernice, "Waveguide-integrated superconducting nanowire single-photon detectors," *Nanophotonics*, vol. 7, no. 11, pp. 1725–1758, 2018.

[37] R. H. Hadfield, "Single-photon detectors for optical quantum information applications," *Nature photonics*, vol. 3, no. 12, p. 696, 2009.

[38] X. Hu, C. W. Holzwarth, D. Masciarelli, E. A. Dauler, and K. K. Berggren, "Efficiently coupling light to superconducting nanowire single-photon detectors," *IEEE Transactions on Applied Superconductivity*, vol. 19, no. 3, pp. 336–340, 2009.

[39] M. K. Akhlaghi, E. Schelew, and J. F. Young, "Waveguide integrated superconducting single-photon detectors implemented as near-perfect absorbers of coherent radiation," *Nature communications*, vol. 6, p. 8233, 2015.

[40] F. Najafi, J. Mower, N. C. Harris, F. Bellei, A. Dane, C. Lee, X. Hu, P. Kharel, F. Marsili, S. Assefa, *et al.*, "On-chip detection of non-classical light by scalable integration of single-photon detectors," *Nature communications*, vol. 6, p. 5873, 2015.

[41] W. H. Pernice, C. Schuck, O. Minaeva, M. Li, G. Goltsman, A. Sergienko, and H. Tang, "High-speed and high-efficiency travelling wave single-photon detectors embedded in nanophotonic circuits," *Nature communications*, vol. 3, p. 1325, 2012.

[42] B. Calkins, P. L. Mennea, A. E. Lita, B. J. Metcalf, W. S. Kolthammer, A. Lamas-Linares, J. B. Spring, P. C. Humphreys, R. P. Mirin, J. C. Gates, *et al.*, "High quantum-efficiency photon-number-resolving detector for photonic on-chip information processing," *Optics express*, vol. 21, no. 19, pp. 22657–22670, 2013.

[43] J. W. Silverstone, D. Bonneau, J. L. O'Brien, and M. G. Thompson, "Silicon quantum photonics," *IEEE Journal of Selected Topics in Quantum Electronics*, vol. 22, no. 6, pp. 390–402, 2016.

[44] D. Marpaung, B. Morrison, R. Pant, C. Roeloffzen, A. Leinse, M. Hoekman, R. Heideman, and B. J. Eggleton, "Si 3 n 4 ring resonator-based microwave photonic notch filter with an ultrahigh peak rejection," *Optics Express*, vol. 21, no. 20, pp. 23286–23294, 2013.

[45] G. Cantarella, C. Klitis, M. Sorel, and M. J. Strain, "Silicon photonic filters with high rejection of both te and tm modes for on-chip four wave mixing applications," *Optics Express*, vol. 25, no. 17, pp. 19711–19720, 2017.

[46] C. M. Gentry, O. S. Magaña-Loaiza, M. T. Wade, F. Pavanello, T. Gerrits, S. Lin, J. M. Shainline, S. D. Dyer, S. W. Nam, R. P. Mirin, *et al.*, "Monolithic source of entangled photons with integrated pump rejection," in *CLEO: QELS_Fundamental Science*, pp. JTh4C–3, Optical Society of America, 2018.

[47] M. Piekarek, *High-extinction ratio optical filtering for silicon-on-insulator quantum photonics platform*.
PhD thesis, University of Bristol, 2017.

[48] N. Matsuda, P. Karkus, H. Nishi, T. Tsuchizawa, W. J. Munro, H. Takesue, and K. Yamada, "On-chip generation and demultiplexing of quantum correlated photons using a silicon-silica monolithic photonic integration platform," *Optics Express*, vol. 22, no. 19, pp. 22831–22840, 2014.

[49] J. R. Ong, R. Kumar, and S. Mookherjea, "Ultra-high-contrast and tunable-bandwidth filter using cascaded high-order silicon microring filters," *IEEE Photonics Technology Letters*, vol. 25, no. 16, pp. 1543–1546, 2013.

[50] N. C. Harris, D. Grassani, A. Simbula, M. Pant, M. Galli, T. Baehr-Jones, M. Hochberg, D. Englund, D. Bajoni, and C. Galland, "Integrated source of spectrally filtered correlated photons for large-scale quantum photonic systems," *Physical Review X*, vol. 4, no. 4, p. 041047, 2014.

[51] N. A. Tyler, J. Barreto, G. E. Villarreal-Garcia, D. Bonneau, D. Sahin, J. L. O'Brien, and M. G. Thompson, "Modelling superconducting nanowire single photon detectors in a waveguide cavity," *Optics Express*, vol. 24, no. 8, pp. 8797–8808, 2016.

[52] A. J. Kerman, E. A. Dauler, J. K. Yang, K. M. Rosfjord, V. Anant, K. K. Berggren, G. N. Gol'tsman, and B. M. Voronov, "Constriction-limited detection efficiency of superconducting nanowire single-photon detectors," *Applied Physics Letters*, vol. 90, no. 10, p. 101110, 2007.

[53] R. Gaudio, K. op't Hoog, Z. Zhou, D. Sahin, and A. Fiore, "Inhomogeneous critical current in nanowire superconducting single-photon detectors," *Applied Physics Letters*, vol. 105, no. 22, p. 222602, 2014.

[54] D. Marcuse, "Theory of dielectric optical waveguides (academic, new york, 1974)," *Google Scholar*, pp. 12–16.

[55] B. E. Saleh and M. C. Teich, *Fundamentals of photonics*.
John Wiley & Sons, 2019.

[56] M. Young, *Optics and lasers: including fibers and optical waveguides*.
Springer Science & Business Media, 2000.

[57] K. Okamoto, *Fundamentals of optical waveguides*.
Academic press, 2006.

[58] G. Lifante, *Integrated photonics: fundamentals*.
Chichester: John Wiley Sons Ltd, 2003.

[59] X. He, M. Xu, X. Zhang, and H. Zhang, "A tutorial introduction to graphene-microfiber waveguide and its applications," *Frontiers of Optoelectronics*, vol. 9, no. 4, pp. 535–543, 2016.

[60] X. Jiang, T. Euser, A. Abdolvand, F. Babic, F. Tani, N. Joly, J. Travers, and P. S. J. Russell, "Single-mode hollow-core photonic crystal fiber made from soft glass," *Optics Express*, vol. 19, no. 16, pp. 15438–15444, 2011.

[61] J. M. Fini, J. W. Nicholson, B. Mangan, L. Meng, R. S. Windeler, E. M. Monberg, A. DeSantolo, F. V. DiMarcello, and K. Mukasa, "Polarization maintaining single-mode low-loss hollow-core fibres," *Nature communications*, vol. 5, p. 5085, 2014.

[62] M. Notomi, A. Shinya, K. Yamada, J.-I. Takahashi, C. Takahashi, and I. Yokohama, "Structural tuning of guiding modes of line-defect waveguides of silicon-on-insulator photonic crystal slabs," *IEEE Journal of Quantum Electronics*, vol. 38, no. 7, pp. 736–742, 2002.

[63] J. Ackert, K. Murray, P. Jessop, and A. Knights, "Photodetector for 1550 nm formed in silicon-on-insulator slab waveguide," *Electronics letters*, vol. 48, no. 18, pp. 1148–1150, 2012.

[64] H. Fukuda, K. Yamada, T. Shoji, M. Takahashi, T. Tsuchizawa, T. Watanabe, J.-i. Takahashi, and S.-i. Itabashi, "Four-wave mixing in silicon wire waveguides," *Optics Express*, vol. 13, no. 12, pp. 4629–4637, 2005.

[65] C. Jie-Rong, Z. Wei, Z. Qiang, F. Xue, H. Yi-Dong, and P. Jiang-De, "Correlated photon pair generation in silicon wire waveguides at 1.5 μm," *Chinese Physics Letters*, vol. 27, no. 12, p. 124208, 2010.

[66] K.-i. Harada, H. Takesue, H. Fukuda, T. Tsuchizawa, T. Watanabe, K. Yamada, Y. Tokura, and S.-i. Itabashi, "Generation of high-purity entangled photon pairs using silicon wire waveguide," *Optics Express*, vol. 16, no. 25, pp. 20368–20373, 2008.

[67] H. Takesue, "Entangled photon pair generation using silicon wire waveguides," *IEEE Journal of Selected Topics in Quantum Electronics*, vol. 18, no. 6, pp. 1722–1732, 2012.

[68] Q. Xu, V. R. Almeida, R. R. Panepucci, and M. Lipson, "Experimental demonstration of guiding and confining light in nanometer-size low-refractive-index material," *Optics Letters*, vol. 29, no. 14, pp. 1626–1628, 2004.

[69] V. R. Almeida, Q. Xu, C. A. Barrios, and M. Lipson, "Guiding and confining light in void nanostructure," *Optics Letters*, vol. 29, no. 11, pp. 1209–1211, 2004.

[70] W.-C. Lai, S. Chakravarty, X. Wang, C. Lin, and R. T. Chen, "On-chip methane sensing by near-ir absorption signatures in a photonic crystal slot waveguide," *Optics Letters*, vol. 36, no. 6, pp. 984–986, 2011.

[71] A. Rickman, G. Reed, and F. Namavar, "Silicon-on-insulator optical rib waveguide loss and mode characteristics," *Journal of Lightwave Technology*, vol. 12, no. 10, pp. 1771–1776, 1994.

[72] D. E. Hagan and A. P. Knights, "Mechanisms for optical loss in soi waveguides for mid-infrared wavelengths around 2 μm," *Journal of Optics*, vol. 19, no. 2, p. 025801, 2016.

[73] S. Suzuki, M. Yanagisawa, Y. Hibino, and K. Oda, "High-density integrated planar lightwave circuits using sio/sub 2/-geo/sub 2/waveguides with a high refractive index difference," *Journal of lightwave technology*, vol. 12, no. 5, pp. 790–796, 1994.

[74] R. Deck, M. Mirkov, and B. Bagley, "Determination of bending losses in rectangular waveguides," *Journal of lightwave technology*, vol. 16, no. 9, p. 1703, 1998.

[75] Z. Han, P. Zhang, and S. I. Bozhevolnyi, "Calculation of bending losses for highly confined modes of optical waveguides with transformation optics," *Optics Letters*, vol. 38, no. 11, pp. 1778–1780, 2013.

[76] J. Saijonmaa and D. Yevick, "Beam-propagation analysis of loss in bent optical waveguides and fibers," *JOSA*, vol. 73, no. 12, pp. 1785–1791, 1983.

[77] W. Gambling, H. Matsumura, C. Ragdale, and R. Sammut, "Measurement of radiation loss in curved single-mode fibres," *IEE Journal on Microwaves, Optics and Acoustics*, vol. 2, no. 4, pp. 134–140, 1978.

[78] M. Cherchi, S. Ylinen, M. Harjanne, M. Kapulainen, and T. Aalto, "Dramatic size reduction of waveguide bends on a micron-scale silicon photonic platform," *Optics Express*, vol. 21, no. 15, pp. 17814–17823, 2013.

[79] S. K. Selvaraja, P. De Heyn, G. Winroth, P. Ong, G. Lepage, C. Cailler, A. Rigny, K. Bourdelle, D. VanThourhout, J. Van Campenhout, *et al.*, "Highly uniform and low-loss passive silicon photonics devices using a 300mm cmos platform," in *Optical Fiber Communication Conference*, pp. Th2A–33, Optical Society of America, 2014.

[80] P. Dumon, W. Bogaerts, V. Wiaux, J. Wouters, S. Beckx, J. Van Campenhout, D. Taillaert, B. Luyssaert, P. Bienstman, D. Van Thourhout, *et al.*, "Low-loss soi photonic wires and ring resonators fabricated with deep uv lithography," *IEEE Photonics Technology Letters*, vol. 16, no. 5, pp. 1328–1330, 2004.

[81] M. J. Shaw, J. Guo, G. A. Vawter, S. Habermehl, and C. T. Sullivan, "Fabrication techniques for low-loss silicon nitride waveguides," in *Micromachining Technology for Micro-Optics and Nano-Optics III*, vol. 5720, pp. 109–119, International Society for Optics and Photonics, 2005.

[82] J. F. Bauters, M. J. Heck, D. John, D. Dai, M.-C. Tien, J. S. Barton, A. Leinse, R. G. Heideman, D. J. Blumenthal, and J. E. Bowers, "Ultra-low-loss high-aspect-ratio si 3 n 4 waveguides," *Optics Express*, vol. 19, no. 4, pp. 3163–3174, 2011.

[83] R. Takei, M. Suzuki, E. Omoda, S. Manako, T. Kamei, M. Mori, and Y. Sakakibara, "Silicon knife-edge taper waveguide for ultralow-loss spot-size converter fabricated by photolithography," *Applied Physics Letters*, vol. 102, no. 10, p. 101108, 2013.

[84] D. Taillaert, W. Bogaerts, and R. Baets, "Efficient coupling between submicron soi-waveguides and single-mode fibers," 01 2003.

[85] W. Bogaerts, D. Taillaert, B. Luyssaert, P. Dumon, J. Van Campenhout, P. Bienstman, D. Van Thourhout, R. Baets, V. Wiaux, and S. Beckx, "Basic structures for photonic integrated circuits in silicon-on-insulator," *Optics Express*, vol. 12, no. 8, pp. 1583–1591, 2004.

[86] A. Bozzola, L. Carroll, D. Gerace, I. Cristiani, and L. C. Andreani, "Optimising apodized grating couplers in a pure soi platform to- 0.5 db coupling efficiency," *Optics Express*, vol. 23, no. 12, pp. 16289–16304, 2015.

[87] L. Chrostowski and M. Hochberg, *Silicon photonics design: from devices to systems*. Cambridge University Press, 2015.

[88] W. S. Zaoui, A. Kunze, W. Vogel, and M. Berroth, "Cmos-compatible polarization splitting grating couplers with a backside metal mirror," *IEEE Photonics Technology Letters*, vol. 25, no. 14, pp. 1395–1397, 2013.

[89] J. Zhang, J. Yang, H. Lu, W. Wu, J. Huang, and S. Chang, "Subwavelength te/tm grating coupler based on silicon-on-insulator," *Infrared Physics & Technology*, vol. 71, pp. 542–546, 2015.

[90] Y. Wang, X. Wang, J. Flueckiger, H. Yun, W. Shi, R. Bojko, N. A. Jaeger, and L. Chrostowski, "Focusing sub-wavelength grating couplers with low back reflections for rapid prototyping of silicon photonic circuits," *Optics Express*, vol. 22, no. 17, pp. 20652–20662, 2014.

[91] D. Taillaert, W. Bogaerts, P. Bienstman, T. F. Krauss, P. Van Daele, I. Moerman, S. Verstuyft, K. De Mesel, and R. Baets, "An out-of-plane grating coupler for efficient butt-coupling

between compact planar waveguides and single-mode fibers," *IEEE Journal of Quantum Electronics*, vol. 38, no. 7, pp. 949–955, 2002.

[92] F. Van Laere, T. Claes, J. Schrauwen, S. Scheerlinck, W. Bogaerts, D. Taillaert, L. O'FAOLAIN, D. Van Thourhout, and R. Baets, "Compact focusing grating couplers for silicon-on-insulator integrated circuits," *IEEE Photonics Technology Letters*, vol. 19, no. 21-24, pp. 1919–1921, 2007.

[93] R. Larrea, A. Gutiérrez, J. Hurtado, J. Ramírez, B. Garrido, and P. Sanchis, "Compact focusing grating couplers for silicon horizontal slot waveguides," *Optics Letters*, vol. 42, no. 3, pp. 490–493, 2017.

[94] R. Orobtchouk, A. Layadi, H. Gualous, D. Pascal, A. Koster, and S. Laval, "High-efficiency light coupling in a submicrometric silicon-on-insulator waveguide," *Applied optics*, vol. 39, no. 31, pp. 5773–5777, 2000.

[95] K. Debnath, H. Arimoto, M. K. Husain, A. Prasmusinto, A. Al-Attili, R. Petra, H. M. Chong, G. T. Reed, and S. Saito, "Low-loss silicon waveguides and grating couplers fabricated using anisotropic wet etching technique," *Frontiers in Materials*, vol. 3, p. 10, 2016.

[96] Y. Tang, Z. Wang, L. Wosinski, U. Westergren, and S. He, "Highly efficient nonuniform grating coupler for silicon-on-insulator nanophotonic circuits," *Optics Letters*, vol. 35, no. 8, pp. 1290–1292, 2010.

[97] Y. Ding, H. Ou, and C. Peucheret, "Ultrahigh-efficiency apodized grating coupler using fully etched photonic crystals," *Optics Letters*, vol. 38, no. 15, pp. 2732–2734, 2013.

[98] F. Van Laere, G. Roelkens, M. Ayre, J. Schrauwen, D. Taillaert, D. Van Thourhout, T. F. Krauss, and R. Baets, "Compact and highly efficient grating couplers between optical fiber and nanophotonic waveguides," *Journal of lightwave technology*, vol. 25, no. 1, pp. 151–156, 2007.

[99] D. Taillaert, F. Van Laere, M. Ayre, W. Bogaerts, D. Van Thourhout, P. Bienstman, and R. Baets, "Grating couplers for coupling between optical fibers and nanophotonic waveguides," *Japanese Journal of Applied Physics*, vol. 45, no. 8R, p. 6071, 2006.

[100] D. Taillaert, P. Bienstman, and R. Baets, "Compact efficient broadband grating coupler for silicon-on-insulator waveguides," *Optics Letters*, vol. 29, no. 23, pp. 2749–2751, 2004.

[101] W. S. Zaoui, A. Kunze, W. Vogel, M. Berroth, J. Butschke, F. Letzkus, and J. Burghartz, "Bridging the gap between optical fibers and silicon photonic integrated circuits," *Optics Express*, vol. 22, no. 2, pp. 1277–1286, 2014.

[102] Y. Ding, C. Peucheret, H. Ou, and K. Yvind, "Fully etched apodized grating coupler on the soi platform with- 0.58 db coupling efficiency," *Optics Letters*, vol. 39, no. 18, pp. 5348–5350, 2014.

[103] X. Chen and H. K. Tsang, "Nanoholes grating couplers for coupling between silicon-on-insulator waveguides and optical fibers," *IEEE Photonics Journal*, vol. 1, no. 3, pp. 184–190, 2009.

[104] R. Halir, P. Cheben, J. Schmid, R. Ma, D. Bedard, S. Janz, D.-X. Xu, A. Densmore, J. Lapointe, and I. Molina-Fernández, "Continuously apodized fiber-to-chip surface grating coupler with refractive index engineered subwavelength structure," *Optics Letters*, vol. 35, no. 19, pp. 3243–3245, 2010.

[105] Y. Wang, H. Yun, Z. Lu, R. Bojko, W. Shi, X. Wang, J. Flueckiger, F. Zhang, M. Caverley, N. A. Jaeger, *et al.*, "Apodized focusing fully etched subwavelength grating couplers," *IEEE Photonics Journal*, vol. 7, no. 3, pp. 1–10, 2015.

[106] G. Cong, K. Suzuki, S. Kim, K. Tanizawa, S. Namiki, and H. Kawashima, "Demonstration of a 3-db directional coupler with enhanced robustness to gap variations for silicon wire waveguides," *Optics Express*, vol. 22, no. 2, pp. 2051–2059, 2014.

[107] H. Yun, Y. Wang, F. Zhang, Z. Lu, S. Lin, L. Chrostowski, and N. A. Jaeger, "Broadband 2× 2 adiabatic 3 db coupler using silicon-on-insulator sub-wavelength grating waveguides," *Optics Letters*, vol. 41, no. 13, pp. 3041–3044, 2016.

[108] Y. Luo, Y. Yu, M. Ye, C. Sun, and X. Zhang, "Integrated dual-mode 3 db power coupler based on tapered directional coupler," *Scientific reports*, vol. 6, p. 23516, 2016.

[109] W.-P. Huang, "Coupled-mode theory for optical waveguides: an overview," *JOSA A*, vol. 11, no. 3, pp. 963–983, 1994.

[110] M. Poot, C. Schuck, X.-s. Ma, X. Guo, and H. X. Tang, "Design and characterization of integrated components for sin photonic quantum circuits," *Optics Express*, vol. 24, no. 7, pp. 6843–6860, 2016.

[111] J. Van Campenhout, W. M. Green, S. Assefa, and Y. A. Vlasov, "Low-power, 2× 2 silicon electro-optic switch with 110-nm bandwidth for broadband reconfigurable optical networks," *Optics Express*, vol. 17, no. 26, pp. 24020–24029, 2009.

[112] C. M. Wilkes, X. Qiang, J. Wang, R. Santagati, S. Paesani, X. Zhou, D. A. Miller, G. D. Marshall, M. G. Thompson, and J. L. O'Brien, "60 db high-extinction auto-configured mach–zehnder interferometer," *Optics Letters*, vol. 41, no. 22, pp. 5318–5321, 2016.

[113] S. Liu, H. Cai, C. DeRose, P. Davids, A. Pomerene, A. Starbuck, D. Trotter, R. Camacho, J. Urayama, and A. Lentine, "High speed ultra-broadband amplitude modulators with ultrahigh extinction> 65 db," *Optics Express*, vol. 25, no. 10, pp. 11254–11264, 2017.

[114] Y. Shoji, K. Kintaka, S. Suda, H. Kawashima, T. Hasama, and H. Ishikawa, "Low-crosstalk 2× 2 thermo-optic switch with silicon wire waveguides," *Optics Express*, vol. 18, no. 9, pp. 9071–9075, 2010.

[115] D. Dai, "Silicon polarization beam splitter based on an asymmetrical evanescent coupling system with three optical waveguides," *Journal of Lightwave Technology*, vol. 30, no. 20, pp. 3281–3287, 2012.

[116] H. Wu, Y. Tan, and D. Dai, "Ultra-broadband high-performance polarizing beam splitter on silicon," *Optics Express*, vol. 25, no. 6, pp. 6069–6075, 2017.

[117] Z. Lu, Y. Wang, F. Zhang, N. A. Jaeger, and L. Chrostowski, "Wideband silicon photonic polarization beamsplitter based on point-symmetric cascaded broadband couplers," *Optics Express*, vol. 23, no. 23, pp. 29413–29422, 2015.

[118] X. Lu, S. Rogers, T. Gerrits, W. C. Jiang, S. W. Nam, and Q. Lin, "Heralding single photons from a high-q silicon microdisk," *Optica*, vol. 3, no. 12, pp. 1331–1338, 2016.

[119] M. Savanier, R. Kumar, and S. Mookherjea, "Photon pair generation from compact silicon microring resonators using microwatt-level pump powers," *Optics Express*, vol. 24, no. 4, pp. 3313–3328, 2016.

[120] C. Reimer, L. Caspani, M. Clerici, M. Ferrera, M. Kues, M. Peccianti, A. Pasquazi, L. Razzari, B. E. Little, S. T. Chu, *et al.*, "Integrated frequency comb source of heralded single photons," *Optics Express*, vol. 22, no. 6, pp. 6535–6546, 2014.

[121] S. F. Preble, M. L. Fanto, J. A. Steidle, C. C. Tison, G. A. Howland, Z. Wang, and P. M. Alsing, "On-chip quantum interference from a single silicon ring-resonator source," *Physical Review Applied*, vol. 4, no. 2, p. 021001, 2015.

[122] M. Gad, J. Ackert, D. Yevick, L. Chrostowski, and P. E. Jessop, "Ring resonator wavelength division multiplexing interleaver," *Journal of Lightwave Technology*, vol. 29, no. 14, pp. 2102–2108, 2011.

[123] P. De Heyn, J. De Coster, P. Verheyen, G. Lepage, M. Pantouvaki, P. Absil, W. Bogaerts, J. Van Campenhout, and D. Van Thourhout, "Fabrication-tolerant four-channel wavelength-division-multiplexing filter based on collectively tuned si microrings," *Journal of Lightwave Technology*, vol. 31, no. 16, pp. 3085–3092, 2013.

[124] T. Claes, J. G. Molera, K. De Vos, E. Schacht, R. Baets, and P. Bienstman, "Label-free biosensing with a slot-waveguide-based ring resonator in silicon on insulator," *IEEE Photonics journal*, vol. 1, no. 3, pp. 197–204, 2009.

[125] M. Mancuso, J. M. Goddard, and D. Erickson, "Nanoporous polymer ring resonators for biosensing," *Optics Express*, vol. 20, no. 1, pp. 245–255, 2012.

[126] T. Taniguchi, S. Yokoyama, Y. Amemiya, T. Ikeda, A. Kuroda, and S. Yokoyama, "Differential si ring resonators for label-free biosensing," *Japanese Journal of Applied Physics*, vol. 55, no. 4S, p. 04EM04, 2016.

[127] S. Yoshida, S. Ishihara, T. Arakawa, and Y. Kokubun, "Highly sensitive optical biosensor based on silicon-microring-resonator-loaded mach–zehnder interferometer," *Japanese Journal of Applied Physics*, vol. 56, no. 4S, p. 04CH08, 2017.

[128] R. Guider, D. Gandolfi, T. Chalyan, L. Pasquardini, A. Samusenko, C. Pederzolli, G. Pucker, and L. Pavesi, "Sensitivity and limit of detection of biosensors based on ring resonators," *Sensing and bio-sensing research*, vol. 6, pp. 99–102, 2015.

[129] A. Ramachandran, S. Wang, J. Clarke, S. Ja, D. Goad, L. Wald, E. Flood, E. Knobbe, J. Hryniewicz, S. Chu, *et al.*, "A universal biosensing platform based on optical micro-ring resonators," *Biosensors and Bioelectronics*, vol. 23, no. 7, pp. 939–944, 2008.

[130] J. Flueckiger, S. Schmidt, V. Donzella, A. Sherwali, D. M. Ratner, L. Chrostowski, and K. C. Cheung, "Sub-wavelength grating for enhanced ring resonator biosensor," *Optics Express*, vol. 24, no. 14, pp. 15672–15686, 2016.

[131] S. T. Chu, B. E. Little, W. Pan, T. Kaneko, S. Sato, and Y. Kokubun, "An eight-channel add-drop filter using vertically coupled microring resonators over a cross grid," *IEEE Photonics Technology Letters*, vol. 11, no. 6, pp. 691–693, 1999.

[132] R. Grover, P. Absil, V. Van, J. Hryniewicz, B. Little, O. King, L. Calhoun, F. Johnson, and P.-T. Ho, "Vertically coupled gainasp–inp microring resonators," *Optics Letters*, vol. 26, no. 8, pp. 506–508, 2001.

[133] Y. Kokubun, Y. Hatakeyama, M. Ogata, S. Suzuki, and N. Zaizen, "Fabrication technologies for vertically coupled microring resonator with multilevel crossing busline and ultracompact-ring radius," *IEEE Journal of Selected Topics in Quantum Electronics*, vol. 11, no. 1, pp. 4–10, 2005.

[134] C. Arlotti, O. Gauthier-Lafaye, A. Monmayrant, and S. Calvez, "Achromatic critically coupled racetrack resonators," *JOSA B*, vol. 34, no. 11, pp. 2343–2351, 2017.

[135] R. A. Integlia, L. Yin, D. Ding, D. Z. Pan, D. M. Gill, and W. Jiang, "Parallel-coupled dual racetrack silicon micro-resonators for quadrature amplitude modulation," *Optics Express*, vol. 19, no. 16, pp. 14892–14902, 2011.

[136] W. M. Green, R. K. Lee, G. A. DeRose, A. Scherer, and A. Yariv, "Hybrid ingaasp-inp mach-zehnder racetrack resonator for thermooptic switching and coupling control," *Optics Express*, vol. 13, no. 5, pp. 1651–1659, 2005.

[137] D. G. Rabus, "Ring resonators: Theory and modeling," *Integrated Ring Resonators: The Compendium*, pp. 3–40, 2007.

[138] W. Bogaerts, P. De Heyn, T. Van Vaerenbergh, K. De Vos, S. Kumar Selvaraja, T. Claes, P. Dumon, P. Bienstman, D. Van Thourhout, and R. Baets, "Silicon microring resonators," *Laser & Photonics Reviews*, vol. 6, no. 1, pp. 47–73, 2012.

[139] L. Stern and U. Levy, "Transmission and time delay properties of an integrated system consisting of atomic vapor cladding on top of a micro ring resonator," *Optics Express*, vol. 20, no. 27, pp. 28082–28093, 2012.

[140] F. Vollmer and S. Arnold, "Whispering-gallery-mode biosensing: label-free detection down to single molecules," *Nature methods*, vol. 5, no. 7, p. 591, 2008.

[141] S. Kaminski, L. L. Martin, and T. Carmon, "Tweezers controlled resonator," *Optics Express*, vol. 23, no. 22, pp. 28914–28919, 2015.

[142] R. D. Mansoor, H. Sasse, M. Al Asadi, S. J. Ison, and A. P. Duffy, "Over coupled ring resonator-based add/drop filters," *IEEE Journal of Quantum Electronics*, vol. 50, no. 8, pp. 598–604, 2014.

[143] A. Dutt, S. Miller, K. Luke, J. Cardenas, A. L. Gaeta, P. Nussenzveig, and M. Lipson, "Tunable squeezing using coupled ring resonators on a silicon nitride chip," *Optics Letters*, vol. 41, no. 2, pp. 223–226, 2016.

[144] C. M. Gentry, "Scalable quantum light sources in silicon photonic circuits," 2018.

[145] P. Rabiei, W. H. Steier, C. Zhang, and L. R. Dalton, "Polymer micro-ring filters and modulators," *Journal of lightwave technology*, vol. 20, no. 11, p. 1968, 2002.

[146] L. B. Soldano and E. C. Pennings, "Optical multi-mode interference devices based on self-imaging: principles and applications," *Journal of lightwave technology*, vol. 13, no. 4, pp. 615–627, 1995.

[147] Y. Shi, D. Dai, and S. He, "Improved performance of a silicon-on-insulator-based multimode interference coupler by using taper structures," *Optics communications*, vol. 253, no. 4-6, pp. 276–282, 2005.

[148] A. Maese-Novo, R. Halir, S. Romero-García, D. Pérez-Galacho, L. Zavargo-Peche, A. Ortega-Moñux, I. Molina-Fernández, J. Wangüemert-Pérez, and P. Cheben, "Wavelength independent multimode interference coupler," *Optics Express*, vol. 21, no. 6, pp. 7033–7040, 2013.

[149] W. Hong-Zhen, Y. Jin-Zhong, L. Zhong-Li, Z. Xiao-Feng, S. Wei, and F. Chang-Shui, "Silicon-on-insulator based 2× 2 multimode interference coupler with large tolerance," *Chinese Physics Letters*, vol. 18, no. 2, p. 245, 2001.

[150] H. Wei, J. Yu, X. Zhang, and Z. Liu, "Compact 3-db tapered multimode interference coupler in silicon-on-insulator," *Optics Letters*, vol. 26, no. 12, pp. 878–880, 2001.

[151] Á. Rosa, A. Gutiérrez, A. Brimont, A. Griol, and P. Sanchis, "High performace silicon 2x2 optical switch based on a thermo-optically tunable multimode interference coupler and efficient electrodes," *Optics Express*, vol. 24, no. 1, pp. 191–198, 2016.

[152] L. Xu, Y. Wang, A. Kumar, D. Patel, E. El-Fiky, Z. Xing, R. Li, and D. V. Plant, "Polarization beam splitter based on mmi coupler with swg birefringence engineering on soi," *IEEE Photon. Technol. Lett.*, vol. 30, no. 4, pp. 403–406, 2018.

[153] J. Xia, J. Yu, Z. Wang, Z. Fan, and S. Chen, "Low power 2× 2 thermo-optic soi waveguide switch fabricated by anisotropy chemical etching," *Optics communications*, vol. 232, no. 1-6, pp. 223–228, 2004.

[154] E. Elfiky, D. Patel, *et al.*, "A high extinction ratio, broadband, and compact polarization beam splitter enabled by cascaded mmis on silicon-on-insulator," in *Optical Fiber Communication Conference*, pp. W2A–8, Optical Society of America, 2016.

[155] Y. Huang, Z. Tu, H. Yi, Y. Li, X. Wang, and W. Hu, "High extinction ratio polarization beam splitter with multimode interference coupler on soi," *Optics Communications*, vol. 307, pp. 46–49, 2013.

[156] D. Wu, Y. Wu, Y. Wang, J. An, and X. Hu, "Reconfigurable optical add-drop multiplexer based on thermally tunable micro-ring resonators," *Optics Communications*, vol. 367, pp. 44–49, 2016.

[157] S. Han, T. J. Seok, N. Quack, B.-W. Yoo, and M. C. Wu, "Large-scale silicon photonic switches with movable directional couplers," *Optica*, vol. 2, no. 4, pp. 370–375, 2015.

[158] L. Lu, S. Zhao, L. Zhou, D. Li, Z. Li, M. Wang, X. Li, and J. Chen, "16× 16 non-blocking silicon optical switch based on electro-optic mach-zehnder interferometers," *Optics Express*, vol. 24, no. 9, pp. 9295–9307, 2016.

[159] L. Qiao, W. Tang, and T. Chu, "32× 32 silicon electro-optic switch with built-in monitors and balanced-status units," *Scientific Reports*, vol. 7, p. 42306, 2017.

[160] K. Kwon, T. J. Seok, J. Henriksson, J. Luo, L. Ochikubo, J. Jacobs, R. S. Muller, and M. C. Wu, "128× 128 silicon photonic mems switch with scalable row/column addressing," in *CLEO: Science and Innovations*, pp. SF1A–4, Optical Society of America, 2018.

[161] H.-L. Han, H. Li, X.-P. Zhang, A. Liu, T.-Y. Lin, Z. Chen, H.-B. Lv, M.-H. Lu, X.-P. Liu, and Y.-F. Chen, "High performance ultra-compact soi waveguide crossing," *Optics Express*, vol. 26, no. 20, pp. 25602–25610, 2018.

[162] P. J. Bock, P. Cheben, J. H. Schmid, J. Lapointe, A. Delâge, D.-X. Xu, S. Janz, A. Densmore, and T. J. Hall, "Subwavelength grating crossings for silicon wire waveguides," *Optics Express*, vol. 18, no. 15, pp. 16146–16155, 2010.

[163] P. Dumais, D. Goodwill, D. Celo, J. Jiang, and E. Bernier, "Three-mode synthesis of slab gaussian beam in ultra-low-loss in-plane nanophotonic silicon waveguide crossing," in *Group IV Photonics (GFP), 2017 IEEE 14th International Conference on*, pp. 97–98, IEEE, 2017.

[164] C.-H. Chen and C.-H. Chiu, "Taper-integrated multimode-interference based waveguide crossing design," *IEEE Journal of Quantum Electronics*, vol. 46, no. 11, pp. 1656–1661, 2010.

[165] A. D. Semenov, G. N. Gol'tsman, and A. A. Korneev, "Quantum detection by current carrying superconducting film," *Physica C: Superconductivity*, vol. 351, no. 4, pp. 349–356, 2001.

[166] S. Dong, Q. Zhou, W. Zhang, Y. He, W. Zhang, L. You, Y. Huang, and J. Peng, "Energy-time entanglement generation in optical fibers under cw pumping," *Optics Express*, vol. 22, no. 1, pp. 359–368, 2014.

[167] J. Zhu, Y. Chen, L. Zhang, X. Jia, Z. Feng, G. Wu, X. Yan, J. Zhai, Y. Wu, Q. Chen, *et al.*, "Demonstration of measuring sea fog with an snspd-based lidar system," *Scientific reports*, vol. 7, no. 1, p. 15113, 2017.

[168] R. E. Warburton, A. McCarthy, A. M. Wallace, S. Hernandez-Marin, R. H. Hadfield, S. W. Nam, and G. S. Buller, "Subcentimeter depth resolution using a single-photon counting time-of-flight laser ranging system at 1550 nm wavelength," *Optics Letters*, vol. 32, no. 15, pp. 2266–2268, 2007.

[169] L. You, X. Yang, Y. He, W. Zhang, D. Liu, W. Zhang, L. Zhang, L. Zhang, X. Liu, S. Chen, *et al.*, "Jitter analysis of a superconducting nanowire single photon detector," *Aip Advances*, vol. 3, no. 7, p. 072135, 2013.

[170] T. Zhong, H. Zhou, R. D. Horansky, C. Lee, V. B. Verma, A. E. Lita, A. Restelli, J. C. Bienfang, R. P. Mirin, T. Gerrits, *et al.*, "Photon-efficient quantum key distribution using time–energy entanglement with high-dimensional encoding," *New Journal of Physics*, vol. 17, no. 2, p. 022002, 2015.

[171] L. Fan, C.-L. Zou, M. Poot, R. Cheng, X. Guo, X. Han, and H. X. Tang, "Integrated optomechanical single-photon frequency shifter," *Nature Photonics*, vol. 10, no. 12, p. 766, 2016.

[172] F. Marsili, V. B. Verma, J. A. Stern, S. Harrington, A. E. Lita, T. Gerrits, I. Vayshenker, B. Baek, M. D. Shaw, R. P. Mirin, *et al.*, "Detecting single infrared photons with 93% system efficiency," *Nature Photonics*, vol. 7, no. 3, p. 210, 2013.

[173] V. Anant, A. J. Kerman, E. A. Dauler, J. K. Yang, K. M. Rosfjord, and K. K. Berggren, "Optical properties of superconducting nanowire single-photon detectors," *Optics Express*, vol. 16, no. 14, pp. 10750–10761, 2008.

[174] A. Banerjee, R. M. Heath, D. Morozov, D. Hemakumara, U. Nasti, I. Thayne, and R. H. Hadfield, "Optical properties of refractory metal based thin films," *Optical Materials Express*, vol. 8, no. 8, pp. 2072–2088, 2018.

[175] A. Korneev, V. Matvienko, O. Minaeva, I. Milostnaya, I. Rubtsova, G. Chulkova, K. Smirnov, V. Voronov, G. Gol'tsman, W. Slysz, *et al.*, "Quantum efficiency and noise equivalent power of nanostructured, nbn, single-photon detectors in the wavelength range from visible to infrared," *IEEE transactions on applied superconductivity*, vol. 15, no. 2, pp. 571–574, 2005.

[176] J. Bardeen, L. N. Cooper, and J. R. Schrieffer, "Theory of superconductivity," *Physical Review*, vol. 108, no. 5, p. 1175, 1957.

[177] A. Pearlman, A. Cross, W. Slysz, J. Zhang, A. Verevkin, M. Currie, A. Korneev, P. Kouminov, K. Smirnov, B. Voronov, *et al.*, "Gigahertz counting rates of nbn single-photon detectors for quantum communications," *IEEE transactions on applied superconductivity*, vol. 15, no. 2, pp. 579–582, 2005.

[178] M. Sidorova, A. Semenov, H.-W. Hübers, I. Charaev, A. Kuzmin, S. Doerner, and M. Siegel, "Physical mechanisms of timing jitter in photon detection by current-carrying superconducting nanowires," *Physical Review B*, vol. 96, no. 18, p. 184504, 2017.

[179] B. Korzh, Q. Zhao, S. Frasca, J. Allmaras, T. Autry, E. Bersin, M. Colangelo, G. Crouch, A. Dane, T. Gerrits, *et al.*, "Demonstrating sub-3 ps temporal resolution in a superconducting nanowire single-photon detector," *arXiv preprint arXiv:1804.06839*, 2018.

[180] T. Yamashita, S. Miki, K. Makise, W. Qiu, H. Terai, M. Fujiwara, M. Sasaki, and Z. Wang, "Origin of intrinsic dark count in superconducting nanowire single-photon detectors," *Applied Physics Letters*, vol. 99, no. 16, p. 161105, 2011.

[181] V. B. Verma, B. Korzh, F. Bussieres, R. D. Horansky, S. D. Dyer, A. E. Lita, I. Vayshenker, F. Marsili, M. D. Shaw, H. Zbinden, *et al.*, "High-efficiency superconducting nanowire single-photon detectors fabricated from mosi thin-films," *Optics express*, vol. 23, no. 26, pp. 33792–33801, 2015.

[182] H. Li, S. Chen, L. You, W. Meng, Z. Wu, Z. Zhang, K. Tang, L. Zhang, W. Zhang, X. Yang, *et al.*, "Superconducting nanowire single photon detector at 532 nm and demonstration in satellite laser ranging," *Optics Express*, vol. 24, no. 4, pp. 3535–3542, 2016.

[183] V. Kovalyuk, S. Ferrari, O. Kahl, A. Semenov, Y. Lobanov, M. Shcherbatenko, A. Korneev, W. Pernice, and G. Goltsman, "Waveguide integrated superconducting single-photon detector for on-chip quantum and spectral photonic application," in *Journal of Physics: Conference Series*, vol. 917, p. 062032, IOP Publishing, 2017.

[184] Y. Xu, J. Wu, W. Fang, L. You, and L. Tong, "Microfiber coupled superconducting nanowire single-photon detectors," *Optics Communications*, vol. 405, pp. 48–52, 2017.

[185] K. M. Rosfjord, J. K. Yang, E. A. Dauler, A. J. Kerman, V. Anant, B. M. Voronov, G. N. Gol'Tsman, and K. K. Berggren, "Nanowire single-photon detector with an integrated optical cavity and anti-reflection coating," *Optics Express*, vol. 14, no. 2, pp. 527–534, 2006.

[186] A. Divochiy, F. Marsili, D. Bitauld, A. Gaggero, R. Leoni, F. Mattioli, A. Korneev, V. Seleznev, N. Kaurova, O. Minaeva, *et al.*, "Superconducting nanowire photon-number-resolving detector at telecommunication wavelengths," *Nature Photonics*, vol. 2, no. 5, p. 302, 2008.

[187] L. You, J. Wu, Y. Xu, X. Hou, W. Fang, H. Li, W. Zhang, L. Zhang, X. Liu, L. Tong, *et al.*, "Microfiber-coupled superconducting nanowire single-photon detector for near-infrared wavelengths," *Optics Express*, vol. 25, no. 25, pp. 31221–31229, 2017.

[188] E. A. Dauler, M. E. Grein, A. J. Kerman, F. Marsili, S. Miki, S. W. Nam, M. D. Shaw, H. Terai, V. B. Verma, and T. Yamashita, "Review of superconducting nanowire single-photon detector system design options and demonstrated performance," *Optical Engineering*, vol. 53, no. 8, p. 081907, 2014.

[189] K. Yee, "Numerical solution of initial boundary value problems involving maxwell's equations in isotropic media," *IEEE Transactions on antennas and propagation*, vol. 14, no. 3, pp. 302–307, 1966.

[190] P. C. Sukanek, "Dependence of film thickness on speed in spin coating," *Journal of The Electrochemical Society*, vol. 138, no. 6, pp. 1712–1719, 1991.

[191] N. Sahu, B. Parija, and S. Panigrahi, "Fundamental understanding and modeling of spin coating process: A review," *Indian Journal of Physics*, vol. 83, no. 4, pp. 493–502, 2009.

[192] M. Born and E. Wolf, "Principles of optics. sixth (corrected) edition," 1997.

[193] W. Hu, K. Sarveswaran, M. Lieberman, and G. H. Bernstein, "Sub-10 nm electron beam lithography using cold development of poly (methylmethacrylate)," *Journal of Vacuum Science & Technology B: Microelectronics and Nanometer Structures Processing, Measurement, and Phenomena*, vol. 22, no. 4, pp. 1711–1716, 2004.

[194] B. Wu, A. Kumar, and S. Pamarthy, "High aspect ratio silicon etch: A review," *Journal of applied physics*, vol. 108, no. 5, p. 9, 2010.

[195] G. S. Oehrlein and H. L. Williams, "Silicon etching mechanisms in a cf4/h2 glow discharge," *Journal of applied physics*, vol. 62, no. 2, pp. 662–672, 1987.

[196] J. Xie, M. K. Borg, L. Gibelli, O. Henrich, D. A. Lockerby, and J. M. Reese, "Effective mean free path and viscosity of confined gases," *Physics of Fluids*, vol. 31, no. 7, p. 072002, 2019.

[197] A. Nagy, "Sidewall tapering in reactive ion etching," *Journal of The Electrochemical Society*, vol. 132, no. 3, pp. 689–693, 1985.

[198] Y. Wang, S. W. Graham, L. Chan, and S. Loong, "Understanding of via-etch-induced polymer formation and its removal," *Journal of The Electrochemical Society*, vol. 144, no. 4, pp. 1522–1528, 1997.

[199] S. C. Abdulla, L. Kauppinen, M. Dijkstra, M. J. de Boer, E. Berenschot, H. V. Jansen, R. De Ridder, and G. J. Krijnen, "Tuning a racetrack ring resonator by an integrated dielectric mems cantilever," *Optics Express*, vol. 19, no. 17, pp. 15864–15878, 2011.

[200] B. Guan, S. S. Djordjevic, N. K. Fontaine, L. Zhou, S. Ibrahim, R. P. Scott, D. J. Geisler, Z. Ding, and S. B. Yoo, "Cmos compatible reconfigurable silicon photonic lattice filters using cascaded unit cells for rf-photonic processing," *IEEE Journal of Selected Topics in Quantum Electronics*, vol. 20, no. 4, pp. 359–368, 2013.

[201] K. De Vos, J. Girones, T. Claes, Y. De Koninck, S. Popelka, E. Schacht, R. Baets, and P. Bienstman, "Multiplexed antibody detection with an array of silicon-on-insulator microring resonators," *IEEE Photonics Journal*, vol. 1, no. 4, pp. 225–235, 2009.

[202] S. Ristic, A. Bhardwaj, M. J. Rodwell, L. A. Coldren, and L. A. Johansson, "An optical phase-locked loop photonic integrated circuit," *Journal of Lightwave Technology*, vol. 28, no. 4, pp. 526–538, 2009.

[203] D. Swinehart, "The beer-lambert law," *Journal of chemical education*, vol. 39, no. 7, p. 333, 1962.

[204] A. Baes and P. Bloom, "Fulvic acid ultraviolet-visible spectra: influence of solvent and ph," *Soil Science Society of America Journal*, vol. 54, no. 5, pp. 1248–1254, 1990.

[205] S. Attal, R. Thiruvengadathan, and O. Regev, "Determination of the concentration of single-walled carbon nanotubes in aqueous dispersions using uv- visible absorption spectroscopy," *Analytical chemistry*, vol. 78, no. 23, pp. 8098–8104, 2006.

[206] S. H. Jeong, K. K. Kim, S. J. Jeong, K. H. An, S. H. Lee, and Y. H. Lee, "Optical absorption spectroscopy for determining carbon nanotube concentration in solution," *Synthetic Metals*, vol. 157, no. 13-15, pp. 570–574, 2007.

[207] J. Matres and W. V. Sorin, "Simple model for ring resonators backscatter," *Optics Express*, vol. 25, no. 4, pp. 3242–3251, 2017.

[208] A. Li, T. Van Vaerenbergh, P. De Heyn, P. Bienstman, and W. Bogaerts, "Backscattering in silicon microring resonators: a quantitative analysis," *Laser & Photonics Reviews*, vol. 10, no. 3, pp. 420–431, 2016.

[209] J. B. Christensen, J. G. Koefoed, K. Rottwitt, and C. McKinstrie, "Engineering spectrally unentangled photon pairs from nonlinear microring resonators by pump manipulation," *Optics Letters*, vol. 43, no. 4, pp. 859–862, 2018.

[210] S. Azzini, D. Grassani, M. J. Strain, M. Sorel, L. Helt, J. Sipe, M. Liscidini, M. Galli, and D. Bajoni, "Ultra-low power generation of twin photons in a compact silicon ring resonator," *Optics Express*, vol. 20, no. 21, pp. 23100–23107, 2012.

[211] S. Azzini, D. Grassani, M. Galli, L. C. Andreani, M. Sorel, M. J. Strain, L. Helt, J. Sipe, M. Liscidini, and D. Bajoni, "From classical four-wave mixing to parametric fluorescence in silicon microring resonators," *Optics Letters*, vol. 37, no. 18, pp. 3807–3809, 2012.

[212] W. McKinnon, D.-X. Xu, C. Storey, E. Post, A. Densmore, A. Delâge, P. Waldron, J. Schmid, and S. Janz, "Extracting coupling and loss coefficients from a ring resonator," *Optics Express*, vol. 17, no. 21, pp. 18971–18982, 2009.

[213] R. Halir, A. Maese-Novo, A. Ortega-Moñux, I. Molina-Fernández, J. Wangüemert-Pérez, P. Cheben, D.-X. Xu, J. Schmid, and S. Janz, "Colorless directional coupler with dispersion engineered sub-wavelength structure," *Optics Express*, vol. 20, no. 12, pp. 13470–13477, 2012.

[214] Z. Lu, H. Yun, Y. Wang, Z. Chen, F. Zhang, N. A. Jaeger, and L. Chrostowski, "Broadband silicon photonic directional coupler using asymmetric-waveguide based phase control," *Optics Express*, vol. 23, no. 3, pp. 3795–3808, 2015.

[215] H. Jayatilleka, H. Shoman, L. Chrostowski, and S. Shekhar, "Photoconductive heaters enable control of large-scale silicon photonic ring resonator circuits," *Optica*, vol. 6, no. 1, pp. 84–91, 2019.

[216] R. Santagati, J. W. Silverstone, M. Strain, M. Sorel, S. Miki, T. Yamashita, M. Fujiwara, M. Sasaki, H. Terai, M. G. Tanner, *et al.*, "Silicon photonic processor of two-qubit entangling quantum logic," *Journal of Optics*, vol. 19, no. 11, p. 114006, 2017.

[217] W. Bogaerts, P. Dumon, D. Van Thourhout, and R. Baets, "Low-loss, low-cross-talk crossings for silicon-on-insulator nanophotonic waveguides," *Optics Letters*, vol. 32, no. 19, pp. 2801–2803, 2007.

[218] T. J. Seok, N. Quack, S. Han, R. S. Muller, and M. C. Wu, "Large-scale broadband digital silicon photonic switches with vertical adiabatic couplers," *Optica*, vol. 3, no. 1, pp. 64–70, 2016.

[219] B. J. Soller, D. K. Gifford, M. S. Wolfe, and M. E. Froggatt, "High resolution optical frequency domain reflectometry for characterization of components and assemblies," *Optics Express*, vol. 13, no. 2, pp. 666–674, 2005.

[220] U. Glombitza and E. Brinkmeyer, "Coherent frequency-domain reflectometry for characterization of single-mode integrated-optical waveguides," *Journal of Lightwave technology*, vol. 11, no. 8, pp. 1377–1384, 1993.

[221] D. Zhao, D. Pustakhod, K. Williams, and X. Leijtens, "High resolution optical frequency domain reflectometry for analyzing intra-chip reflections," *IEEE Photonics Technology Letters*, vol. 29, no. 16, pp. 1379–1382, 2017.

[222] E. Hecht, *Optics*.
Pearson education, Addison-Wesley, 2002.

[223] D. Celo, D. Goodwill, P. Dumais, J. Jiang, and E. Bernier, "Low-loss waveguide crossings for photonic integrated circuits on soi technology," in *Group IV Photonics (GFP), 2014 IEEE 11th International Conference on*, pp. 189–190, IEEE, 2014.

[224] Y. Ma, Y. Zhang, S. Yang, A. Novack, R. Ding, A. E.-J. Lim, G.-Q. Lo, T. Baehr-Jones, and M. Hochberg, "Ultralow loss single layer submicron silicon waveguide crossing for soi optical interconnect," *Optics Express*, vol. 21, no. 24, pp. 29374–29382, 2013.

[225] A. Melloni, F. Morichetti, and M. Martinelli, "Polarization conversion in ring resonator phase shifters," *Optics Letters*, vol. 29, no. 23, pp. 2785–2787, 2004.

[226] F. Morichetti, A. Canciamilla, C. Ferrari, M. Torregiani, A. Melloni, and M. Martinelli, "Roughness induced backscattering in optical silicon waveguides," *Physical review letters*, vol. 104, no. 3, p. 033902, 2010.

[227] D.-K. Liu, S.-J. Chen, L.-X. You, Y.-L. Wang, S. Miki, Z. Wang, X.-M. Xie, and M.-H. Jiang, "Nonlatching superconducting nanowire single-photon detection with quasi-constant-voltage bias," *Applied Physics Express*, vol. 5, no. 12, p. 125202, 2012.

[228] Y. Korneeva, I. Florya, A. Semenov, A. Korneev, and G. Goltsman, "New generation of nanowire nbn superconducting single-photon detector for mid-infrared," *IEEE transactions on applied superconductivity*, vol. 21, no. 3, pp. 323–326, 2011.

[229] C. Lv, W. Zhang, L. You, P. Hu, H. Wang, H. Li, C. Zhang, J. Huang, Y. Wang, X. Yang, *et al.*, "Improving maximum count rate of superconducting nanowire single-photon detector with small active area using series attenuator," *AIP Advances*, vol. 8, no. 10, p. 105018, 2018.

[230] D.-X. Xu, A. Densmore, P. Waldron, J. Lapointe, E. Post, A. Delâge, S. Janz, P. Cheben, J. H. Schmid, and B. Lamontagne, "High bandwidth soi photonic wire ring resonators using mmi couplers," *Optics Express*, vol. 15, no. 6, pp. 3149–3155, 2007.

[231] J. S. Orcutt, B. Moss, C. Sun, J. Leu, M. Georgas, S. Urosevic, H. Li, J. Sun, M. Weaver, E. Zgraggen, *et al.*, "Low loss waveguide integration within a thin-soi cmos foundry," in *Optical Interconnects Conference, 2012 IEEE*, pp. 25–26, IEEE, 2012.

[232] W. Zhang, L. You, H. Li, J. Huang, C. Lv, L. Zhang, X. Liu, J. Wu, Z. Wang, and X. Xie, "Nbn superconducting nanowire single photon detector with efficiency over 90% at 1550 nm wavelength operational at compact cryocooler temperature," *Science China Physics, Mechanics & Astronomy*, vol. 60, no. 12, p. 120314, 2017.

[233] O. Reshef, M. G. Moebius, and E. Mazur, "Extracting loss from asymmetric resonances in micro-ring resonators," *Journal of Optics*, vol. 19, no. 6, p. 065804, 2017.

[234] M. P. Nezhad, O. Bondarenko, M. Khajavikhan, A. Simic, and Y. Fainman, "Etch-free low loss silicon waveguides using hydrogen silsesquioxane oxidation masks," *Optics Express*, vol. 19, no. 20, pp. 18827–18832, 2011.

[235] M. Gnan, S. Thoms, D. Macintyre, R. De La Rue, and M. Sorel, "Fabrication of low-loss photonic wires in silicon-on-insulator using hydrogen silsesquioxane electron-beam resist," *Electronics Letters*, vol. 44, no. 2, pp. 115–116, 2008.

[236] J. Wang, D. Bonneau, M. Villa, J. W. Silverstone, R. Santagati, S. Miki, T. Yamashita, M. Fujiwara, M. Sasaki, H. Terai, *et al.*, "Chip-to-chip quantum photonic interconnect by path-polarization interconversion," *Optica*, vol. 3, no. 4, pp. 407–413, 2016.

[237] T. Meany, L. A. Ngah, M. J. Collins, A. S. Clark, R. J. Williams, B. J. Eggleton, M. Steel, M. J. Withford, O. Alibart, and S. Tanzilli, "Hybrid photonic circuit for multiplexed heralded single photons," *Laser & photonics reviews*, vol. 8, no. 3, pp. L42–L46, 2014.

[238] L. Liu, Q. Deng, and Z. Zhou, "Subwavelength-grating-assisted broadband polarization-independent directional coupler," *Optics Letters*, vol. 41, no. 7, pp. 1648–1651, 2016.

[239] W. C. Jiang, X. Lu, J. Zhang, O. Painter, and Q. Lin, "Silicon-chip source of bright photon pairs," *Optics Express*, vol. 23, no. 16, pp. 20884–20904, 2015.

[240] X. Tu, C. Song, T. Huang, Z. Chen, and H. Fu, "State of the art and perspectives on silicon photonic switches," *Micromachines*, vol. 10, no. 1, p. 51, 2019.

[241] J. M. Shainline, S. M. Buckley, R. P. Mirin, and S. W. Nam, "Superconducting optoelectronic circuits for neuromorphic computing," *Physical Review Applied*, vol. 7, no. 3, p. 034013, 2017.

[242] J. Chiles, S. Buckley, N. Nader, S. W. Nam, R. P. Mirin, and J. M. Shainline, "Multi-planar amorphous silicon photonics with compact interplanar couplers, cross talk mitigation, and low crossing loss," *APL Photonics*, vol. 2, no. 11, p. 116101, 2017.

[243] L. Chen and Y.-k. Chen, "Compact, low-loss and low-power 8× 8 broadband silicon optical switch," *Optics Express*, vol. 20, no. 17, pp. 18977–18985, 2012.

[244] D. Nikolova, D. M. Calhoun, Y. Liu, S. Rumley, A. Novack, T. Baehr-Jones, M. Hochberg, and K. Bergman, "Modular architecture for fully non-blocking silicon photonic switch fabric," *Microsystems & Nanoengineering*, vol. 3, p. 16071, 2017.

[245] Y. Yun, A. Vetter, R. Stegmueller, S. Ferrari, W. H. Pernice, C. Rockstuhl, and C. Lee, "Superconducting nanowire single-photon spectrometer exploiting cascaded photonic crystal cavities," *arXiv preprint arXiv:1908.01681*, 2019.